

A NEW PROCEDURE FOR
SPECIFIC CUTTING FORCE ASSESSMENT
IN HIGH-SPEED END MILLING

A NEW PROCEDURE FOR
SPECIFIC CUTTING FORCE ASSESSMENT
IN HIGH-SPEED END MILLING

By
Omar E. E. K. M. H. Omar, B.Sc., M.A.Sc.

A Thesis
Submitted to the School of Graduate Studies
in Partial Fulfilment of the Requirements
for the Degree of
Doctor of Philosophy

McMaster University
© Copyright by Omar E.E.K. Omar, April 2010

To My Beloved

DOCTOR OF PHILOSOPHY (2010)
(Mechanical Engineering)

McMaster University
Hamilton, Ontario

TITLE: A NEW PROCEDURE FOR SPECIFIC CUTTING FORCE
ASSESSMENT IN HIGH-SPEED END MILLING
AUTHOR: Omar E. E. K. M. H. Omar, B.Sc. (Cairo University),
M.A.Sc.(McMaster University)
SUPERVISOR: Dr. M. A. Elbestawi
CO-SUPERVISOR: Dr. E.-G. Ng
NUMBER OF PAGES: xxxvii, 260

ABSTRACT

High-speed machining (HSM) concepts were developed in response to productivity, quality and cost concerns. Significant advancements in controls and machining technologies have recently come together to enable the wide spread use of HSM on the plant floor. However, with the advancement of HSM technology, dynamic problems associated with modern machine-tool structures have not been fully addressed and are currently limiting performance in some applications.

A key aspect in the modelling of HSM processes is capturing the dynamics of the system during cutting. Machining over a wide range of rotational speeds necessitates the inclusion of many more higher modes in the system than traditionally considered. In addition many of the instruments used to assess performance such as force dynamometers are not designed to measure the cutting forces at high rotational speeds and hence the specific cutting force values being used are often times not being estimated properly.

Thus the focus of this research is to develop a new procedure for predicting the specific cutting forces in the end-milling process for high-speed machining. An improved mechanistic model to predict the specific cutting force using acceleration data captured from the workpiece fixture was developed. The development of the new procedure has also lead to an improvement in the extraction technique used to establish the modal parameters of a machining system. This new extraction technique was found to be more flexible and easier to use than other available techniques.

The new procedure was investigated to test the effect of choosing the number of modes of the improved modal parameters extraction technique on the estimation of the specific cutting force. The effect of filtrating the acceleration signal and the importance of including the run-out of the cutting tool in the model were also investigated.

The new procedure was tested on different setups and with different cutting force models. Experimental validation of the proposed estimation procedure was carried out, analyzed and compared to the open literature. The new procedure was found to be more accurate while being easier to implement.

ACKNOWLEDGEMENTS

I would like to thank my supervisor Dr. M. A. Elbestawi and my co-supervisor Dr. E.-G. Ng for their support throughout this journey.

I would like to express my gratitude to Dr. N. Tounsi for his valuable advice and support. I owe him much.

Many thanks to the MMRI team, Mr. W. Reynolds and Mr. J. McLaren who helped me finish my experiments in the MMRI laboratory. Also many thanks to Mr. M. Khanna and Mr. M. Bruhis for their assistance in the preparation of my experiments.

Also special thanks to the undergraduate laboratory staff and to the administration of the mechanical engineering department.

The financial support provided by the AUTO21 research program, which is supported by the Government of Canada through the Networks of Centers of Excellence Directorate and Industry, in the form of a Research Scholarship and by McMaster University in the form of teaching assistantship and Departmental Scholarship is gratefully acknowledged.

I would like to express my gratitude to my mother and father, for without their continuous support and prayers this work might not have seen the light. I also would like to thank my bigger family especially my grandmother for her continuous prayers for me and her encouragement.

Last but not least, to my wife, my companion on this lengthy journey, I would like to thank her for her patience with me and with our kids. Without her continuous support I could not have accomplished this humble work. And to my kids, I would like to thank them for being patient even though they never understood what kept me away from them. I hope that, one day, when they grow up and read these words they will be able to understand.

TABLE OF CONTENTS

TITLE	i
TABLE OF CONTENTS	xi
LIST OF TABLES	xv
LIST OF FIGURES	xvii
LIST OF SYMBOLS	xxv
GLOSSARY	xxxvii
1 INTRODUCTION	1
1.1 Motivation & Background	1
1.2 Scope of the Work	3
1.3 Thesis Outline	3
2 LITERATURE REVIEW	7
2.1 Introduction	7
2.2 End-Milling Process	7
2.3 Force Models	10
2.3.1 Analytical models	10
2.3.2 Mechanistic models	11
2.4 Addition of System Imperfections	12
2.4.1 Spindle Tilt	12

2.4.2	Tool run-out	14
2.5	System Dynamics	15
2.6	High-Speed Machining Technology	24
2.6.1	Tooling in HSM	26
2.6.2	Machine tool requirements in HSM	27
2.6.3	Mechanics of cutting in HSM	27
2.6.4	Areas of application of HSM	28
2.7	Instrumentation	30
2.8	Summary	32
3	INVESTIGATION OF MODAL PARAMETERS EXTRACTION	35
3.1	Introduction	35
3.2	Rational Fraction Polynomial	36
3.3	Investigation of the RFP Method	38
3.4	Summary	48
4	THE MODIFIED RFP METHOD	51
4.1	Introduction	51
4.2	Optimized RFP Method	51
4.2.1	Formulation of the constraints	54
4.2.2	Formulation of the objective function	54
4.2.3	Assessment of the objective function	55
4.2.4	Convergence (Stopping) criteria	58
4.2.5	Coding the variables	60
4.2.6	Flexibility of the Optimized Rational Fraction Polynomial (ORFP) method	62
4.2.7	Investigation of the ORFP method	69
4.3	Summary	71
5	MODEL FOR CUTTING FORCE SIMULATION	79
5.1	Introduction	79
5.2	Basic Model	80
5.2.1	Background	80
5.2.2	Rigid tool/rigid system model	80
5.3	Extended Model	85

TABLE OF CONTENTS

5.3.1	Introduction	85
5.3.2	Force model	87
5.3.3	System dynamics	98
5.3.4	Run-out	102
5.4	Summary	104
6	EXPERIMENTAL DESIGN & SETUP	107
6.1	Introduction	107
6.2	Methodology	107
6.3	Experimental Design Consideration	110
6.3.1	Cutting test related considerations	110
6.3.2	Impact hammer test considerations	116
6.3.3	General considerations	119
6.4	Experimental Setup	119
6.4.1	Cutting test setup	119
6.4.2	Cutting test matrix	123
6.4.3	Dynamic test setup	124
6.4.4	Tool run-out and unbalance mass estimation	125
6.4.5	Cutting test material's properties	127
6.5	Summary	129
7	RESULTS & DISCUSSION	131
7.1	Introduction	131
7.2	Re-building of Tlusty's Model	131
7.3	Obtaining the SCF from the Force Signal	133
7.4	Obtaining the SCF from the Acceleration Signal	134
7.5	Analysis of the Suggested Dynamic Model	141
7.5.1	Selection of the number of modes	141
7.5.2	Filtration of the simulated acceleration	145
7.6	Run-out Effect	151
7.7	Verification of the Suggested Estimation Procedure	160
7.7.1	Mechanistic force model	160
7.7.2	Analytical model	182
7.8	Conclusion	185

8 SUMMARY & FUTURE WORK	191
8.1 Summary	191
8.2 Future Work	196
APPENDICES	199
A DERIVATIONS	201
A.1 Temperature Dependent Material's Density	201
A.2 Derivation of the RFP Model in Time Domain	202
B UNBALANCE MASS ESTIMATION	207
B.1 Unbalance Mass	207
C PROPERTIES OF TEST MATERIAL	211
C.1 Tensile Test	211
C.2 Specific Heat Capacity C_p	212
C.3 Thermal Conductivity K	213
D CUTTING TEST RESULTS	217
D.1 Introduction	217
D.2 Fixture's Acceleration using Setup # 1	218
D.3 Fixture's Acceleration using Setup # 2	240
BIBLIOGRAPHY	253

LIST OF TABLES

- 2.1 Summary of mechanistic models 13
- 3.1 Modal parameters for experimental data in Figure 3.1 fitted to 25 modes 49
- 4.1 Summary of different objective functions' convergence 58
- 4.2 Comparison of different objective functions' outcome for different systems 58
- 4.3 Modal parameters after fitting the experimental data in Figure 3.1
using the Forsythe method 63
- 4.4 Modification of the modal parameters obtained from fitting the exper-
imental data in Figure 3.1 using the Forsythe method 65
- 4.5 Modal parameters for experimental data in Figure 3.1 using ORFP af-
ter modifying the modal parameters obtained from using the Forsythe
method 65
- 4.6 Modal parameters for experimental data in Figure 3.1 using ORFP af-
ter modifying the modal parameters obtained from using the Forsythe
method 68
- 6.1 Varying cutting condition used in the calibration process 111
- 6.2 Fixed condition used in the cutting process 111
- 6.3 Test matrix used for the calibration of the SCF 123
- 6.4 Test matrix used for the verification of the calibrated SCF 123
- 6.5 Constants used in Equations 5.29 and 5.30 (Johnson-Cook material
model) for Aluminum 6061-T6 used in this study 127
- 7.1 Summary of in-cut time for different cutting tests 134

7.2	SCF estimated using the acceleration	135
7.3	Demonstration of how to estimate the SCF using the acceleration . .	135
7.4	Optimum number of modes and their corresponding modal parameters	145
7.5	Estimated SCF using the fixture acceleration for setup # 1	161
7.6	SCF predicted using Equations 6.1 - 6.3 and compared against the experimental ones using setup # 1	162
7.7	Values used in Equations 7.4 - 7.6	163
7.8	Estimated SCF using the fixture's acceleration for setup # 2	167
7.9	SCF predicted using Equations 6.1 - 6.3 and compared against the experimental ones for setup # 2.	167
7.10	Mass and damping coefficient used in Equations 7.10 and 7.11	172
7.11	Mass and damping coefficient used in Equations 7.10 and 7.11 for tests 5 - 9	173
7.12	Mass and damping coefficient used in Equations 7.10 and 7.11	176
7.13	Mass and damping coefficient used in Equations 7.10 and 7.11	176
7.14	Percentage difference between SCF predicted using fixture setup # 1 and fixture setup # 2	177
7.15	Analytical parameters calibrated using setup # 1	186
C.1	Specific heat capacity of Aluminum 6061-T6 varying with temperature as obtained from [90]	212
C.2	Thermal conductivity of Aluminum 6061-T6 varying with temperature as obtained from [90]	213

LIST OF FIGURES

2.1	Basic types of milling [7].	9
2.2	Nomenclature of the milling cutter [7].	9
2.3	Operational modes of the end milling process [7].	9
2.4	Definition of tilt.	13
2.5	Including the tilt in the cutting force model.	14
2.6	Definition of run-out.	14
2.7	Including the history of previous cuts [6].	15
2.8	Summary of curve fitting methods [66].	20
2.9	Summary of curve fitting methods in the frequency domain [66].	20
2.10	Summary of curve fitting methods in the time domain [66].	21
2.11	Effect of cutting speed on cutting temperature [74].	25
2.12	Reviewing Dr. Solomon’s theory [72].	25
2.13	Definition of HSM [73].	26
2.14	HSM application range [6].	29
2.15	A typical process for measuring the cutting forces.	30
2.16	Typical strain gauge device [79].	31
2.17	Typical load cell [81].	32
3.1	FRF of the fixture in the X -direction.	39
3.2	FRF of the cutting tool in the X -direction.	40
3.3	Effect of the cut-off ratio and the total number of suggested fitted modes on the number of stable modes for the fixture in the X -direction.	42

3.4	Effect of the cut-off ratio and the total number of suggested fitted modes on the number of stable modes for the cutting tool in the X -direction.	42
3.5	Effect of the cut-off ratio and the total number of suggested fitted modes on the mean percentage error due to fitting for the fixture in the X -direction.	43
3.6	Effect of the cut-off ratio and the total number of suggested fitted modes on the mean percentage error due to fitting for the cutting tool in the X -direction.	43
3.7	Effect of the cut-off ratio and the total number of suggested fitted modes on the maximum percentage error due to fitting for the fixture in the X -direction.	44
3.8	Effect of the cut-off ratio and the total number of suggested fitted modes on the maximum percentage error due to fitting for the cutting tool in the X -direction.	44
3.9	Effect of the cut-off ratio and the total number of suggested fitted modes on the ratio of the number of stable modes to the total number of suggested fitted modes for the fixture in the X -direction.	45
3.10	Effect of the cut-off ratio and the total number of suggested fitted modes on the ratio of the number of stable modes to the total number of suggested fitted modes for the cutting tool in the X -direction.	45
3.11	FRF of the cutting tool fitted to 25 modes.	49
4.1	Flow chart of the suggested ORFP method.	53
4.2	Investigation of different objective functions.	60
4.3	Effect of varying the number of iterations on the mean and maximum percentage error between the fitted and the experimental FRF respectively.	60
4.4	Coding procedure.	62
4.5	Fixture FRF, X -direction, fitted to 7 modes using the Forsythe method.	63
4.6	Fixture FRF, X -direction, regenerated after eliminating modes 1 and 6 using the Forsythe method.	66

LIST OF FIGURES

4.7	Fixture FRF, X-direction, regenerated after eliminating modes 1 and 6 and modifying the remaining mode's natural frequencies using the Forsythe method.	66
4.8	Fixture FRF, X-direction, regenerated using the ORFP method after eliminating modes 1 and 6 and modifying the remaining modes to match the experimental ones.	67
4.9	Fixture FRF, X-direction, regenerated using the ORFP method after eliminating modes 1 and 6 and modifying the remaining modes to match the experimental ones and guessing the initial values of the damping.	69
4.10	Effect of varying the suggested number of fitted modes on the normalized objective function (χ) using the ORFP method over different number iterations.	73
4.11	Effect of varying the suggested number of fitted modes on the normalized objective function (χ) using the ORFP method.	74
4.12	Effect of varying the suggested number of fitted modes on the mean percentage error between the fitted and the experimental FRF.	75
4.13	Investigation of the variation of the suggested number of fitted modes on the maximum percentage error between the fitted and the experimental FRF.	76
4.14	Investigation of the variation of the suggested number of fitted modes on the simulation time.	77
5.1	Trochoidal path.	81
5.2	Simulation of the end milling process, engagement angle.	81
5.3	Simulation of the end milling process, teeth engagement.	82
5.4	Cutting tool discretization.	82
5.5	Cutting force convention.	84
5.6	Flow chart of basic simulation model.	86
5.7	Orthogonal cutting.	90
5.8	Merchant's model adapted to end milling process.	91
5.9	Analytical cutting force model.	91
5.10	Merchant's circle.	93
5.11	Model dynamics.	99

5.12 Convolution theorem.	100
5.13 Relative displacement between the tool & the workpiece/fixture [11].	102
5.14 Definition of run-out.	103
5.15 Centrifugal force due to run-out.	104
6.1 Summary of description of cutting test.	113
6.2 Fixture design.	114
6.3 Dynamometer alignment to the machine tool’s axis using a dial gauge.	114
6.4 Power supply used to amplify the accelerometer’s signal.	115
6.5 Miniature accelerometer.	116
6.6 Description of miniature accelerometer mounting and usage.	117
6.7 Accelerometers used in the hammer test.	118
6.8 Usage of hot melt adhesive to fix the accelerometer to the fixture. . .	119
6.9 Details of fixture setup # 1.	120
6.10 Details of fixture setup # 2.	121
6.11 Machine tool used in conducting the experiments.	121
6.12 Schematic for the experimental setup.	122
6.13 Schematic for the cutting tool’s dynamic test setup.	125
6.14 Schematic for the fixture dynamic test setup.	126
6.15 Dial gauge indicator used to measure the tool/tool holder’s run-out. Curtesy [http://www.mitutoyo.com].	126
7.1 Comparison of Tlusty’s model as published in [74] (a) and the re-built model (b).	132
7.2 Cutting forces for cutting test # 2, 30k rev./min, see notes page 133.	136
7.3 Cutting forces for cutting test # 7, 58k rev./min, see notes page 133.	137
7.4 Estimation of the SCF using the fixture’s acceleration for cutting test # 2, 30k rev./min.	138
7.5 Estimation of the SCF using the fixture’s acceleration for cutting test # 7, 58k rev./min.	139
7.6 Explanation of the suggested estimation method of the SCF using the fixture’s acceleration for cutting test # 2, 30k rev./min.	140
7.7 Investigation of the effect of choosing the number of modes on the estimation of the SCF using the fixture’s acceleration for cutting test # 2, 30k rev./min.	143

LIST OF FIGURES

7.8 Investigation of the effect of choosing the number of modes on the estimation of the SCF using the fixture’s acceleration for cutting test # 7, 58k rev./min. 144

7.9 Acceleration signal (experimental vs. simulated) before filtration for cutting test # 1, 30k rev./min. 147

7.10 FFT of the acceleration signal (experimental vs. simulated) before filtration for cutting test # 1, 30k rev./min. 148

7.11 Acceleration signal (experimental vs. simulated) after filtration for cutting test # 1, 30k rev./min. 149

7.12 FFT of the acceleration signal (experimental vs. simulated) after filtration for cutting test # 1, 30k rev./min. 150

7.13 Investigation of the importance of including the run-out in the dynamic model. Acceleration data used is for test # 2 (*X*-direction), 30k rev./min. 153

7.14 Investigation of the importance of including the run-out in the dynamic model. Acceleration data used is for test # 2 (*Y*-direction), 30k rev./min. 154

7.15 Investigation of the importance of including the run-out in the dynamic model. Acceleration data used is for test # 2 (*Z*-direction), 30k rev./min. 155

7.16 Investigation of the importance of including the run-out in the dynamic model. Acceleration data used is for test # 7 (*X*-direction), 58k rev./min. 156

7.17 Investigation of the importance of including the run-out in the dynamic model. Acceleration data used is for test # 7 (*Y*-direction), 58k rev./min. 157

7.18 Investigation of the importance of including the run-out in the dynamic model. Acceleration data used is for test # 7 (*Z*-direction), 58k rev./min. 158

7.19 Receptance of the fixture (setup # 1) in the three cutting directions; *X*, *Y*, and *Z*. 159

7.20 Variation of K_t , K_r , and K_a with the cutting velocity and using setup # 1. 164

7.21 Variation of K_t , K_r , and K_a with the feed/tooth using setup # 1. . . 165

7.22 Variation of the frictional component of the SCF with the cutting speed as published in [96]. 166

7.23 Variation of the SCF, frictional (a) and normal (b), with the effective chip thickness as published in [96]. 166

7.24 Variation of the SCF, frictional (a) and normal (b), with the feedrate as published in [97]. 166

7.25	Modeling of dynamometer and fixture to reproduce the measured forces $F_{measured}$ (X and Y directions).	169
7.26	Modeling of dynamometer and fixture to reproduce the measured forces $F_{measured}$ (Z -direction).	169
7.27	Regenerated measured forces plotted against actual measure forces using the dynamometer for test # 1 and using setup # 1.	170
7.28	Regenerated measured forces plotted against actual measure forces using the dynamometer for test # 5 and using setup # 1.	171
7.29	Regenerated measured forces obtained from the displacement of the dynamometer and plotted against actual measure forces for test # 1 and using setup # 1.	174
7.30	Regenerated measured forces obtained from the displacement of the dynamometer and plotted against actual measure forces for test # 5 and using setup # 1.	175
7.31	Regenerated measured force in the Z -direction using a mass of 1.1 kg.	176
7.32	Variation of K_t , K_r , and K_a with the cutting velocity and using setup # 2.	178
7.33	Variation of K_t , K_r , and K_a with the feed/tooth using setup # 2. . .	179
7.34	Comparison between the cutting forces' magnitude generated using the mechanistic model and the experimental one using setup # 1.	180
7.35	Correlation between the resultant experimental cutting force and the simulated one (tooth # 1).	181
7.36	Correlation between the resultant experimental cutting force and the simulated one (tooth # 2).	181
7.37	Comparison between the cutting forces's magnitude generated using different setups and different force models on tooth # 1 in all three directions X , Y , and Z	187
7.38	Comparison between the forces generated using different setups and different force models on tooth # 2 in all three directions X , Y , and Z .	188
B.1	Regenerating a CAD model of the cutting tool's holder using actual dimensions.	208
C.1	Curve fitting tensile test data to obtain the constants A , B , and n of Equations 5.29 and 5.30.	212

LIST OF FIGURES

C.2 Specific heat variation with temperature for Aluminum 6061-T6. . . . 213

C.3 Thermal conductivity variation with temperature for Aluminum 6061-T6. 214

D.1 Fixture’s acceleration using setup # 1 - calibration test # 1. 218

D.2 Fixture’s acceleration using setup # 1 - calibration test # 2. 219

D.3 Fixture’s acceleration using setup # 1 - calibration test # 3. 220

D.4 Fixture’s acceleration using setup # 1 - calibration test # 4. 221

D.5 Fixture’s acceleration using setup # 1 - calibration test # 5. 222

D.6 Fixture’s acceleration using setup # 1 - calibration test # 6. 223

D.7 Fixture’s acceleration using setup # 1 - calibration test # 7. 224

D.8 Fixture’s acceleration using setup # 1 - calibration test # 8. 225

D.9 Fixture’s acceleration using setup # 1 - calibration test # 9. 226

D.10 Fixture’s acceleration using setup # 1 - verification test # 1. 227

D.11 Fixture’s acceleration using setup # 1 - verification test # 2. 228

D.12 Fixture’s acceleration using setup # 1 - verification test # 3. 229

D.13 Fixture’s acceleration using setup # 1 - verification test # 4. 230

D.14 Fixture’s acceleration using setup # 1 - verification test # 5. 231

D.15 Fixture’s acceleration using setup # 1 - verification test # 6. 232

D.16 Fixture’s acceleration using setup # 1 - verification test # 7. 233

D.17 Fixture’s acceleration using setup # 1 - verification test # 8. 234

D.18 Fixture’s acceleration using setup # 1 - verification test # 9. 235

D.19 Fixture’s acceleration using setup # 1 - verification test # 10. 236

D.20 Fixture’s acceleration using setup # 1 - verification test # 11. 237

D.21 Fixture’s acceleration using setup # 1 - verification test # 12. 238

D.22 Fixture’s acceleration using setup # 1 - verification test # 13. 239

D.23 Fixture’s acceleration using setup # 1 - calibration test # 1. 240

D.24 Fixture’s acceleration using setup # 2 - calibration test # 2. 241

D.25 Fixture’s acceleration using setup # 2 - calibration test # 3. 242

D.26 Fixture’s acceleration using setup # 2 - calibration test # 4. 243

D.27 Fixture’s acceleration using setup # 2 - calibration test # 5. 244

D.28 Fixture’s acceleration using setup # 2 - calibration test # 6. 245

D.29 Fixture’s acceleration using setup # 2 - calibration test # 7. 246

D.30 Fixture’s acceleration using setup # 2 - calibration test # 8. 247

LIST OF FIGURES

D.31 Fixture's acceleration using setup # 2 - calibration test # 9. 248
D.32 Fixture's acceleration using setup # 2 - verification test # 1. 249
D.33 Fixture's acceleration using setup # 2 - verification test # 2. 250

LIST OF SYMBOLS

α	Radial helix angle, (rad)
$\alpha(\omega)$	System's receptance in frequency domain, (m/N)
α_o	A complex constant used in Equation 2.8, (m/N)
$\alpha_{j,k}(\omega)$	Receptance response at an angular velocity ω at point j due to a force at point k , (m/N)
β	Helix angle, (rad)
\ddot{x}	System's acceleration in the X -direction, (m/s ²)
\ddot{x}^i	System's acceleration in the X -direction at time i , (m/s ²)
\ddot{y}^i	System's acceleration in the Y -direction at time i , (m/s ²)
$\delta(t)$	Response of the system subject to an impulse force, (m)
$\Delta\phi$	Angular increment corresponding to a time increment Δt , (rad)
$\Delta\psi$	Angular increment when moving on the tooth's helix from one discretization level n to another $n + 1$, (rad)
$\Delta A_{s,j,n}^i$	Instantaneous elemental area of the shear zone at time i , tooth j , and discretization n , (m ²)
Δd_a	Axial depth of cut increment, (m)

$\Delta F_{a,j,n}^i$	Instantaneous elemental axial cutting force (vertical direction) at time i , tooth j , and discretization level n , (N)
$\Delta F_{c,j,n}^i$	Instantaneous elemental cutting force on rake face at time i , tooth j , and discretization level n , (N)
$\Delta F_{e,n}^i$	Instantaneous elemental centrifugal force due to run-out a time i , tooth j , and discretization level n , (N)
$\Delta F_{r,j,n}^i$	Instantaneous elemental radial cutting force (normal to feed direction) at time i , tooth j , and discretization level n , (N)
$\Delta F_{rx,j,n}^i$	Instantaneous elemental radial cutting force (normal to feed direction) in the X -direction at time i , tooth j , and discretization level n , (N)
$\Delta F_{ry,j,n}^i$	Instantaneous elemental radial cutting force (normal to feed direction) in the Y -direction at time i , tooth j , and discretization level n , (N)
$\Delta F_{s,j,n}^i$	Instantaneous elemental shearing force at time i , tooth j , and discretization level n , (N)
$\Delta F_{t,j,n}^i$	Instantaneous elemental tangential cutting force (feed direction) at time i , tooth j , and discretization level n , (N)
$\Delta F_{tx,j,n}^i$	Instantaneous elemental tangential cutting force (feed direction) in the X -direction at time i , tooth j , and discretization level n , (N)
$\Delta F_{ty,j,n}^i$	Instantaneous elemental tangential cutting force (feed direction) in the Y -direction at time i , tooth j , and discretization level n , (N)
ΔF_c	Elemental cutting force on rake face acting inwards, (N)
ΔF_r	Elemental force in radial direction, (N)
Δf_t	Feed per tooth increment corresponding to a time increment Δt , (m/tooth)
ΔF_{cc}	Elemental cutting force on rake face and acting axially upwards, (N)
ΔF_{cr}	Radial component (normal to feed direction) of the elemental cutting force on rake face acting inwards, (N)

LIST OF SYMBOLS

ΔF_{ct}	Tangential component (feed direction) of the elemental cutting force on rake face acting inwards, (N)
$\Delta m_{e,n}$	Discretized unbalance mass at discretization level n , (kg)
$\Delta N_{c,j,n}^i$	Instantaneous elemental force normal to $\Delta F_{c,j,n}^i$ at time i , tooth j , and discretization level n , (N)
$\Delta N_{s,j,n}^i$	Instantaneous elemental cutting force normal to shearing force $\Delta F_{s,j,n}^i$ at time i , tooth j , and discretization level n , (N)
ΔN_c	Elemental cutting force normal to ΔF_c , (N)
ΔN_{cr}	Radial component (normal to feed) of the elemental cutting force normal to ΔF_c , (N)
ΔN_{ct}	Tangential component of the elemental cutting force normal to ΔF_t , (N)
$\Delta x_v(t)$	System's response at time t due to a sequence of impulses (Duhamel's integral), (m)
$\dot{\gamma}$	Strain rate encountered during cutting, (s^{-1})
$\dot{\gamma}_{j,n}^i$	Instantaneous strain rate at time i , tooth j , and discretization level n , (s^{-1})
$\dot{\gamma}_o$	Reference strain rate, (s^{-1})
\dot{x}	System's velocity in the X -direction, (m/s)
\dot{x}^i	System's velocity in the X -direction at time i , (m/s)
\dot{y}^i	System's velocity in the Y -direction at time i , (m/s)
η_r	Damping loss factor for mode r
γ	Strain encountered during cutting
$\Gamma_{j,n}^i$	Instantaneous fraction of the total heat generated in the primary deformation zone at time i , tooth j , and discretization level n
$\gamma_{j,n}^i$	Instantaneous strain at time i , tooth j , and discretization level n , (s^{-1})

\hat{y}_f	Fitted value of FRF, $f = 1 \dots n$, n is the total number of points in the record
λ	System's pole
λ^*	Conjugate of system's pole
λ_r^*	Conjugate of system's pole for mode r
λ_r	Run-out angle, (rad)
λ_r	System's pole for mode r
μ	Ratio between ΔF_t and ΔF_r in Equation 5.2, friction coefficient between F_c and N_c in Equation 5.20
μ_c	Coefficient of friction between the rake face (upwards) and the chip
ω	Rotation angle, (rad/s)
ω_d	Damped natural frequency, (rad/s)
ω_r	Natural frequency of mode r , (rad/s)
$\omega_{d,r}$	Damped natural frequency for mode r , (rad/s)
Φ	A rotation angle that reflects the influence of out-of-range modes, used in Equation 2.8
ϕ	Angular position, (rad)
ϕ_e	End angle, angular position at which the cutter's tooth ends cutting, (rad)
ϕ_i	Instantaneous cutter's angular position, (rad)
ϕ_n	Angular cutter position at discretization level n in Figure 5.6, (rad)
ϕ_p	Pitch angle, the angle between one tooth and the next one, (rad)
ϕ_s	Starting angle, angular position at which the cutter's tooth starts cutting, (rad)
ϕ_{n+1}	Angular cutter position at discretization level $n + 1$ in Figure 5.6, (rad)

LIST OF SYMBOLS

$\rho_{j,n}^i$	Instantaneous material density at time i , tooth j , and discretization level n , (kg/m ³)
σ	Damping coefficient
$\sigma_{ut,i,n}^i$	Instantaneous material's tensile strength at time i , tooth j , and discretization level n , (N/m ²)
σ_r	Damping coefficient for mode r
$\tau_{ut,i,n}^i$	Instantaneous material's shearing strength at time i , tooth j , and discretization level n , (N/m ²)
$\theta_{f,j,n}^i$	Instantaneous average temperature rise in the secondary deformation zone at time i , tooth j , and discretization level n , (°C)
$\theta_{m,j,n}^i$	Instantaneous maximum temperature rise in the secondary deformation zone at time i , tooth j , and discretization level n , (°C)
$\theta_{s,j,n}^i$	Instantaneous average temperature rise in the primary deformation zone at time i , tooth j , and discretization level n , (°C)
φ_s	Shear angle
ξ_j	Starting values of the damping ratios for Equation 4.7 for mode j
ξ_r	Damping ratio of mode r
${}_r A_{jk}^*$	Complex conjugate of residue ${}_r A_{jk}$
${}_r A_{jk}$	Residue corresponding to mode r at point j due to a force at point k
A	Yield of test material in Johnson-Cook equation, (MPa), constant in Equation 5.55, system's residue in Equation 3.1
A^*	Conjugate of system's residue
A_r^*	Conjugate of system's residue for mode r
A_i	Calibration coefficients for Equations 5.12, 5.13 and 5.15 where $i \in 1, 2, 3$ respectively

a_i	Calibration coefficients for Equations 5.12, 5.13 and 5.15 where $i \in 1, 2, 3$ respectively
A_r	System's residue for mode r , constants used in Equation 2.8
B	Strain hardening of test material, used in Johnson-Cook equation, (MPa)
b_i	Calibration coefficients for Equations 5.12, 5.13 and 5.15 where $i \in 1, 2, 3$ respectively
B_r	Constants used in Equation 2.8
C	Strain rate constant of test material in Johnson-Cook equation
$C1$	Mean absolute percentage error between experimental and fitted FRF
$C2$	Maximum absolute percentage error between experimental and fitted FRF
$C_{p,j,n}^i$	Instantaneous specific heat of test material at time i , tooth j , and discretization level n , (J/kg $^{\circ}$ C)
c_i	Calibration coefficients for Equations 5.12, 5.13 and 5.15 where $i \in 1, 2, 3$ respectively
C_r	Real quantity constant for mode r used in Equation 2.9
C_x	Damping matrix or vector of the system's equation of motion in the X -direction, (Nsm $^{-1}$)
c_x	System's damping in the X -direction, (Nsm $^{-1}$)
c_y	System's damping in the Y -direction, (Nsm $^{-1}$)
d_r	Radial depth of cut, (m)
e	Run-out value, eccentricity, (m)
$F(\omega)$	Force applied on the system in the frequency domain, (N)
$F_{m,j,n}^i$	Instantaneous momentum force at time i , tooth j , and discretization level n , (N)

LIST OF SYMBOLS

$f_{t,j,n}^i$	Instantaneous feed per tooth at time i , tooth j , and discretization level n , (m/tooth)
F_x^i	Instantaneous cutting force in the X -direction at time i , (N)
F_x^i	Instantaneous force applied to the system in the X -direction at time i , (N)
F_y^i	Instantaneous cutting force in the Y -direction at time i , (N)
F_y^i	Instantaneous force applied to the system in the Y -direction at time i , (N)
F_z^i	Instantaneous cutting force in the Z -direction at time i , (N)
F_C	Cost function
F_c	Cutting force on rake face acting inwards, (N)
F_n	Cutting force in normal direction (normal to feed direction), (N)
F_t	Cutting force in tangential direction (direction of feed), (N)
f_t	Feed per tooth, (m/tooth)
F_x	External force applied to the system in the X -direction, (N)
F_{cc}	Cutting force on rake face and acting axially upwards, (N)
f_{n_j}	Starting values of the natural frequencies for Equation 4.7 for mode j , (Hz)
F_{xk}	Cutting force in the X -direction corresponding to an incremental time unit Δt , Figure 5.6, (N)
F_{yk}	Cutting force in the Y -direction corresponding to an incremental time unit Δt , Figure 5.6, (N)
h	Instantaneous chip thickness, (m)
$H(\omega)$	System's receptance in the frequency domain, (m/N)

$H(\omega)_{exp,i}$	Experimental receptance in frequency domain, $i = 1 \dots n$, n is the total number of points in the record, (m/N)
$H(\omega)_{fit,i}$	Fitted receptance in frequency domain, $i = 1 \dots n$, n is the total number of points in the record, (m/N)
$h(t)$	System's transfer function in the time domain
i	Time index, Ch.5
j	Complex operator in Equation 3.1, tooth number, Ch.5
k	Iteration number
$K_{j,n}^i$	Instantaneous thermal conductivity of test material at time i , tooth j , and discretization level n , (J/kg°C)
K_a	Specific cutting force in axial direction (vertical direction), (N/m ²)
K_n	Specific cutting force in normal direction (normal to feed direction), (N/m ²)
K_r	Specific cutting force in radial direction (normal to feed direction), (N/m ²)
K_t	Specific cutting force in tangential direction (direction of feed), (N/m ²)
K_x	Stiffness matrix or vector of the system's equation of motion in the X -direction, (Nm ⁻¹)
k_x	System's stiffness in the X -direction, (Nm ⁻¹)
k_y	System's stiffness in the Y -direction, (Nm ⁻¹)
m	Temperature exponent in Johnson-Cook equation, number of teeth engaged in cut, Figure 5.6
M_x	Mass matrix or vector of the system's equation of motion in the X -direction, (kg)
m_x	System's mass in the X -direction, (kg)
m_y	System's mass in the Y -direction, (kg)

LIST OF SYMBOLS

N	Total number of modes used in Equation 3.3
n	Discretization level, Ch.5, total number of points of the Experimental/Fitted FRF in Equations 3.5, and 3.6
N_c	Cutting force normal to F_c , (N)
OF	Objective function
OF_i	Objective function value at iteration i
$p_{f,j,n}^i$	Instantaneous rate of heat generation in the secondary deformation zone that takes place at time i , tooth j , and discretization level n
$p_{m,j,n}^i$	Instantaneous rate of energy consumption in cutting at time i , tooth j , and discretization level n
$p_{s,j,n}^i$	Instantaneous rate of heat generation in the primary shearing zone that takes place at time i , tooth j , and discretization level n
$R_{j,n}^i$	Instantaneous thermal number at time i , tooth j , and discretization level n
r_e	Center of gravity of the unbalance mass, (m)
T	Temperature, ($^{\circ}\text{C}$)
t	Time operator, (s)
$t_{c,j,n}^i$	Instantaneous uncut chip thickness at time i , tooth j , and discretization level n , (m)
$T_{j,n}^i$	Instantaneous temperature of the shearing zone that takes place at time i , tooth j , and discretization level n , ($^{\circ}\text{C}$)
$T_{max,j,n}^i$	Instantaneous maximum cutting temperature at time i , tooth j , and discretization level n , ($^{\circ}\text{C}$)
t_c	Uncut chip thickness, (m)
T_m	Melting temperature of the material tested, ($^{\circ}\text{C}$)

T_r	Reference temperature, i.e. room temperature, ($^{\circ}\text{C}$)
$u_{a,j,n}^i$	Instantaneous specific energy to produce a new uncut surface at time i , tooth j , and discretization level n , (hp/in/min)
$u_{f,j,n}^i$	Instantaneous specific energy due to friction at time i , tooth j , and discretization level n , (hp/in/min)
$u_{j,n}^i$	Instantaneous total specific energy during machining at time i , tooth j , and discretization level n , (hp/in/min)
$u_{m,j,n}^i$	Instantaneous specific energy required to accelerate the chip at time i , tooth j , and discretization level n , (hp/in/min)
$u_{s,j,n}^i$	Instantaneous specific energy due to shearing at time i , tooth j , and discretization level n , (hp/in/min)
V	Cutting velocity, (m/min)
$v_{f,j,n}^i$	Displacement in the chip thickness direction for the fixture at time i , tooth j , and discretization level n , (m)
$v_{r,j,n}^i$	Displacement in the chip thickness direction due to run-out at time i , tooth j , and discretization level n , (m)
$v_{t,j,n}^i$	Displacement in the chip thickness direction for the tool at time i , tooth j , and discretization level n , (m)
$v_{f,j,n}^p$	Previous displacement in the chip thickness direction for the fixture for tooth j , and discretization level n , (m)
$v_{t,j,n}^p$	Previous displacement in the chip thickness direction for the tool for tooth j , and discretization level n , (m)
V_c	Velocity on the rake face, (m/min)
X	Coordinate system's axis in the feed direction
x	System's displacement in the X -direction, (m)
$X(\omega)$	System's response in the frequency domain, (m)

LIST OF SYMBOLS

x^i	System's displacement in the X -direction at time i , (m)
$x_{f,j,n}^i$	Fixture's displacement in the X -direction at time i , tooth j , and discretization level n , (m)
$x_{t,j,n}^i$	Cutting tool's displacement in the X -direction at time i , tooth j , and discretization level n , (m)
Y	Coordinate system's axis normal to the feed direction
y^i	System's displacement in the Y -direction at time i , (m)
$y_{f,j,n}^i$	Fixture's displacement in the Y -direction at time i , tooth j , and discretization level n , (m)
$y_{t,j,n}^i$	Cutting tool's displacement in the Y -direction at time i , tooth j , and discretization level n , (m)
y_f	Experimental value of FRF, $f = 1 \dots n$, where n is the total number of points in the record
Z	Coordinate system's axis in the vertical direction
z_n	Vibration of the cutting tool at time n , (m)
$z_{f,n-i}$	Vibration of the fixture at time $n - i$, $i \in 1, 2, 3$, (m)
$z_{f,n}$	Vibration of the fixture at time n , (m)
z_{n-i}	Vibration of the cutting tool at time $n - i$, $i \in 1, 2, 3$, (m)

GLOSSARY

DAQ	Data Acquisition.
FFT	Fast Fourier Transform.
FRF	Frequency Responce Function.
HSM	High-Speed Machining.
MIMO	Multiple-Input Multiple-Output.
ORFP	Optimized Rational Fraction Polynomial.
R & D	Research and Development.
RFP	Rational Fraction Polynomial.
SCF	Specific Cutting Forces.
SIMO	Single-Input Multiple-Output.
SISO	Single-Input Single-Output.
WWII	World War II.

CHAPTER 1

INTRODUCTION

1.1 Motivation & Background

The milling process is one of the most common metal removal operations used in industry [1]. In the last couple of decades the trend in the field of automotive and aerospace parts as well as thin-walled component manufacturing was to strive for better part quality as well as low cost and high efficiency production in order to compete on a global scale [2]. As it evolved, high-speed machining (HSM) played a successful and increasing role in this competition as it helped in producing very intricately shaped thin walled, and pocketed surfaces at less cost and with higher productivity. This had a direct impact on the part complexity that is achievable and on time to market for new parts [3]. Moreover, parts produced by HSM are

characterized by their lower surface roughness and reduced amount of distortion. However, with the advancement of HSM technology dynamic problems related to modern machine-tool structures are currently limiting performance.

Conventional machine-tools generally have rotational speeds up to 10000 RPM; this can generate a tooth passing frequency of 600 Hz for a 4 flute end mill. For such a low operating frequency, there is often only one dominant mode that affects the cutting process. In addition, the dynamometers used can measure the cutting forces without the need to compensate for the dynamic effects of the system [4]. In HSM, spindle speeds are rated as high as 60k rev./min, if not higher, which can generate a tooth passing frequency of 4000 Hz for a 4 flute end mill. For such a high operating frequency, it cannot be assumed that one mode will be dominant and thus modeling must include the higher modes of the multi-degree of freedom system. Also the high operating frequency might interfere with the natural frequency of the dynamometer. This will necessitate the compensation of this effect when estimating the cutting forces.

The prediction of cutting forces is becoming increasingly important as more process planning activity is being done prior to actual machining studies. This is being done in an effort to keep expenses for the research and development (R & D) from increasing and generating significant overhead expenses. Therefore this activity must be low cost and easy to implement. In general, experimentally driven process improvements have high investment costs and are often times not easy to interpret. Currently establishing practical cutting conditions in HSM for a particular part is often done using trial and error and/or is based on conservative cutting conditions. In addition to that when new parts are introduced or a change in the design of the original part occurs, the previous procedure will need to be repeated at significant cost. This clearly results in lower productivity and added cost. Due to these limitations there

is a trend within industry to move more toward a model-based product development process. This trend is driven by the need to reduce product development time and cost.

A better solution to address this problem is to model the HSM process to be able to better predict the cutting forces by taking into account the various parameters that will affect the quality of the end product. Simulating such processes will assist manufacturers in selecting cutting conditions in a relatively short time and at low cost. Recent advancements in personal computers make the use of simulation of those processes practical for many applications and are currently expanding their use in industry.

1.2 Scope of the Work

The scope of this dissertation is on the development of a new and improved model that is able to predict the specific cutting force specific cutting forces (SCF) using the acceleration of the system comprised of the workpiece fixture and the cutting tool used in the cutting process during HSM. The model is developed using a sharp solid carbide end mill, it also uses a set of general purpose accelerometers. The development of the dynamic model has led to other improvements in the area of modal parameters identification. The model features and problems will be treated and developed independently and then integrated to form the final model.

1.3 Thesis Outline

In the following, a brief description of the thesis's structure is given as a fast overview of the different issues dealt with throughout this dissertation.

This thesis is comprised of eight chapters and four appendices. Chapter 2 provides a comprehensive review of the approaches and techniques used for cutting force estimation, modal parameter extraction and the different dynamic models that are available in the open literature and that are commonly used to address the problems outlined in this work. It also discusses the HSM benefits, challenges and how it relates to the different issues of modal parameter extraction and system dynamics that have triggered this research effort.

In Chapter 3, the Rational Fraction Polynomial (RFP) model, originally developed by Richardson [5], was investigated to predict modal parameters from experimental data. The drawbacks, pointed out by Richardson, are then addressed in Chapter 4, which proposes an improved optimization technique. This approach extracts the modal parameters by using a technique that is based on the RFP model. The new technique ensures the generation of stable modes and is flexible in choosing the natural frequencies so that it matches those of the experimental Frequency Response Function FRF. In addition, special issues during programming were discussed and analyzed, which included the use of different objective functions, coding and decoding of the initial estimate used to start the optimization process.

Chapter 5 describes a model that is capable of simulating the cutting forces resulting from the end milling process during HSM. It details the assumptions upon which the model was built and the mathematical relations between the different process parameters. It also covers the algorithm behind the suggested dynamic model. The proposed dynamic force model is an extension to the model initially developed by Tlustý [6] however it proposes a new and improved procedure to estimate the SCF using the acceleration of the workpiece. A basic and ideal model is first presented, and then gradually more complexities are added to the model to address the problems pointed out in Chapter 2. To include a wider range of frequencies relevant to

HSM problems a multi-degree of freedom system is implemented. With the modal parameters being extracted using the improved optimization technique. The modal parameters are then used to estimate the system's response in the time domain using the convolution theorem integrated with the cutting force model. The tool/tool holder's run-out effect is also added to the cutting force model.

Chapter 6 covers the experimental design, methods used to collect and pre/post process the experimental data along with the experimental setup that will be used to verify the suggested model.

Chapter 7 deals with the analysis and the experimental verification of the introduced model suggested earlier in Chapter 5. First the methodology to test the new model was introduced. Then the model was subjected to an investigation to test: (1) the effect of choosing the number of fitted modes on the estimated SCF, (2) the effect of filtering the simulated acceleration, and (3) the effect of including the tool/tool holder run-out in the dynamic model. Afterwards, a set of cutting tests was used to predict the SCF using a setup (setup # 1) which includes a dynamometer. The same set of cutting tests was used to predict the SCF using another setup (setup # 2) which does not include a dynamometer. In those two setups two different force models were used: (1) a mechanistic cutting force model, and (2) an analytical cutting force model. The SCF estimated for both setups and for both cutting force models was then compared and analyzed. An attempt was also made to reproduce the measured forces analytically. These were then compared and analyzed against the experimental ones.

In Chapter 8, the conclusions, contributions, and recommendations for future research work are presented. Four appendices are also included and cover the technical details related to the mathematical derivations and provide the detailed illustrations that are not presented in the main text of the thesis.

CHAPTER 2

LITERATURE REVIEW

2.1 Introduction

In this chapter a comprehensive literature review will be carried out to cover the areas of interest that will be tackled throughout this dissertation. This study is comprised of two main directions: (1) the assessment of the specific cutting forces using an alternative means other than the dynamometers typically used in HSM end milling processes, (2) an improved technique for modal parameter extraction.

2.2 End-Milling Process

Machining operations are an important part of the world's manufacturing industry. Machining processes are widely used in industry for discrete part production. In

general they can be classified into two categories: (1) single cutting edge processes in which a single point tool removes unwanted material to produce the desired part, (2) multi-cutting edge processes which involves the use of multi-point cutting tools to produce the desired surface.

The milling operation is a multi-cutting edge process that is distinguished from other machining operations by: (1) the cutting tool used has one or more teeth (flutes), (2) those teeth rotate around a fixed axis while being moved with respect to the workpiece.

In general, the formed chip is short and discontinuous. This is due to the nature of the process and to the geometry of the cutting tool. Furthermore due to the rotation of the tool it will engage the workpiece producing a variable chip thickness. This leads to non steady-state cyclical conditions of force and temperature [7]. The dynamics and thermal cycles of the milling process is detrimental to its life especially when a heavy depth of cut is used. The cyclic variation of force can provide the necessary energy to excite a natural mode of vibration in the machine-tool-workpiece system, which leads in most cases to poor surface finish and decreased tool life [7].

There are three basic types of milling processes [7]: planing, facing and end milling, this is illustrated in Figure 2.1. Each and every case is unique in its application, and operation. The most common nomenclature of the milling cutter and its operational modes is illustrated in Figures 2.2 and 2.3 respectively. In end milling two operational modes exist which depend essentially on the rotational direction of the tool when compared with the progress of the workpiece. They are known as:(1) up milling, also known as conventional milling, and (2) down milling, also known as climb milling. See Figures 2.3a and 2.3b respectively.

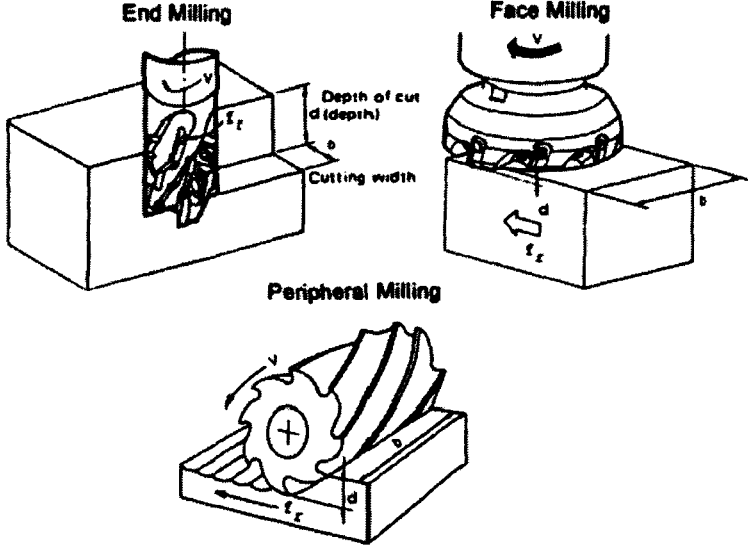


Figure 2.1 – Basic types of milling [7].

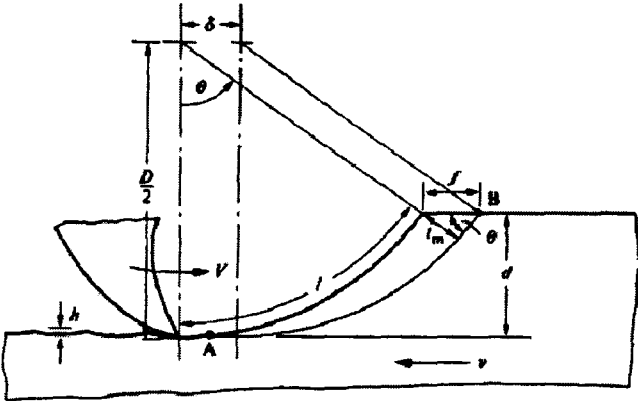


Figure 2.2 – Nomenclature of the milling cutter [7].

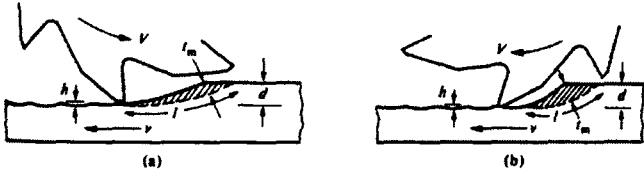


Figure 2.3 – Operational modes of the end milling process [7].

2.3 Force Models

The quality of the surface produced, the machining time and the power consumed during the end milling process depends mainly on the magnitude of the cutting forces. Since the first half of the last century many researchers tried to come up with different models to estimate the cutting force in end milling. In general, they can be classified into the following categories:

1. Analytical models
2. Mechanistic models

2.3.1 Analytical models

The use of analytical models started in the early 1940's when researchers such as Merchant, Shaffer, and Lee represented cutting mechanics in a mathematical form. Their estimation of the cutting forces was based on defining the metal cutting process as being a plastic-flow process. They derived a set of analytical equations for the cutting forces that relates different parameters such as the shear angle, the friction between the tool and the workpiece, and some material constants such as the shear stress. In order to develop these models several assumptions were made regarding the behavior of the material used.

The application of slip line theory was also developed but it is difficult to apply because the representation of the primary deformation zone by a simple shear plane may be unrealistic and the mean angle of friction was found to be insufficient to completely define the frictional conditions on the tool face [8]. In addition, the analytical models couldn't accurately predict the cutting forces in practical cutting conditions especially when the system dynamics are included. Merchant presented one of the most recognized analytical models known to date [7]. More detailed infor-

mation about analytical models and different relationships between forces acting on the tool can be found in [7, 9].

2.3.2 Mechanistic models

Mechanistic force models have been adopted by many researchers [10–18] in the analysis of the milling process. This approach refers to the estimation of the cutting force by means of the uncut chip thickness and the use of a set of calibration coefficients known as the specific cutting pressures [17, 19] (or SCF [14, 20]).

In 1941, Martellotti [21], developed the basic theory of the mechanistic cutting force model. He developed a mathematical equation that calculates the uncut chip thickness that was used in most of the available mechanistic models. He simplified it to Equation 2.1.

$$t_c = f_t \sin(\phi) \quad (2.1)$$

where t_c is the uncut chip thickness, f_t is the feed per tooth and ϕ is the angular position of the cutter. Predicting the uncut chip thickness using Equation 2.1 is valid for a small feed rate ($f_t = 0.0025 - 0.025$ mm [22]). The cutting force was then estimated using the following general equation:

$$F_t = K_t h t_c \quad (2.2)$$

$$F_n = K_n h t_c \quad (2.3)$$

where F_t is the cutting force in the tangential direction (direction of feed), F_n is the cutting force in the normal direction (normal to feed direction), h is the instantaneous chip thickness, K_t and K_n are the specific cutting forces for the tangential and normal directions respectively and are determined experimentally. Ever since the mechanistic

model was established, several researchers have tried to study the specific cutting forces and understand their behavior. Several researchers have revealed that the specific cutting forces are process dependent, they generally depend on the feed rate, axial and radial depth of cut [23], and the effective cutting speed [24]. Table 2.1 summarizes several mechanistic models.

The models presented so far to estimate cutting forces are commonly used by researchers. Work done by Zheng et al. and others in [25–30] was based on the model given by Tlustý et al. and Sabberwal in [31, 32]. Whereas work done by Altintas et al. and others in [29, 33–35] was carried out using the model given in [36]. Finally, Shirase et al. [37, 38] used the model given by Altintas et al. [39]. The simplicity of the model presented in [40, 41] has led several researchers to implement it in their models.

2.4 Addition of System Imperfections

The tilt in the axis of the cutting tool and/or the run-out that exists in the rotation of the cutting tool affects the interaction of the tool with the workpiece and thus the measurement of the cutting forces. These factors are considered to be some of the main imperfections that might exist in the machining system.

2.4.1 Spindle Tilt

Spindle tilt results from the fact that the centerline of both the spindle and the cutter are not always parallel, as illustrated in Figure 2.4. This offset usually results from small debris between the tool and the tool holder. The tilt effect can be added to the cutting force model as an offset from the centerline of the cutter [42–44]. This offset varies while moving up vertically towards the spindle, see Figure 2.5.

Table 2.1 – Summary of mechanistic models

#	Force model	Author	Notes
1	$F_t = K_t b C_t$ $F_n = K_n F_t$	[45]	b is the axial depth of cut, C_t is the uncut chip thickness K_n is a ratio,
2	$F_t = K b h$ $F_n = 0.3 F_t$	[32]	K is the specific cutting force. The model is simplified from 1
3	$F_t = K b h^p$ $F_n = 0.3 F_t$	[31]	$p = 0.3$
4	$F_t = K_s a h + K_s a h^*$ $F_n = K_s a r_1 h + K_s a r_2 h^*$	[36]	h^* , r_1 and r_2 are determined experimentally a is the axial depth of cut
5	$F_t = K_{tc} h dz + K_{te} dz$ $F_r = K_{rc} h dz + K_{re} dz$ $F_z = K_{zc} h dz + K_{ze} dz$	[38, 39, 46, 47]	dz is incremental axial depth of cut K_{tc} , K_{rc} and K_{zc} are tangential, radial, and axial cutting force coefficients K_{te} , K_{re} and K_{ze} are tangential, radial, and axial force coefficients relating to rubbing All constants are determined experimentally
6	$F_t = K_t h dz$ $F_r = K_r F_t dz$ $F_a = K_a F_t dz$	[29, 33, 47, 48]	$K_t = k_t \bar{h}^{-k_p}$ $K_r = k_r \bar{h}^{-k_q}$ $K_a = k_z \bar{h}^{-k_a}$, k_t , k_r , k_z , k_p , k_q and k_a are determined experimentally

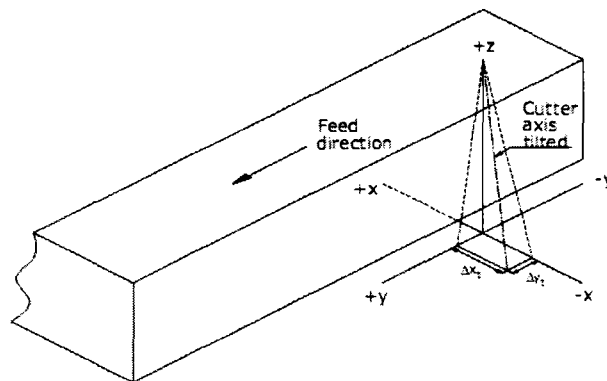


Figure 2.4 – Definition of tilt.

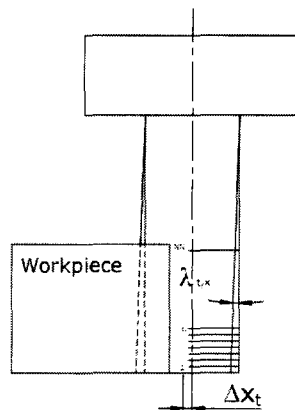


Figure 2.5 – Including the tilt in the cutting force model.

2.4.2 Tool run-out

The cutter run-out in most available literature [15, 16, 38, 49–53] is introduced as a uniform misalignment that exists between the spindle center and the centre axis of the cutting tool. The run-out is introduced as an offset that takes place in the position of the tool center and is a constant along its length. Usually the run-out is defined by a linear distance ρ between centers, and an angle λ locating its position relative to one of the teeth of the cutter, this is illustrated in Figure 2.6. In [52] the run-out was defined slightly different than was introduced earlier.

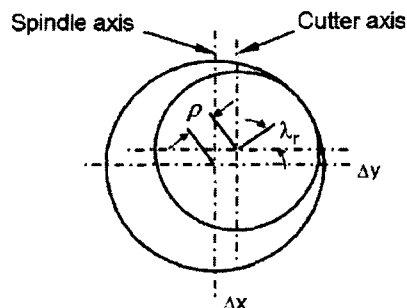


Figure 2.6 – Definition of run-out.

2.5 System Dynamics

In the previously presented mechanistic models the cutting force was, in the majority of the cases, directly proportional to the uncut chip thickness as well as the axial depth of cut. The axial depth of cut is constant and the uncut chip thickness is also assumed to be constant given a specific angular position. In real life the uncut chip thickness, for a given angular position, can vary due to the dynamics of the system. This will eventually leave a surface with undulations that will affect future cuts. This is illustrated in Figure 2.7.

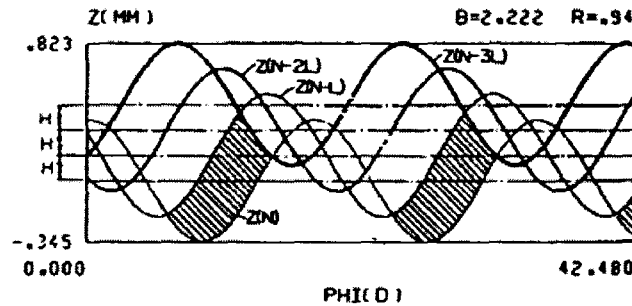


Figure 2.7 – Including the history of previous cuts [6].

Regenerative models account for the history of previous cuts. The regenerative force model was originally developed by Tlustý et al. [6] for turning and milling. Hence Equation 2.1 will be modified to incorporate the effect of the surfaces left behind that were generated by previous cuts as given by Equation 2.4.

$$t_c = f_t \sin(\phi) + z_n - \min(z_{n-i}) \quad (2.4)$$

where z_n is the vibration of the cutter at time n resulting from the cutter's motion due to the dynamics of the system and z_{n-i} are the deflections of the cutting tool due to the system dynamics for i ($i \in 1, 2, 3$) previous periods because as the vibrations grow more preceding cuts than just one might be involved in the estimation of the uncut

chip thickness. This model is most useful when investigating chatter and system dynamics. For the scope of this dissertation, all tests carried out were stable and hence the deflection of the cutting tool was considered for only one previous period leading to Equation 2.5. Equation 2.5 was adopted by many researchers [54–57]

$$t_c = f_t \sin(\phi) + (z_n - z_{n-1}) \quad (2.5)$$

The cutting tool's vibration results from applying the cutting force on the cutting tool system. This system responds to this excitation by vibrating which impacts the uncut chip thickness. At any time, if the value of t_c is negative, the cutter is no longer engaged in cut and t_c is forced to zero; basic non-linearity effect. It should be noted that the model presented in [54] indirectly took into account the effect of previous cuts on the surface by actually simulating the cutting process and the interaction between the tool and the workpiece which is more accurate since Equation 2.5 is based on the assumption that the tool encounters a circular path rather than a trochoidal one which is valid only for small feed/tooth ranges.

So far in this review the workpiece/fixture was considered to be fixed with no relative motion between the tool and the workpiece/fixture. Additional models have been developed to account for this relative motion [11, 58]. Hence Equation 2.4 becomes

$$t_c = f_t \sin(\phi) + z_n - z_{f,n} - (z_{n-1} - z_{f,n-1}) \quad (2.6)$$

where $z_{f,n}$ is the vibration of the fixture at time n resulting from the cutting forces applied to the fixture system and $z_{f,n-1}$ is the vibration of the fixture resulting from the cutting forces applied to the fixture system during one previous period.

Once t_c is estimated the resultant instantaneous cutting force can be determined

and is then applied to the system comprised of the cutting tool and workpiece/fixture. The new response enters into the force calculation at the next time step through the uncut chip thickness value.

The response of the system, be it the fixture or the machine tool, has to be determined at each instant by applying the estimated cutting force to the transfer function of the system. The transfer function can then be determined by: (1) choosing the appropriate dynamic model that suites the case under investigation, and then (2) estimating whatever parameters are needed to make the selected model work (modal parameter extraction).

In most of the literature lumped mass models are used, depending on the actual physical system, and are comprised of one or several masses related to each other by translational and/or rotational stiffnesses and simple dashpots to add the damping effect [58–64]. Lumped mass models can be broadly divided into: (1) single-degree of freedom, (2) multi-degree of freedom models. Single-degree of freedom models are the most commonly used by researchers due to the ease in which their different components can be identified and the ease in which they can be used in different mechanistic models. On the other hand, the use of multi-degree of freedom models is less common due to the complexity of building a model that describes the real life system, let alone the challenge of identifying its different components. Once identified, the response of the system can be obtained by solving the equation of motion given by Equation 2.7.

$$M_u \ddot{u} + C_u \dot{u} + K_u u = F_u \quad (2.7)$$

where \ddot{u} , \dot{u} and u are the acceleration, the velocity and the displacement respectively in an arbitrary direction u (or any other direction). M_u , C_u , and K_u are the mass,

the damping and the stiffness of the system under investigation respectively in the u -direction. They can take a scalar form for a single-degree of freedom model or a matrix form for multi-degree of freedom models. Equation 2.7 can be solved using several techniques such as finite difference or Runge-Kutta differential equation solving techniques [54, 58].

Machine tools have become more complex in part to satisfy the requirements of non-traditional machining processes such as HSM technology. As a result their system transfer functions have also become more complicated increasing the need to use a multi-degree of freedom approach especially to capture the existence of closely spaced or weak modes [65]. Not just that, but hiding different parts behind closed panels makes the process of estimating the mass and stiffness of different parts even harder. Assuming that it is still reasonable to model a specific machine using lumped masses this model is really only valid for that particular machine due to the uniqueness of its manufacturing. In other words, if there is a need to model another machine, one should go through the lengthy and uncertain procedure to estimate the masses, etc. . .

Once the masses and stiffnesses of the system are estimated there remains the challenging process of estimating the damping factors between the different structural parts. This falls into another approximation procedure. In the previous approach, the number of modes estimated in the system depends on the number of masses used in the approximation of the real system. To obtain the modal parameters (M_u, C_u, K_u) there should be a sufficient number of responses equal to the number of assumed masses. This is necessary to be able to optimize the selection of the modal masses. This necessitates the use of several accelerometers and hence results in a higher cost setup with a lengthy experimental process. This is further exasperated by the fact that access to the the system under study is generally limited and the use of certain measurement instruments pose additional accessibility problems. Furthermore, the

targeted area of the system to be studied is relatively small in size and cannot allow measurements at different points.

The process of identifying the individual components of M , C , and K is called modal parameter extraction and is a curve fitting process using different techniques depending on the model itself. Curve fitting techniques for modal parameter extraction can be divided into two main categories:

1. Curve fitting in the frequency domain
2. Curve fitting in the time domain

Each of those categories provides direct and indirect fitting techniques for single and multi-degree of freedom systems characterized by single-input single-output (SISO), single-input multiple-output (SIMO) or multiple-input multiple output (MIMO) methods. The direct methods refer to the identification using the general equation of dynamic equilibrium. The indirect methods refer to identification using the modal parameters such as the natural frequencies and the damping ratios. Figure 2.8 illustrates a summary of the curve fitting methods available for single/multi-degree of freedom systems in the frequency and the time domain.

Each category is sub-divided into several techniques. A summary of the techniques existing under each category is illustrated in Figures 2.9 and 2.10 for the frequency and the time domain respectively.

Given the confined space the fitting techniques based on measuring the mode shape are generally not applicable in this case. In machining where the small area of contact between the cutting tool and the workpiece could be assimilated to a point contact, since this contact area is of the same order of magnitude with the contact area of the instruments used for the FRF measurements found through hammer impact testing.

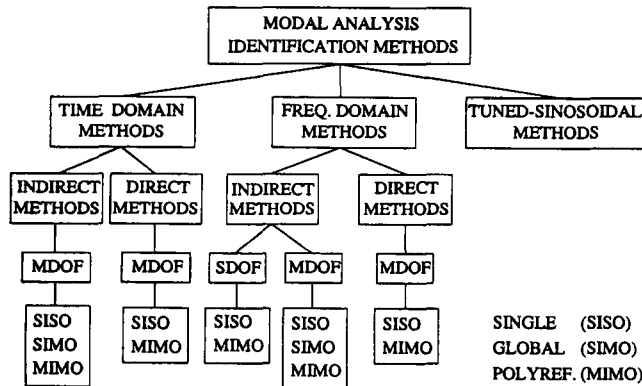


Figure 2.8 – Summary of curve fitting methods [66].

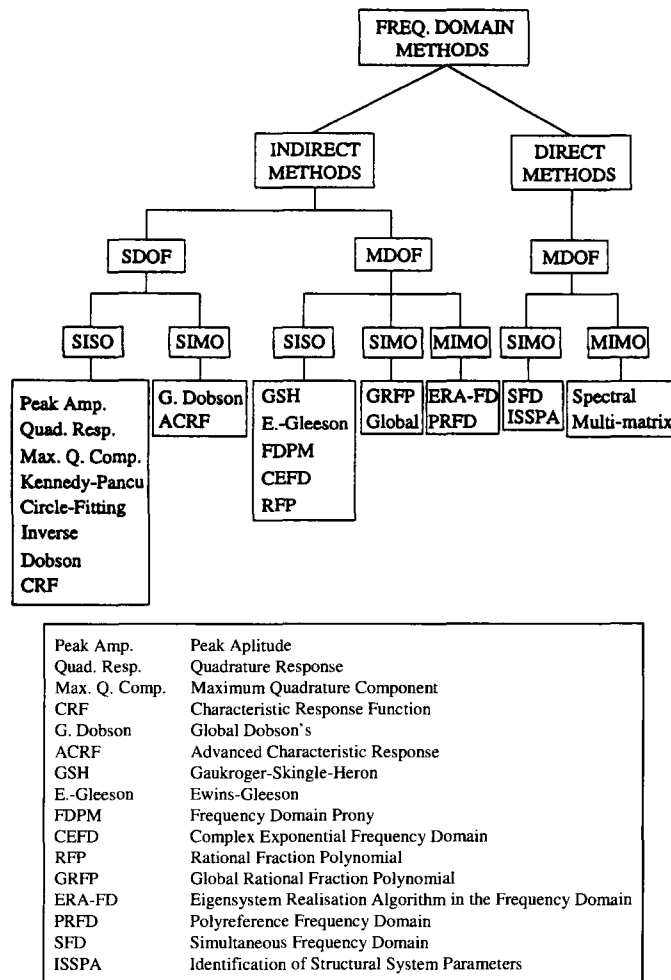


Figure 2.9 – Summary of curve fitting methods in the frequency domain [66].

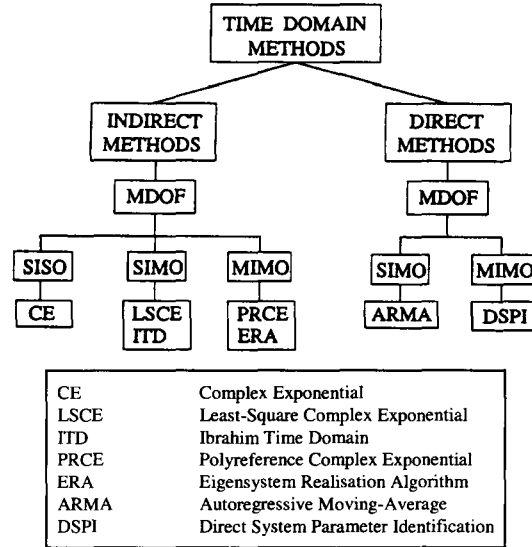


Figure 2.10 – Summary of curve fitting methods in the time domain [66].

The hammer impact testing is one of the most convenient and popular methods of exciting the structure of interest [67]. The resulting FRF in this study corresponds to a SISO system and will include content from the multi-degrees of freedom. The appropriate frequency-domain fitting techniques to this type of FRF are composed of: (1) Gaukroger-Skingle-Heron method, Ewins-Gleeson method, Frequency Domain Prony method, the Complex Exponential Frequency Domain method and the Rational Fraction Polynomial method for curve fitting in the frequency domain and (2) the Complex Exponential method for curve fitting in the time domain. Of those methods, the Rational Fraction Polynomial method and the Complex Exponential method are the most commonly used ones due to their accuracy and ease of use [66, 67].

The Gaukroger-Skingle-Heron method is based on a least-square fit of the receptance response of an N degree of freedom system as given by Equation 2.8.

$$\alpha(\omega) = \alpha_0 + \left(\sum_{r=1}^N \frac{A_r + i \omega B_r}{\omega_r^2 - \omega^2 + i 2 \xi_r \omega_r \omega} \right) e^{i\Phi} \quad (2.8)$$

where α_0 is a complex constant, Φ is an angle that represents the out-of-range modes, ω_r is the natural frequency of mode r , ω is the rotation angle, and ξ_r is the damping ratio of mode r . The model assumes viscous damping and is interactive allowing the user to take decisions such as the initial estimates for the modal parameters. An initial guess equal to zero for both α_0 and Φ was found to be satisfactory. A_r and B_r are constants that are obtained using a least-square analysis. Once A_r and B_r are known all the modal parameters are then known and the iterative process of minimizing a predefined error function can begin. Even though this method gives satisfactory results, the whole process is generally very slow [66].

The Ewins-Gleeson method is dedicated to identify the modal parameters for structures that are slightly damped (typically less than 10% [66] and in many cases less than 5% [68]) and the mathematical model is given by Equation 2.9.

$$\alpha(\omega) = \sum_{r=1}^N \frac{C_r}{\omega_r^2 - \omega^2 + i \eta_r \omega_r^2} \quad (2.9)$$

where C_r is a real quantity due to the assumption of slightly damped system, and η_r Damping loss factor for mode r . This method works very well if the structure under investigation is in fact lightly damped. The main disadvantage is that this method is sensitive to selection of the FRF's point data that is used to perform the curve fitting. To overcome this drawback, a different approach derived from the Rational Fraction Polynomial method was developed by Maia and Ewins [69]. In this new method, results are obtained with minimum intervention and experience of the user.

The Complex Exponential method is expressed in mathematical form in terms of displacement at point j due to a force applied at point k , as given by Equation 2.10.

$$\alpha_{jk}(\omega) = \sum_{r=1}^N \left(\frac{{}_r A_{jk}}{\omega_r \xi_r + (\omega - \omega_r \sqrt{1 - \xi_r^2})} + \frac{{}_r A_{jk}^*}{\omega_r \xi_r + (\omega + \omega_r \sqrt{1 - \xi_r^2})} \right) \quad (2.10)$$

where ${}_r A_{jk}$ is the residue corresponding to mode r and $*$ denotes the complex conjugate. The Complex Exponential method was designed to analyze a single response function. It is simple and doesn't require pre-estimation of the modal parameters. The only parameter that needs to be defined is the number of modes N for which the modal parameters will be extracted. The natural frequencies of the different modes ω_r , the damping factors ξ_r and the residues ${}_r A_{jk}$ can be determined through a series of matrix manipulations and operations. This process is further explained in detail in [67, 69]. One of the major disadvantages of the Complex Exponential method is its sensitivity to noise [65, 70].

Tuned-sinusoidal methods are considered as a special class of modal identification methods which are based on tuning the real modes of vibration of a system by means of exciting the structure at each natural frequency by a set of exciters. This necessitate the pre-use of another identification method to establish those natural modes. This added step is why some researchers do not consider it a genuine identification method [71].

The Rational Fraction Polynomial (RFP) method is one of the most popular and widely used multi degree of freedom models in the frequency domain. It has been adopted and implemented by many commercial software packages of modal analysis. The FRF in terms of receptance can be given in partial fraction form as in Equation 2.11.

$$\alpha(\omega) = \sum_{r=1}^N \frac{A_r + i\omega B_r}{\omega_r^2 - \omega^2 + i 2 \xi_r \omega_r \omega} \quad (2.11)$$

where A_r and B_r are constants and are called residues. The natural frequencies of different modes ω_r , the damping factors ξ_r and the residues A_r and B_r can be determined through a series of matrix manipulations and operations. This process is further explained in detail in [67, 69]. The Rational Fraction Polynomial method was found to generate the most accurate damping ratio estimate [65] and provides very good estimates of the dynamic parameters if the FRF does not include noise.

2.6 High-Speed Machining Technology

The history of HSM goes back as early as before WWII. Dr. Carl J. Salomon conducted a series of tests at speeds up to 16500 (m/min) using helical milling cutters on aluminum, copper and bronze during the period from 1924 - 1931. His research work is documented under German patent number 523594 and dated April 27th 1931. He argued that while increasing the cutting speed the cutting temperature increases till it reaches a maximum then decreases. He also suggested that there is a regime in which machining cannot occur as illustrated in Figure 2.11. A review conducted by Longbottom et al. [72] has revealed that the theory claimed by Dr. Salomon, when compared to several researchers work, has some discrepancies. It can be applied when considering the workpiece temperature but not for the tool-chip interface. As the cutting speed increases there is less time for the heat to be transferred to the workpiece and hence the temperature starts increasing up to a point after which it starts decreasing.

After passing this point, the rest of the heat is transferred to the tool-chip interface which leads to the continuous increase in temperature of the tool tip. See Figure 2.12. Defining HSM was just machining at rotational speeds above a certain value (around 10000 rev./min). Then a more clear and specific definition was concluded; HSM is material dependent [73] as shown in Figure 2.13.

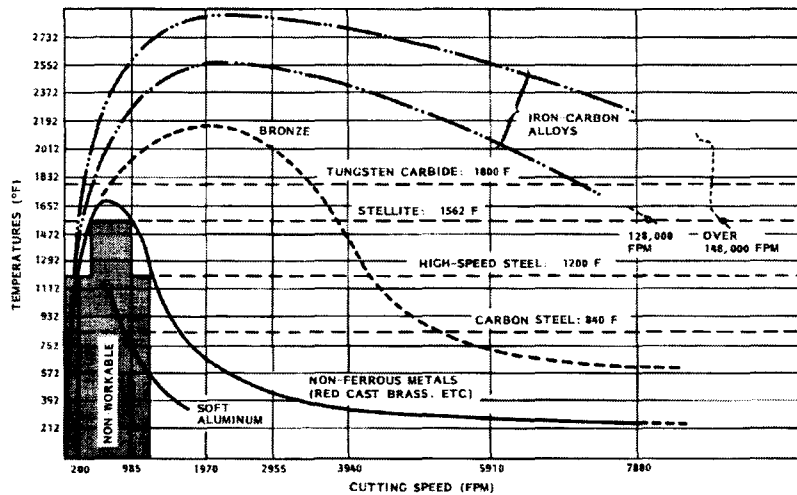


Figure 2.11 – Effect of cutting speed on cutting temperature [74].

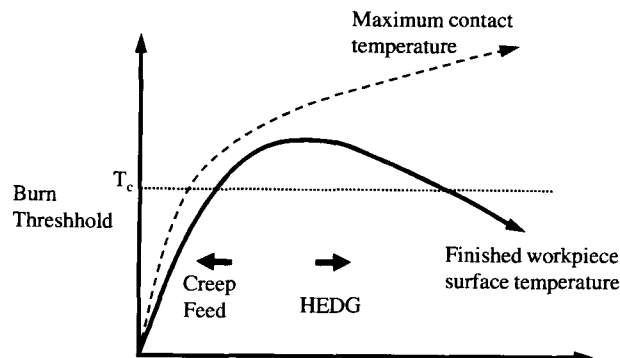


Figure 2.12 – Reviewing Dr. Solomon’s theory [72].

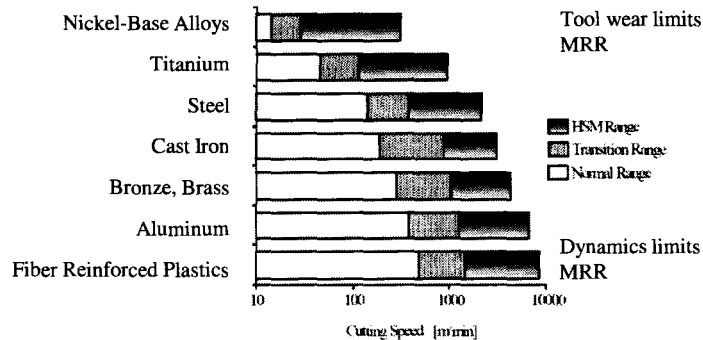


Figure 2.13 – Definition of HSM [73].

In general, research areas in HSM can be classified into: (1) tooling, (2) machine tool requirements, and (3) mechanics of cutting [73].

2.6.1 Tooling in HSM

Tooling in HSM is concerned with the kind of material alloys used for cutting tools, the coating applied on those tools, optimum selection of tool geometry, design of custom tools and the special means used for tool mounting.

It has been reported that, since cutting forces decrease with an increase in cutting speed, diffusion wear is the most dominant form of wear that takes place in tools used in HSM. To avoid this, several attempts have been carried out to add coating materials that have high heat resistance or using uncoated tools with cutter materials that are more resistant to heat. Also tool geometry changes have been tried in an effort to reduce the temperature. Other problems arise due to high cutting speeds; extreme stresses takes place in the vicinity of the clamping zone of the cutting inserts, which can make them quite unsafe during machining. Tool mounting and problems that arise from centrifugal forces, unbalance and position accuracy have to be considered carefully when HSM since the rotational speeds used are much higher than those

used in conventional machining. Such problems should be taken into account when designing new machine tools.

2.6.2 Machine tool requirements in HSM

In HSM, machine tools should be designed in a way that satisfies HSM technology, this include the foundation, machine base and structure right through to the main spindle. This also includes the guideways, feeding drives, chip removal, cooling and motion control system as well as the security and safety features. Foundations and bases should be designed in a way that ensures vibration energy is absorbed but is not transferred into the system. Several kinds of main spindles have been introduced to industry such as active magnetic bearings, and air operated bearings. These bearings have better performance characteristics in order to comply with HSM needs. Due to the high feed rates needed in HSM generally only low friction roller bearing guideways are used in design. As for the feed drives, conventional power screws are no longer used due to backlash concerns but rather ball-screw drives or more recently, linear motors are being applied. Linear motors are characterized by their high rigidity, zero backlash and very high response and accuracy (up to nanometers). Conventional controllers were generally too slow to control the required response of the HSM machine tool, so new controllers have been built which meet the processing demands associated with feed forward control and complex look ahead algorithms. Finally, security and safety features need to be enhanced in order to prevent accidents and protect the worker.

2.6.3 Mechanics of cutting in HSM

Recent test results showed that continuous chip formation as well as chip segmentation occurs during high speed machining as outlined by Ng et al. [75]. Shear localization

takes place also in high speed machining with such materials as titanium alloys. One important thing to be noted here is that it was thought that the cutting temperature will start to decrease with an increase in the cutting speed once it reaches a certain value, however this is not completely true. McGee [40] showed that the cutting temperature of aluminum increases with the increase of the cutting speed till it reaches the melting point of the material. But the rate of increase slows as cutting speed goes up due to the softening effect of the material. It has been reported by Komanduri et al. [76] that it reaches a minimum then further increases take place. Few attempts have been made to model cutting forces in HSM [77]. In this model a polynomial equation was used in order to predict the cutting forces. Other attempts were carried out to optimize the cutting process. Abdou et al. [78] proposed a heuristic model to determine the optimal operating parameters for high speed milling machines.

Machining aluminum is one of the most important applications of HSM due to the volume of material machined in related applications and the properties of aluminum. Thus increased attention has been paid to the dynamics and stability of the cutting process in HSM. Although, substantial research has been carried out in different area of interest, it is clearly seen from the previous discussion that HSM is still a rich technology that started to grow a couple of decades ago and still needs more effort and work to be fully exploited. Many research topics visited in conventional machining need to be reinvestigated for high speed machining especially with the introduction of highly advanced equipment specifically targeting these applications.

2.6.4 Areas of application of HSM

HSM technology application is summarized in Figure 2.14. Some of the advantages of HSM:

1. Increasing the machining accuracy
2. Increasing productivity
3. Improving the surface finish
4. Reduction of burr formation
5. High tendency for stability in cutting

Some limitations and disadvantages of HSM

1. Machining of most aluminum alloys using HSM is almost not limited by the tool life or hardware availability, however these problems do exist when machining difficult-to-machine materials such as titanium alloys, and hardened steel alloys, etc.
2. One important limitation that could take place in the future is the momentum energy. An extra energy needs to be supplied to the cutting process in order to help the cut chip to pass the shear zone. The momentum energy is about 10% of the cutting energy at 10000 rev./min and becomes almost the same as the cutting energy at 30000 rev./min [6].

Technological advantage	Application field	Application examples
Big cutting volume/time	Light metal alloys Steel and cast iron	Aircraft and aerospace production Tool and die mould manufacturing
High surface quality	Precision machining Special workpieces	Optical industry, fine mechanical parts Spiral compressors
Low cutting forces	Processing of thin-walled workpieces	Aircraft and aerospace industry, automotive industry, household equipments
High frequencies of excitation	No machining in critical frequencies	Precision mechanics and optical industry
Cutting heat transport by the chips	Machining of workpieces with critical heat influence	Precision mechanics magnesium alloys

Figure 2.14 – HSM application range [6].

2.7 Instrumentation

During experimentation it is important to measure the cutting forces in order to: (1) have a basic understanding of the response of the system, (2) analyze and hence understand the behavior of the material tested during the cutting process, and (3) monitor the system during cutting to prevent/detect cutting tool breakage or chipping or detect cutting tool wear. This can be done by using several instruments. All instruments go through the same process from applying the force to the final capturing of the forces in a format that can be easily analyzed by the researcher. It starts by capturing the signal using a calibrated measuring mean such as a load cell. Then the signal is subject to conditioning where unwanted signals, such as high frequency noise, are removed. Finally the signal is digitized and stored in a personal computer (PC) for further analysis. This is summarized in Figure 2.15.

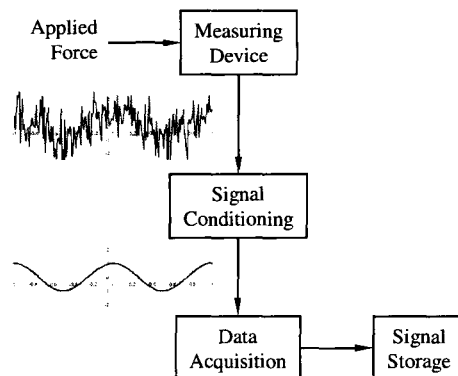


Figure 2.15 – A typical process for measuring the cutting forces.

Many sensor types exist for a variety of applications to measure different physical quantities. Force measurement is one of those sub-categories. Many sensors for force measurement exist:

Strain Gauges

A strain gauge is a device initially used to measure the strain of an object. It can also be used to measure the forces applied on a structural body by making use of Hooke's law. It consists of a tiny electric wire arranged in a defined pattern on the structure of the machine. When the structure deforms in response to the load the wire is stretched, the resistance of the metallic wire changes changing the voltage sensed across it. With proper calibration it is then possible to relate this voltage to displacement and when the stiffness of the structure is known force can be estimated. Since the force measurement in this device relies on member deflection, it necessitates that this deflection be relatively high (several micrometers) for this technique to be feasible. Depending on the range required this can add undesirable compliance to the system. In general strain gauges are good for measuring impulsive and slowly varying forces. A typical strain gauge device is illustrated in Figure 2.16.

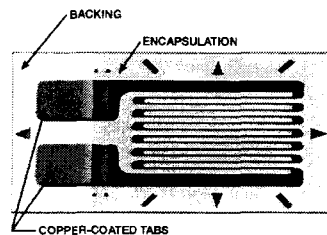


Figure 2.16 – Typical strain gauge device [79].

Load Cells

Load cells are electronic devices that are used to measure forces. They can be either strain gauge based load cells or piezoelectric based as discussed further in the next section. The advantage of using a load cell is that it can be tuned for a specific application and requires minimal change to the structure of the machine. In general the strain gauge load cells are used for measuring large, static or slowly varying loads and they are relatively accurate (0.1% of the full-scale reading [80]). A typical load

cell is illustrated in Figure 2.17.

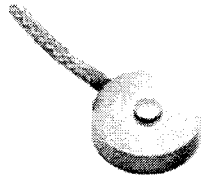


Figure 2.17 – Typical load cell [81].

Piezoelectric Transducers

A piezoelectric transducer is a device that uses the piezoelectric effect to measure force by converting the force to a charge signal. Similar to strain gauges, it is capable of measuring both impulsive forces and slowly varying forces. They are widely used in dynamometers to measure cutting forces which are commonly used instruments [80] for cutting force measurement. One drawback of these devices is that they are highly affected by their own natural frequency ”*self-dynamic behavior*” [80] which given the high frequency excitation associated with high speed machining can cause distortion in the output signal.

Other Methods

Other methods for measuring forces include pneumatic and hydraulic devices. They are more commonly used in industrial applications where there is a need to weigh heavy objects. They are rarely used in measuring cutting forces.

2.8 Summary

Throughout this chapter a review of the approaches and techniques used for cutting force estimation, modal parameters extraction and the different dynamic models that are available in the open literature have been outlined. Special emphasis was placed

on the importance of these issues for HSM. This section also discusses the benefits of HSM, some of its challenges and how it relates to the different issues of modal parameter extraction and system dynamic identification that have motivated this research effort. At the end several instrumentation techniques used for cutting force measurement were outlined and discussed.

CHAPTER 3

INVESTIGATION OF MODAL PARAMETERS EXTRACTION

3.1 Introduction

The estimation of cutting forces while taking into consideration the effect of the system's dynamics implies that a dynamic model needs to be integrated with the conventional cutting force model. The system's response affects the instantaneous cutting forces estimation which in turn will affect the future cutting force estimates. The system's response, i.e. the system's displacement, can be estimated using several models as discussed earlier in Section 2.5. The RFP method will be used in this study to estimate the system response based on its modal parameters due to its accuracy and ease of use. This approach forms the basis of the improved modal parameter

extraction method that will be presented in this study. Throughout this chapter the estimation of the modal parameters using Forsythe method [82] will be investigated to point out the key issues that need improvement.

3.2 Rational Fraction Polynomial

The FRF is a complex function, which is defined over a specified frequency range. It can be obtained experimentally through using an impact hammer test, which is often the easiest and quickest technique for measuring the FRF used in modal analysis [67]. The FRF resulting from an impact test is called accelerance when an accelerometer is used to capture the output signal. Integrating the accelerance signal twice in the frequency domain generates the receptance. The choice of receptance in this work is related to our intention for the time domain simulation of the high speed machining, where the dynamic relative displacement between the tool and the workpiece will affect and will be affected by the instantaneous cutting forces. The system's modal parameters can be estimated by curve fitting a dynamic model such as the RFP model to the experimental receptance. A typical RFP model for a single degree of freedom system is described by Equation 3.1.

$$H(\omega) = \frac{X(\omega)}{F(\omega)} = \frac{A}{i\omega - \lambda} + \frac{A^*}{i\omega - \lambda^*} \quad (3.1)$$

where

$$\lambda = \sigma + i \omega_d \quad (3.2)$$

$H(\omega)$ is the system's receptance in the frequency domain, $X(\omega)$ is the system's response in the frequency domain, $F(\omega)$ is the force applied on the system in the

frequency domain, A is the residue, ω_d is the damped natural frequency, and λ is the system's pole.

For a multi-degrees of freedom system the final FRF is obtained by summing the FRF of all individual modes (N modes) of relevance existing in the system as shown in Equation 3.3.

$$H(\omega) = \frac{X(\omega)}{F(\omega)} = \sum_{r=1}^N \left(\frac{A_r}{j\omega - \lambda_r} + \frac{A_r^*}{j\omega - \lambda_r^*} \right) \quad (3.3)$$

where

$$\lambda_r = \sigma_r + j \omega_{d,r} \quad (3.4)$$

Once the poles and zeros (often called poles and residues [67]) are identified, the experimental FRF can be reproduced and the dynamic model can be integrated with the cutting force model. Richardson [5, 83, 84] developed an effective curve fitting technique to extract a system's poles and zeros from the experimental FRF by making use of the Forsythe method as well as the orthogonality of the polynomials themselves. More details about the RFP method and the Forsythe method can be found in [5] and [82] respectively.

The simplified Forsythe method presented by Richardson [5] was reported in [65] to be accurate, effective, and easy to use to for extracting the system's modal parameters. However, our investigation, which will be detailed hereafter, has revealed that some key issues in this method require improvement.

3.3 Investigation of the RFP Method

Richardson [5] pointed out that in order to account for the effect of other modes or resonances outside the curve fitting band of interest the number of modes should be over specified. If the apparent number of modes is for example 4, then enhancing the curve-fitting results requires that a number of modes larger than 4 is specified. For example 9 could be suggested in order, to account for the extra modes that do not show in the frequency spectrum of interest.

In our investigation it was found that over-specifying blindly the number of natural modes could result in the estimation of fictitious natural frequencies and the estimation of modal parameters that do not necessarily describe a stable system. In addition, Richardson pointed out that the orthogonality of the polynomials can break down when the frequency resolution is very low in the frequency band of interest, which is equivalent to what is observed when under-sampling conditions.

To illustrate these shortcomings, let's consider the following case study where a fixture was subject to an impact hammer test. During this test, the structure starts to vibrate after receiving a blow from the hammer. The vibration will decay to rest after a certain period of time due to the structural damping that exists in the system. The real part of the poles of an RFP model that describes such a stable system is expected to be negative. Due to the problems mentioned earlier by Richardson, it is quite possible to obtain erroneous results when identifying the modal parameters of such a system, such as poles with positive real parts.

The number of stable modes obtained, i.e. poles with negative real part, the mean percentage error and maximum percentage error between the fitted and the experimental FRF will be investigated for only one direction of each system for illustration. Results of other directions are similar. Figures 3.1 and 3.2 illustrates the

experimental FRFs of the fixture and the cutting tool in the X direction respectively. This data will be used to investigate the RFP method as described above. This data is the result of averaging of over 5 measurements using Exponential windowing. The sampling frequency was equal to 16384 Hz. Data below 500 Hz were ignored since the coherence of the signals was very low in this range, indicating that the data in this range is not reliable.

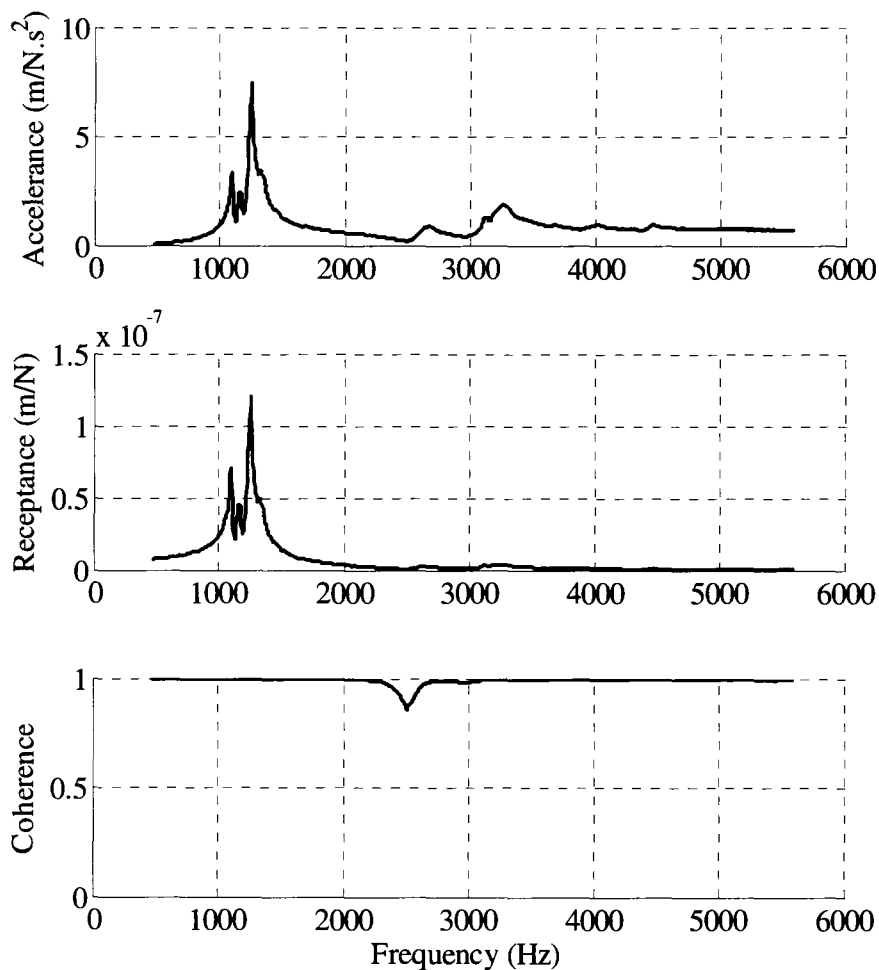


Figure 3.1 – FRF of the fixture in the X -direction.

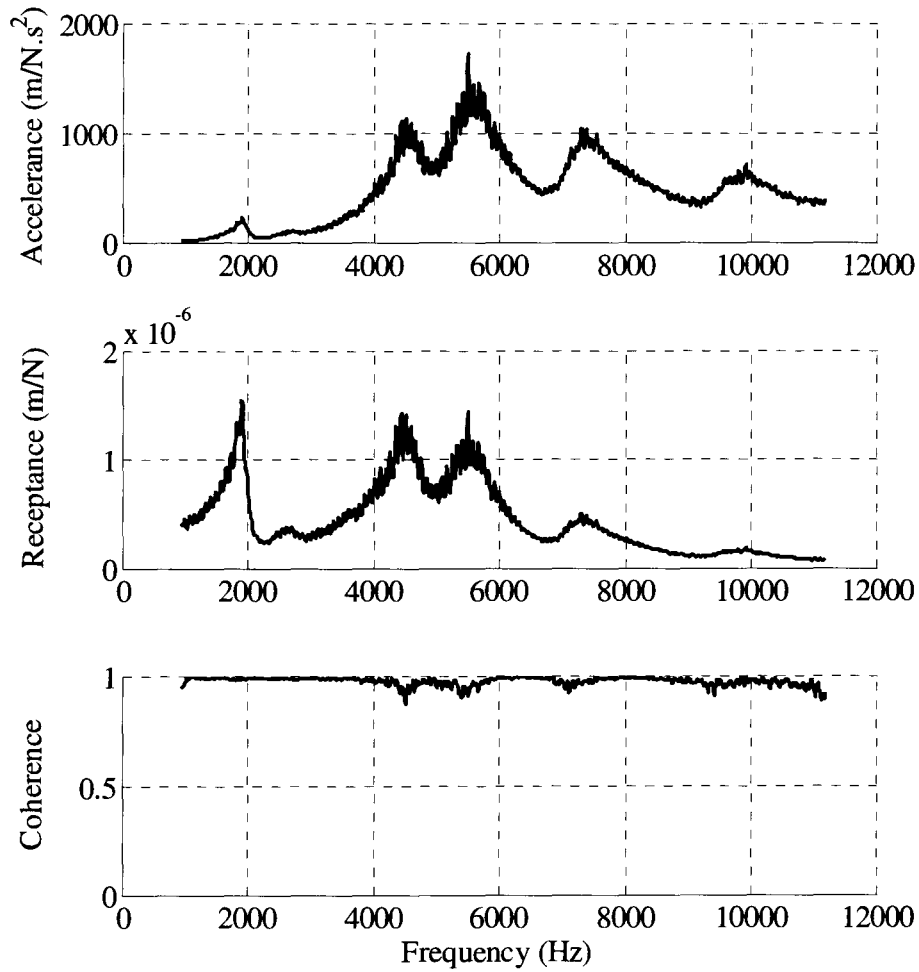


Figure 3.2 – FRF of the cutting tool in the X-direction.

When filtering the experimental FRF, modes can be lost but at the same time the curve fitting procedure might be enhanced resulting in a more stable system. The stability of the fitted FRF was investigated in light of filtering the experimental FRF using low-pass filters with different cut-off ratios to generate different frequency bands of interest. The cut-off ratio is identified as the ratio of the cut-off frequency to half the sampling rate and ranged from 0.0625 to 0.2500. The corresponding cut-off frequencies ranged from 512 Hz to 2048 Hz. This range was selected to cover at least the major apparent dominant frequencies and the filtering took place before choosing the frequency range of interest.

In addition and for each frequency band, the number of natural modes used in the curve fitting process of the RFP model was varied from 8 to 40. The number of modes 8 was obtained by examining the measured FRF plotted in Figure 3.1. The receptance FRF shows 3 dominant frequencies in the range of 1000 - 1500 Hz and 3 other frequencies with very low amplitude close to 2800, 3300 and 4500 Hz. In addition to those six modes, 2 other modes were considered to account for potential modes outside the range of frequency under consideration. The upper limit of investigating the number of modes, 40, was actually driven by the investigation itself since adding more modes was not of any benefit to the analysis as will be seen later. This was also applied to the FRF illustrated in Figure 3.4.

The performance of the RFP technique is assessed in terms of the number of resulting stable modes and the goodness of fit. The latter is assessed by two criteria, which are the absolute mean percentage error and the absolute maximum percentage error between the fitted and the experimental FRF. They are defined by Equations 3.5 and 3.6 respectively. Results for the fixture and the cutting tool are illustrated in Figures 3.5 - 3.8 respectively.

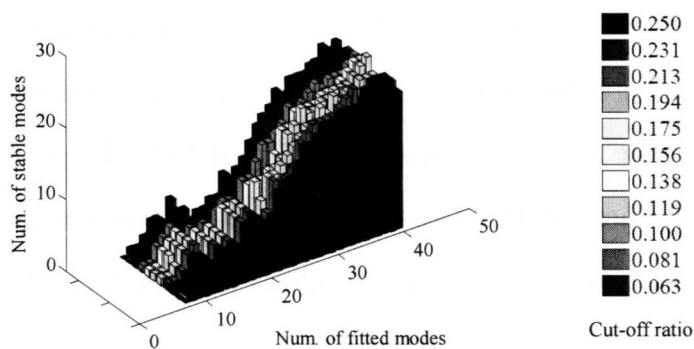


Figure 3.3 – Effect of the cut-off ratio and the total number of suggested fitted modes on the number of stable modes for the fixture in the *X*-direction.

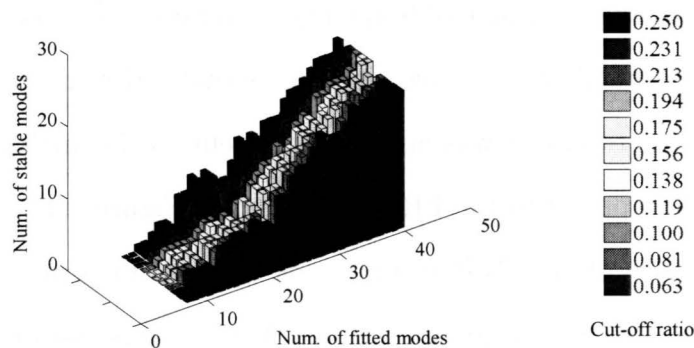


Figure 3.4 – Effect of the cut-off ratio and the total number of suggested fitted modes on the number of stable modes for the cutting tool in the *X*-direction.

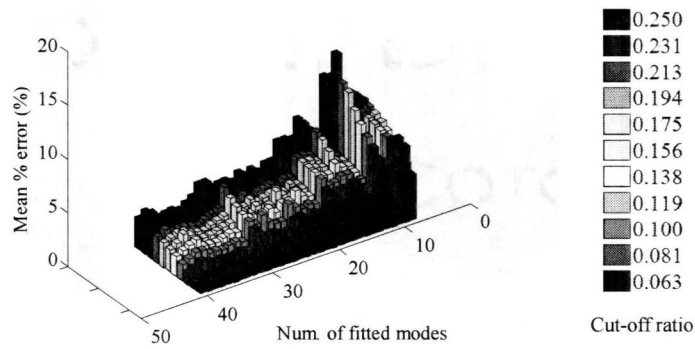


Figure 3.5 – Effect of the cut-off ratio and the total number of suggested fitted modes on the mean percentage error due to fitting for the fixture in the *X*-direction.

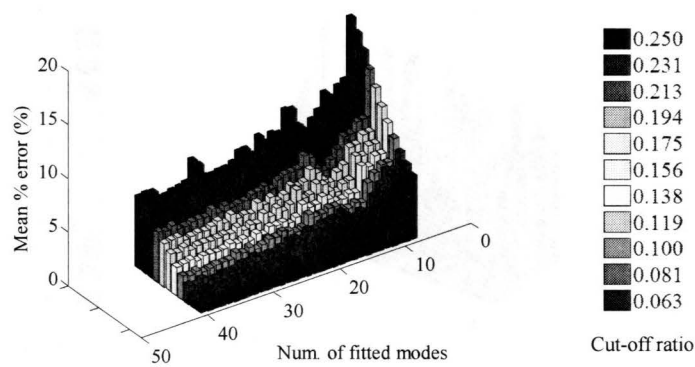


Figure 3.6 – Effect of the cut-off ratio and the total number of suggested fitted modes on the mean percentage error due to fitting for the cutting tool in the *X*-direction.

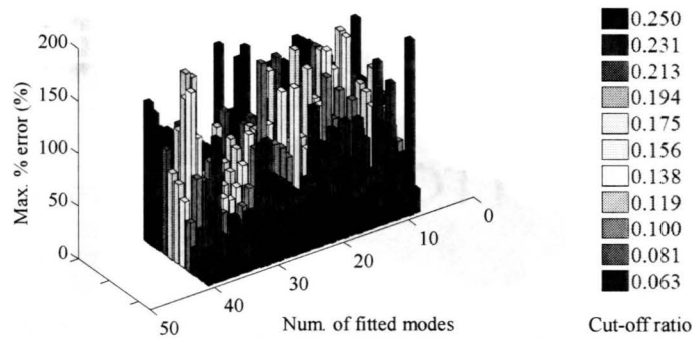


Figure 3.7 – Effect of the cut-off ratio and the total number of suggested fitted modes on the maximum percentage error due to fitting for the fixture in the *X*-direction.

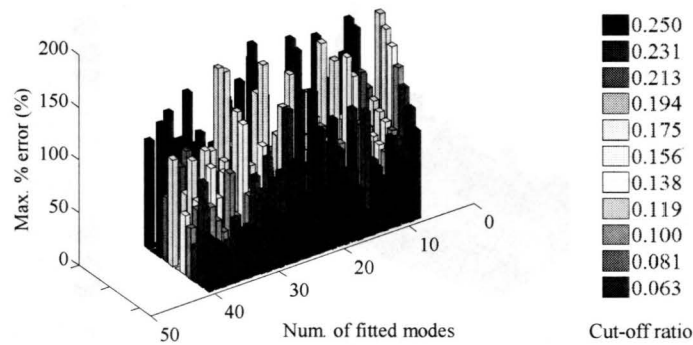


Figure 3.8 – Effect of the cut-off ratio and the total number of suggested fitted modes on the maximum percentage error due to fitting for the cutting tool in the *X*-direction.

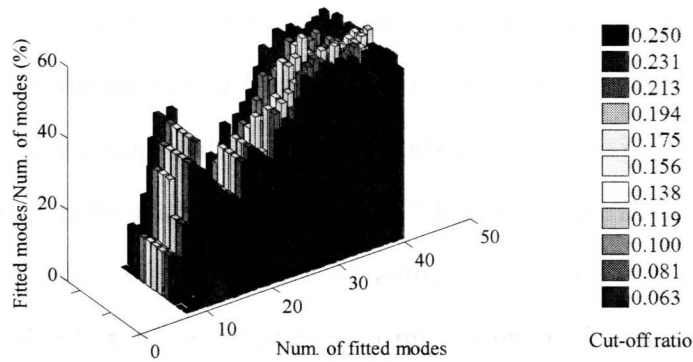


Figure 3.9 – Effect of the cut-off ratio and the total number of suggested fitted modes on the ratio of the number of stable modes to the total number of suggested fitted modes for the fixture in the *X*-direction.

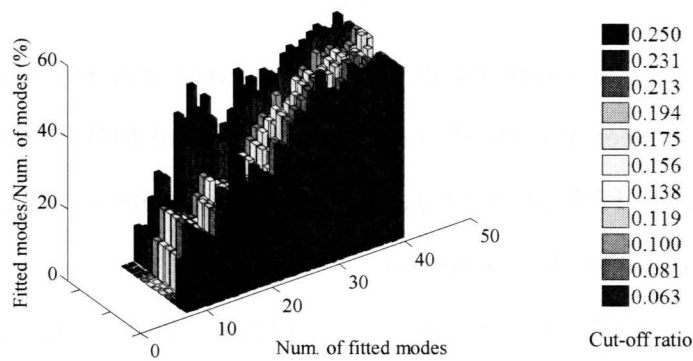


Figure 3.10 – Effect of the cut-off ratio and the total number of suggested fitted modes on the ratio of the number of stable modes to the total number of suggested fitted modes for the cutting tool in the *X*-direction.

It is noted that changing the cut-off ratio did not have an effect on the number of stable modes. Also, the number of stable modes increased with the increase of the number of suggested modes fitted to Equation 3.3 however at any time they did not reach the value of the suggested modes. In other words, it was not possible to obtain a number of stable modes that is equal to the number of suggested ones. Furthermore, the ratio of the fitted stable modes to the suggested ones was calculated and is illustrated in Figures 3.9 and 3.10. It is noted that after a certain number of suggested modes, this ratio asymptotes to a certain value that it cannot surpass. From observations, as will be shown later, it is believed that this happens due to the increase of the number of suggested modes, a number of fitted modes exists in pairs in such a way that they cancel out each other and hence the ratio asymptotes to a certain specific value ($\sim 50\%$).

$$C_1 = \frac{1}{n} \sum_{f=1}^n \left| \frac{y_f - \hat{y}_f}{y_f} \right| \quad (3.5)$$

$$C_2 = \max_{f \in \{1, \dots, n\}} \left[\frac{|y_f - \hat{y}_f|}{y_f} \right] \quad (3.6)$$

where C_1 , C_2 are the absolute mean percentage error and the absolute maximum percentage error between the fitted and the experimental FRF respectively, y_f is the experimental value of FRF at point f , \hat{y}_f is the fitted value of FRF at point f , n is the total number of points in the record.

The number of stable modes is plotted in Figure 3.3a as a function of the cut-off ratio and the total number of natural modes used for fitting. The number of stable modes is not significantly affected by the cut-off ratio. However, it increases as the number of natural modes increases. The ratio of the number of stable modes to the total number of modes increases abruptly from 15% up to approximately 50% as the

total number of modes increases from 8 up to approximately 11, then it causes a drop to a minimum of 30% at 16 to increase again and reach a plateau at 55% near the total number of modes of 40, as shown in Figure 3.3b. It will be shown later on that with the increase of the number of total modes beyond a specific value, certain modes are estimated in pairs so that they cancel each other out and hence, the ratio asymptotes to a specific value. This gives an indication that the most appropriate number of natural modes should be in the neighbourhood of 11, where the ratio of the number of stable modes to the total number of modes reaches the first extreme. Having a number of modes larger than that will not significantly enhance the solution. In addition, since the number of stable modes did reach only 55% of the number of the total modes in the best case, the modal parameters extracted using the technique described by Richardson do not result in a stable system.

It was found that the mean percentage error decreases with the decrease of the cut-off ratio or with the increase of the number of suggested fitted modes as shown in Figure 3.5. By decreasing the cut-off ratio, filtering the measured FRF results in a higher loss of information and possibly loss of some apparent or closely spaced modes. Having fewer apparent natural modes to fit makes the process of curve fitting using the RFP model easier and with results in smaller fitting errors. More over, the increase of the total number of modes generates pairs of poles with opposite signs that are estimated only for the sake of numerical balance. On the other hand, there is no clear trend for the maximum percentage error with either changing the cut-off ratio or the number of suggested fitted modes, as shown in Figure 3.7.

The experimental FRF shown in Figure 3.1 was filtered using a cut-off ratio of 0.0625, then fitted to 25 modes using the RFP model and the Forsythe method. The magnitude and phase of the filtered experimental and the fitted FRFs are plotted in Figure 3.11. It is clear that filtering resulted in reducing the amplitude of the FRF.

For example the amplitude of the natural mode 1300 Hz was reduced from 1.5×10^{-7} to 0.7×10^{-7} m/N, shifting some natural modes and losing one natural mode around 1200 Hz.

A close match between the RFP model and the filtered experimental FRF can be observed for both the amplitude and the phase. However, an investigation of the estimated modal parameters, which are summarized in Table 3.1, reveals that natural modes number 19 and 20 at 4969 Hz and 5231 Hz are hardly noticeable in the FRF plotted in Figure 3.11, which suggests that they result only due to the least square fit of the Forsythe method. Similar conclusion can also be made about the pair of natural modes number 22 and 23. It was also noticed that the obtained natural frequencies do not necessarily line up with the experimental ones. For example in the experimental FRF mode number 2 has a frequency of 1090 Hz while in the fitted FRF it shows that it has a frequency of 1074 Hz.

3.4 Summary

Throughout this chapter experimental data was used to curve fit the RFP model using Richardson's approach to predict modal parameters. Results showed agreement between experimental and calculated with the drawbacks pointed out by Richardson outlined. The major drawbacks found while implementing the approach are the prediction of unstable modal parameters despite the expectation of predicting stable ones and the existence of unnecessary modes that are only present to satisfy the numerical balance. This is especially relevant when choosing an overly estimated number of modes. Moreover, there is no control over predicting the natural frequencies to match those of the experimental FRF.

Table 3.1 – Modal parameters for experimental data in Figure 3.1 fitted to 25 modes

Mode	Freq.(Hz)	$\xi\%$	Pole
1	821.46	11.96	-621.62 + 5161.39i
2	1074.62	-4.54	306.55 + 6752.04i
3	1158.71	-8.33	608.76 + 7280.41i
4	1251.33	-4.06	319.46 + 7862.36i
5	1364.13	-4.39	376.94 + 8571.14i
6	1686.48	0.01	-0.01 + 10596.51i
7	2081.62	-3.90	510.94 + 13079.18i
8	2631.09	-3.17	524.91 + 16531.65i
9	2781.41	-1.83	320.29 + 17476.11i
10	3126.36	-2.72	533.84 + 19643.49i
11	3246.18	-2.07	423.28 + 20396.36i
12	3560.51	-0.41	90.81 + 22371.33i
13	3776.84	-0.89	212.71 + 23730.61i
14	3994.37	-1.96	494.08 + 25097.31i
15	4259.07	-0.49	132.43 + 26760.51i
16	4460.77	-1.27	358.44 + 28027.86i
17	4625.22	-0.69	202.66 + 29061.13i
18	4967.87	0.24	-76.25 + 31214.04i
19	4969.41	-1.51	471.53 + 31223.71i
20	5230.94	1.40	-460.97 + 32866.95i
21	5240.24	-1.14	374.04 + 32925.42i
22	5466.16	1.32	-454.61 + 34344.90i
23	5471.74	-1.14	393.33 + 34379.93i
24	5562.72	-0.17	59.58 + 34951.58i
25	5681.66	-0.38	136.49 + 35698.90i

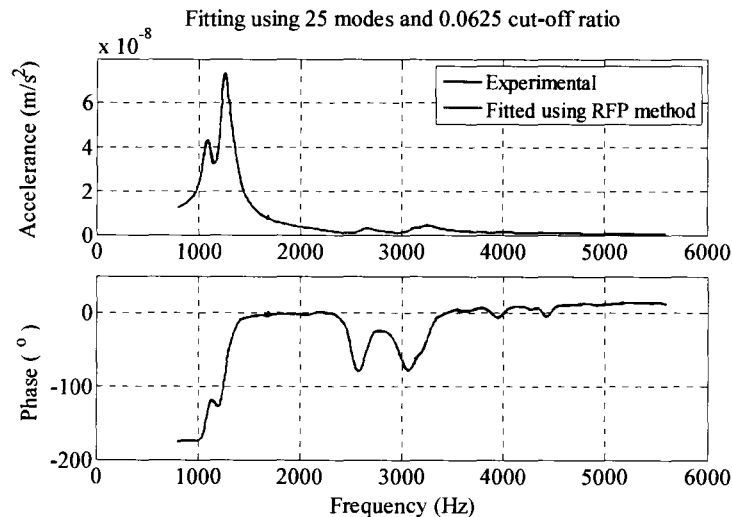


Figure 3.11 – FRF of the cutting tool fitted to 25 modes.

CHAPTER 4

THE MODIFIED RFP METHOD

4.1 Introduction

In this chapter an improved method for modal parameters extraction will be presented. It is based on the RFP method originally developed by Richardson [5]. This method will be investigated and tested throughout this chapter.

4.2 Optimized RFP Method

As mentioned in Chapter 3, Section 3.3, the FRF resulting from a hammer impact testing is expected to have its poles' real part negative. When using the technique suggested by Richardson [5], the obtained poles' real part, are not necessarily negative, especially when accounting for a large number of modes. In addition, the

obtained natural frequencies do not necessarily line up with the experimental ones. The RFP model will be used to analytically simulate the experimental FRF, however instead of using the simplified Forsythe method adopted by Richardson, a constraint optimization algorithm will be used to identify the system's modal parameters. The constraint optimization algorithm, illustrated in Figure 4.1, is suggested to extract the modal parameters.

In this algorithm, the poles and zeros obtained from Richardson's technique will be used as a starting point for the optimization. The MatlabTM function *fmincon* will be used as the optimizer. The *fmincon* function is a gradient-based method that works only with continuous objective and constraint functions and that have continuous first derivatives. Further details about the *fmincon* function can be found in [85]. The optimization process is subject to the minimization of the objective function while maintaining a certain number of constraints.

The optimization algorithm starts by identifying the desired number of modes for which the RFP model will be fitted to and then loading the accelerance obtained from the hammer impact testing. The receptance is obtained by integrating the accelerance twice in the frequency domain. The subroutine developed subroutine for the simplified Forsythe method was then called and applied to the experimental receptance and the poles and zeros were obtained. It was found that those poles and zeros form an excellent start point for the optimizer. Before being passed to the cost function's subroutine, each pole's real part is multiplied by (-1) and then coded. In the cost function's subroutine, the starting point is decoded and then substituted in the objective function.

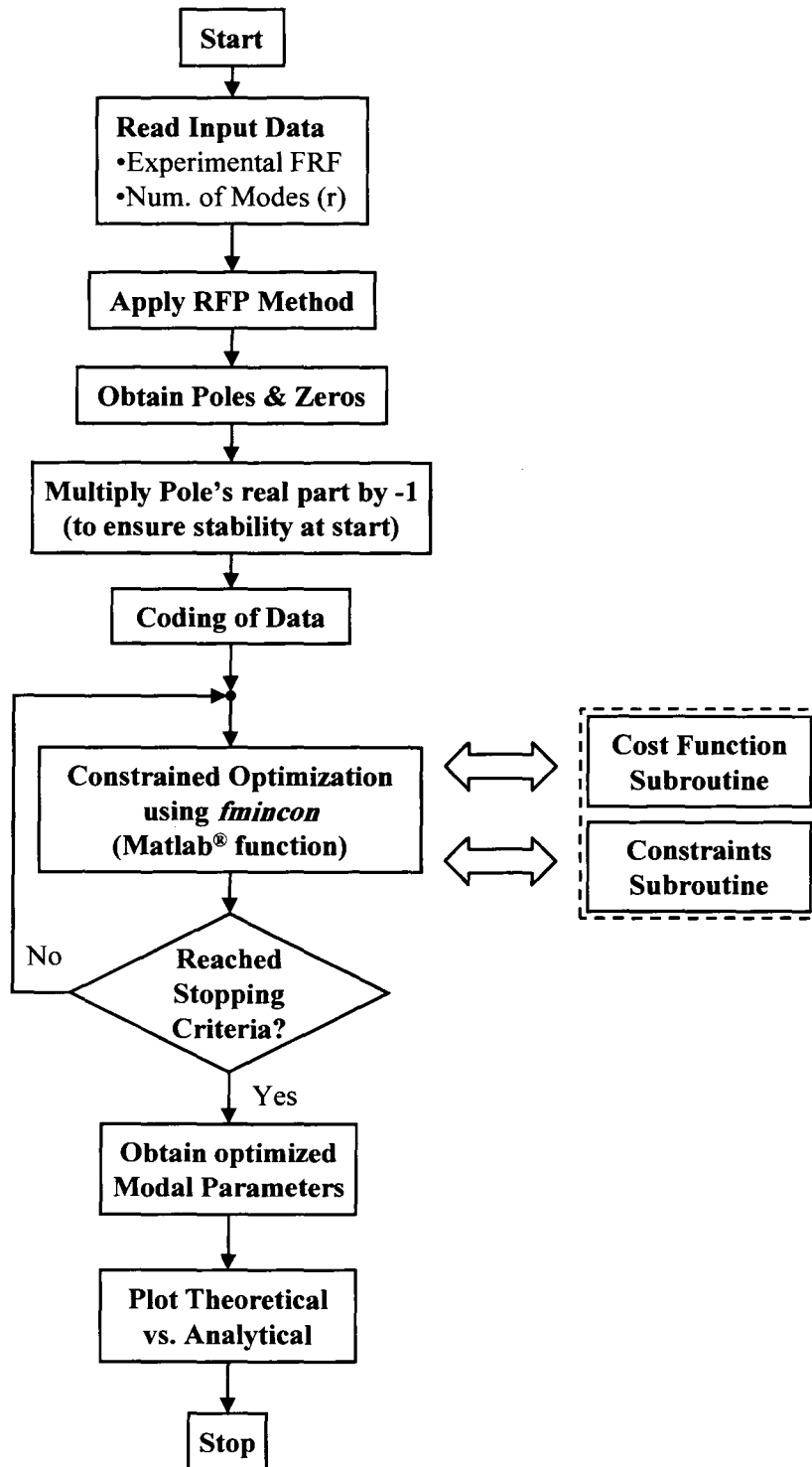


Figure 4.1 – Flow chart of the suggested ORFP method.

4.2.1 Formulation of the constraints

The optimizer tries to minimize the cost function while maintaining the following constraints:

- The damping ratio ζ should be greater than zero and less than 10%.
- The system's natural frequencies are maintained unchanged by keeping them as constants during the optimization process. Later on in this chapter, it will be shown that this constraint can be loosened allowing to choose the system's natural frequency to be chosen.
- In Equation 3.4 each pole's real part is maintained less than zero ($\sigma_r < 0$) to ensure that a stable system is obtained at all times.

The optimization process stops after a certain number of iterations that has to be pre-determined before starting the optimization as this forms the stopping criterion of the whole process as compared to other stopping criterion such as the tolerance on the objective function. It should be noted that the final solution obtained by this optimization method is not necessarily the global solution. Since the number of variables being evaluated is large the chances that another solution that satisfies the problem constraints exist is always possible.

4.2.2 Formulation of the objective function

Several objective functions were formulated and were consequently assessed for better convergence. They include:

- Absolute mean error, which is defined by Equation 4.1:

$$\text{Mean}_{ab,e} = \frac{1}{2N} \sum_{r=1}^N |\text{Re}(y(\omega_r)) - \text{Re}(\hat{y}(\omega_r))| + \frac{1}{2N} \sum_{r=1}^N |\text{Im}(y(\omega_r)) - \text{Im}(\hat{y}(\omega_r))| \quad (4.1)$$

where N is the total number of data points in the record, Re and Im are the real and imaginary part of the FRF being investigated.

- Maximum error, which is defined by Equation 4.2:

$$\text{Max}_e = \max_{r \in \{1, \dots, N\}} \left(\frac{1}{2} |\text{Re}(y(\omega_r)) - \text{Re}(\hat{y}(\omega_r))| + \frac{1}{2} |\text{Im}(y(\omega_r)) - \text{Im}(\hat{y}(\omega_r))| \right) \quad (4.2)$$

- Mean percentage error, which is defined by Equation 4.3:

$$\text{Mean}_{e,p} = \frac{50}{N} \sum_{r=1}^N \left| \frac{\text{Re}(y(\omega_r)) - \text{Re}(\hat{y}(\omega_r))}{\text{Re}(y(\omega_r))} \right| + \frac{50}{N} \sum_{r=1}^N \left| \frac{\text{Im}(y(\omega_r)) - \text{Im}(\hat{y}(\omega_r))}{\text{Im}(y(\omega_r))} \right| \quad (4.3)$$

- Maximum percentage error, which is defined by Equation 4.4:

$$\text{Max}_e = \max_{r \in \{1, \dots, N\}} \left(50 \left| \frac{\text{Re}(y(\omega_r)) - \text{Re}(\hat{y}(\omega_r))}{\text{Re}(y(\omega_r))} \right| + 50 \left| \frac{\text{Im}(y(\omega_r)) - \text{Im}(\hat{y}(\omega_r))}{\text{Im}(y(\omega_r))} \right| \right) \quad (4.4)$$

- Least square error, which is defined by Equation 4.5:

$$\text{LS}_e = \left(\frac{0.5}{N} \sqrt{\sum_{r=1}^N [\text{Re}(y(\omega_r)) - \text{Re}(\hat{y}(\omega_r))]^2} \right) + \left(\frac{0.5}{N} \sqrt{\sum_{r=1}^N [\text{Im}(y(\omega_r)) - \text{Im}(\hat{y}(\omega_r))]^2} \right) \quad (4.5)$$

4.2.3 Assessment of the objective function

The performance of the different objective functions will be evaluated in terms of the occurrence of the convergence, the number of iterations required for convergence and the goodness of the fit. The latter is assessed by the following two criteria:

- **Criterion 1:** is defined as the mean percentage error between the fitted and the experimental FRF and is defined by Equation 3.5.

- **Criterion 2:** is defined as the maximum percentage error between the fitted and the experimental FRF and is defined by Equation 3.6.

Those objective functions were tested for:

- **Convergence:** Each objective function was tested to converge/not converge for a given experimental FRF data set.
- **Level of convergence:** At the end of the optimization process and to facilitate the comparison of the different objective functions, a normalization of these functions was required to harmonize their values in terms of magnitudes. The normalization is accomplished by dividing each objective function by its maximum value obtained over all the iterations required for the convergence of the optimization process. The maximum value of each objective function is generally obtained in the first iteration and consequently the normalized objective functions are expressed by Equation 4.6.

$$\chi|_k = \frac{OF|_k}{OF_1} \quad (4.6)$$

where $\chi|_k$ is the normalized objective function at iteration k , $OF|_k$ is the value of the objective function at iteration k and OF_1 is the value of the objective function at the first iteration.

- **Outcome:** The mean and maximum percentage error between the fitted and experimental FRF is evaluated and analyzed.

Several fitting runs were carried out for the experimental FRF obtained for the workpiece's fixture and the cutting tool in the X -direction. Figures 3.1 and 3.2 illustrate the experimental FRFs of the fixture and the cutting tool respectively. The

experimental data of the fixture and the cutting tool was fitted to 15 and 13 modes, and each record set contained 480 and 900 points respectively. The maximum number of iterations was selected to be 2500 iterations and the cut-off ratio was 0.3125 which (corresponds to 2560 Hz).

The results on the occurrence of the convergence are reported in Table 4.1. They indicate that, among all the objective functions, the maximum percentage error and the least square error did not lead the ORFP to converge. The objective functions that resulted in the convergence of the ORFP were plotted against the progressive number of iterations as illustrated in Figure 4.2. The plot of each normalized objective function features a high decrease rate or high convergence rate at the starting of the optimization process, followed by a low decrease rate or low convergence rate, which might lead to a plateau corresponding to the convergence if the number of iterations is sufficiently high. The starting point plays an important role in the convergence of the objective function. In the case that any condition of the constraints mentioned earlier in Section 4.2.1 is broken it will result in that the optimizer will fail to find a direction to converge.

For the maximum error, the mean error and the mean percentage error, the corresponding slow convergence phases start at approximately 1100, 1400 and 2000 iterations and they are at the levels of 0.5, 0.1 and 0.15, respectively. Therefore, the ORFP based on the maximum error is the fastest to converge while the one based on the mean error is the slowest to converge.

The two criteria of the goodness of the fit will be used to select the most appropriate objective function. The corresponding values are listed in Table 4.2. The objective function defined by the mean error resulted in the values of 1.66% and 31.23% for criteria 1 and 2, respectively for the fixture and 2.12% and 9.16% respectively for the cutting tool. These values are at least 3 times lower than those achieved

by the objective function defined by the mean percentage error and at least 14 times lower than those achieved by the objective function defined by the maximum error.

It becomes obvious that the objective function defined by the mean error provides the best fit at the expense of slower convergence, which means a higher number of iterations and consequently higher computing time.

Table 4.1 – Summary of different objective functions' convergence

Objective function	Convergence status
Mean error	Converged
Max. error	Converged
Mean % error	Converged
Max. % error	Did not converge
Least square error	Did not converge

Table 4.2 – Comparison of different objective functions' outcome for different systems

Object	Objective function	C_1	C_2
Fixture X -dir.	Mean error	1.66	31.23
	Max. error	82.85	440.07
	Mean % error	5.05	137.23
Tool X -dir.	Mean error	2.12	9.16
	Max. error	22.75	82.43
	Mean % error	9.03	61.57

4.2.4 Convergence (Stopping) criteria

The optimization process stops if the specified number of iterations is reached or if the rate of variation of both the objective function and the solution are within specified tolerances. The selection of the number of iterations in this work is dictated by the goodness of the fit, which is defined by the two criteria mentioned above: the mean percentage error and the maximum percentage error. It was found that

after a certain number of iterations, the goodness of the fit cannot be enhanced any further as the number of iterations increases while the objective function defined by the mean error could achieve smaller value. Selecting the number of iterations based on the tight convergence of the objective function will result in therefore increasing the computing time without enhancing the goodness of the fit. This can be illustrated through the following example. Using the same experimental FRF as before and the objective function defined by the mean error, the optimization process was conducted with different number of iterations, ranging from 200 up to 3000. For each specific number of iterations, the two criteria for the goodness of the fit were evaluated and the results are shown in Figure 4.3. This figure indicates that both criteria started at a relatively high value then converge to a plateau starting approximately at 2000 and 1400 iterations for criteria 1 and 2, respectively. These numbers of iterations are smaller than the number of iterations required by the objective function defined by the mean error to converge, which exceeds 2500 as per Figure 4.2. It can be concluded that the convergence of this objective function guarantee the goodness of the fit. In addition, the specified tolerance on the rate of variation of the objective function could be loosened in order to match the number of iterations required for the convergence of the objective function and the criteria of the goodness of fit. Since there is a difference in the number of iterations required by the two criteria to converge, these two criteria need to be monitored at the same time to save unnecessary computational time.

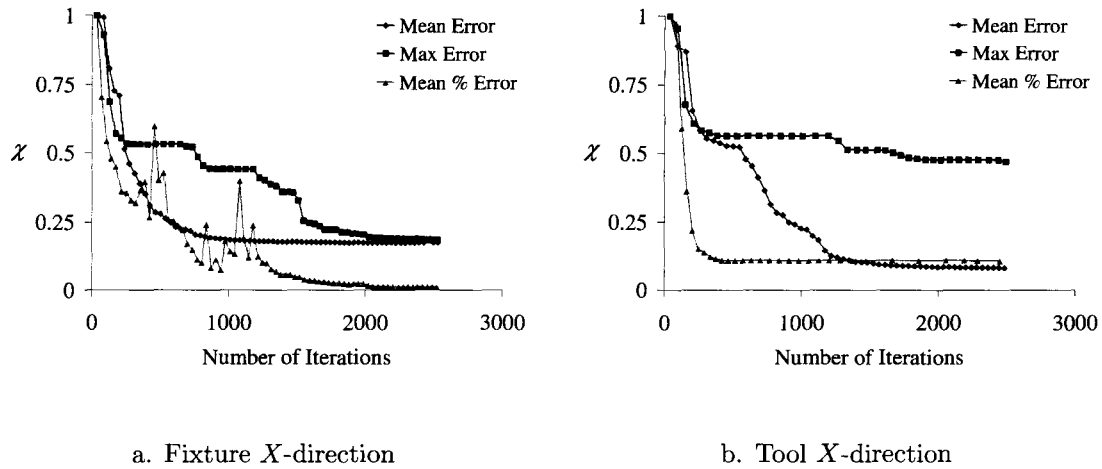


Figure 4.2 – Investigation of different objective functions.

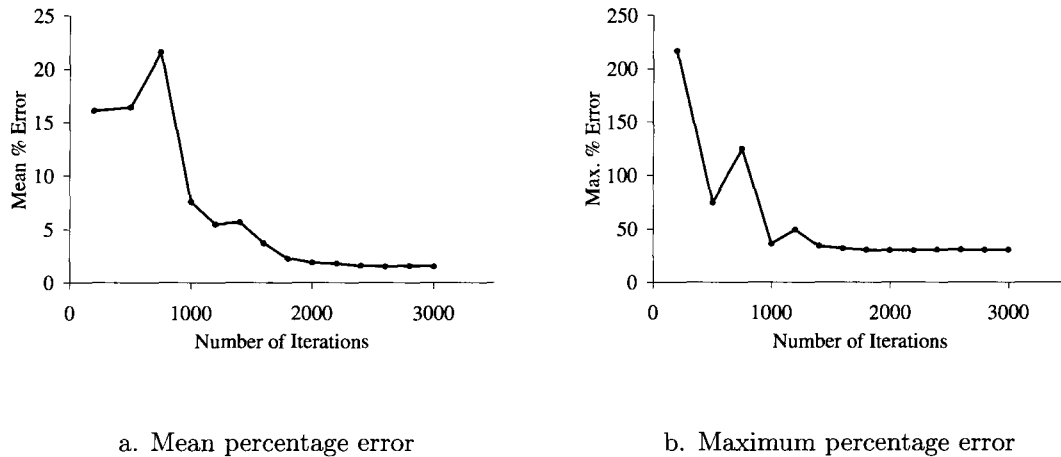


Figure 4.3 – Effect of varying the number of iterations on the mean and maximum percentage error between the fitted and the experimental FRF respectively.

4.2.5 Coding the variables

In the optimization process, the residues and the poles of the complex rational polynomial equation need to be identified including both the real and imaginary parts. Consequently, there are 4 terms to be identified for each mode. For the moment the

imaginary part of the pole, which represents the natural frequency, will be obtained directly from the Forsythe method after applying it to the experimental FRF. The other three terms, which are the real and imaginary parts of the residue and the real part of the pole, highly differ in their orders of magnitude. To enhance the robustness and the rate of convergence of the optimization process and to avoid ill-conditioned matrices, all the variables should be harmonized in terms of magnitudes. In the objective function and in the constraints, each variable x will be expressed as the product of a modified variable x_{mod} by the order of magnitude. The vector of order of magnitudes will remain constant during the optimization process. However, the modified variables have similar order of magnitudes and will be treated as the unknown. Since the magnitude of each variable is not known before-hand, it is suggested to use the initial guess defined earlier as an indicative of the expected order of magnitudes for the different variables. The initial guess denoted x_o is coded as follows. The values in vector x_o are transformed to the scientific number format. The exponent of each number (the part after the e) indicates the order of magnitude of the variable. The different exponents are saved in a specific vector, which will be used in the objective function and the constraints to scale up or down the modified variables. The remaining part (mantissa) of the values in vector x_o have the same order of magnitude and constitutes the vector of modified variables denoted x_{mod} . This vector can be used as the initial guess for the optimizer. The final solution of the optimization process is obtained by decoding the modified variables through multiplying the modified variables by the vector of the order of magnitudes. The coding procedure is summarized in Figure 4.4.

$$x_o = \begin{pmatrix} 4.1934 \times 10^{-9} \\ -4.2040 \times 10^{-8} \\ -1.2425 \times 10^{-6} \\ -1.2088 \times 10^{-6} \\ 4.2443 \times 10^{-6} \\ -1.7920 \times 10^{-6} \\ 4.6873 \times 10^{-8} \\ -3.6724 \times 10^{-8} \\ 8.8186 \times 10^{-8} \\ -1.2266 \times 10^{-7} \end{pmatrix}$$

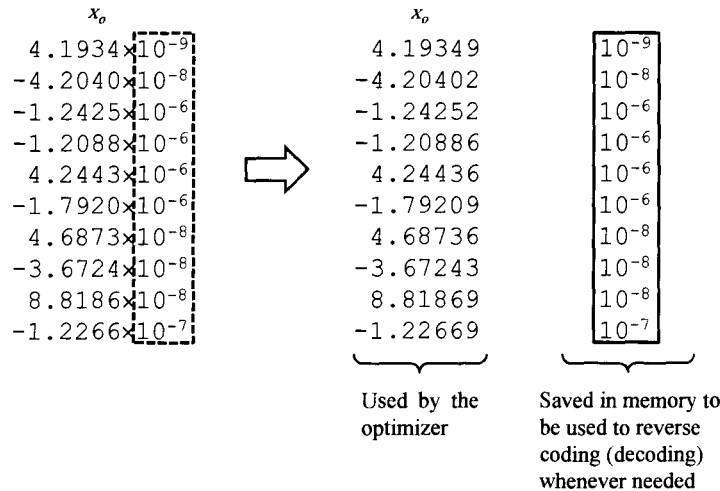


Figure 4.4 – Coding procedure.

4.2.6 Flexibility of the Optimized Rational Fraction Polynomial (ORFP) method

When using the Forsythe method, the poles and zeros obtained are directly derived from a least square fit using matrices relations and orthogonality of polynomials which cannot be controlled all the time. When using the ORFP method, there is more flexibility to pick and choose modes that one would think are better for the fitting. The experimental FRF, illustrated in Figure 3.1, was fitted to 7 modes with

a cut-off ratio of 0.25 and a frequency range of 800 - 2000 Hz using the RFP method. The resultant modal parameters are listed in Table 4.3 and the fitting is illustrated in Figure 4.5.

Table 4.3 – Modal parameters after fitting the experimental data in Figure 3.1 using the Forsythe method

Mode #	Freq. (Hz)	ξ
1	893.16	-10.61
2	1110.09	-3.01
3	1227.92	-1.61
4	1291.36	0.38
5	1366.87	-7.87
6	1698.49	-2.02
7	1902.84	-0.62

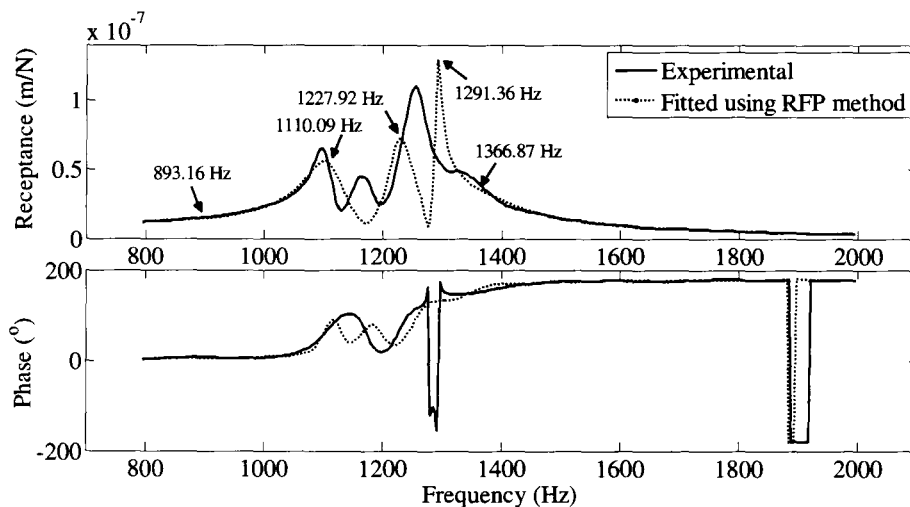


Figure 4.5 – Fixture FRF, X-direction, fitted to 7 modes using the Forsythe method.

Aside from the negative (-ve) sign of the pole's real part, which is also reflected in the sign of the damping ratios' sign, the following is noticed:

- Mode 1 has about 10% damping ratio, which is relatively high for structural

damping. When closely looking at the vicinity of 900 Hz the magnitude of the signal is very small and thus is removed.

- Modes 2 - 5's fitted natural frequencies do not line-up with the corresponding experimental ones.
- Mode 6 needs to be removed as it also is very small in magnitude.

So, modes 1 and 6 need to be eliminated, and the natural frequencies for modes 2-5 needs to be modified to match the experimental ones. If modes 1 and 6 are eliminated and the fitted FRF is regenerated using the remaining modes (without modifying the natural frequencies) and by making use of Equation 3.3, Figure 4.6 is obtained.

Clearly, the fit worsened, let alone the misalignment that exists between the fitted and experimental natural frequencies. If the fitted FRF is regenerated one more time with modes 1 and 6 eliminated and having the remaining mode's natural frequencies modified as summarized in Table 4.4 and by making use of Equation 3.3, Figure 4.7 is obtained.

Also this did not help with obtaining a better fit in fact it has only worsened it. When the ORFP method is used it is possible to choose the modes and their natural frequencies that are relevant to the experimental FRF and obtain the modal parameters for them. From Figure 4.5 it is desirable to modify the modes as shown in Figure 4.4.

The ORFP method can overcome this problem by modifying the modal parameters then optimizing them following the same procedure explained earlier. The poles' imaginary part is modified to account for the desired natural frequencies. The poles' real part as well as the residues, real and imaginary part, will be kept unchanged as they form a good starting point for the optimizer. The modal parameters summarized

in Table 4.5 are obtained after the optimization process.

Table 4.4 – Modification of the modal parameters obtained from fitting the experimental data in Figure 3.1 using the Forsythe method

Before modification			After modification		
Mode		Freq. (Hz)	Mode		Freq. (Hz)
1	×	893.16	-	→	-
2		1110.09	1	→	1100
3		1227.92	2	→	1170
4		1291.36	3	→	1255
5		1366.87	4	→	1340
6	×	1698.49	-	→	-
7		1902.84	5	→	1903

Table 4.5 – Modal parameters for experimental data in Figure 3.1 using ORFP after modifying the modal parameters obtained from using the Forsythe method

Mode #	Freq. (Hz)	ξ
1	1100	1.51
2	1170	1.55
3	1255	1.60
4	1340	2.44
5	1903	3.84

Figure 4.8 illustrates the analytical FRF obtained using the ORFP method versus the experimental one. Clearly there has been an improvement on the modified modes giving a better fit than the one shown earlier in Figure 4.5 using the Forsythe method. Moreover, the damping ratios obtained are within the norms of structural damping ($< 10\%$) and the poles' real part are all positive, which guarantees a system with a stable response.

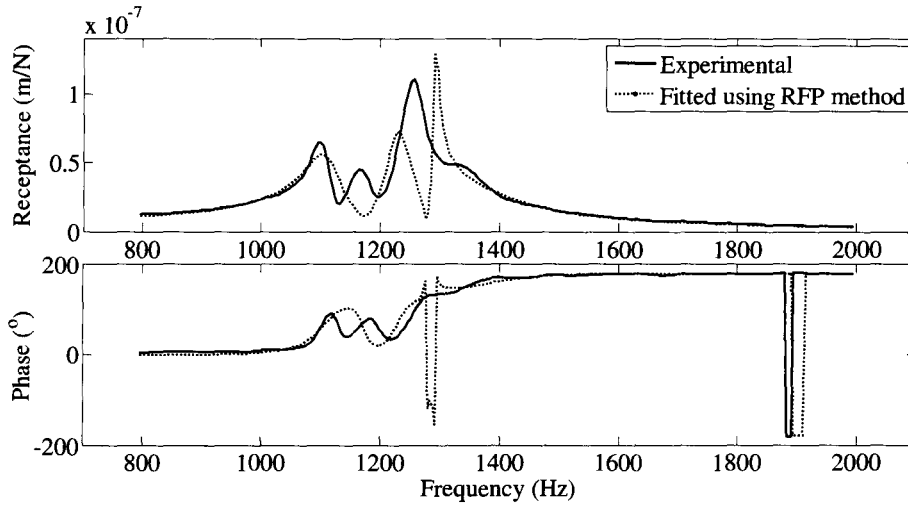


Figure 4.6 – Fixture FRF, X-direction, regenerated after eliminating modes 1 and 6 using the Forsythe method.

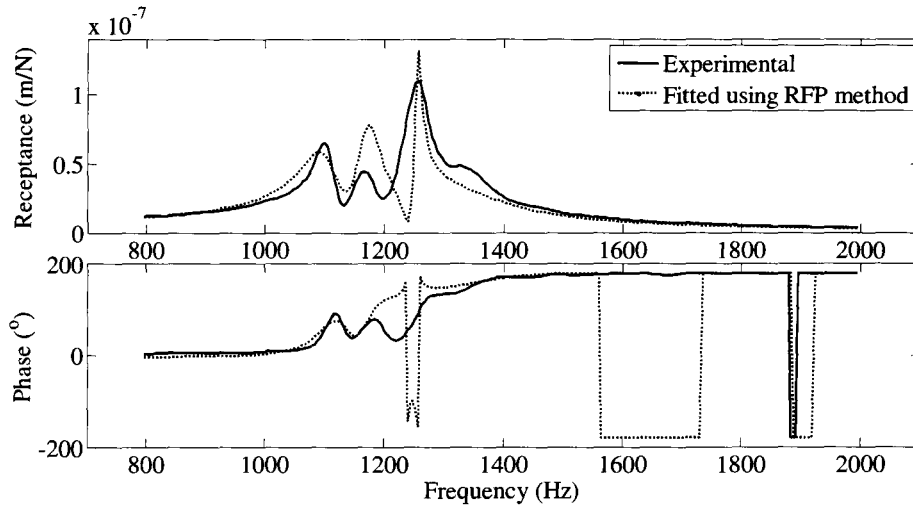


Figure 4.7 – Fixture FRF, X-direction, regenerated after eliminating modes 1 and 6 and modifying the remaining mode's natural frequencies using the Forsythe method.

In the modal parameters extraction process the modified ORFP relied on obtaining its starting point from the Forsythe method. The ORFP was further developed to obtain its starting point independently from the Forsythe method. To obtain a starting point four values needs to be determined beforehand which are as follows:

1. The number of modes to which the experimental FRF will be fitted to.
2. The natural frequencies desired corresponding to each mode. This can be obtained graphically from the experimental FRF.
3. The maximum absolute magnitude value of the FRF to be fitted.
4. The maximum structural damping ratio that will be used in the fit.

Once those values are defined, a starting point can be obtained. For example the experimental natural frequencies of the fixture’s FRF illustrated in Figure 3.1 can be determined from the figure as such

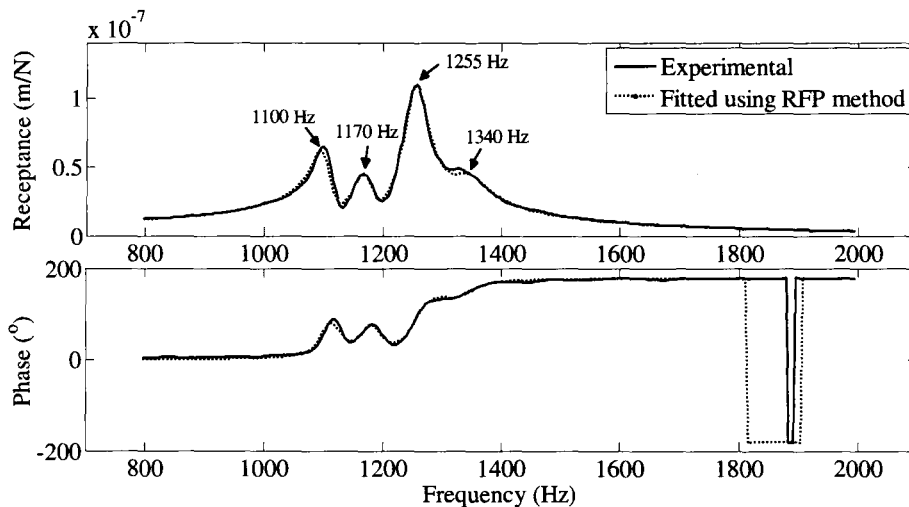


Figure 4.8 – Fixture FRF, X-direction, regenerated using the ORFP method after eliminating modes 1 and 6 and modifying the remaining modes to match the experimental ones.

$$f_n = \begin{pmatrix} 1100 \\ 1170 \\ 1255 \\ 1340 \\ 1903 \end{pmatrix} (\text{Hz})$$

The poles can be defined as

$$Poles = 2\pi \cdot f_{n_j} \left(\frac{-\xi_j}{100} + i \right) \quad j \in \{1 \dots n\} \quad (4.7)$$

where ξ_j can be chosen to be 4% for all n modes. While the poles represents the position of the modes and how much they are spread (damping), the residues form the amplitude of the mode itself. Hence the residues can be chosen to be the maximum absolute magnitude value of the FRF to be fitted. They can all be chosen to have the same value and it does not matter what is their sign as the optimizer will take care of this issue. Then the procedure presented in Section 4.2 can be followed to extract the modal parameters. Figure 4.9 compares the fixture's FRF (X -direction) with the fitted one. The mean and maximum percentage error values were found to be 3.12% and 22.20% respectively. The modal parameters extracted are listed down below in Table 4.6.

Table 4.6 – Modal parameters for experimental data in Figure 3.1 using ORFP after modifying the modal parameters obtained from using the Forsythe method

Mode #	Freq. (Hz)	ξ
1	1100	1.51
2	1170	1.55
3	1255	1.60
4	1340	2.43
5	1903	3.23

Comparing these results with those obtained when using the Forsythe method to provide the initial start point, summarized in Table 4.5, there is almost no difference

between both results. Thus the same performance is achieved but the ORFP approach is even more flexible.

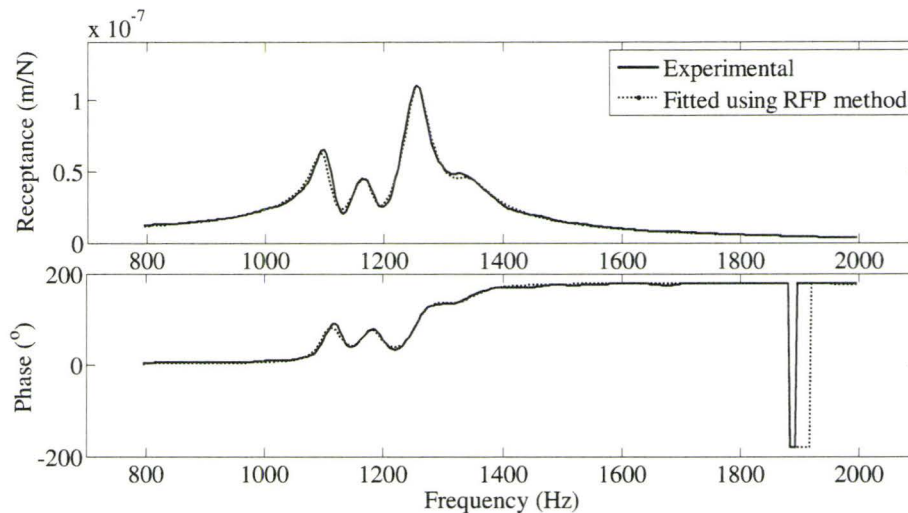


Figure 4.9 – Fixture FRF, X-direction, regenerated using the ORFP method after eliminating modes 1 and 6 and modifying the remaining modes to match the experimental ones and guessing the initial values of the damping.

4.2.7 Investigation of the ORFP method

In this study, the ORFP method will be integrated with the conventional cutting force model to obtain the response of both the workpiece's fixture and the cutting tool and in so doing hence accounting for the system dynamics during the cutting process.

However the ORFP method needs further investigation before proceeding to this step. Thus it will be investigated using the following parameters: accuracy in choosing the different number of modes on the normalized objective function, the mean and maximum percentage error, the optimization process' computational time, and the meaningfulness of the suggested number of modes. The investigation will be carried out for both the workpiece fixture and the cutting tool systems.

The experimental FRF data, of the cutting tool, illustrated in Figure 3.2 was

fitted to a different number of modes using the mean error as the objective function and a cut-off ratio of 0.125. All fitting runs were carried out using the same number of iterations (3000 iterations). From Figure 4.10 it can be seen that all runs exhibit the same trend; a higher rate of convergence at the beginning then slowing down towards the end. This occurs because at the beginning of the optimization process there is a bigger margin for changing different parameters but once the process heads in the direction of the solution the gap becomes smaller and making a change in the parameters becomes harder. Even though this trend is true, increasing the suggested number of modes to be fitted stretches the normalized objective function over a wider span of number of iterations. For example, in Figure 4.10b fitting the experimental FRF data to 16 modes takes a larger number of iterations to reach a solution. On the other hand, when fitting the same experimental FRF data to 9 modes it converges in less iterations, this takes place at the expense of the final value of the normalized objective function as seen in Figure 4.11b and the mean and the maximum percentage error as can be seen in Figures 4.12b and 4.13b respectively. A smaller number of suggested modes (9) will make the optimizer converge to a larger normalized objective function value as compared to a smaller value when using a larger number of suggested modes (15). Increasing the number of modes from 9 to 15 has dropped the normalized objective function value from 0.11 to 0.09, the mean percentage error from $\sim 5\%$ to $\sim 2\%$ and the maximum percentage error from $\sim 26\%$ to $\sim 8\%$. Although the drop in the normalized objective function value and the mean percentage error does not seem to be significant, it is indicative, as shown in Section 4.2.2, especially when the maximum percentage error has dropped significantly. This was also noticed for the fitting runs that were carried out for the experimental FRF of the fixture. In conclusion, in order to obtain a fit with the lowest maximum percentage error (less than 12%) it is desirable to reach the smallest possible mean percentage error (usually

less than 3.5%).

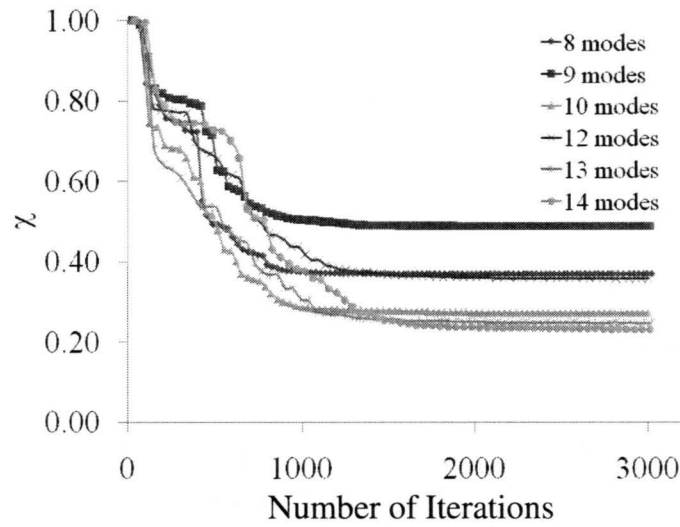
Not all extracted modal parameters can be used; some fitting runs give erroneous results although they were obtained from converged runs. For example results illustrated in Figures 4.11a, 4.12a, and 4.13a indicate that results of modes 9 and 14 cannot be used. While the trend of the normalized objective function's value, and the mean and the maximum percentage error decreases with the increase of the number of suggested modes, the outcome at those two modes does not agree with the is off the general trend.

The computational time of the fitting run's computational time was also affected by the number of suggested modes; increasing the suggested number of modes increases the computational time, this is illustrated in Figure 4.14. It should be noted that for the same suggested number of modes, the run carried out for fitting the experimental FRF data of the fixture, Figure 4.14a was almost half that needed for fitting the experimental FRF data of the cutting tool, Figure 4.14b. That was mainly caused by the data record of the cutting tool's FRF was almost double in size of that of the fixture.

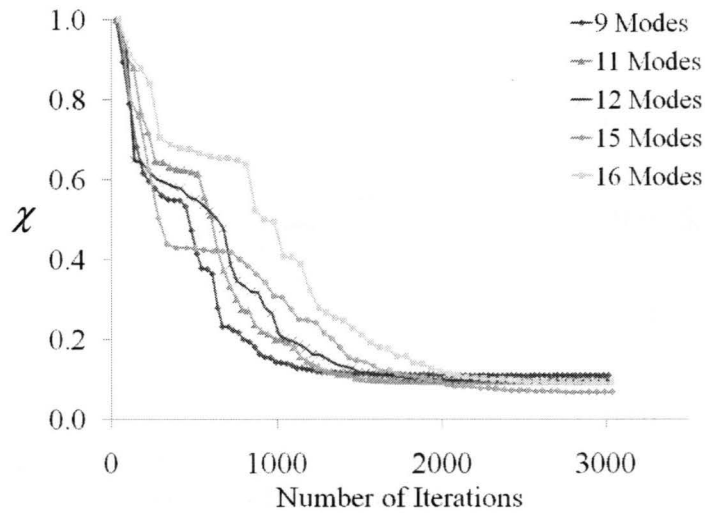
4.3 Summary

Throughout this chapter the modified RFP method was presented and investigated. A constraint optimization process was developed and used to identify the modal parameters for structures that undergo a hammer impact testing. The method is mainly based on the RFP model presented by Richardson [5]. The constraints ensure that the solution will to always have the pole's real part negative, this is necessary to obtain a stable system, also and that the damping ratio does not exceed a certain reasonable value, which is, typically less than 10%. Special issues during programming

were discussed and analyzed. These, which included the use of different objective functions, coding and decoding of the input used in the optimization process. It also discussed the flexibility of the ORFP method and showed how it was able to extract the modal parameters given the number of modes desired, their natural frequencies and their damping ratios. Finally, the stability and accuracy of the ORFP method was investigated.

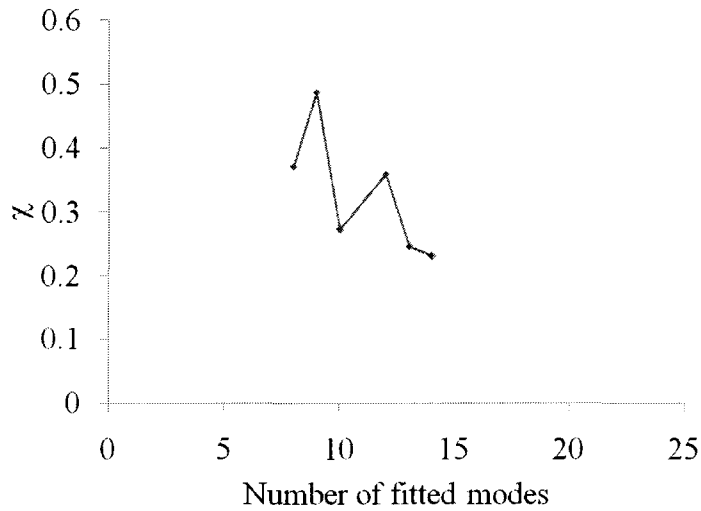


a. Fixture *X*-direction

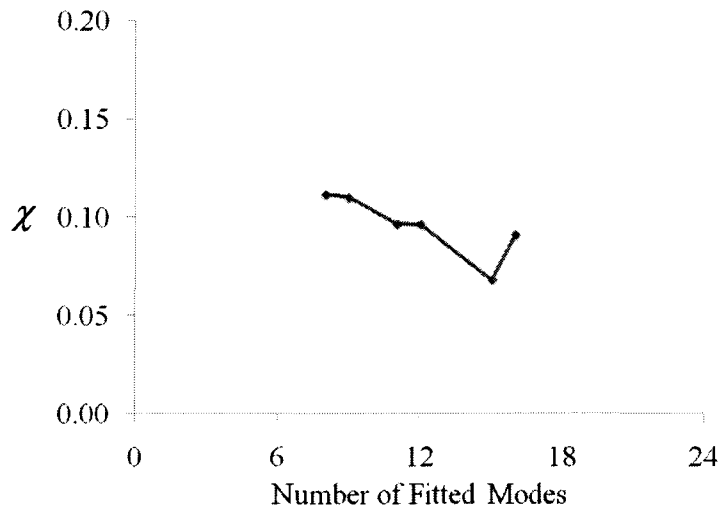


b. Tool *X*-direction

Figure 4.10 – Effect of varying the suggested number of fitted modes on the normalized objective function (χ) using the ORFP method over different number iterations.

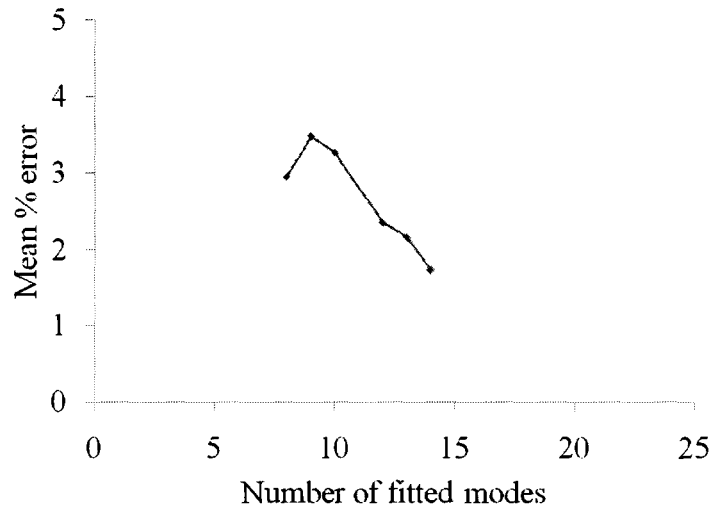


a. Fixture X-direction

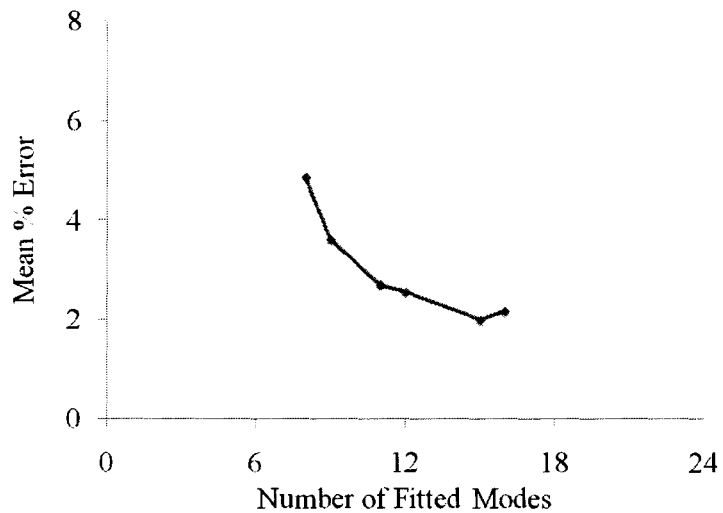


b. Tool X-direction

Figure 4.11 – Effect of varying the suggested number of fitted modes on the normalized objective function (χ) using the ORFP method.

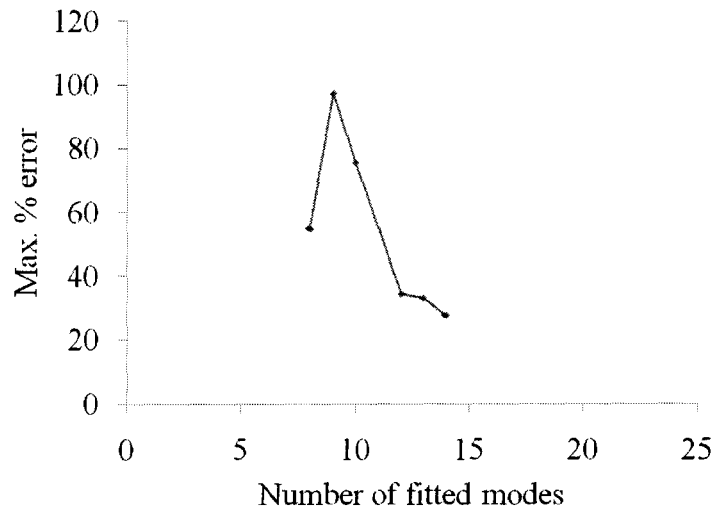


a. Fixture X-direction

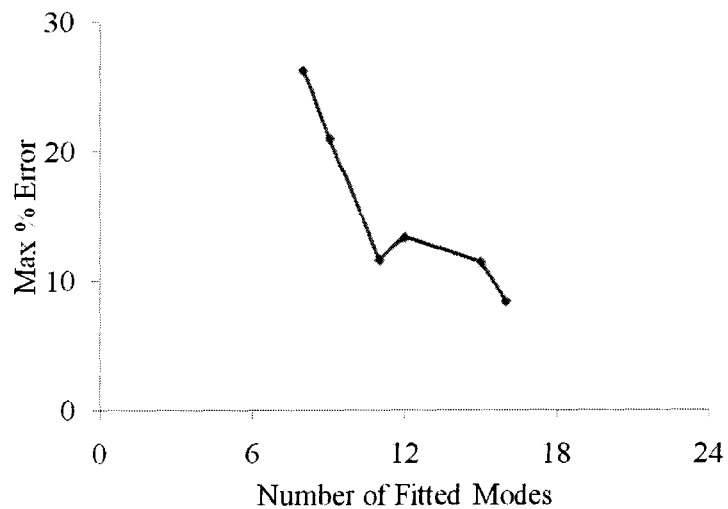


b. Tool X-direction

Figure 4.12 – Effect of varying the suggested number of fitted modes on the mean percentage error between the fitted and the experimental FRF.

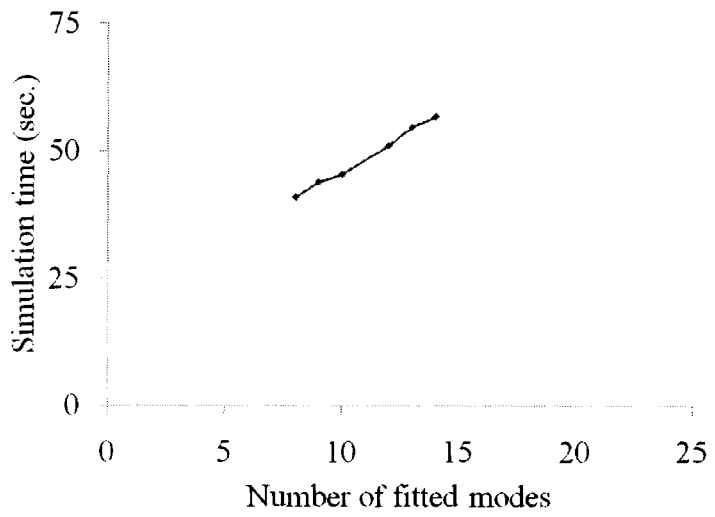


a. Fixture X-direction

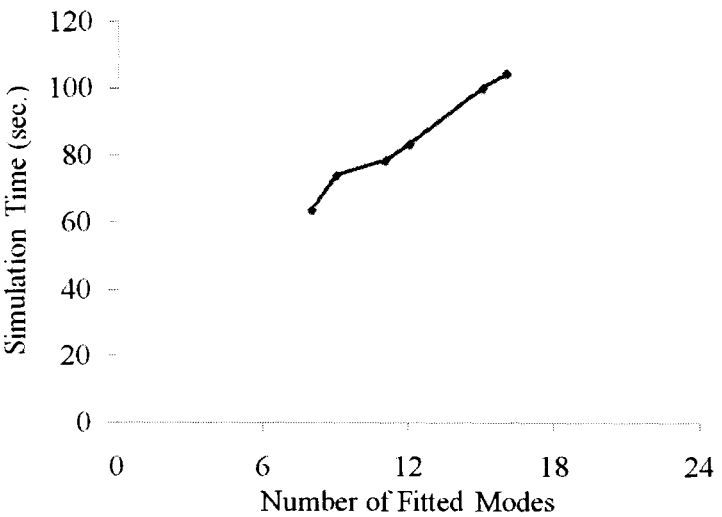


b. Tool X-direction

Figure 4.13 – Investigation of the variation of the suggested number of fitted modes on the maximum percentage error between the fitted and the experimental FRF.



a. Fixture X-direction



b. Tool X-direction

Figure 4.14 – Investigation of the variation of the suggested number of fitted modes on the simulation time.



CHAPTER 5

MODEL FOR CUTTING FORCE SIMULATION

5.1 Introduction

The model used throughout this study will be presented in detail in this chapter. This model was used to predict the specific cutting forces during HSM. The model captures the end milling process with a sharp solid carbide end mill. It should be noted that this model was previously developed by Tlustý et al. [6]. It is being presented here in depth because it forms the basis of this study and it has been modified to include issues of importance to HSM that have not been included before.

5.2 Basic Model

5.2.1 Background

The core of the model proposed in this study is based on the model originally presented by Tlustý et al. [6] that estimates the cutting forces resulting from simulating the end milling process by considering a rigid tool/rigid workpiece system model. A rigid system is one that does not vibrate under the variable loading resulting from the intermittent cutting process, which is theoretical. Alternatively, a flexible system is one that considers the stiffness that exists within different parts of the system and causes it to vibrate, which is closer to the real life problem. For simplicity of explanation the ideal model will be considered first followed by the more complex one that includes flexible structures.

5.2.2 Rigid tool/rigid system model

Simulating the end milling process

Normally, during the end milling process, the end milling cutter exhibits two motions; translational and rotational. Together these form a trochoidal path [86] as illustrated in Figure 5.1. In this model the motion of the end milling cutter was simplified, based on Martellotti's approximation [21], to consider only rotational motion, this leads to a circular path. This assumption is acceptable as long as the feed/tooth is maintained within a range of 0.0025 - 0.025 mm/tooth [22].

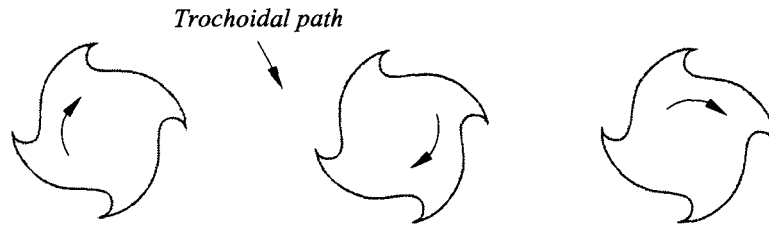


Figure 5.1 – Trochoidal path.

Figure 5.2a illustrates a typical straight end mill that is cutting a workpiece along its side. The edge of the cutting tool starts cutting at the bottom when point *a* engages with the workpiece. At this instant, the angular position of point *a* is called the start angle ϕ_s . Point *a*'s position progresses while the cutter rotates until it exits the material as illustrated in Figure 5.2b. The angle at this instant is called the exist angle ϕ_e . At any time during the cut, there can be a partial or full engagement of one or more of the cutting edges with the workpiece. The engagement depends on the axial depth of cut, the radial depth of cut and the helix angle [32], this is illustrated in Figures 5.3a and 5.3b respectively. The cutting forces are then estimated instantaneously along all of the edge portions that are engaged with the workpiece, summed, and then decomposed into the main coordinate system directions.

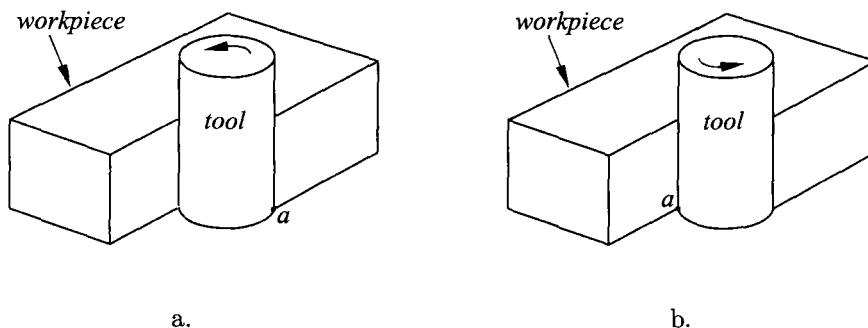


Figure 5.2 – Simulation of the end milling process, engagement angle.

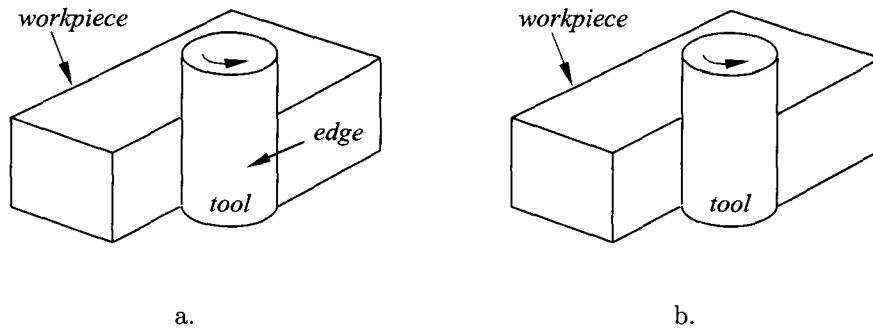


Figure 5.3 – Simulation of the end milling process, teeth engagement.

Estimating the cutting forces

The cutting tool's portion engaged with the workpiece is discretized into n levels in the vertical direction, see Figure 5.4, leaving each level with an incremental axial depth of cut Δd_a . At each discretization level n , and tooth j , elemental conventional cutting forces are being estimated in two directions; tangential and normal to the cutting direction using the following set of equations

$$\Delta F_t = K_t \Delta d_a t_c \quad (5.1)$$

$$\Delta F_r = \mu \Delta F_t \quad (5.2)$$

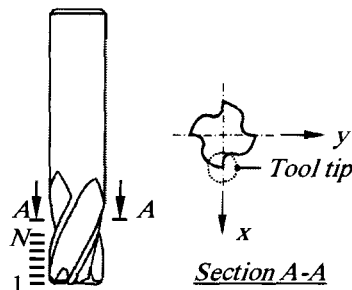


Figure 5.4 – Cutting tool discretization.

where ΔF_t is the incremental cutting forces in the tangential direction, ΔF_r is the incremental cutting forces in the radial direction (normal to the cutting direction), K_t is the specific cutting force in the tangential direction and μ is a constant of proportionality.

Since the cutter's motion was assumed to be only rotational, t_c is evaluated as a function of the rotational angle ϕ_i at time i and tooth j and discretization level n using Equation 5.3

$$t_{c,j,n}^i = f_t \sin(\phi_i) \quad (5.3)$$

It is also assumed that there is always a constant ratio between ΔF_t and ΔF_r maintained by μ . This is not always the case as was shown in [24, 36, 39, 87].

Hence, F_t and F_r will be estimated independently. The elemental conventional cutting forces are then decomposed into the main coordinate system directions, as shown in Figure 5.5, using Equations 5.4 - 5.7.

$$\Delta F_{tx,j,n}^i = +\Delta F_{t,j,n}^i \sin(\phi_i) \quad (5.4)$$

$$\Delta F_{ty,j,n}^i = -\Delta F_{t,j,n}^i \cos(\phi_i) \quad (5.5)$$

$$\Delta F_{rx,j,n}^i = -\Delta F_{r,j,n}^i \cos(\phi_i) \quad (5.6)$$

$$\Delta F_{ry,j,n}^i = -\Delta F_{r,j,n}^i \sin(\phi_i) \quad (5.7)$$

where $\Delta F_{tx,j,n}^i$, $\Delta F_{ty,j,n}^i$, $\Delta F_{rx,j,n}^i$, and $\Delta F_{ry,j,n}^i$ are the instantaneous elemental tangential and radial cutting force in the X and Y direction at time i , tooth j , and discretization level n respectively.

It should be noted that this set of equations can vary according to the coordinate system or the force directions desired. For example, if one would simulate the cutting forces generated on the cutting tool with a rotating coordinate frame it would have a

different set of equations than simulating the cutting forces acting on the workpiece being machined.

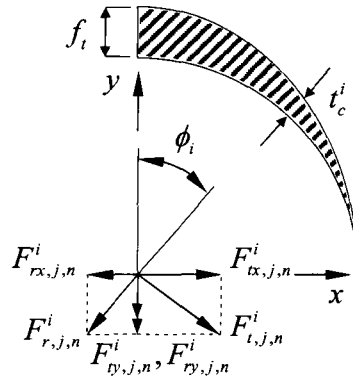


Figure 5.5 – Cutting force convention.

The elemental conventional cutting forces, which are already decomposed into the main coordinate system, are then summed along all the edges engaged in the cut, each edge at a time using Equations 5.8 and 5.9.

$$F_x^i = \sum_{j=1}^J \left(\sum_{n=1}^N (\Delta F_{rx,j,n}^i + \Delta F_{tx,j,n}^i) \right) \quad (5.8)$$

$$F_y^i = \sum_{j=1}^J \left(\sum_{n=1}^N (\Delta F_{ry,j,n}^i + \Delta F_{ty,j,n}^i) \right) \quad (5.9)$$

where F_x^i , and F_y^i are the instantaneous cutting forces decomposed in the X and Y direction respectively.

The position of the cutting tool ϕ_i is then increased by an angular increment $\Delta\phi$ and the forces at the next angular position are re-estimated using the same methodology.

At a given instant i the cutting tool is at position ϕ_i . The engaged portion of the cutting edge is discretized into a finite number n of small sectors each having an angle $\Delta\psi$. When moving along the helix of the cutting edge j each axial level n is

increased by a distance Δd_a and an angular increment of $\Delta\psi$ while maintaining a consistent check for not falling out of the engagement region, i.e. ψ_n should always be greater than ϕ_s and smaller than ϕ_e for the cutter to be in cut. The whole process is summarized in the flow chart illustrated in Figure 5.6.

5.3 Extended Model

5.3.1 Introduction

The model presented in Section 5.2 was an idealized model. In that model it was assumed, under certain conditions, that the uncut chip thickness was a function of the feed/tooth f_t and the rotational angle ϕ . It was also assumed that any flexibility in the system, i.e. the dynamics of the system, was not considered. In reality it is quite common for run-out to exist in the tool/tool holder arrangement which in turn affects the estimation of the SCF especially in HSM. All of those factors were not yet considered in the model. Although the force model used so far has been demonstrated to be simple and effective, there was a need for a more complex model which captures issues of particular importance to HSM. This will be discussed in more detail in Chapter 7. The basic model, presented in Section 5.2, will be further modified and extended to account for a wider range of system dynamics and include tool run-out. The dynamics of the system were considered by integrating the RFP model in the cutting force model and the tool run-out was considered by including a run-out model as described in [88].

While further developing the basic model, the following general assumptions are considered:

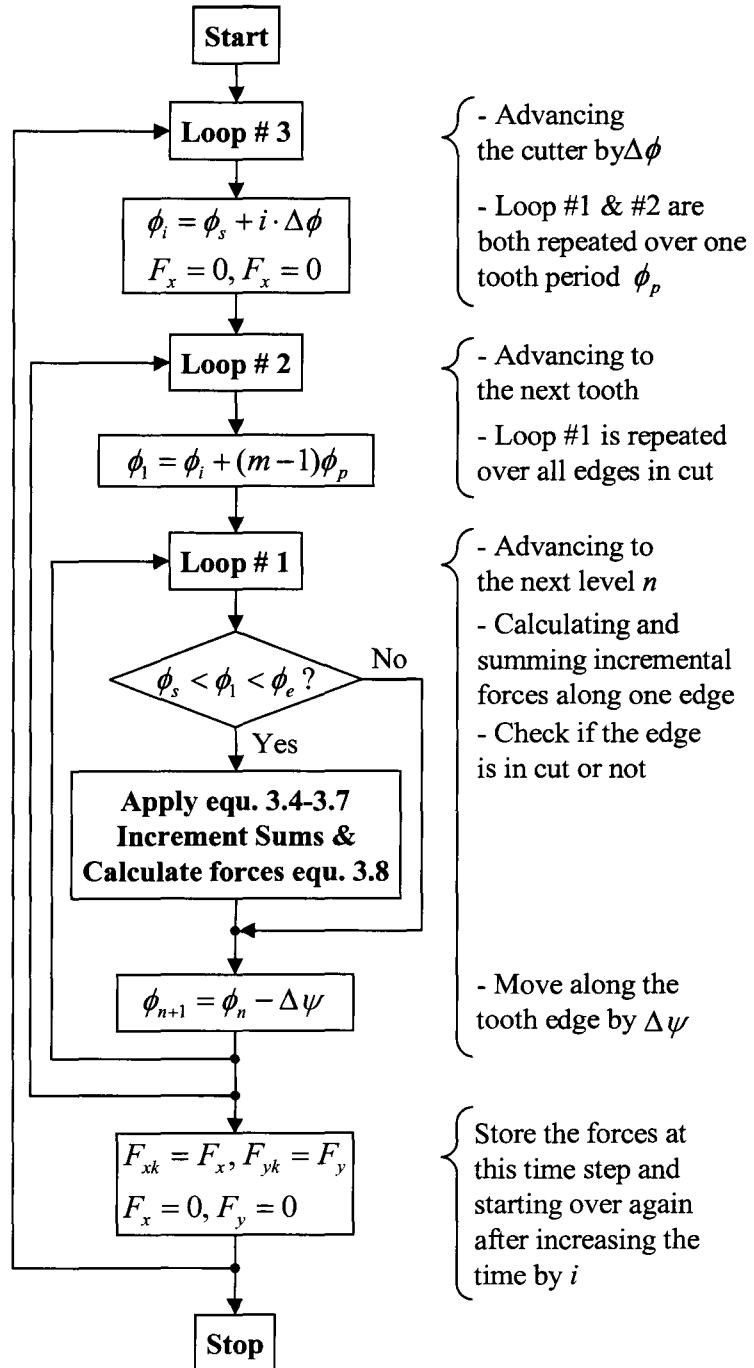


Figure 5.6 – Flow chart of basic simulation model.

- The cutting tool is sharp
- Equations 5.1 and 5.2 will be modified becoming

$$\Delta F_t = K_t \Delta d_a t_c \quad (5.10)$$

$$\Delta F_r = K_r \Delta d_a t_c \quad (5.11)$$

where K_r is the specific cutting force in the radial direction. Since K_t and K_r are each dependent on the cutting conditions, they will be evaluated independently.

- The cutting tool is performing side end milling as described in Figure 5.2.
- In addition to the forces estimated in the X and Y direction, the axial force, Z , will be considered.

5.3.2 Force model

- **Specific cutting force**

In the past, the SCF was estimated in several ways, mainly depending on the cutting force. For example, for certain cutting conditions, an initial value for the SCF was assumed and the cutting force was calculated and compared to the experimental one. Then the value of the SCF was fine-tuned by increasing or decreasing its value until the calculated cutting force matches the experimental one thus yielding the right value of the specific cutting force for that specific cutting condition. Then the same procedure was repeated for another cutting condition. This process was repeated until the SCF is determined for the entire range of cutting conditions of interest. Then an equation, that is function of the cutting conditions variables can be fitted using the obtained SCF.

In this study a new technique for evaluating the SCF is presented. It is mainly based on estimating the acceleration of the fixture and comparing it to the experimental one. An accelerometer is mounted on the fixture and is used for: (1) measuring the acceleration of the fixture during the cutting process, (2) obtaining the experimental FRF, at the same position on the fixture, and extracting its modal parameters. The modal parameters of the cutting tool are then extracted the same way but using a different miniature accelerometer. Once the modal parameters of the fixture and the cutting tool are extracted then it is possible to obtain the displacement of the system analytically with the acceleration being obtained by differentiating the displacement twice. A comparison could then be made between the analytical and the experimental acceleration. It should be noted that the displacement of the fixture results from applying the cutting force on the fixture FRF in the time domain and where the cutting force is a function of both the specific cutting force and the current/previous uncut chip thickness t_c^i and t_c^{i-1} respectively. The uncut chip thickness takes into account the relative displacement, current and previous, between the fixture and the cutting tool. In this way the SCF can be fine-tuned so that the analytical and experimental FRF can be matched.

- **Extended force model**

The cutting force model presented by Equation 5.1 is a relatively simple model where the SCF obtained after calibration from such a model will vary using one set of cutting conditions to another even for the same material. Furthermore the constant ratio between their different components do not hold. The SCF will then be considered independent of each other and only dependent on the cutting conditions

as described by Equations 5.12 and 5.13.

$$K_t = A_1 V^{a_1} f_t^{b_1} d_r^{c_1} \quad (5.12)$$

$$K_r = A_2 V^{a_2} f_t^{b_2} d_r^{c_2} \quad (5.13)$$

V is the cutting speed, d_r is the radial depth of cut. Furthermore, this cutting force model only considered the force generated in the X and Y directions, the force in the Z direction was considered by assuming an incremental axial component of the cutting force at each time i , cutting edge j and discretization level n as given by Equation 5.14.

$$\Delta F_{a,j,n}^i = K_a \Delta d_a t_{c,j,n}^i, \quad (5.14)$$

where

$$K_a = A_3 V^{a_3} f_t^{b_3} d_r^{c_3} \quad (5.15)$$

that is summed along each edge j engaged in the cut, at time i , and axial level n using Equation 5.16.

$$F_z^i = \sum_{j=1}^J \left(\sum_{n=1}^N (\Delta F_{a,j,n}^i) \right) \quad (5.16)$$

A_i , a_i , b_i and c_i ($i \in 1 \dots 3$) are all constants that are calibrated and determined experimentally. F_z^i is the instantaneous cutting forces in the axial direction.

• Extended orthogonal force model

The cutting force model presented by Equation 5.1 is a mechanistic model and the specific cutting force obtained after calibration from such a model does not necessarily represent the material being machined as it forms a constant of proportionality that is affected by the cutting conditions. In this case one might end up having similar specific cutting forces for two different materials with each of them obtained under

different cutting conditions. To avoid this condition an analytical cutting force model will be used to reflect the material being machined to show that regardless of the cutting force model used the new measurement technique will be able to predict the same cutting forces and workpiece fixture acceleration obtained using the mechanistic model.

Merchant presented an idealized orthogonal cutting force model that can be used in 2D under certain conditions [7]. This cutting force model will be extended in order to account for axial force.

In Merchant's model, illustrated in Figure 5.9, as the cutting tool progresses it is always cutting a constant uncut chip thickness. This is not the same for the case of end milling. To make it usable for the end milling process Merchant's model will be applied instantaneously as shown in Figure 5.7. This means that at each time i , tooth j and discretization level n different model parameters will be calculated instantaneously as the uncut chip thickness $t_{c,j,n}^i$, progresses from one instant to the next.

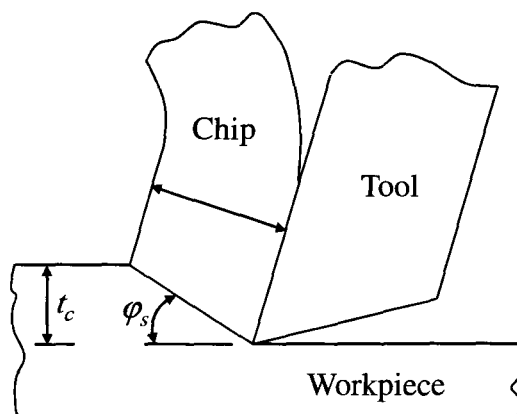


Figure 5.7 – Orthogonal cutting.

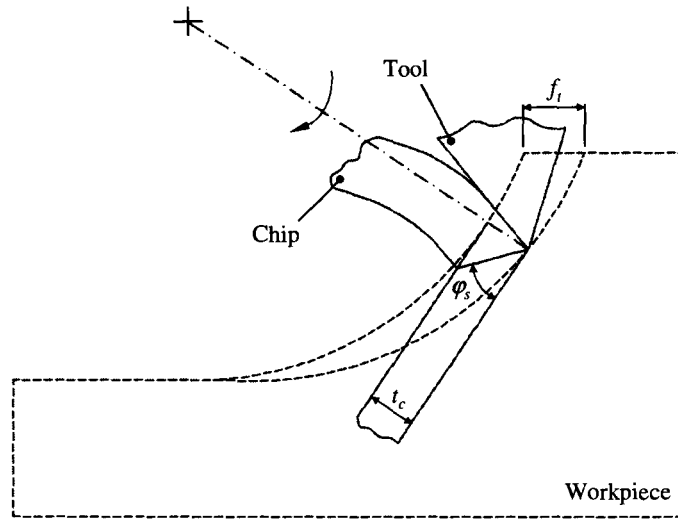
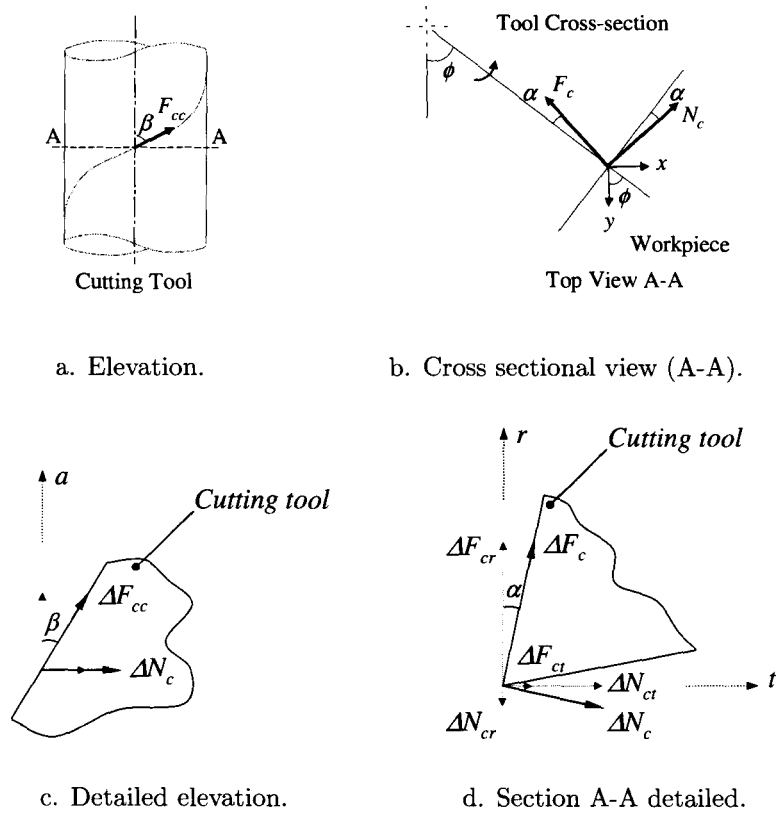


Figure 5.8 – Merchant’s model adapted to end milling process.



a. Elevation.

b. Cross sectional view (A-A).

c. Detailed elevation.

d. Section A-A detailed.

Figure 5.9 – Analytical cutting force model.

Incremental cutting forces are evaluated at each discretization level n , summed up across each cutting edge that is engaged in cut and then decomposed into the main coordinate system in the same way as explained earlier in Section 5.2.2.

The model consists of an incremental friction force ΔF_c between the chip and the rake face and acts inwards along the rake face of the cutting tool parallel to the level of the discretization plane. An incremental force ΔN_c , normal to the friction force, is concentrated at the tip of the cutting tool and acts in opposition to the motion of the tool. Another incremental friction force ΔF_{cc} acts axially on the rake face but upwards on the helix to represent the chip flow action. This is illustrated in Figures 5.9c and 5.10 respectively.

At time i , tooth j and discretization level n the cutting forces are being estimated in the main coordinate directions X , Y and Z using Equations 5.8, 5.9 and 5.16 respectively. The three force components tangential, radial and axial are derived from Figures 5.9 and 5.10 and are estimated using Equations 5.17 - 5.19.

$$\Delta F_{t,j,n}^i = \Delta F_{c,j,n}^i \sin(\alpha) + \Delta N_{c,j,n}^i \cos(\alpha) \quad (5.17)$$

$$\Delta F_{r,j,n}^i = \Delta F_{c,j,n}^i \cos(\alpha) - \Delta N_{c,j,n}^i \sin(\alpha) \quad (5.18)$$

$$\Delta F_{a,j,n}^i = \Delta F_{cc,j,n}^i \cos(\beta) - \Delta N_{c,j,n}^i \sin(\beta) \quad (5.19)$$

$\Delta F_{c,j,n}^i$ and $\Delta N_{c,j,n}^i$ are estimated using Equations 5.20 and 5.21 respectively.

$$\Delta F_{c,j,n}^i = \mu \Delta N_{c,j,n}^i \quad (5.20)$$

$$\Delta N_{c,j,n}^i = \sqrt{\frac{(\Delta F_{s,j,n}^i)^2 + (\Delta N_{s,j,n}^i)^2}{1 + \mu^2}} \quad (5.21)$$

where α is the radial helix angle, β is the helix angle, $\Delta F_{s,j,n}^i$, $\Delta N_{s,j,n}^i$ are the instantaneous elemental shearing force and its normal at time i , tooth j , and discretization level n respectively, and μ is the friction coefficient.

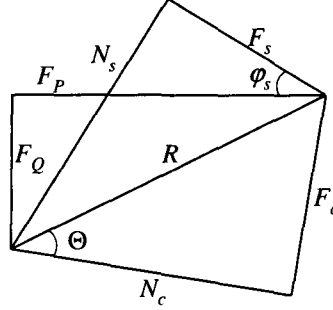


Figure 5.10 – Merchant's circle.

$F_{s,j,n}^i$ and $N_{s,j,n}^i$ are estimated using Equations 5.22 and 5.23 respectively.

$$\Delta F_{s,j,n}^i = \tau_{ut,j,n}^i dA_{s,j,n}^i \quad (5.22)$$

$$\Delta N_{s,j,n}^i = \sigma_{ut,j,n}^i dA_{s,j,n}^i \quad (5.23)$$

$\Delta A_{s,j,n}^i$ is the elemental area of the shear zone at time i , tooth j and level n and is estimated using Equation 5.24.

$$\Delta A_{s,j,n}^i = \frac{\Delta d_a t_{j,n}^i}{\sin(\varphi_s)} \quad (5.24)$$

where φ_s is the shear angle. In this model it is assumed that the material's ultimate tensile τ_{ut} and shear strength σ_{ut} will change instantaneously based on the strain γ , strain rate $\dot{\gamma}$ and the temperature $T_{j,n}^i$ of the primary shear zone at each time i , tooth j and discretization level n . The tensile and shear strength of the material will be

evaluated using Johnson-Cook equation [89], which is given by Equations 5.25 and 5.26 respectively.

$$\tau_{ut,j,n}^i = \frac{1}{\sqrt{3}} \left[A + B \left(\frac{\dot{\gamma}_{j,n}^i}{\sqrt{3}} \right)^n \right] \left[1 + C \ln \left(\frac{\dot{\gamma}_{j,n}^i}{\dot{\gamma}_o} \right) \right] \left[1 - \left(\frac{T - T_r}{T_m - T_r} \right)^m \right] \quad (5.25)$$

$$\sigma_{ut,j,n}^i = \left[A + B \left(\frac{\dot{\gamma}_{j,n}^i}{\sqrt{3}} \right)^n \right] \left[1 + C \ln \left(\frac{\dot{\gamma}_{j,n}^i}{\dot{\gamma}_o} \right) \right] \left[1 - \left(\frac{T - T_r}{T_m - T_r} \right)^m \right] \quad (5.26)$$

A , B , C , n and m are all material constants that are determined experimentally.

$$\gamma = \frac{\cos(\alpha)}{\sin(\varphi_s) \cos(\varphi_s - \alpha)} \quad (5.27)$$

$$\dot{\gamma} = \frac{V \sin(\varphi_s)}{t_c} \quad (5.28)$$

In Equations 5.22 and 5.23 the instantaneous tensile and shear strength were estimated in the primary shear zone [9]. This implies that the temperature T in Equations 5.25 and 5.26 should be evaluated at the primary shear zone as well. Since the instantaneous uncut chip thickness $t_{j,n}^i$ in Equation 5.24 varies at each instant i , tooth j and level n , T should also vary accordingly hence becoming $T_{j,n}^i$ and Equations 5.25 and 5.26 becomes

$$\tau_{ut,j,n}^i = \frac{1}{\sqrt{3}} \left[A + B \left(\frac{\dot{\gamma}_{j,n}^i}{\sqrt{3}} \right)^n \right] \left[1 + C \ln \left(\frac{\dot{\gamma}_{j,n}^i}{\dot{\gamma}_o} \right) \right] \left[1 - \left(\frac{T_{j,n}^i - T_r}{T_m - T_r} \right)^m \right] \quad (5.29)$$

$$\sigma_{ut,j,n}^i = \left[A + B \left(\frac{\gamma_{j,n}^i}{\sqrt{3}} \right)^n \right] \left[1 + C \ln \left(\frac{\gamma_{j,n}^i}{\gamma_o} \right) \right] \left[1 - \left(\frac{T_{j,n}^i - T_r}{T_m - T_r} \right)^m \right] \quad (5.30)$$

The melting temperature of the material tested T_m as well as the reference temperature (room temperature) T_r will be obtained from the literature. The temperature at the primary shearing zone was evaluated using Equation 5.31.

$$T_{j,n}^i = T_r + \theta_{s,j,n}^i \quad (5.31)$$

The average temperature rise in the primary shear zone $\theta_{s,j,n}^i$ and in the secondary shear zone $\theta_{f,j,n}^i$ were evaluated instantaneously at each time i , tooth j and level n using Equations 5.32 and 5.33 respectively.

$$\theta_{s,j,n}^i = \frac{(1 - \Gamma_{j,n}^i) p_{s,j,n}^i}{\rho_{j,n}^i C_{p,j,n}^i V t_{c,j,n}^i \Delta d_a} \quad (5.32)$$

$$\theta_{f,j,n}^i = \frac{p_{f,j,n}^i}{\rho_{j,n}^i C_{p,j,n}^i V t_{c,j,n}^i \Delta d_a} \quad (5.33)$$

where

$$\Gamma_{j,n}^i = 0.15 \ln \left(\frac{27.5}{R_{j,n}^i \tan(\varphi_s)} \right) \quad (5.34)$$

$$R_{j,n}^i = \frac{\rho_{j,n}^i C_{p,j,n}^i V t_{c,j,n}^i}{K_{j,n}^i} \quad (5.35)$$

The maximum temperature rise in the secondary heating zone was given by Equation 5.36 and the maximum cutting temperature could then be estimated using Equation 5.37.

$$\theta_{m,j,n}^i = \theta_{f,j,n}^i 1.13 \sqrt{\frac{R_{j,n}^i}{1 + \tan(\varphi_s - \alpha)}} \quad (5.36)$$

$$T_{max,j,n}^i = T_r + \theta_{s,j,n}^i + \theta_{m,j,n}^i \quad (5.37)$$

$\Gamma_{j,n}^i$ is the instantaneous fraction of the total heat generated in the primary deformation zone at time i , tooth j , and discretization level n . The heat generation rate in the primary shearing zone is given by Equation 5.38.

$$p_{s,j,n}^i = p_{m,j,n}^i - p_{f,j,n}^i \quad (5.38)$$

where

$$p_{m,j,n}^i = \Delta F_{p,j,n}^i V \quad (5.39)$$

$$p_{f,j,n}^i = \Delta F_{c,j,n}^i V_c \quad (5.40)$$

$$V_c = \frac{V \sin(\varphi_s)}{\cos(\varphi_s - \alpha)} \quad (5.41)$$

V_c is the velocity on the rake face, $\rho_{j,n}^i$, $C_{p,j,n}^i$, and $K_{j,n}^i$ are the instantaneous density, the instantaneous specific heat, and the instantaneous thermal conductivity of test material respectively. It should be noted that those are material constants that are affected by the temperature [90]. So during the simulation those constants are evaluated every time the temperature is evaluated.

The incremental friction force due to the chip flow $\Delta F_{cc,j,n}^i$ is a function of conditions between the tool and workpiece and varies along the helix and is represented

by Equation 5.42 in this model.

$$\Delta F_{cc,j,n}^i = \mu_c \Delta N_{c,j,n}^i \quad (5.42)$$

The specific energy can be used to express how difficult it is to machine a certain material and is measured by the power per unit volume per unit time. The total specific energy during machining is the sum of four components: (1) specific energy due to shear u_s , (2) specific energy due to friction u_f , (3) specific energy required to accelerate the chip u_m and (4) the specific energy to produce a new uncut surface u_a . The components u_m and u_a are usually very small and can generally be neglected. However for high cutting speeds u_m needs to be accounted for. Typically, u_s and u_f represents $\sim 75\%$ and $\sim 25\%$ of u respectively. The total specific energy is the sum of all four components previously mentioned as shown in Equation 5.43. It should be noted that the specific energy will be evaluated instantaneously at each time i , tooth j and level n as given by Equations 5.43 - 5.47.

$$u_{j,n}^i = u_{s,j,n}^i + u_{f,j,n}^i + u_{m,j,n}^i + u_{a,j,n}^i \quad (5.43)$$

$$\simeq u_{s,j,n}^i + u_{f,j,n}^i + u_{m,j,n}^i \quad (5.44)$$

and

$$u_{s,j,n}^i = \frac{\tau_{ut,j,n}^i \cos(\alpha)}{\sin(\varphi_s) \cos(\varphi_s - \alpha)} \quad (5.45)$$

$$u_{f,j,n}^i = \frac{F_{c,j,n}^i \sin(\varphi_s)}{\cos(\varphi_s - \alpha) t_{j,n}^i \Delta d_a} \quad (5.46)$$

$$u_{m,j,n}^i = \frac{F_{m,j,n}^i \cos(\alpha)}{\cos(\varphi_s - \alpha) t_{j,n}^i d_a} \quad (5.47)$$

where

$$F_{m,j,n}^i = \rho_{j,n}^i V^2 t_{c,j,n}^i \omega \gamma_{j,n}^i \sin(\varphi_s) \quad (5.48)$$

From Equations 5.17 - 5.48 it can be seen that they depend mainly on three values; φ_s , μ and μ_c . Those variables are the main calibration parameters through which the simulated acceleration will be matched with the experimental one. The simulation will start with an initial value of φ_s , μ , and μ_c then vary until the simulated acceleration matched with the experimental one.

5.3.3 System dynamics

Introduction

Generally speaking, most models available in the literature consider the system as comprised of the tool/tool holder, spindle and the machine-tool to be two single degree of freedom systems each comprised of a mass, spring and a damper. Each system acts in the direction of the main coordinate system. This is illustrated in Figure 5.11. At a given instant i , the tangential and radial forces are decomposed to the main coordinate system, X and Y , and each is considered as an input force to the equation of motion of the single degree of freedom system representing that direction. This is described by the following set of equations.

$$m_x \ddot{x}^i + c_x \dot{x}^i + k_x x^i = F_x^i \quad (5.49)$$

$$m_y \ddot{y}^i + c_y \dot{y}^i + k_y y^i = F_y^i \quad (5.50)$$

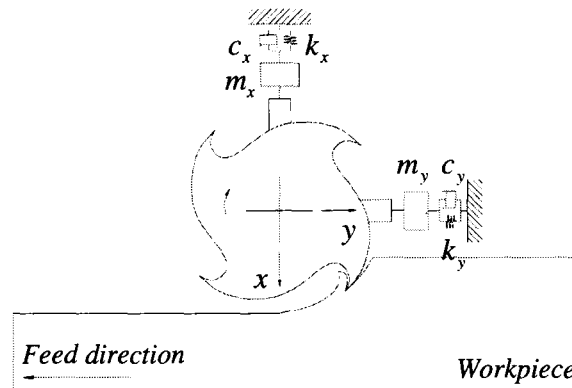


Figure 5.11 – Model dynamics.

The equation of motion can be solved numerically using a Runge-Kutta 4th order or a finite difference algorithm. The displacement due to that force will cause the centre of the cutting tool center to vibrate which in turn will have an effect on the uncut chip thickness t_c at this instant. The uncut chip thickness t_c is then adjusted to incorporate that effect.

Using two single degree of freedom systems to represent the dynamics of the milling machine can be a good approximation when there is one dominant mode within the range of the spindle speeds used. Now with higher spindle speeds a larger dynamic range must be considered. In addition, the dynamics of the dynamometer used to capture the cutting forces signal will impact the measurements so it must be accounted for or else an alternative means must be found to capture the cutting force.

It was very important to accurately capture the cutting forces as they were used to estimate the respective SCF and study how they vary under different cutting conditions. Capturing the cutting force for that specific reason would not be necessary if there was an alternative means to estimate the SCF. However this would require a more complex dynamic model that accounts for several modes. In this case the RFP model worked well at representing the multi-modes of interest and was easy to use and was accurate [65] however it needed to be modified for use in the time domain.

Simulation in the time domain

The RFP model gives the response of the system in the frequency domain, however the simulation model required that the dynamic response be obtained in the time domain so that it could be integrated in the cutting force simulation model. To add the dynamic effect at any time i it is necessary to get the response of the system to modify the position of the tool center, and hence its uncut chip thickness t_c^i at this instant. The convolution theorem (sometimes referred to as 'Duhamel's Method') will be used to get the response of the system in the time domain given the analytical FRF in the frequency domain after extracting the modal parameters of the system using the ORFP method presented in the previous chapter.

The response of a single degree of freedom system subject to an impulse force $f(t')$ as that illustrated in Figure 5.12 is given by Equation 5.51.

$$\delta_x(t) = h(t - t') f(t') dt' \quad (5.51)$$

where

$$h(t) = \mathcal{L}^{-1}(H(\omega)) \quad (5.52)$$

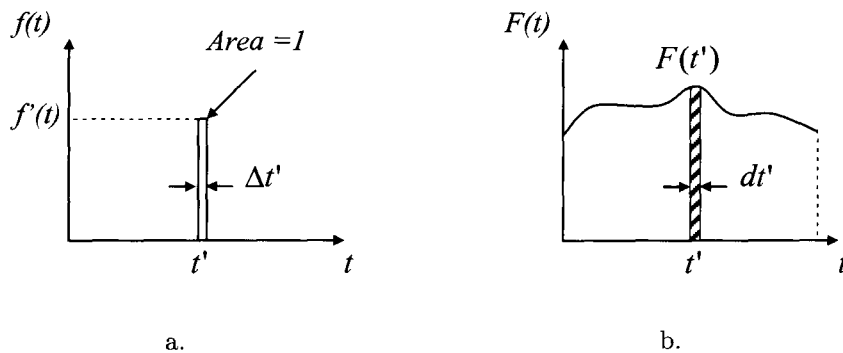


Figure 5.12 – Convolution theorem.

An arbitrary sequence of force varying in time can be assumed to be a sequence of impulses. The response of the system due to that sequence of impulses can be calculated by adding or superimposing all of the incremental responses as shown in Equation 5.53. Note that, in this context, the asterisk denotes convolution.

$$\Delta x_v(t) = \int_{-\infty}^{\infty} h(t-t') * f(t') dt' \quad (5.53)$$

For a continuous system the analytical FRF can be expressed as shown in Equation 3.3, likewise the response in the time domain will be the summation of the responses of each mode in the time domain as given by Equation 5.54.

$$h(t) = \sum_{r=1}^R h_r(t) \quad (5.54)$$

There is no direct form in the time domain of Equation 3.3, so the inverse laplace transform was applied to it yielding Equation 5.55.

$$h(t) = \sum_{r=1}^N \left(2e^{\sigma_r t} (Re(A) \cos(w_r t) - Img(A) \sin(w_r t)) \right) \quad (5.55)$$

The derivation of Equation 5.55 is given in Appendix A. During the cutting process the generated cutting force affects two systems; the cutting tool/spindle structure and the workpiece fixture. Each of those systems will respond under the generated force that is applied to it and correspond to its FRF in the time domain. So, the final uncut chip thickness was found from the relative displacement between the fixture and the cutting tool taking into consideration the time history effect of previous cuts, this is illustrated in Figure 5.13 and the instantaneous uncut chip thickness is given by Equation 5.56.

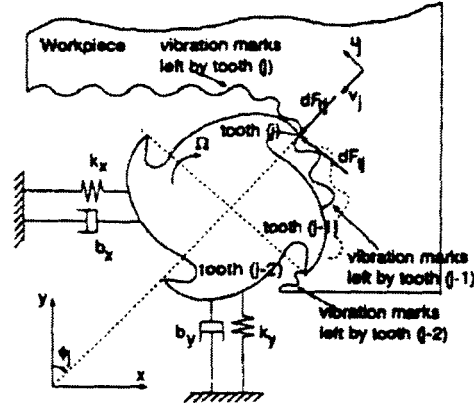


Figure 5.13 – Relative displacement between the tool & the workpiece/fixture [11].

$$t_{c,j,n}^i = f_{t,j,n}^i \sin(\phi_i) + (v_{t,j,n}^i - v_{f,j,n}^i) - (v_{t,j,n}^p - v_{f,j,n}^p) \quad (5.56)$$

where,

$$v_{t,j,n}^i = (x_{t,j,n}^i \sin(\phi_i)) + (y_{t,j,n}^i \cos(\phi_i)) \quad (5.57)$$

$$v_{f,j,n}^i = (x_{f,j,n}^i \sin(\phi_i)) + (y_{f,j,n}^i \cos(\phi_i)) \quad (5.58)$$

and

$$v_{t,j,n}^p = v_{t,j,n}^{i-N} \quad (5.59)$$

$$v_{f,j,n}^p = v_{f,j,n}^{i-N} \quad (5.60)$$

5.3.4 Run-out

A cutting tool with run-out is almost inevitable and at high speeds, its effect on the cutting forces must be accounted for. The run-out is defined by the eccentricity that takes place between the geometrical axis of the cutter and/or the tool holder and the

rotational axis. The presence of the run-out results in a varying chip load over the rotation of the cutter which in turn causes an uneven cutting force distribution over one complete revolution of the tool. There are two parameters that govern the run out of the cutter [16, 39, 88]; the run-out distance ρ (eccentricity) and the run-out angle λ_r as shown in Figure 5.14. For each cutting edge j and each discretization level n the run-out value was added to the instantaneous uncut chip thickness $t_{c,j,n}^i$. Equation 5.56 was then modified becoming

$$t_{j,n}^i = f_{t,j,n}^i \sin(\phi_i) + (v_{t,j,n}^i + v_{r,j,n}^i - v_{f,j,n}^i) - (v_{t,j,n}^p - v_{f,j,n}^p) \quad (5.61)$$

where,

$$v_{r,j,n}^i = e \cos(\phi_i - \lambda_r) \quad (5.62)$$

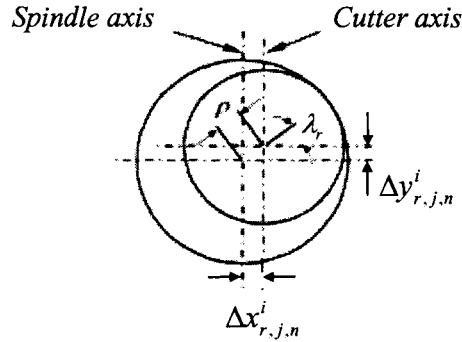


Figure 5.14 – Definition of run-out.

The run-out results in an unbalance mass m_e that caused a centrifugal force F_e that acts outwards on the center of rotation and normal to it. For conventional speeds the effect of the centrifugal force was minor and can be ignored, but for high speeds such as that used in this study, it has to be accounted for in the cutting force estimation. The unbalance mass was then discretized into n portions $\Delta m_{e,n}$

as illustrated in Figure 5.15a by the crescent-shaped gray area. The mass $m_{e,n}$ was concentrated in its center of gravity at a radius $r_{e,n}$ and the elemental centrifugal force $\Delta F_{e,n}^i$ at time i and level n was estimated by Equation 5.63 and acts outwards off the center of rotation of the cutting tool as shown in Figure 5.15b.

$$\Delta F_{e,n}^i = \Delta m_{e,n} r_e \omega^2 \quad (5.63)$$

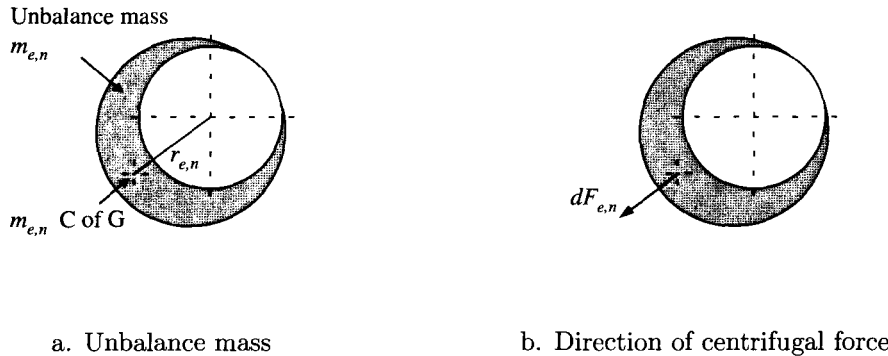


Figure 5.15 – Centrifugal force due to run-out.

$\Delta F_{e,n}^i$ is then decomposed into the main coordinate system X , and Y and is added to the terms of Equations 5.8 and 5.9 respectively.

5.4 Summary

A simulation model that was previously developed by Tlustý et al. [6] was used as the basis of the new model developed in this study. Both, base and extended, models were presented in this chapter. A basic simulation model that estimated the cutting forces was first presented and then was extended to include the axial cutting force components as well as the dynamics of the system. The dynamics of the system were then included by making use of the FRF of the system. The displacement

was then obtained by applying the convolution theorem to the FRF of the system. The extended model was modified so that it included the effect of the run out of the cutting tool to accommodate its effect at high rotational speeds. The extended model presented a new and improved method to estimate the specific cutting force which provided a model which was more suitable for simulating high speed machining purposes.

CHAPTER 6

EXPERIMENTAL DESIGN & SETUP

6.1 Introduction

This chapter discusses the experimental design and setup considerations that were used during the process of modal parameter extraction and data collection. Information is also provided for the equipment used in conducting the experiments and their respective setup.

6.2 Methodology

In this section, the methodology used to analyze and show the importance of the work presented throughout this dissertation is presented.

The core simulation model based on which the dynamic model was implemented is originally developed by Thusty [6]. This core model had to be re-built and compared with Thusty's own literature to make sure that it works.

The re-built model was then used, before implementing the improved dynamic model, to simulate the cutting forces resulting from the conducted experimental tests to understand the nature of the dynamics taking place during the cutting test.

An alternative mean to estimate the specific cutting forces, or the analytical model's main parameters φ_s , μ , and μ_c , is then suggested using the structure's acceleration.

Before verifying the suggested dynamic model it needs to go through a series of investigations to understand its behavior. The suggested dynamic model will be investigated for the following:

Selection of the number of modes during modal parameters extraction

The estimation of the specific cutting forces is affected by the process dynamics namely the selection of the number of modes that will be used in generating the analytical FRF of the workpiece/fixture setup so that it can be used in the proposed dynamic model.

Filtration of the simulated acceleration

The suggested model originally generates the displacement of the system. To be able to compare it to the experimental acceleration it needs to be differentiated with respect to time. Differentiation is very sensitive to noise hence filtrating of the simulated acceleration was necessary.

Effect of the run-out on the SCF estimation

Obtaining a tool that has no run-out is extremely difficult and with the increase of the rotational speed the effect of the centrifugal forces cannot either be ignored as it is directly proportional with ω^2 . Hence, the effect of the run-out has to be included in the model and investigated.

The methodology used can be summarized in the following points:

- Building and testing the core simulation model on which this study is based on.
- Showing the need to use an alternative method to estimate the SCF.
- Presentation of the suggested technique.
- Estimation of the SCF using the suggested technique.
- Analysis and investigation of the suggested technique.
- Fitting a non-linear model for the SCF using the suggested technique and verify it using a certain workpiece/fixture setup (setup # 1).
- Fitting the same non-linear model for the SCF and verify it but using a different workpiece/fixture setup (setup # 2).
- Estimating the analytical model's main parameters (φ_s , μ , and μ_c) using the suggested technique and using a certain workpiece/fixture setup (setup # 1).
- Estimating the analytical model's main parameters (φ_s , μ , and μ_c) using the suggested technique and using a certain workpiece/fixture setup (setup # 2).
- Comparing and discussing the SCF obtained using setup # 1 and setup # 2.
- Comparing and discussing the analytical model's main parameters using setup # 1 and setup # 2.
- Comparing and discussing the cutting forces resulting from the simulation using the mechanistic model and the analytical model with setup # 1 and setup # 2.

6.3 Experimental Design Consideration

Special considerations were taken when designing the experiments. Considerations included the selection of the cutting conditions, the experimental plan used to conduct the experiments, the design and the mounting of the fixture used to hold the specimen to be cut on top of the dynamometer and the data acquisition system used to capture the cutting forces. It also included the hammer test setup to extract the modal parameters of the cutting tool and of the workpiece fixture.

6.3.1 Cutting test related considerations

Cutting conditions selection

In this study the cutting conditions for the end milling process was limited to the variation of only three cutting parameters: (1) rotational speed (rev./min), (2) feed per tooth (f_t), and (3) radial depth of cut (d_r). The rest of the cutting parameters that can affect the cutting process were kept constant. This included the axial depth of cut d_a , the helix angle of the end milling cutter β , the number of teeth in the cutter and its diameter. The end milling cutter used was a solid carbide coated tool to minimize the effect of tool wear throughout the experiments and thus minimize the effect of plowing. The cutting conditions for the varying cutting parameters were chosen so that they reflect realistic operating conditions.

The lower limit of the spindle rotational speed was 30k rev./min while its higher limit was set to 60k rev./min based on the capability of the machine used. The lower value of the feed/tooth was chosen to be not less than 0.025 mm/tooth to ensure that there will always be an adequate metal to be removed by the cutting edge and thus minimize rubbing which can heat up the cutting tool and cause it to break. The upper value of the feed/tooth was governed by choosing two other values; the axial depth of

cut and the radial depth of cut. The axial depth of cut was held constant. The radial depth of cut values was chosen so that the combination of the feed/tooth-radial depth of cut-RPM would result in a cutting force that does not exceed the limits set by the manufacturer of the dynamometer in any of the three orthogonal cutting directions, which was ~ 250 N [91]. This was evaluated by a set of trial experiments that was initially conducted to investigate the cutting process outcome under different cutting conditions. It was also necessary to perform those trial experiments to choose the best settings for the data acquisition system. The final cutting conditions used are summarized in Tables 6.1 and 6.2 respectively.

Table 6.1 – Varying cutting condition used in the calibration process

Cutting parameter	Lower limit	Centre point	Upper limit
Feed/tooth (mm)	0.03	0.055	0.08
Radial depth of cut (mm)	0.4	0.65	0.9
Rotational speed (krev/min)	30	44	58

Table 6.2 – Fixed condition used in the cutting process

Cutting parameter	Parameter's value
Axial depth of cut (mm)	3.175
Helix angle ($^{\circ}$)	30

The cutting test matrix for calibration and verification are summarized in Tables 6.3 and 6.4 respectively.

Description of cutting test

The cutting test was plain side end milling as shown in Figure 5.2. The machine tool used has a fixed table with the feed action provided by the motion of the spindle driven by linear motors. For each cutting test the spindle was stopped a short distance from the workpiece while the spindle was left to dwell for a few seconds until it reached the desired rotational speed. Then the tool was moved towards the workpiece at the desired feed rate. Sufficient stand off was used to ensure that the axis reached the desired feed rate before cutting occurred. The tool moved past the workpiece after it finished the cut to ensure that its motion does not affect the data captured. This is summarized in Figure 6.1.

Before each cutting test the workpiece's side surface was squared and cleaned using another tool to ensure that the test tool was kept sharp.

Fixture design and mounting

The fixture shown in Figure 6.2b was the second in a two stage design. It was specially designed to accommodate some dynamic considerations. The hammer manufacturer highly recommended that the workpiece be mounted to a bigger mass (the fixture) otherwise the FRF of the system will be altered. The mass should be at least 10 times larger than that of the workpiece [92]. Having said that, the first design, which is shown in Figure 6.2a, had a weight close to the fixture, hence it needed to be redesigned. After another set of trial experiments, the fixture design was then changed to that shown in Figure 6.2b. The fixture was made of steel and the workpiece fixing technique was also considered to ensure a large mass and that an evenly distributed fixation force be applied along the length of the workpiece.

The fixture was mounted on the dynamometer which in turn was mounted on a

massive block fixed to the table of the machine tool. During mounting, the surface between the different parts was cleaned to ensure no debris was in the contact region. In addition, when mounting the dynamometer on the massive block a dial gage was used to ensure the parallelism of the dynamometer sides to the main axes of the machine, X and Y . The dial gage base was fixed by means of a powerful magnet nearby the spindle on a flat surface. A dial gage was used to true the dynamometer to within $10\ \mu\text{m}$, see Figure 6.3. A similar check was done in the other orthogonal direction. This check was essential because the dynamometer was of high sensitivity and any imperfection can contaminate the data captured.

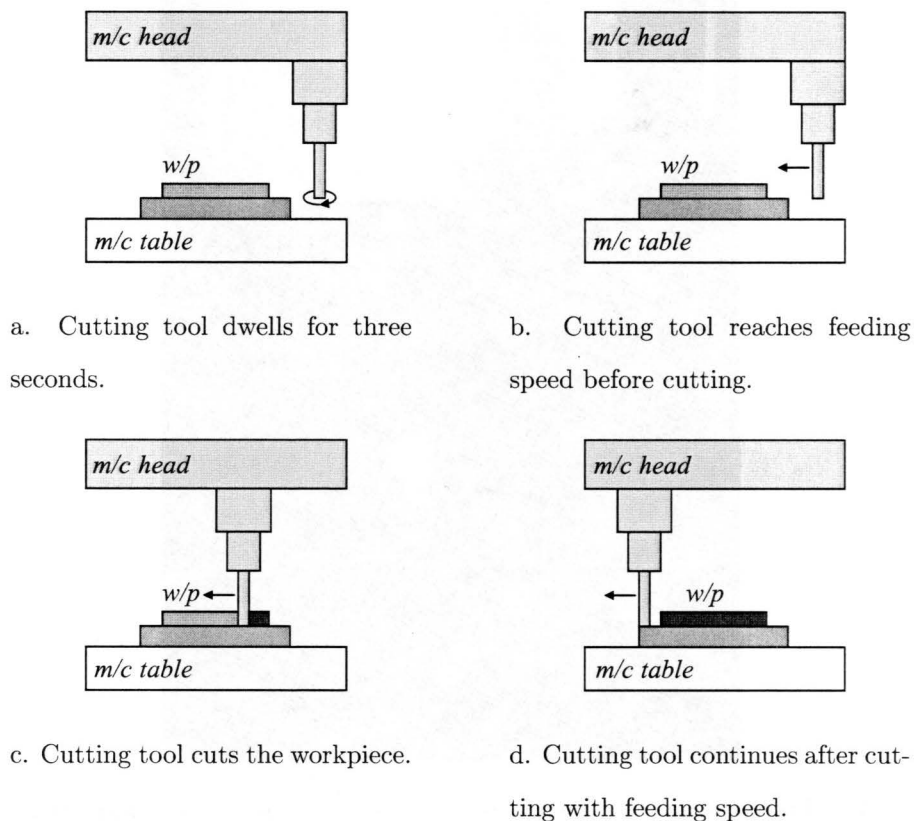
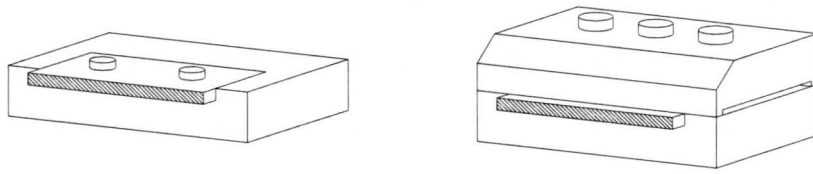


Figure 6.1 – Summary of description of cutting test.



a. Initial design.

b. Modified design.

Figure 6.2 – Fixture design.

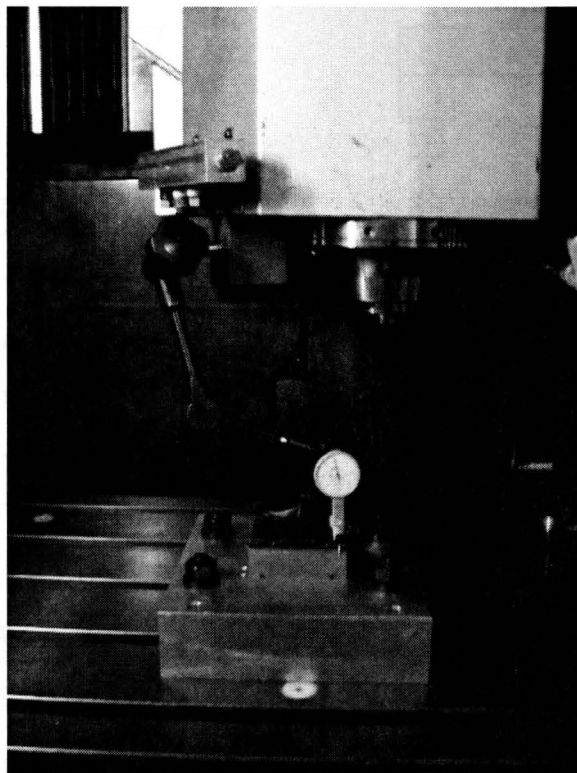


Figure 6.3 – Dynamometer alignment to the machine tool's axis using a dial gauge.

Data acquisition considerations

To avoid aliasing it was important to select an appropriate sampling rate. A detailed calculations of the sampling frequency can be found in Appendix D of [54].

A gain amplifier (power supply, Figure 6.4) was used to magnify the output from the accelerometers. The gain factor was chosen so that that average value was mid range for the data acquisition (DAQ) card but did not saturate it or provide values that were too small so as to be lost in background noise. The data acquisition instrumentation is comprised of the accelerometers, a dynamometer, a gain amplifier, and a DAQ card installed in a PC. The data acquisition system was turned on for approximately an hour before conducting the experiments to ensure that the instruments had reached steady state.

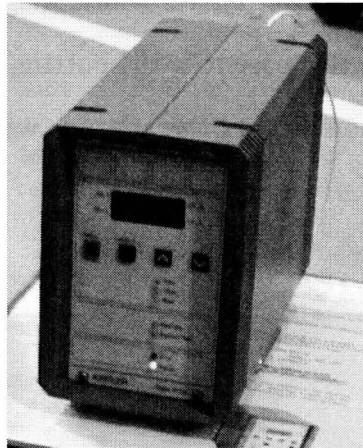


Figure 6.4 – Power supply used to amplify the accelerometer’s signal.

6.3.2 Impact hammer test considerations

Cutting tool

The hammer test was conducted on the cutting tool in two directions X and Y to obtain their FRFs. For the impact test of the cutting tool a miniature accelerometer (KISTLER type 8778A500) was used, illustrated in Figure 6.5¹. The accelerometer was mounted on the tool as shown in Figure 6.6 by means of a glue gun as it forms the best and cheapest means of fixation [67]. The impact hammer (KISTLER type 9726A5000) was used to strike a special aluminum adapter also fixed by a glue gun on the tool on the opposite side of the accelerometer. The special adapter was necessary to withstand the hammer blow and to transfer it to the tool/spindle structure while at the same time not chipping and/or damaging the tip of the cutting tool. Also, its material was deliberately chosen to be aluminum to ensure light weight and reasonable strength to withstand the impact. A common practice to ensure accuracy of the obtained FRF is to choose an accelerometer which weighs no more than one tenth of the structure being tested; in this case it is the cutting tool. It should be noted that the cutting tool, the accelerometer and the adapter weigh ~ 18.2 gm , ~ 0.4 gm and ~ 0.8 gm respectively.

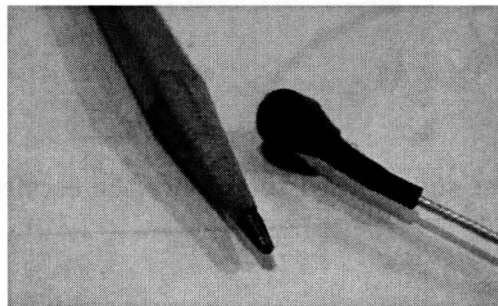


Figure 6.5 – Miniature accelerometer.

¹Courtesy of KISTLER Corp. <http://www.kistler.com>

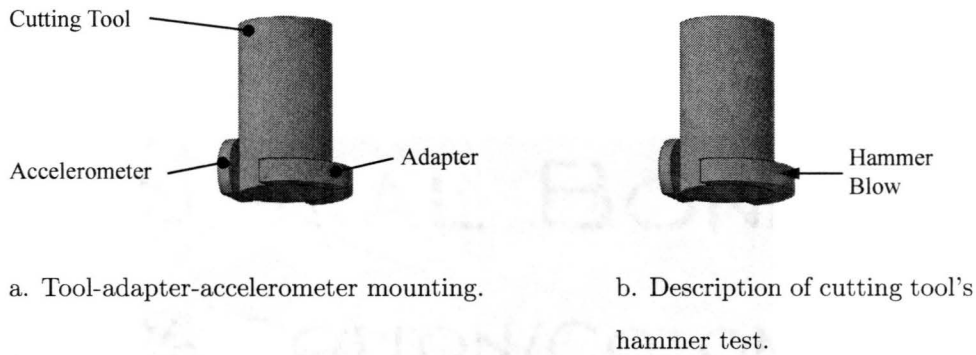
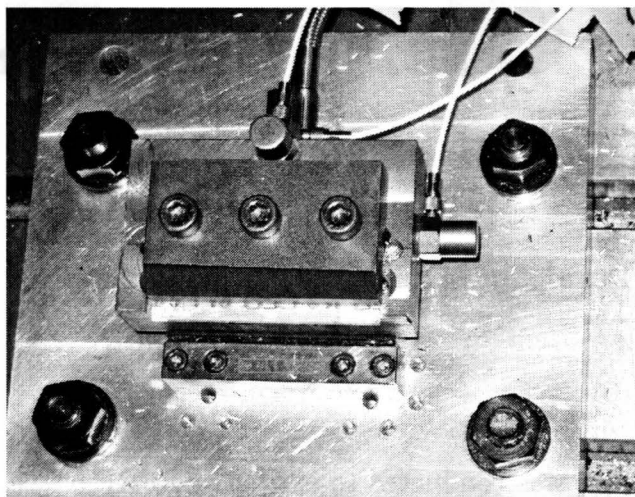


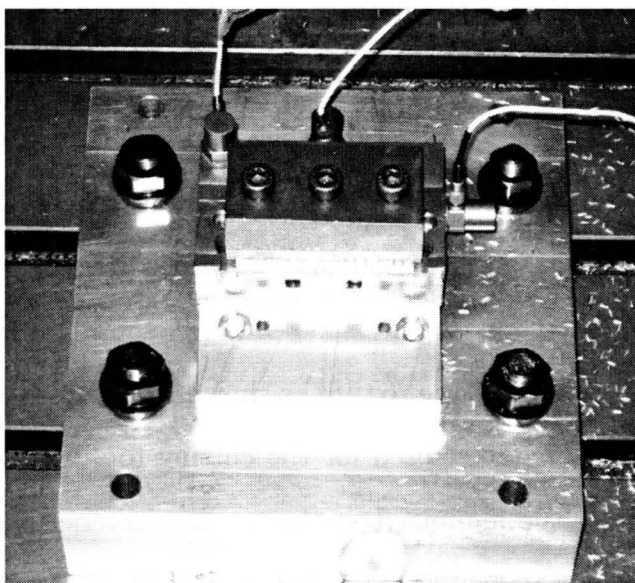
Figure 6.6 – Description of miniature accelerometer mounting and usage.

Fixture

A hammer impact test was conducted to extract the FRF of the fixture. Two setups existed for the fixture; one having the fixture setup directly on top of the dynamometer and the other one having the fixture setup directly on the large block fixed on the table of the machine tool (without the dynamometer). The details of those two setups will be explained later in Section 6.4.1. The hammer test was conducted on the fixture, for both setups, in three directions X , Y , and Z using three generic accelerometers (KISTLER type 8702B50) one for each direction. The accelerometers were placed, for both setups, in the same place as shown in Figure 6.7. The accelerometers were mounted on the fixture as shown in Figure 6.8 by means of a glue gun. The same impact hammer used for the cutting tool was used in this hammer test. After conducting the hammer test the accelerometers mounted on the fixture were used for measuring its acceleration during the cutting test. The accelerometer to fixture weight ratio was $\sim 0.6\%$.



a. Fixture setup # 1, with a dynamometer.



b. Fixture setup # 2, without a dynamometer.

Figure 6.7 – Accelerometers used in the hammer test.

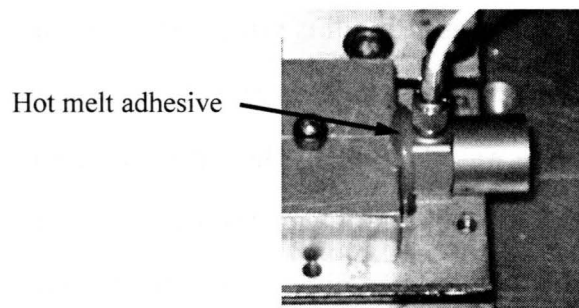


Figure 6.8 – Usage of hot melt adhesive to fix the accelerometer to the fixture.

6.3.3 General considerations

During each cutting test the signals were checked to ensure that no overload had occurred, as recommended by the FFT analyzer's manufacturer. All hammer tests were conducted while making sure that the setup of the impact hammer as well as the FFT analyzer was in accordance with the manufacturer's instructions. For each direction, the hammer test was repeated for at least 5 times (and 8 in most of the cases) and averaged as outlined by the hammer manufacturer [92] to reduce the probability of errors and the noise in the data. The coherence between the input and the output was checked as a sign of correlation. In all tests the coherence of the data used was not less than 85%.

6.4 Experimental Setup

6.4.1 Cutting test setup

Several cutting tests were initially used to establish the operating parameters both with and without the dynamometer. For all cutting tests the experimental setup was

the same except for the presence of the dynamometer; this is illustrated in Figure 6.7. The workpiece material used in all cutting test experiments is Aluminum 6061-T6 conforming with ASTM B221 standards and of dimensions 3.175 mm \times 24.50 mm \times 70 mm. The workpiece was clamped in the fixture by means of an upper jaw that was tightened to the fixture by screws. For the case of the first setup, illustrated in Figure 6.9, the fixture base was fixed on a piezo type dynamometer (KISTLER type 9256B1) capable of measuring the three orthogonal components of force along the three axes X , Y , and Z . The dynamometer and the fixture were both placed on top of an intermediate block that was fixed in turn on the table of the machine. For the second setup, illustrated in Figure 6.10, the base of the fixture was fixed directly on a small block that was fixed on the intermediate block when the dynamometer was removed. All cutting tests were conducted on the Matsuura LX-1 machining center, see Figure 6.11.

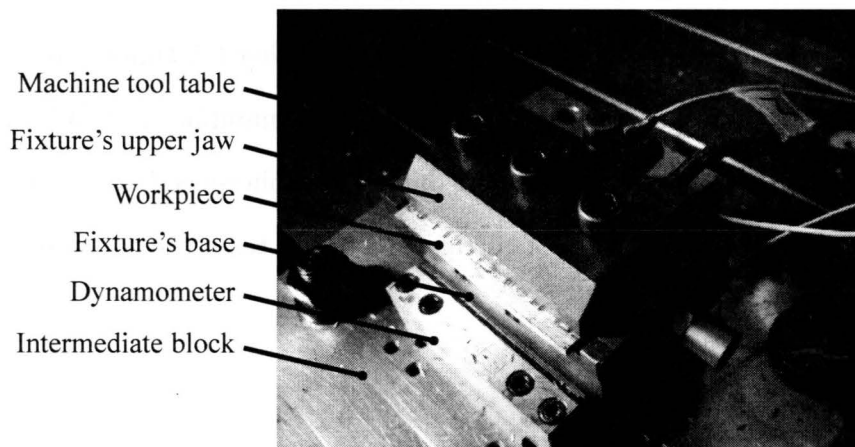


Figure 6.9 – Details of fixture setup # 1.

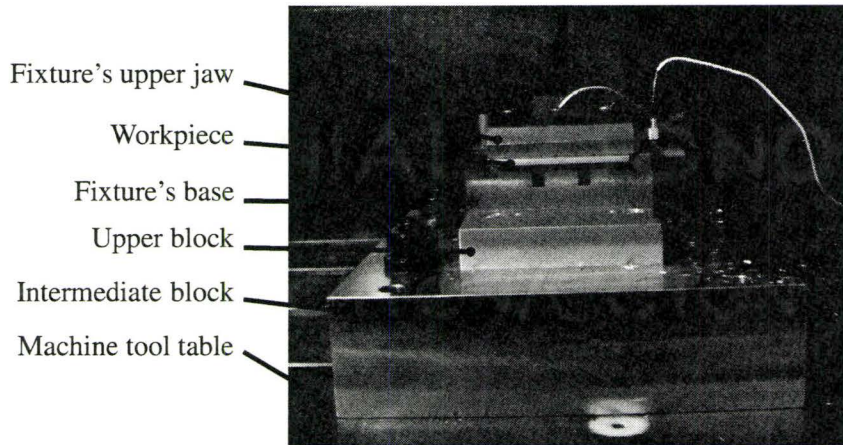


Figure 6.10 – Details of fixture setup # 2.



Figure 6.11 – Machine tool used in conducting the experiments.

In both setups three accelerometers (KISTLER type 8702B50) were fixed to the fixture by means of a hot melt adhesive as shown in Figure 6.7 one in each cutting direction. Afterwards, the dynamometer was connected to a charge amplifier (KISTLER type 5814A10) by means of a 3-conductor connecting cable with armoring (KISTLER type 1693A). A remote control box (KISTLER type 5663) was attached to the charge amplifier using a 6-conductor cable (KISTLER type 1595), which was

used to reset the charge amplifier each time a new test was conducted or when an overload occurred. After the sensitivity of each channel was set, the output of the amplifier was sent to a data acquisition card (National Instruments type PCI-6023E), through a connector block (NI BNC-2110), and captured by the Labview software package. The accelerometers, attached to the fixture, were connected to a gain amplifier (KISTLER type 5134A) using coaxial cables. The amplified signal was then sent to the data acquisition card, through the connector block, and captured. The dynamometer and the accelerometer signals were all captured simultaneously. Captured data was saved in a *.txt format then analyzed using Matlab™. The general experimental setup for all cutting test is illustrated in Figure 6.12. The cutting test descriptions are summarized in Section 6.3.1.

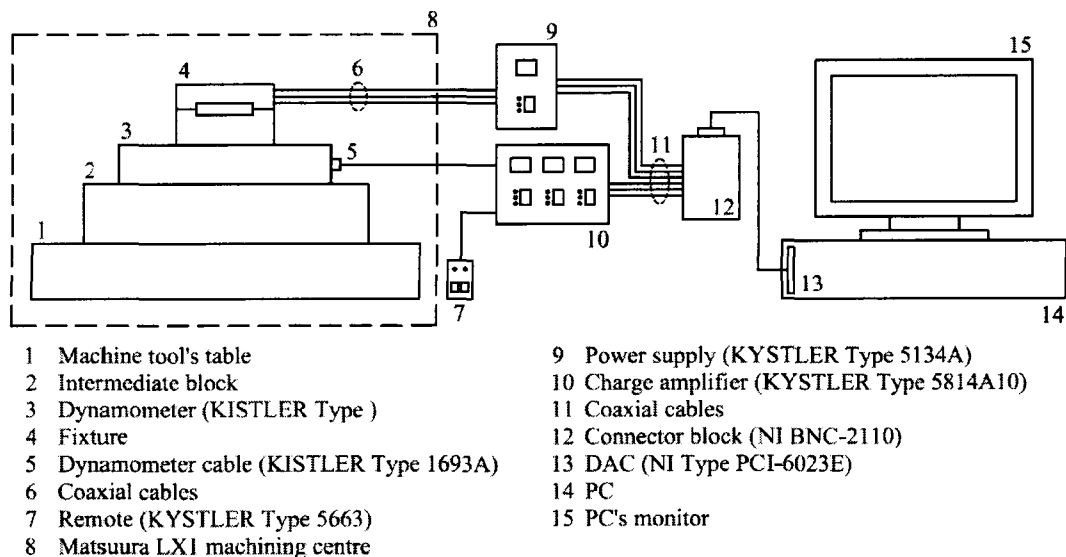


Figure 6.12 – Schematic for the experimental setup.

6.4.2 Cutting test matrix

A set of cutting test conditions was used when conducting the experiments. The same set was used with fixture setup # 1 and fixture setup # 2. Tables 6.3 and 6.4 summarizes the cutting conditions used for the calibration and verification of the SCF respectively.

Table 6.3 – Test matrix used for the calibration of the SCF

Test #	RPM (krev/min)	f_t (mm)	d_r (mm)
1	30	0.030	0.40
2	30	0.080	0.40
3	30	0.030	0.90
4	30	0.080	0.90
5	58	0.030	0.40
6	58	0.080	0.40
7	58	0.030	0.90
8	58	0.080	0.90
9	44	0.055	0.65

Table 6.4 – Test matrix used for the verification of the calibrated SCF

Test #	RPM (krev/min)	f_t (mm)	d_r (mm)
1	37	0.043	0.53
2	51	0.068	0.78
3	30	0.040	0.60
4	40	0.040	0.60
5	35	0.035	0.65
6	32	0.035	0.50
7	18	0.050	0.50
8	58	0.030	0.40
9	50	0.050	0.60
10	19	0.100	0.80
11	55	0.050	0.80
12	55	0.080	1.20
13	55	0.100	0.80

The SCF was estimated for each cutting test condition. Once all of them were obtained they are fitted to a non-linear equation. The equation for each SCF; K_t , K_r , and K_a , was of the following form respectively.

$$K_t = A_1 \times V^{a_1} \times f_t^{b_1} \times d_r^{c_1} \quad (6.1)$$

$$K_r = A_2 \times V^{a_2} \times f_t^{b_2} \times d_r^{c_2} \quad (6.2)$$

$$K_a = A_3 \times V^{a_3} \times f_t^{b_3} \times d_r^{c_3} \quad (6.3)$$

Constants A_i , a_i , b_i and c_i are obtained by linearizing Equations 6.1 - 6.3 and applying a least square fitting technique.

6.4.3 Dynamic test setup

The dynamic test was comprised of two sub-tests: (1) a dynamic test for the cutting tool, and (2) a dynamic test for the fixture. Both tests were intended for the same purpose which was to obtain the FRF of the structure being tested.

Cutting tool dynamic test

A miniature accelerometer (KISTLER type 8778A500) was fixed to the tip of the tool by means of a miniature adapter illustrated in Figure 6.6a. The accelerometer and the hammer (KISTLER type 9726A5000) are both connected to an FFT analyzer (HP analyzer type 35670A) using a coaxial cable. A hammer blow was given to the system at the tip of the tool as shown in Figure 6.6b. Captured data was converted instantaneously in the FFT analyzer to the frequency domain, saved in **.txt* format and then reloaded using the MatlabTM program for further analysis. The experimental setup for the dynamic test is illustrated in Figure 6.13.

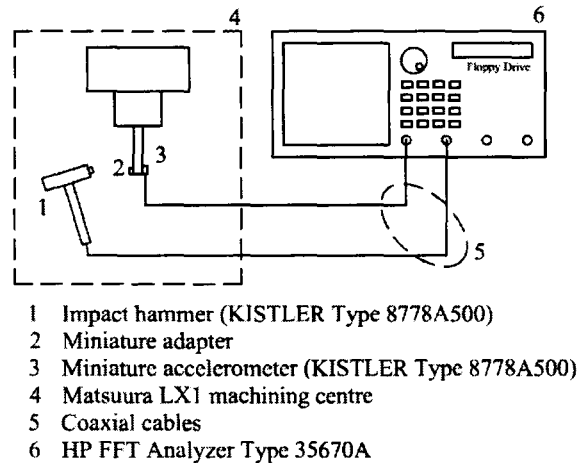


Figure 6.13 – Schematic for the cutting tool's dynamic test setup.

Fixture dynamic test

The fixture dynamic test setup was the same for the existing two fixture setups; with/without a dynamometer. As mentioned in Section 6.3.2, three accelerometers (KISTLER type 8702B50) were fixed onto the upper jaw of the fixture in the three component directions; X , Y , and Z as illustrated in Figure 6.7. A similar dynamic test setup was carried out for each direction. For each direction the accelerometer and the hammer (KISTLER type 9726A5000) were both connected to the FFT analyzer (HP analyzer type 35670A) using a coaxial cable. A hammer blow was given to the system at the side for which the FRF was being extracted. The captured data was converted in real time in the FFT analyzer into the frequency domain, saved in **.txt* format and then reloaded using the MatlabTM program for further analysis. The experimental setup for the dynamic test is illustrated in Figure 6.14.

6.4.4 Tool run-out and unbalance mass estimation

Tool run-out

To include the run-out effect of the cutting tool, the value of the run-out distance

needed to be determined. Based on the assumptions laid out in Section 5.3.4 the run-out was measured using a dial gauge indicator as the one shown in Figure 6.15.

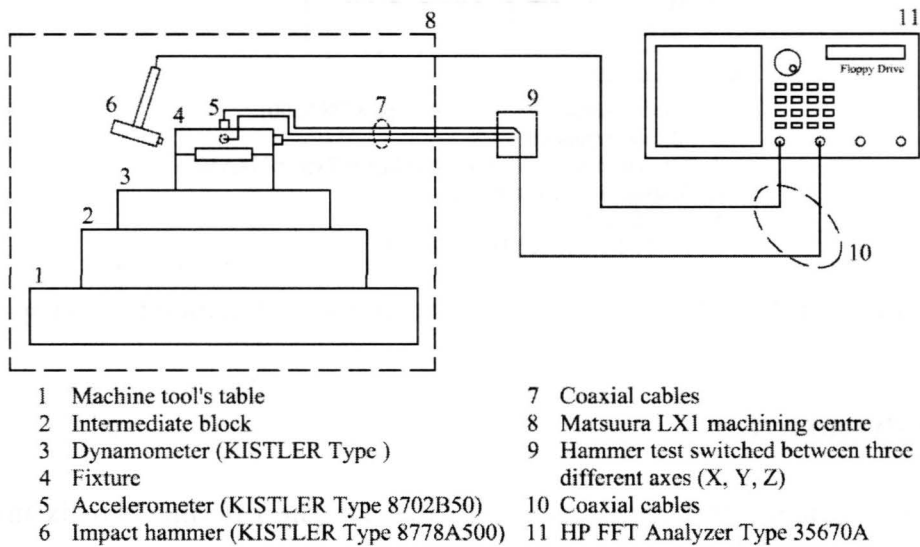


Figure 6.14 – Schematic for the fixture dynamic test setup.

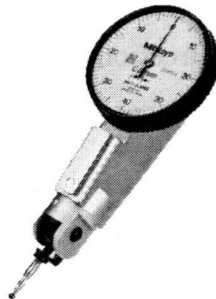


Figure 6.15 – Dial gauge indicator used to measure the tool/tool holder's run-out. Curtesy [<http://www.mitutoyo.com>].

The dial gauge tip was positioned inline with the radius of the tool holder and then the tool holder was rotated manually for several complete rotations. The variation in the radius of the tool holder was then recorded. A typical value for run-out was found to be ~ 0.004 mm.

Unbalance mass

The measured run-out distance ~ 0.004 mm would also lead to an unbalanced mass in the tool/tool holder system. The unbalance mass m_e and its center of gravity radius r_e were both estimated using the technique described in Appendix B and were found to be 0.036 gm and 4.93 mm respectively.

6.4.5 Cutting test material's properties

The material used in this study was Aluminum 6061-T6. Equations 5.29, 5.30 and 5.35 have some constants that are material dependent. Generally speaking all those constants have to be determined experimentally unless they are generic enough to be taken from the literature.

- **Constant of Equations 5.29 5.30** Looking into the literature [93–95] it was found that the variation in the values of C , m , T_{mt} and $\dot{\gamma}_o$ was small and hence it was taken directly from the literature. On the other hand, A , B and n varied substantially from one sources to the other and hence a tensile test was conducted and the constants were evaluated from that test. The tensile test results are summarized in Appendix C. Table 6.5 summarizes the values for the constants A , B , C , n and m .

Table 6.5 – Constants used in Equations 5.29 and 5.30 (Johnson-Cook material model) for Aluminum 6061-T6 used in this study

Constant	Value	Source
A (MPa)	276.376	Tensile test
B (MPa)	122.928	Tensile test
C	0.002	[94]
n	0.3336	Tensile test
m	1.34	[94]
T_{mt} ($^{\circ}\text{C}$)	582	[94]
$\dot{\gamma}_o$ (s^{-1})	0.01	[95]

• **Variables of of Equation 5.35** Variables ρ , C_p , and K in Equation 5.35 are affected by the temperature [90]. So during the simulation those constants were evaluated every time the temperature was evaluated. To reflect their temperature dependence a temperature dependent formula was fitted to the material properties found in the open literature [90] for C_p , and K . The formulas used are given by Equations 6.4 and 6.5 for C_p and K respectively. The data collected from the literature can be found in Appendix C.

$$C_p(T) = 215.01 \ln(T) - 336.11 \quad (6.4)$$

$$K(T) = 3 \times 10^{-8}T^4 - 4 \times 10^{-5}T^3 + 0.0224T^2 - 4.73T + 591.9 \quad (6.5)$$

For ρ , a temperature dependent equation, Equation 6.6, was derived which related the volumetric change due to the temperature to the density of the material. The derivation of Equation 6.6 can be found in Appendix A.

$$\rho(T) = \frac{\rho_o}{1 + \beta(T - T_r)} \quad (6.6)$$

The following should be noted:

- Temperature in Equations 6.4, 6.5 and 6.6 are in Kelvin (K).
- β (coefficient of volumetric thermal expansion) is $70 \times 10^{-6} \text{ (m}^{-1} \text{ }^\circ\text{C}^{-1}\text{)}$.
- T_r (reference room temperature) is 22 ($^\circ\text{C}$).
- ρ_o used is 2700 (kg/m^3).

6.5 Summary

This chapter presented the methodology followed to conduct the experimental work. It also presented the experimental design considerations used to conduct the cutting test experiments as well as the impact hammer dynamic test. This included special considerations for the selection of the cutting conditions, fixture design and mounting, impact hammer used in the dynamic test, and data acquisition system. In addition, it discussed the experimental setup for both the cutting test and the dynamic test. The technique for measuring the run-out of the tool holder was included and the material properties used in the analytical model were also presented.

CHAPTER 7

RESULTS & DISCUSSION

7.1 Introduction

In this chapter the results of the suggested simulation model will be compared to the experimental data collected. The comparison reveals that the performance of the model is acceptable and that it fulfills the main objectives of this dissertation.

7.2 Re-building of Tlusty's Model

Figure 7.1 illustrates a comparison of the cutting force estimation generated by Tlusty and published in [74] and that generated by the author using the re-developed model for the three different cutting conditions (1 - 3). Figure 7.1b clearly shows that the re-developed model is able to generate the same force levels estimated by Tlusty's

model when using the same cutting conditions for all three cases. The cutting conditions for the three cases are constant ($r = 15$ mm, $\beta = 30^\circ$, $d_r = 15$ mm, $f_t = 0.1$ mm, number of teeth = 4, $K_t = 2 \times 10^9$ N/m², $K_r = 0.3 \times K_t$, RPM = 1000 rev./min) except for the radial depth of cut that is variable ($r_{dc} = 10$ mm, 25 mm, and 50 mm for cases 1, 2, and 3 respectively).

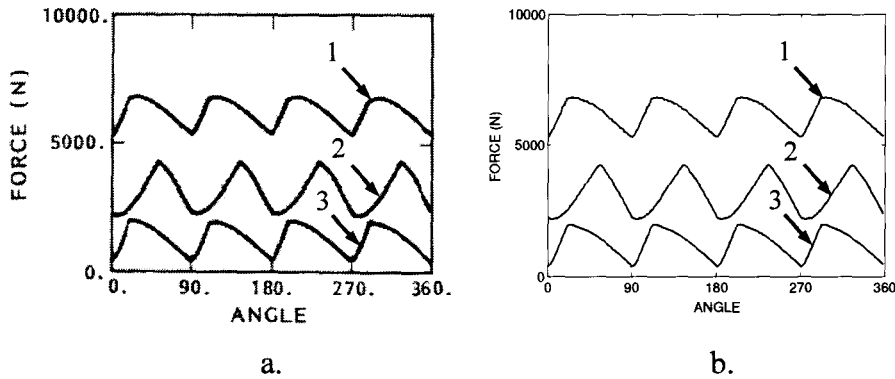


Figure 7.1 – Comparison of Tlustý’s model as published in [74] (a) and the re-built model (b).

It should be noted that Tlustý’s model was originally developed to estimate the cutting forces in only two directions (X and Y) as compared to the model outlined earlier that was developed to estimate the cutting forces for three directions X , Y , and Z . In those runs, the force in the third direction (Z) was purposely ignored and set to zero for the purpose of making the comparison. It should also be noted that the estimated cutting forces are the resultant force (F_R) evaluated by Equation 7.1. Figure 7.1 shows that there is excellent agreement between the original model and the one that was re-developed for the purpose of this study.

$$F_R = \sqrt{F_x^2 + F_y^2} \quad (7.1)$$

7.3 Obtaining the SCF from the Force Signal

Figures 7.2 and 7.3 compare the simulated cutting forces versus the experimental ones using the cutting conditions for test # 2 and # 7 (see Table 6.3) in the X , Y , and Z direction. The analytical model used: (1) $K_t = 1.85 \times 10^9$ N/m², $K_r = 2.10 \times 10^9$ N/m², $K_a = 2.10 \times 10^9$ N/m², (2) $K_t = 1.00 \times 10^9$ N/m², $K_r = 0.80 \times 10^9$ N/m², $K_a = 1.20 \times 10^9$ N/m² for simulating test # 2 and # 7 respectively.

Notes A - D in Figures 7.2 and 7.3 point to key issues in the simulation as well as in the collected experimental data that helped understanding the nature of the system dynamics and hence aided in finding a solution for it.

Note A:

From the coordinate system convention used in this study and the fixture/dynamometer setup as well as the cutting conditions used in test # 2 and # 7 it is not expected that any signal will be recorded during the time at which there is no tool contact with the workpiece. This is illustrated by the dotted circle in Figures 7.2 and 7.3. The only output present in the reported force data is due to the dynamic response of the dynamometer to the cutting force spike. In this case the response of the dynamometer does not have enough time to settle down before the next tooth starts cutting and hence the part encircled by the dotted line appears in the recorded cutting force signal.

Note B & C:

From the given cutting conditions of test # 2 and # 7 the time during which the cutting tool is in cut can be calculated by hand and then compared to B (experimental) and C (simulated). Those times are summarized in Table 7.1.

From Table 7.1 it can be clearly seen that time C extracted from the simulation highly agrees with hand calculations and in the same time there is a big difference

between them and those measured. This makes the process of analyzing the cutting force signal even harder because it is not clear when the cut starts and when it ends.

Table 7.1 – Summary of in-cut time for different cutting tests

Test #	Time B (sec.)	Time C sim. (sec.)	Time C hand calc. (sec.)
2	5.97×10^{-4}	3.66×10^{-4}	3.61×10^{-4}
7	4.79×10^{-4}	2.36×10^{-4}	2.31×10^{-4}

Note D:

The dotted circle in Figure 7.3 points at a problem that exists in the force signal but is only present at ultra high speed (58k rev./min) tests. It was not found in lower speeds (review Figure 7.2) as will be shown later. This happened despite the fact that both experiments were carried out using the same cutting tool and the same setup. Further investigation has attributed this problem to be mainly due to the presence of run-out in the cutting tool. While the run-out is always there its effect becomes magnified at very high speeds.

Clearly from Figures 7.2 and 7.3 the specific cutting forces cannot be estimated using these measured cutting forces as there are many other factors in the signals.

7.4 Obtaining the SCF from the Acceleration Signal

From the discussion in the previous section it becomes necessary to find an alternative mean to estimate the specific cutting forces. In this study making use of the structure acceleration helps estimating the specific cutting forces in an easy and reliable way. Details of this new technique are explained in Chapter 5, Section 5.3.3. Figures 7.4 and 7.5 illustrate a comparison between the experimental and simulated acceleration

of the fixture, that holds the workpiece, in the X , Y , and Z directions for cutting test # 2 and # 7 respectively. The specific cutting forces estimated using the acceleration for test # 2 and # 7 are summarized in Table ??.

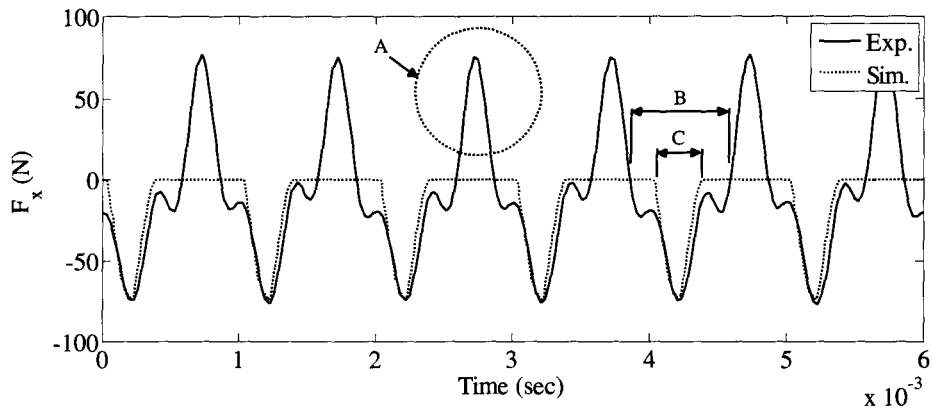
Table 7.2 – SCF estimated using the acceleration

Test #	K_t (N/m ²)	K_r (N/m ²)	K_a (N/m ²)
2	1.76×10^9	1.20×10^9	1.20×10^9
7	1.56×10^9	0.80×10^9	0.95×10^9

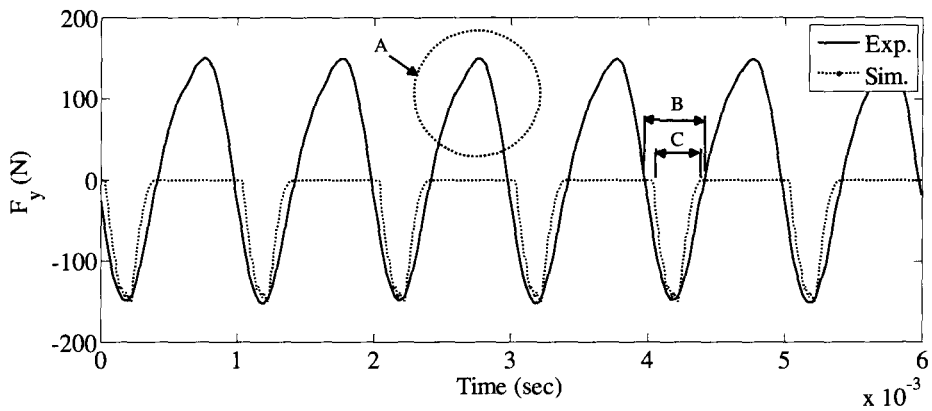
For each test case, the values of the specific cutting forces, summarized in Table 7.2, were obtained by simulating the acceleration and comparing it to the experimental one using a starting value of each of the SCFs. Afterwards K_t , K_r , and K_a were each varied gradually until the simulated acceleration matched the experimental one. Test # 2 was used to illustrate this process. The SCF values for each step taken until reaching the optimum value are summarized in Table 7.3. Figure 7.6 illustrates a comparison of the simulated acceleration as compared to the experimental one for each step until reaching the optimum value. It should be noted that the estimated K_t and K_r are correlated as given by Equations 5.8 and 5.9. On the other hand, K_a is not directly affected by the variation of K_t nor K_r because it is being assessed independently as defined by Equation 5.14. The SCF for test # 7 in Table 7.2 are obtained likewise.

Table 7.3 – Demonstration of how to estimate the SCF using the acceleration

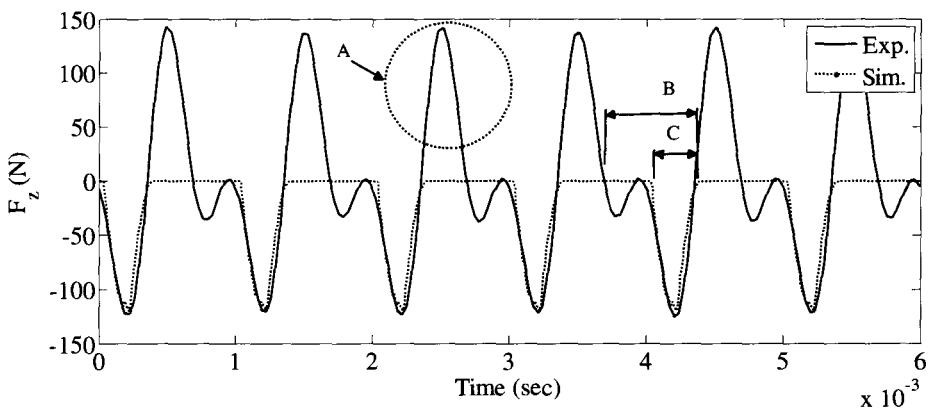
Step #	K_t (N/m ²)	K_r (N/m ²)	K_a (N/m ²)
1	1.30×10^9	1.00×10^9	1.00×10^9
2	1.60×10^9	1.15×10^9	1.15×10^9
3	1.76×10^9	1.20×10^9	1.20×10^9



a. X-direction.

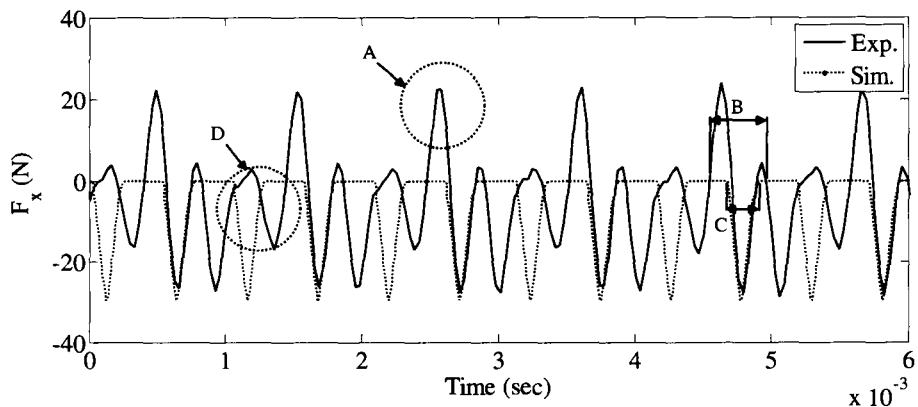


b. Y-direction.

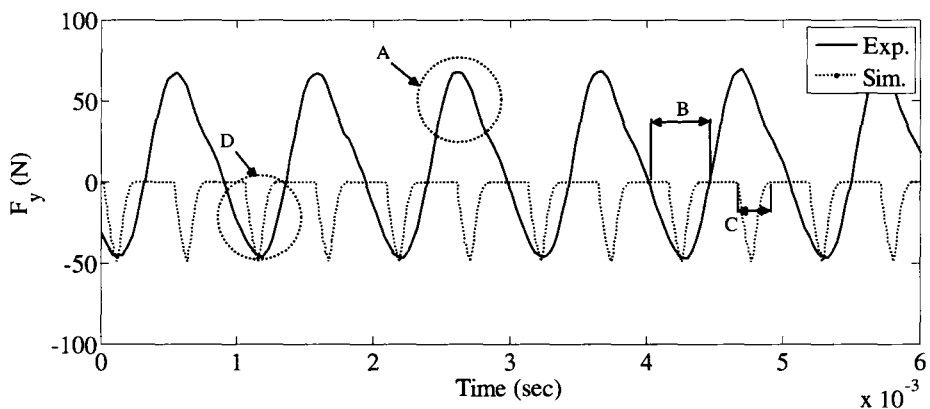


c. Z-direction.

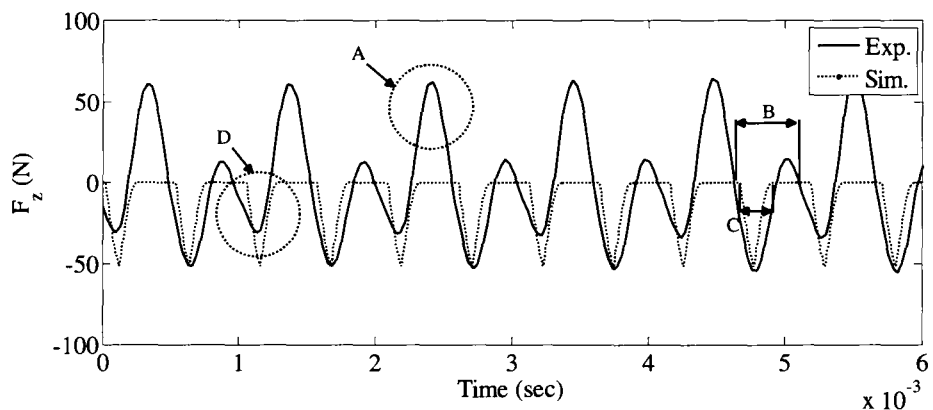
Figure 7.2 – Cutting forces for cutting test # 2, 30k rev./min, see notes page 133.



a. X-direction.

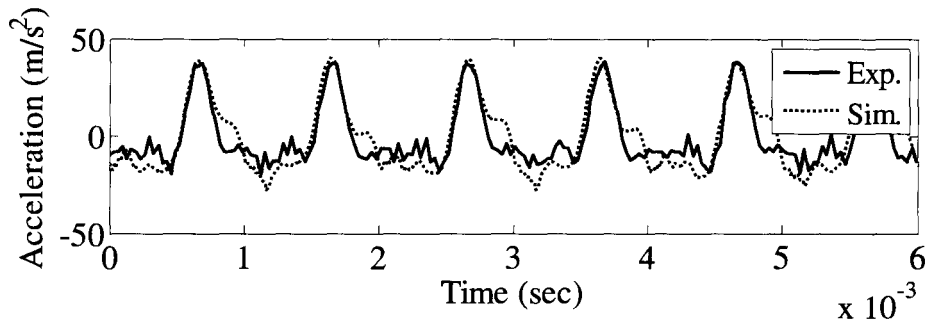


b. Y-direction.

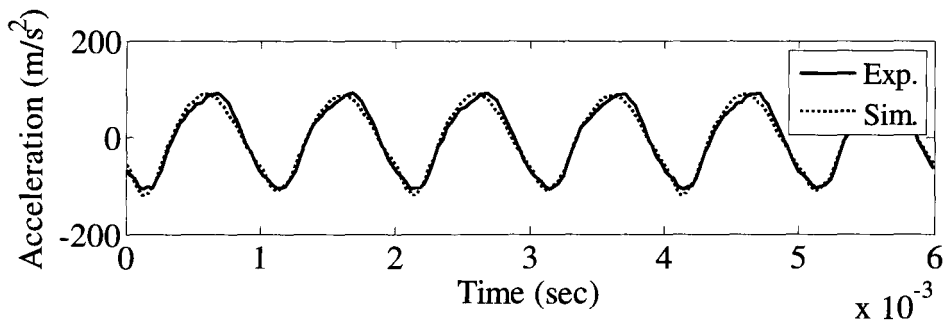


c. Z-direction.

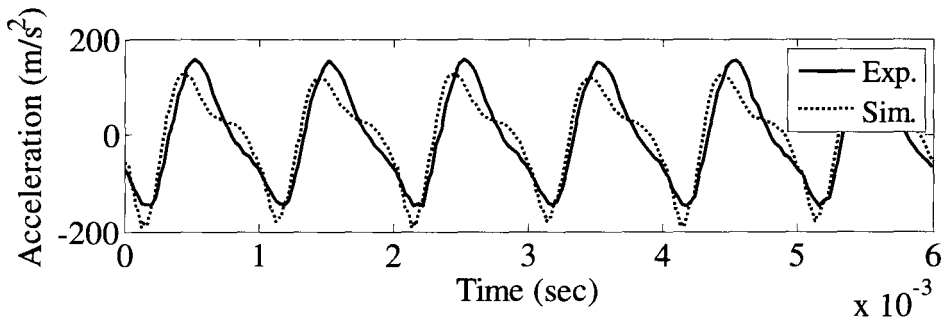
Figure 7.3 – Cutting forces for cutting test # 7, 58k rev./min, see notes page 133.



a. X-direction.

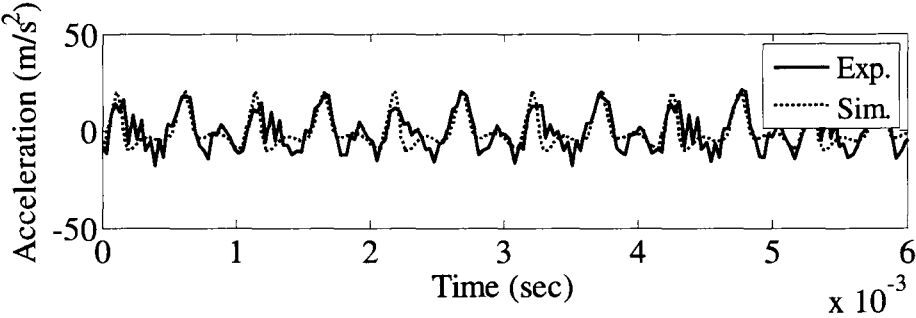


b. Y-direction.

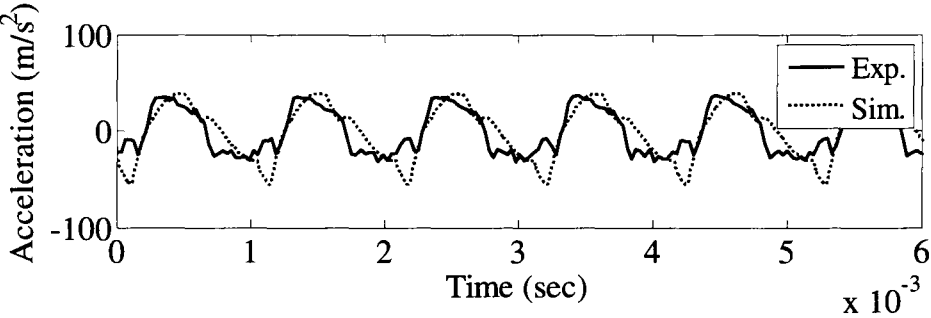


c. Z-direction.

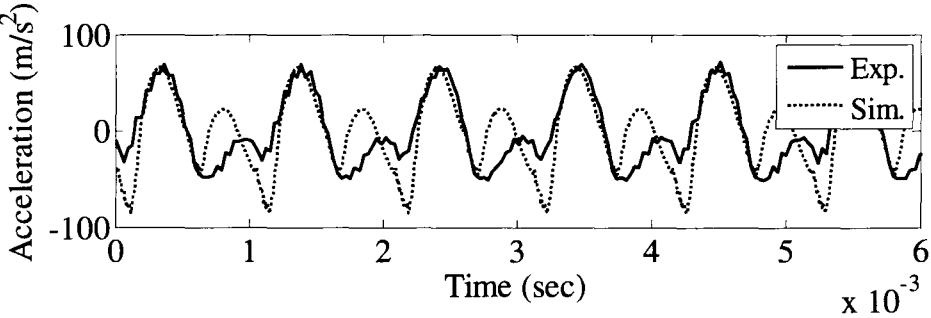
Figure 7.4 – Estimation of the SCF using the fixture's acceleration for cutting test # 2, 30k rev./min.



a. X-direction.

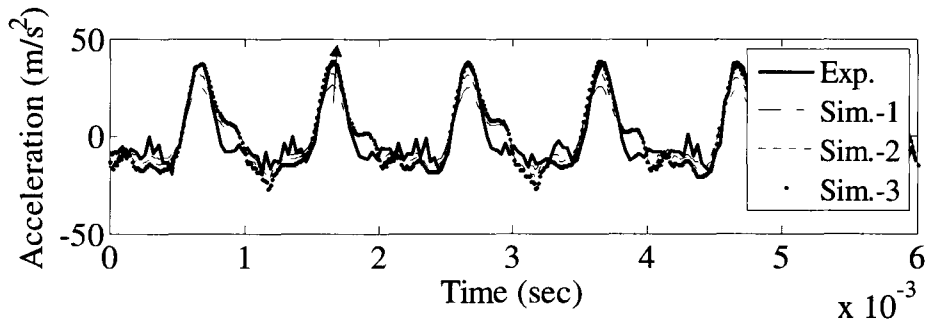


b. Y-direction.

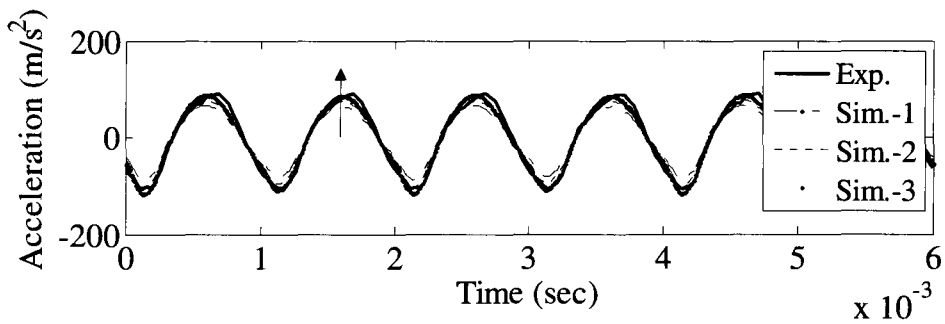


c. Z-direction.

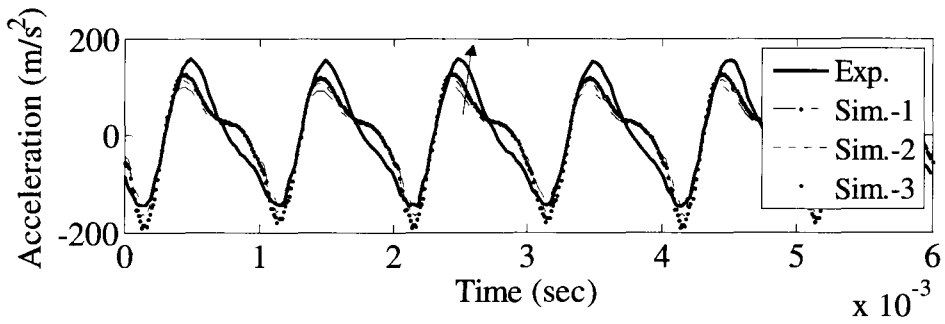
Figure 7.5 – Estimation of the SCF using the fixture’s acceleration for cutting test # 7, 58k rev./min.



a. X-direction.



b. Y-direction.



c. Z-direction.

Figure 7.6 – Explanation of the suggested estimation method of the SCF using the fixture’s acceleration for cutting test # 2, 30k rev./min.

7.5 Analysis of the Suggested Dynamic Model

Before verifying the suggested dynamic model and using it further in this research it needed to go through a series of investigations to understand its behavior. The suggested dynamic model was investigated for the following:

- Selection of the number of modes during modal parameter extraction.
- Filtration of the simulated acceleration.
- Effect of the run-out on the SCF estimation.

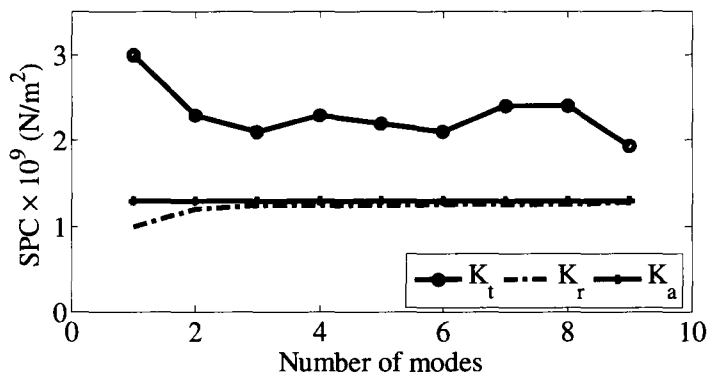
7.5.1 Selection of the number of modes

The estimation of the specific cutting forces was affected by the process dynamics namely the selection of the number of modes that will be used in generating the analytical FRF of the workpiece/fixture setup so that it can be used later in the proposed dynamic model. For a given workpiece/fixture setup the following analysis steps were applied to the system FRF:

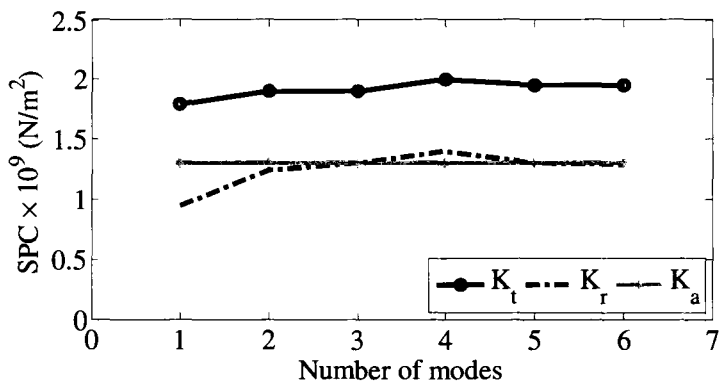
1. The analytical FRF of the system was generated using a relatively large number of modes (6 - 12 modes depending on the FRF shape) and the corresponding modal parameters were extracted for each cutting direction X , Y , and Z . The optimum number of modes selected was derived through an iterative process as described hereafter.
2. To obtain the optimum number of modes in one direction, for example X , the analytical FRF was generated using a specific number of modes based on the method outlined earlier in Chapter 4 and the corresponding modal parameters is then estimated. The modal parameters for the other two directions (for this case Y , and Z) are kept unchanged.

3. The modal parameters obtained using this procedure for the three directions were then used in the dynamic model to predict the analytical acceleration and hence estimate the SCF for a certain cutting condition using the approach explained earlier in Section 7.4.
4. While maintaining the modal parameters of the other two directions (in this case Y and Z) the number of modes in the X direction will be gradually increased and the corresponding SCF will be estimated each time.
5. The variation of the estimated SCF (K_t , K_r , and K_a) will then be plotted versus the variation of the number of modes used in extracting the modal parameters of the system (X in this case).
6. Steps 2-5 are repeated for the Y and Z directions while keeping the number of modes unchanged in the remaining two directions X and Z , and X and Y respectively.
7. For each direction, the investigation of the variation of the SCF with the number of modes leads to the optimum number of modes.

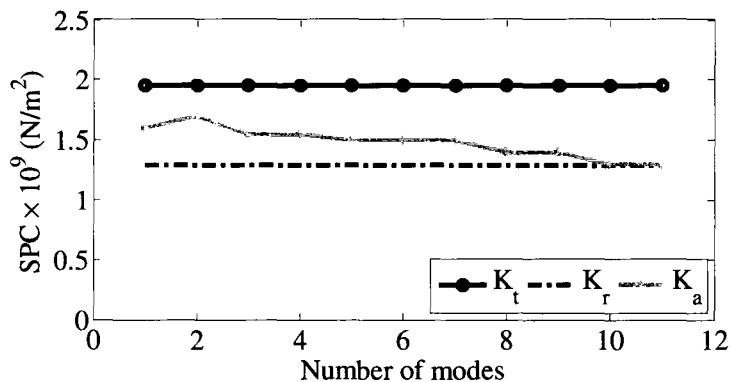
Two test cases were investigated; test # 2 and # 7 and are illustrated in Figures 7.7 and 7.8 respectively. Both figures illustrate the variation of the SCF with the number of modes for the three cutting directions X , Y , and Z . It can be noticed that for a small number of modes the calibrated SCF was relatively high then it started decreasing rapidly as the number of modes increased until it reached a plateau. This can be seen in Figures 7.7 and 7.8. It was also noticed that during the variation of the number of modes in the X -direction (or Y) K_r varied with K_t . This was because K_t and K_r are tied together by Equations 5.8 and 5.9 while K_a was not affected because it is independent, see Equation 5.14. On the other hand when varying the number of modes in the Z -direction only K_a was affected (same reason mentioned above).



a. X-direction.

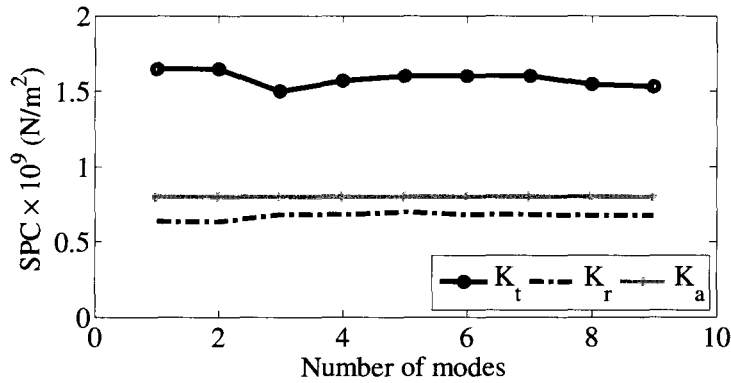


b. Y-direction.

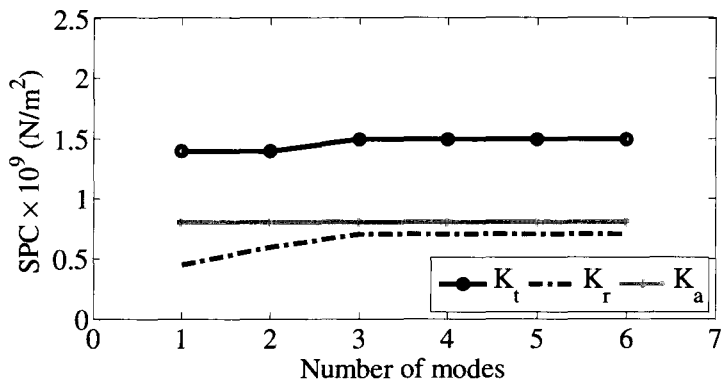


c. Z-direction.

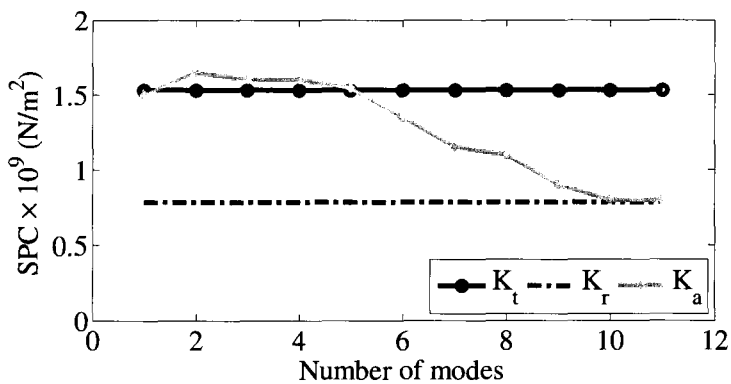
Figure 7.7 – Investigation of the effect of choosing the number of modes on the estimation of the SCF using the fixture’s acceleration for cutting test # 2, 30k rev./min.



a. X-direction.



b. Y-direction.



c. Z-direction.

Figure 7.8 – Investigation of the effect of choosing the number of modes on the estimation of the SCF using the fixture’s acceleration for cutting test # 7, 58k rev./min.

The analysis presented earlier generates an optimum number of modes to be used in extracting the modal parameters for each cutting direction X , Y , and Z . The modal parameters are summarized in Table 7.4.

Table 7.4 – Optimum number of modes and their corresponding modal parameters

Mode #	Natural frequency (Hz)			Damping ratio (%)		
	X-dir.	Y-dir.	Z-dir.	X-dir.	Y-dir.	Z-dir.
1	1100	625	691	1.53	9.00	9.00
2	1165	757	787	1.15	2.06	3.87
3	1257	893	917	1.41	2.15	6.05
4	1332	945	953	2.84	2.31	1.90
5	1705	1054	1137	8.82	4.33	2.88
6	2097	1320	1380	6.07	0.67	1.25
7	2638	-	1642	2.61	-	5.07
8	2660	-	1685	2.99	-	0.90
9	3110	-	1749	0.01	-	5.75
10	-	-	1885	-	-	8.95

7.5.2 Filtration of the simulated acceleration

The dynamic model outputs the displacement of the fixture which can then be transformed into acceleration by means of differentiation as described by the following formulas.

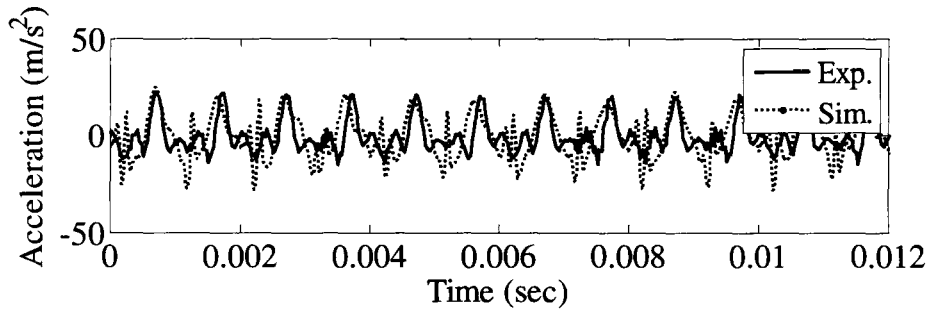
$$\dot{x} = \frac{\Delta x}{\Delta t} \quad (7.2)$$

$$\ddot{x} = \frac{\Delta \dot{x}}{\Delta t} \quad (7.3)$$

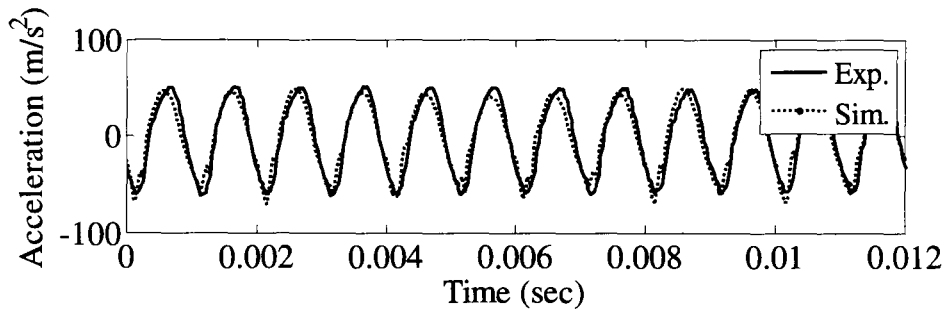
The problem of using such a technique was that at some instances the differentiation resulted in large values due to sensor noise. Figure 7.9 illustrates an example of such a phenomenon that takes place in the three cutting directions X , Y , and Z .

The superimposed high frequency signal was also be identified when the Fast Fourier Transform (FFT) to the simulated acceleration signal was performed and compared to the experimental one as shown in Figure 7.10.

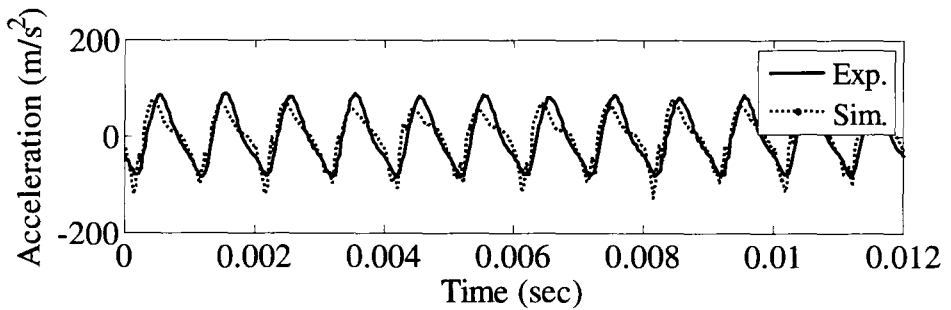
To overcome such a problem a high order, 6th order, low-pass Butterworth filter with zero phase shift was used to filter the simulated acceleration signal at a reasonable cutoff frequency. In the case of the example shown in Figure 7.10 the cutoff frequency was 4.2 kHz. Figures 7.11 and 7.12 illustrate the simulated acceleration after being filtered and its FFT respectively. It is clear from both figures that the frequency that was causing the noise was eliminated without affecting the amplitude of the original simulated acceleration signal. This facilitated the process of calibrating the SCF.



a. X-direction.

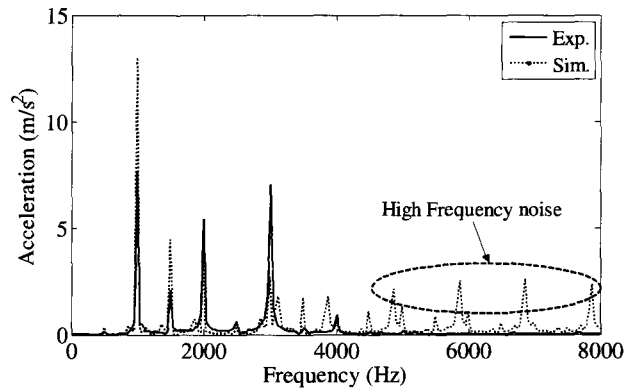


b. Y-direction.

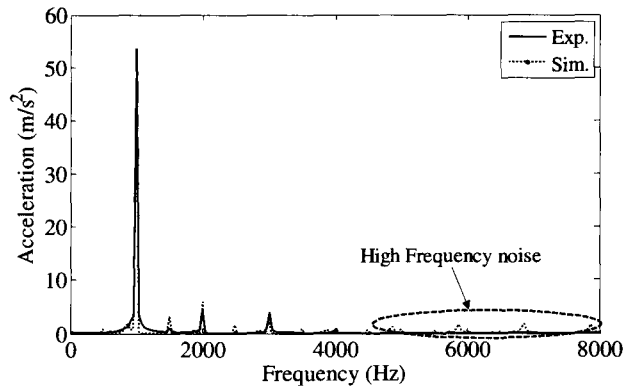


c. Z-direction.

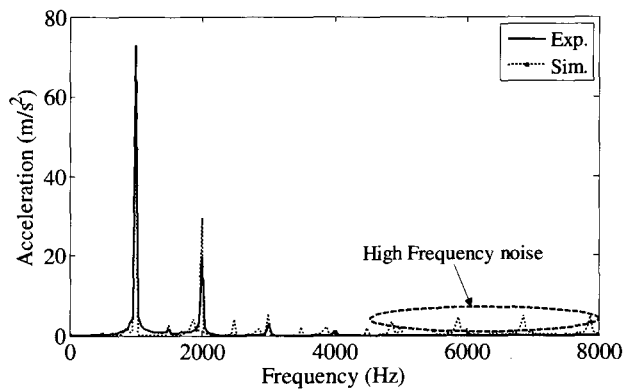
Figure 7.9 – Acceleration signal (experimental vs. simulated) before filtration for cutting test # 1, 30k rev./min.



a. X-direction.

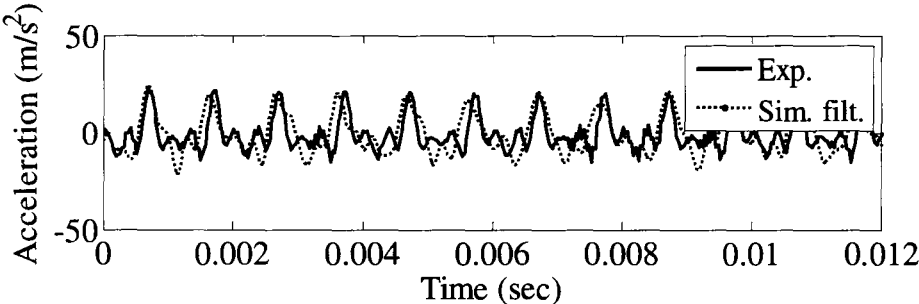


b. Y-direction.

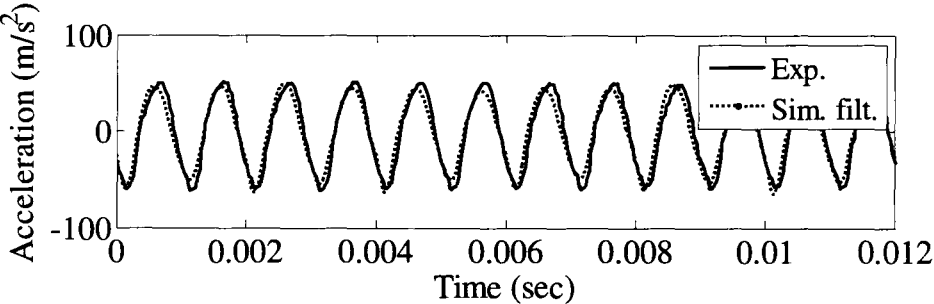


c. Z-direction.

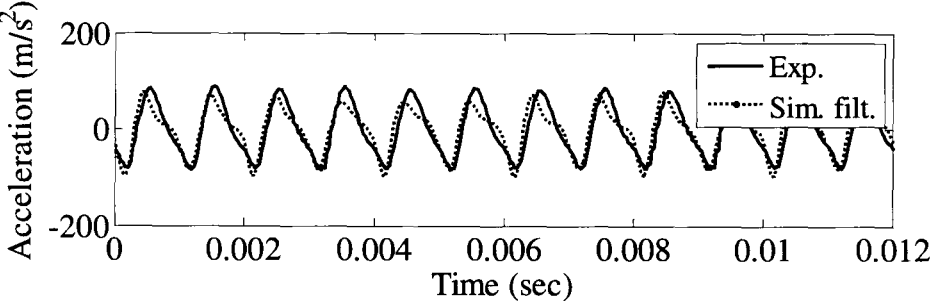
Figure 7.10 – FFT of the acceleration signal (experimental vs. simulated) before filtration for cutting test # 1, 30k rev./min.



a. X-direction.

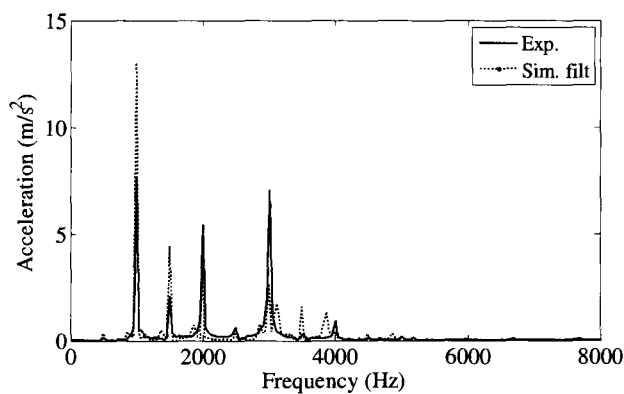


b. Y-direction.

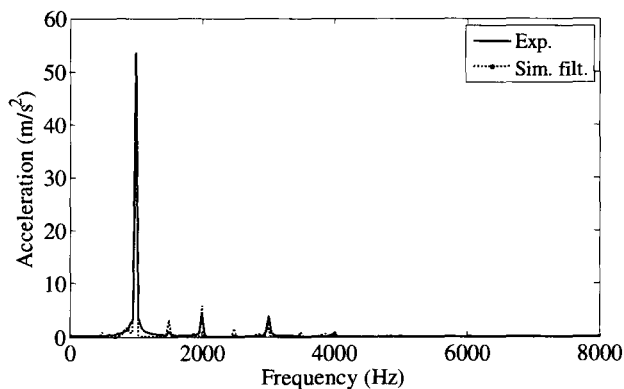


c. Z-direction.

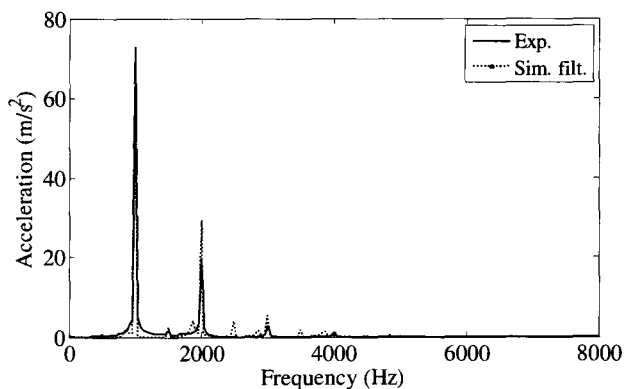
Figure 7.11 – Acceleration signal (experimental vs. simulated) after filtration for cutting test # 1, 30k rev./min.



a. X-direction.



b. Y-direction.



c. Z-direction.

Figure 7.12 – FFT of the acceleration signal (experimental vs. simulated) after filtration for cutting test # 1, 30k rev./min.

7.6 Run-out Effect

The effect of run-out was investigated by running the suggested dynamic model with and without the presence of run-out. When the run-out was present, the run-out value e was considered as well as the unbalance mass m . Two cutting test cases were chosen; one at low RPM (calibration test # 2) and the other at high RPM (calibration test # 7). For both cases the simulated acceleration was compared with the experimental one for the three main coordinates X , Y , and Z . The FFT was applied to both the simulated and experimental acceleration to study the content of the signal. It should be noted that the SCF that was used during the simulation for each cutting test was the same when that was running for the cases both with/without run-out.

Figures 7.13 - 7.15 and 7.16 - 7.18 illustrate the simulated acceleration versus the experimental one as well as their corresponding FFT with and without the presence of run-out for test # 2 and test # 7 respectively. Typically the run-out frequency should correspond to the RPM frequency. For example for the acceleration signal in the Y direction of test # 2 the run-out frequency was not present for the case without the run-out while it was present with run-out, see Figure 7.14c.

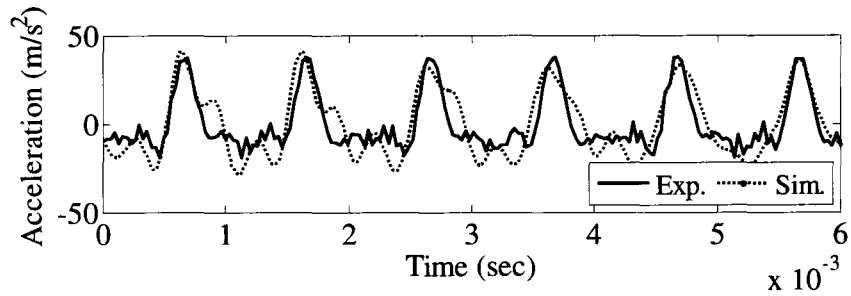
Although the simulation was run for the no run-out case, no significant change was noticed in the magnitude of the simulated acceleration, because the magnitude of the run-out frequency was very small in comparison to that of the tooth-passing frequency (~ 1000 Hz), which was near to the major mode of the fixture (Figure 7.19b), this was illustrated in Figures 7.14a and 7.14b.

On the other hand, when investigating the run-out for the same direction Y but for test # 7 it was noticed that the run-out frequency disappeared for the case when there was no run-out because it takes place near the major mode of the fixture (Figure 7.19b) and also because of the centrifugal force has substantially increased ($\sim 4 \times$).

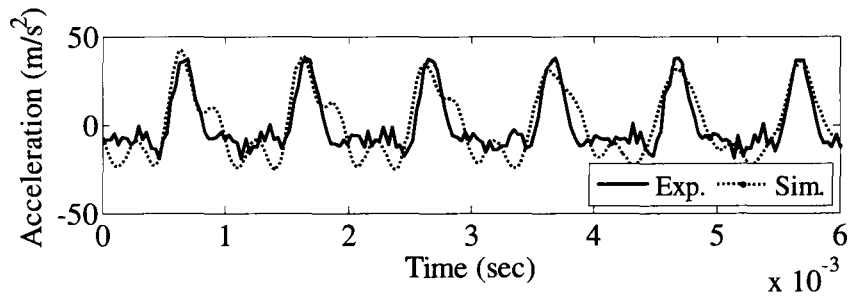
Recall that $F_c = m\epsilon\omega^2$. The Z direction data experienced the same phenomena that took place in the Y direction since the major mode of the fixture was near ~ 1000 Hz, see Figures 7.15, 7.18 and 7.19c.

The behavior of the X direction was also similar to that of the Y and the Z directions however it was not as noticed as in the Y and in the Z direction because the magnitude of the acceleration in the X direction was much smaller than that of the Y or Z as can be seen in Figures 7.13 - 7.18.

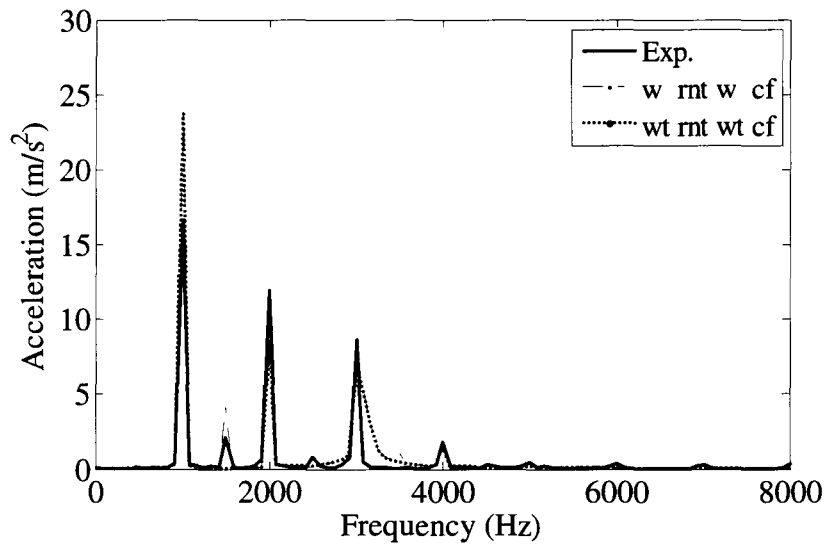
In addition to that, both the run-out frequency and the tooth-passing frequency for tests # 2 and # 7 are far from the major mode of the fixture in the X direction. This makes its participation in the signal even smaller. It should be noted that the SCF was not changed when running the simulation for the cases with/without run-out for tests # 2 and # 7. From Figures 7.13 - 7.18 it can be noticed that when the run-out was not included the simulated acceleration did not match the experimental one either in magnitude or in frequency. This implied that the SCF, in the case of the absence of the run-out, needed to be increased so that the simulated acceleration matched the experimental one. The requirement is not realistic. In addition the experimental and simulated signatures did not match. The investigation of the experimental acceleration signal has led to the necessity of including the effect of the tool run-out as explained earlier in Section 5.3.4 to obtain a proper SCF calibration.



a. With run-out.

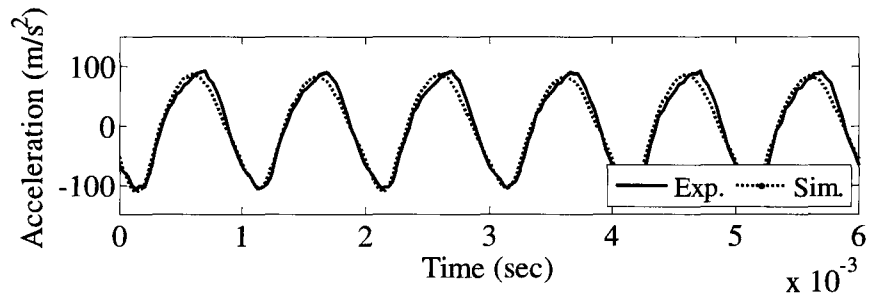


b. Without run-out.

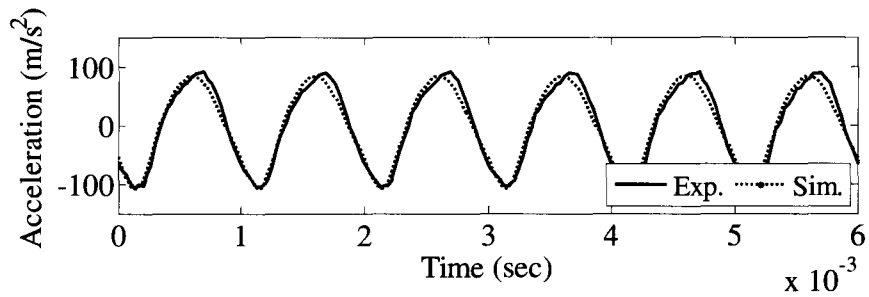


c. Fast Fourier Transform.

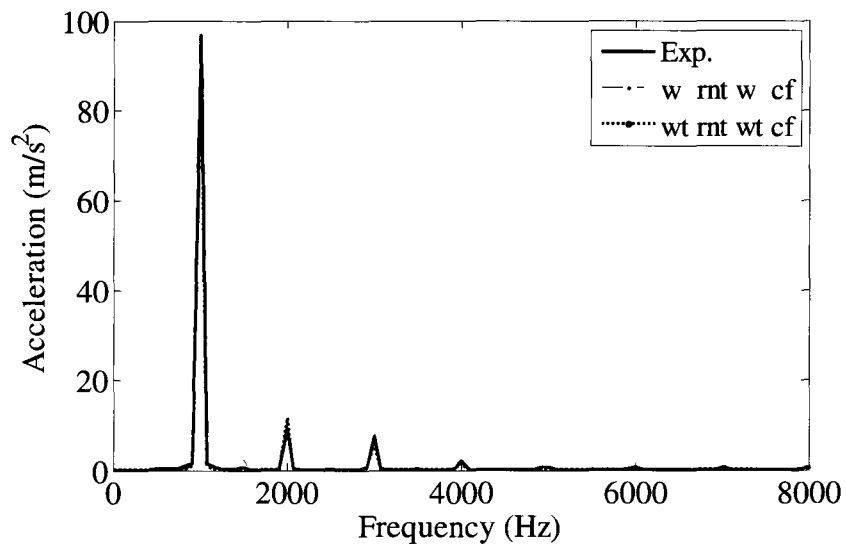
Figure 7.13 – Investigation of the importance of including the run-out in the dynamic model. Acceleration data used is for test # 2 (X-direction), 30k rev./min.



a. With run-out.

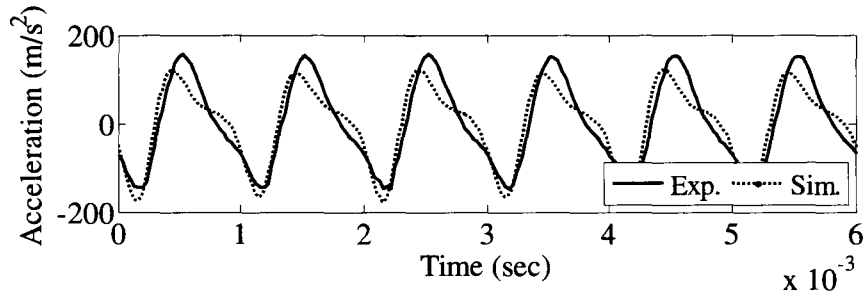


b. Without run-out.

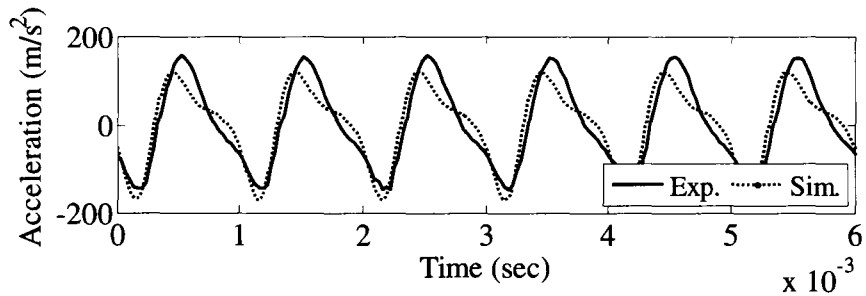


c. Fast Fourier Transform.

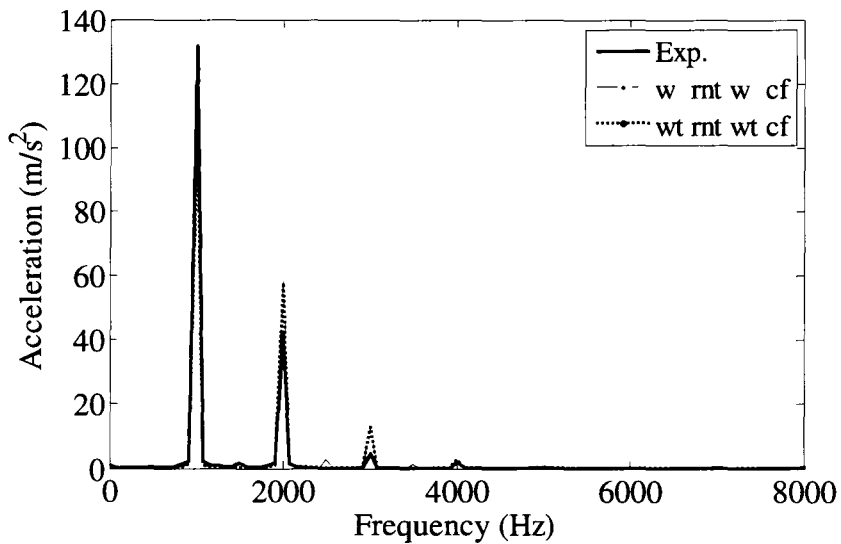
Figure 7.14 – Investigation of the importance of including the run-out in the dynamic model. Acceleration data used is for test # 2 (Y-direction), 30k rev./min.



a. With run-out.

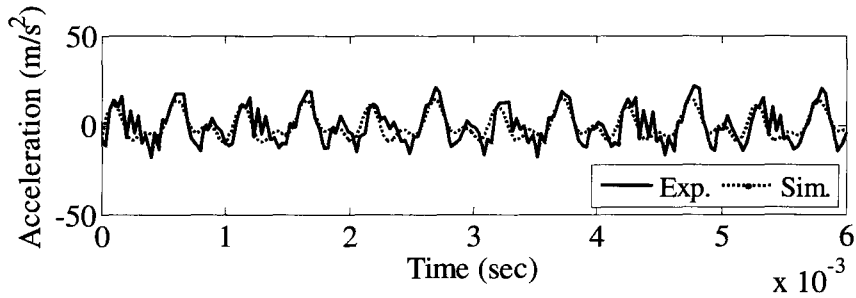


b. Without run-out.

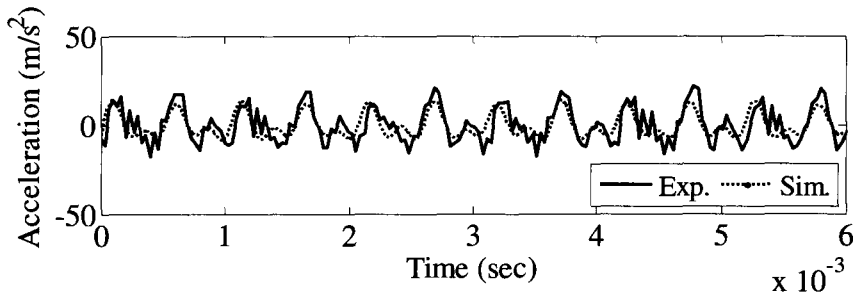


c. Fast Fourier Transform.

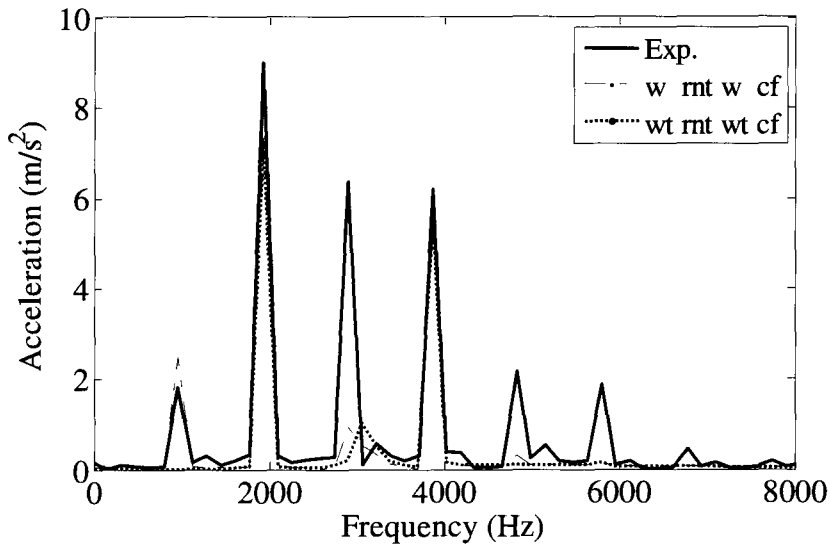
Figure 7.15 – Investigation of the importance of including the run-out in the dynamic model. Acceleration data used is for test # 2 (Z-direction), 30k rev./min.



a. With run-out.

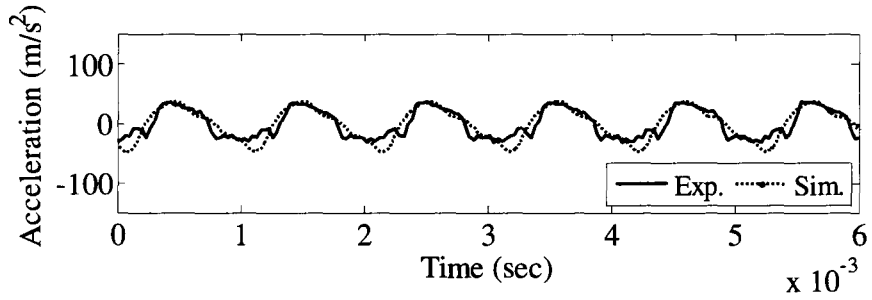


b. Without run-out.

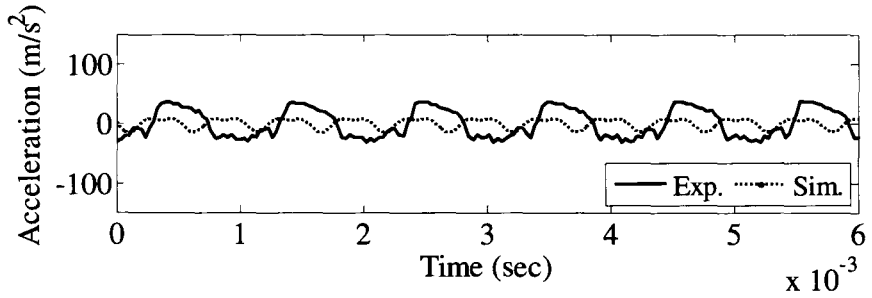


c. Fast Fourier Transform.

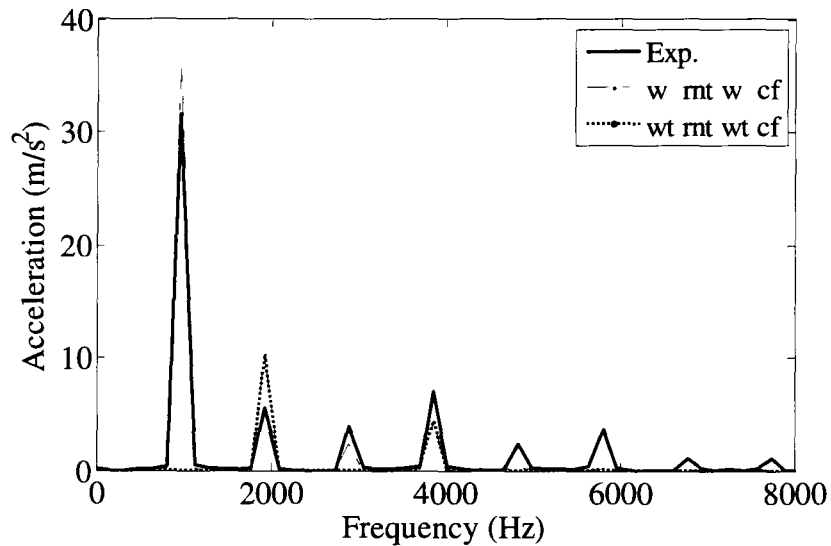
Figure 7.16 – Investigation of the importance of including the run-out in the dynamic model. Acceleration data used is for test # 7 (X-direction), 58k rev./min.



a. With run-out.

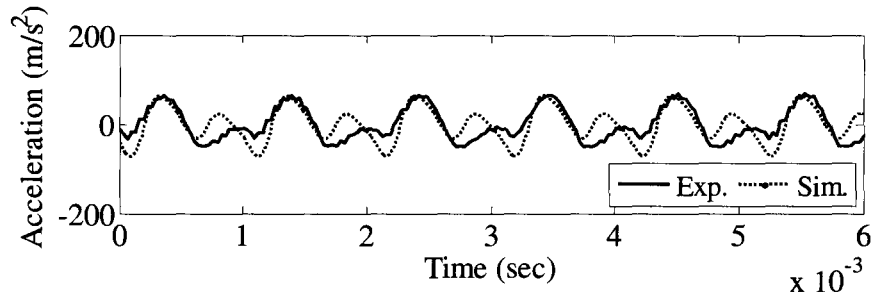


b. Without run-out.

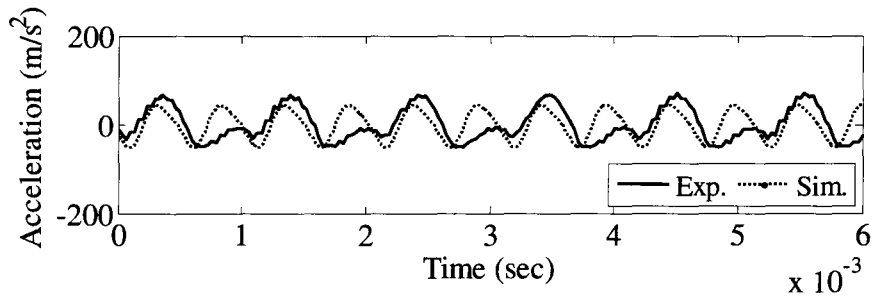


c. Fast Fourier Transform.

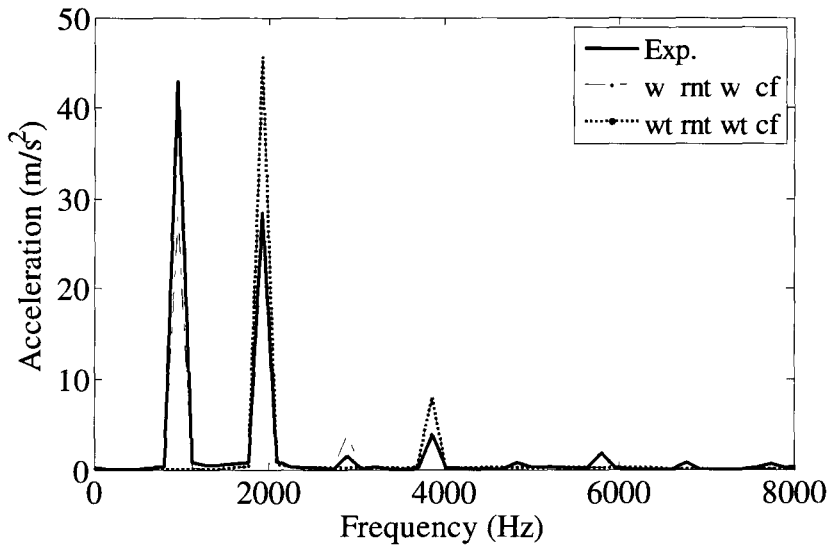
Figure 7.17 – Investigation of the importance of including the run-out in the dynamic model. Acceleration data used is for test # 7 (Y-direction), 58k rev./min.



a. With run-out.

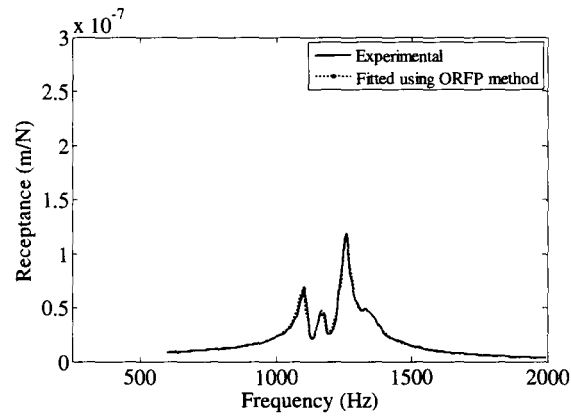


b. Without run-out.

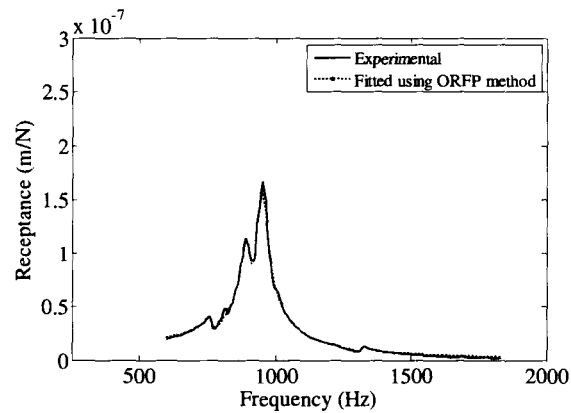


c. Fast Fourier Transform.

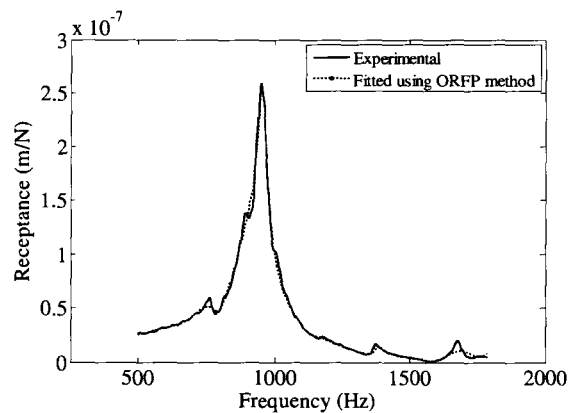
Figure 7.18 – Investigation of the importance of including the run-out in the dynamic model. Acceleration data used is for test # 7 (Z-direction), 58k rev./min.



a. X-direction.



b. Y-direction.



c. Z-direction.

Figure 7.19 – Receptance of the fixture (setup # 1) in the three cutting directions; X, Y, and Z.

7.7 Verification of the Suggested Estimation Procedure

In this section the two force models presented earlier in Chapter 5 will be used to verify and analyze the suggested estimation procedure that includes the improved dynamic model: (1) the mechanistic force model described earlier in Section 5.3.2 and (2) the analytical model presented in Section 5.3.2.

7.7.1 Mechanistic force model

SCF using setup # 1

For the mechanistic model, the specific cutting forces will be estimated for each test case using the procedure described earlier in Section 7.4 and iterated on until the simulated acceleration matches the experimental one. Calibration tests were used to fit the non-linear equation described by Equations 6.1 - 6.3 for K_t , K_r , and K_a respectively, while the verification set was used to verify the estimated specific cutting forces from the experimental data versus those predicted using the fitted equation. This was repeated for setup # 1 and setup # 2. The magnitude of the simulated cutting forces were compared to the experimental ones and analyzed for both setups.

Calibration test cases, using setup # 1, for which the experimental acceleration has been matched with the simulated ones are illustrated along with verification cases in Appendix D.2. The specific cutting forces corresponding to those cases are summarized in Table 7.5. These were also used to fit the non-linear equations given by Equations 6.1 - 6.3 leading to Equations 7.4 - 7.6. Table 7.6 summarizes the specific cutting forces that were obtained using the verification set and the percentage difference between the experimental and the predicted specific cutting force was cal-

culated. The average of the percentage difference between the experimental and fitted specific cutting forces was found to be 9.31%, 14.20% and 11.19% for K_t , K_r and K_a respectively. It should be noted that the cutting parameters of the verification set were general; some cutting tests had cutting parameters that were entirely within the range of cutting parameters used in the calibration process, for example test # 1 and # 2, while other cutting tests had cutting parameters that were outside the boundary of the cutting parameters.

The feed/tooth f_t and the radial depth of cut d_r used in the calibration tests were used in Equations 7.4 - 7.6 while varying the cutting velocity (summarized in Table 7.7) to generate Figure 7.20. This figure shows the variation of the fitted specific cutting forces with the cutting velocity. For a given specific cutting force the trend shown in Figure 7.20 matches that reported in [96] as illustrated in Figures 7.22. Moreover, the magnitude of the specific cutting forces estimated using the proposed calibration method was within the same order of magnitude of that reported in [97]. It was not possible to establish an exact matching value due to the difference in the cutting conditions and in the modelling approach implemented, however the same trend in behavior could be noticed.

Table 7.5 – Estimated SCF using the fixture acceleration for setup # 1

Test #	K_t (N/m ²)	K_r (N/m ²)	K_a (N/m ²)
1	2.40×10^9	1.70×10^9	1.70×10^9
2	1.76×10^9	1.20×10^9	1.20×10^9
3	1.65×10^9	1.30×10^9	1.37×10^9
4	1.65×10^9	1.00×10^9	1.10×10^9
5	1.65×10^9	1.85×10^9	1.15×10^9
6	1.35×10^9	0.80×10^9	0.70×10^9
7	1.56×10^9	0.80×10^9	0.95×10^9
8	1.20×10^9	0.55×10^9	0.55×10^9
9	1.42×10^9	0.73×10^9	0.73×10^9

Table 7.6 – SCF predicted using Equations 6.1 - 6.3 and compared against the experimental ones using setup # 1

Test #	$K_t \times 10^9$ (N/m ²)			$K_r \times 10^9$ (N/m ²)			$K_a \times 10^9$ (N/m ²)		
	Exp.	Fit.	Diff. %	Exp.	Fit.	Diff. %	Exp.	Fit.	Diff. %
1	1.45	1.77	22.22	1.35	1.26	6.50	1.10	1.20	9.11
2	1.27	1.32	4.30	0.58	0.69	19.68	0.55	0.71	28.13
3	2.30	1.90	17.20	0.90	1.37	52.52	1.50	1.41	5.93
4	2.20	1.70	22.58	1.00	1.17	17.31	1.50	1.13	24.56
5	2.00	1.81	9.28	1.05	1.29	22.81	1.25	1.30	4.11
6	2.00	1.98	1.19	1.35	1.55	15.18	1.35	1.48	9.96
7	2.00	2.30	14.98	1.65	1.79	8.78	1.85	1.98	7.26
8	1.62	1.69	4.29	1.35	1.36	0.79	1.03	1.06	2.85
9	1.40	1.49	6.68	0.78	0.93	19.66	0.75	0.87	15.69
10	1.70	1.79	5.24	0.90	0.98	8.50	1.30	1.27	2.43
11	1.35	1.36	0.85	0.85	0.76	10.42	0.62	0.75	21.43
12	1.20	1.15	4.54	0.50	0.49	1.78	0.55	0.56	1.80
13	1.10	1.18	7.67	0.55	0.55	0.64	0.50	0.56	12.28
Mean			9.31			14.20			11.19
Max			22.58			52.52			28.11
Min			0.85			0.64			1.80

$$K_t = 1.06 \times 10^{10} V^{-0.3881} \times f_t^{-0.2010} \times d_r^{-0.1930} \quad (7.4)$$

$$K_r = 0.72 \times 10^{10} V^{-0.5461} \times f_t^{-0.4785} \times d_r^{-0.5268} \quad (7.5)$$

$$K_a = 4.12 \times 10^{10} V^{-0.7669} \times f_t^{-0.4233} \times d_r^{-0.2395} \quad (7.6)$$

In [97] it was concluded that the effect of the cutting speed on the estimated cutting coefficients was negligible. This contradicts the findings in [96]. This might be true in that particular case because of the small variation in the range of cutting speeds reported in [97] (79, 95, 111 m/min). By taking a closer look at Figure 7.22 it can be noticed that the findings reported in [97] might be true for a localized area but are not true for the overall range (500 - 1600 m/min). In Figure 7.22 it was also noticed that as the value of the chip thickness increased the curve of the specific cutting force became lower. The same behavior was also noticed in Figure 7.20. For the same radial depth of cut, the specific cutting force curve goes lower as the feed/tooth increased, which in our case was similar to the chip thickness effect

reported in [96].

In addition, Equations 7.4 - 7.6 were further investigated by evaluating the specific cutting forces K_t , K_r , and K_a while varying the feed/tooth and keeping the radial depth of cut constant. For each specific cutting force, four curves were generated with each of them being for a given cutting speed. Figure 7.21 summarizes these cases. It was found that for a given feed/tooth and as the cutting velocity increases the value of the specific cutting force decreases. This was also affirmed by the observations reported in [96, 97], see Figures 7.23a - 7.23b, 7.24a - 7.24b respectively.

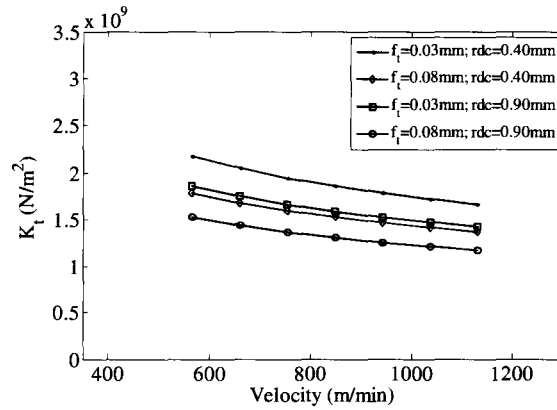
Good agreement between the experimental and the fitted specific cutting forces along with the agreement of the trend in the fitted equations with the open literature confirms the accuracy of the experimental values obtained in the present study.

Table 7.7 – Values used in Equations 7.4 - 7.6

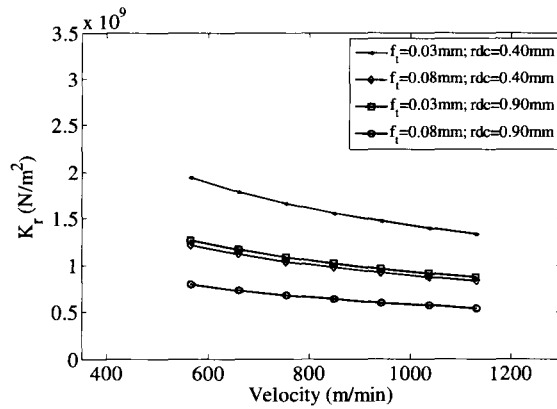
Cutting Velocity (m/min)	565	659	754	848	942	1037	1131
--------------------------	-----	-----	-----	-----	-----	------	------

SCF using setup # 2

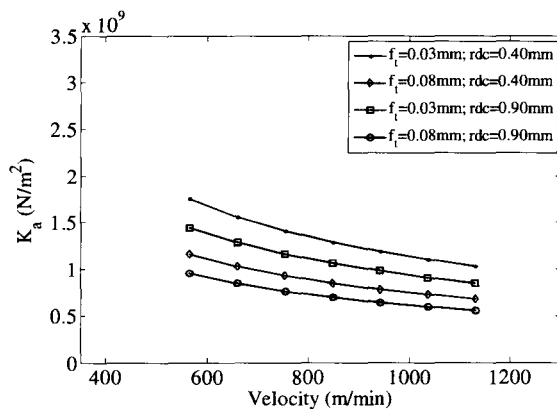
The procedure followed in Section 7.7.1 was repeated for setup # 2. Calibration cases (1 - 9) using setup # 2 are illustrated in Appendix D.3. Verification cases # 1 and # 2 are used to verify the model using setup # 2 and are also summarized in Appendix D.3. Table 7.8 summarizes the specific cutting forces that were used in fitting the non-linear equation and Table 7.9 summarizes the specific cutting forces that were obtained when using the verification set. The non-linear equations fitted for K_t , K_r , and K_a are given by Equations 7.7 - 7.9.



a. Variation of K_t with the cutting velocity.

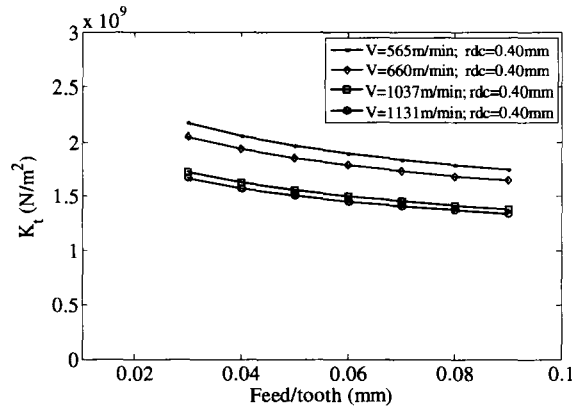


b. Variation of K_r with the cutting velocity.

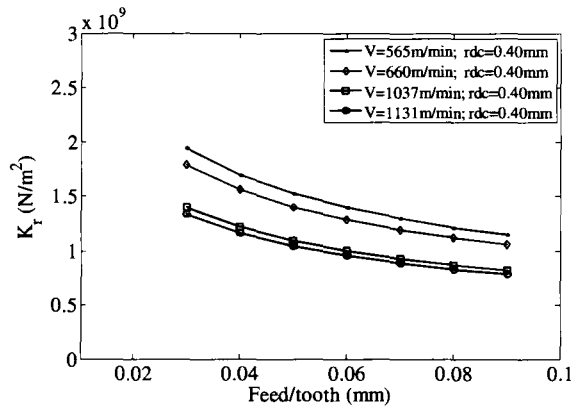


c. Variation of K_a with the cutting velocity.

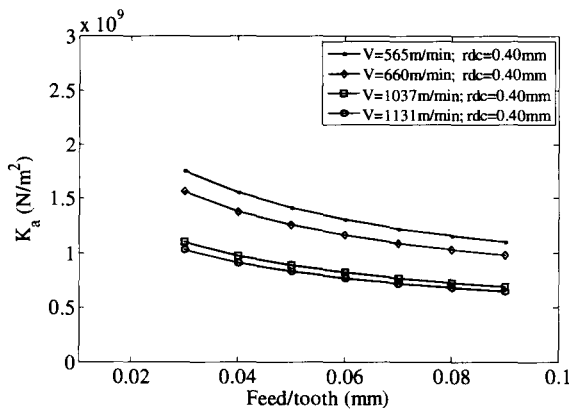
Figure 7.20 – Variation of K_t , K_r , and K_a with the cutting velocity and using setup # 1.



a. Variation of K_t with the feed/tooth.



b. Variation of K_r with the feed/tooth.



c. Variation of K_a with the feed/tooth.

Figure 7.21 – Variation of K_t , K_r , and K_a with the feed/tooth using setup # 1.

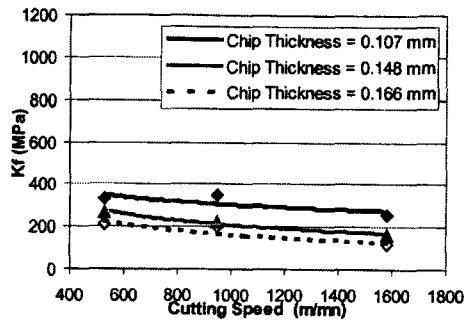
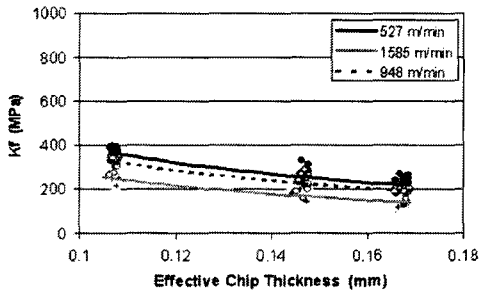
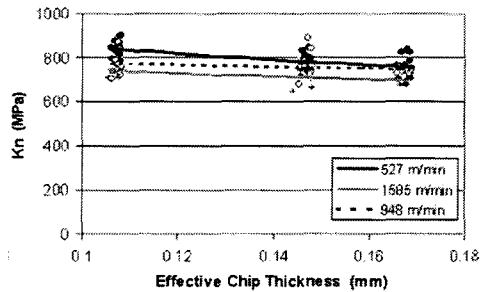


Figure 7.22 – Variation of the frictional component of the SCF with the cutting speed as published in [96].

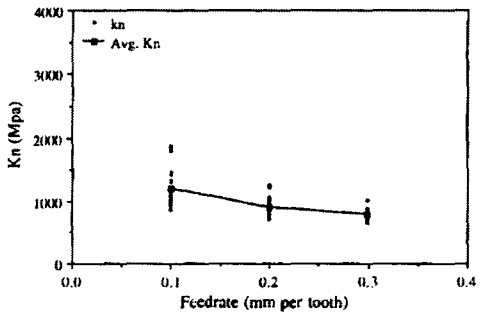


a.

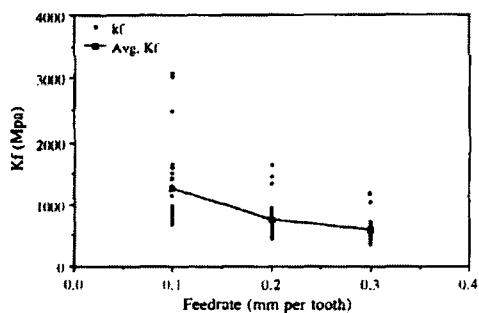


b.

Figure 7.23 – Variation of the SCF, frictional (a) and normal (b), with the effective chip thickness as published in [96].



a.



b.

Figure 7.24 – Variation of the SCF, frictional (a) and normal (b), with the feedrate as published in [97].

Table 7.8 – Estimated SCF using the fixture’s acceleration for setup # 2

Test #	K_t (N/m ²)	K_r (N/m ²)	K_a (N/m ²)
1	2.20×10^9	1.30×10^9	1.65×10^9
2	1.82×10^9	1.15×10^9	1.15×10^9
3	1.70×10^9	1.22×10^9	1.37×10^9
4	1.70×10^9	0.90×10^9	1.00×10^9
5	1.75×10^9	1.00×10^9	1.00×10^9
6	1.40×10^9	0.80×10^9	0.80×10^9
7	1.56×10^9	0.74×10^9	0.95×10^9
8	1.25×10^9	0.50×10^9	0.65×10^9
9	1.42×10^9	0.70×10^9	0.72×10^9

$$K_t = 0.87 \times 10^{10} V^{-0.3402} \times f_t^{-0.1670} \times d_r^{-0.1763} \quad (7.7)$$

$$K_r = 2.65 \times 10^{10} V^{-0.6585} \times f_t^{-0.2748} \times d_r^{-0.3422} \quad (7.8)$$

$$K_a = 2.38 \times 10^{10} V^{-0.6441} \times f_t^{-0.3402} \times d_r^{-0.1949} \quad (7.9)$$

Table 7.9 – SCF predicted using Equations 6.1 - 6.3 and compared against the experimental ones for setup # 2.

Test #	$K_t \times 10^9$			$K_r \times 10^9$			$K_a \times 10^9$		
	Exp.	(N/m ²) Fit.	Diff. %	Exp.	(N/m ²) Fit.	Diff. %	Exp.	(N/m ²) Fit.	Diff. %
1	1.45	1.77	22.22	1.35	1.26	6.49	1.10	1.20	9.12
2	1.27	1.32	4.28	0.58	0.69	19.67	0.55	0.70	28.11

Similarly to setup # 1 Equations 7.7 - 7.9 were used to evaluate the specific cutting forces while varying the cutting velocity. This resulted in Figure 7.32. The specific cutting forces were also generated while varying the feed/tooth and keeping the radial depth of cut d_r constant. When compared to setup # 1 the trend of the fitted equations using setup # 2 behaved in a similar fashion to that of setup # 1, see Figure 7.33.

Furthermore, the specific cutting forces predicted using setup # 1 have been compared to those predicted using setup # 2 and an average percentage difference

between both cases was found to be 3.20%, 10.38% and 9.87% for K_t , K_r , and K_a respectively. This implies the effectiveness and the accuracy of the proposed calibration procedure. Note that the same procedure of predicting the specific cutting forces has been used for both setups. In addition, this affirms that the specific cutting forces are independent of the system dynamics. This is summarized in Table 7.14.

More investigation was carried out to see how the magnitude and signature of the simulated cutting forces compares to that measured using the dynamometer. This was only possible for setup # 1 since it had the dynamometer mounted underneath it. However, a link to setup # 2 can still be established by comparing the simulated cutting forces of setup # 1 to those of setup # 2. This will be shown later in Section 7.7.2. An attempt was carried out to reproduce the forces that are measured using the dynamometer. In this attempt a model was used in which the dynamometer with the mass of the fixture was assumed to be a single degree of freedom system, see Figure 7.25. The force was measured through the piezoelectric material in which $F_{measured} \simeq k \cdot x$ and can only be used for the X and Y directions. k is the stiffness of the piezoelectric material. Its equation of motion is given by Equation 7.10. In the Z -direction the weight of the mass on top of the piezoelectric cell was considered in the equation of motion given by Equation 7.11 and the model is illustrated in Figure 7.26.

$$F_{x,Measured} = F_{x,App.} - m \cdot \ddot{x} - c \cdot \dot{x} \quad (7.10)$$

$$F_{x,Measured} = F_{x,App.} - m \cdot \ddot{x} - c \cdot \dot{x} - W \quad (7.11)$$

The measured forces $F_{Measured}$ were estimated by making use of the velocity \dot{x} and the acceleration \ddot{x} that were obtained from the simulation model. Please note

that those quantities were obtained at the fixture. Figures 7.27 and 7.28 illustrate the regenerated measured forces $F_{Measured,Sim}$ plotted against the actual experimental forces measured $F_{Measured,Exp}$ using the dynamometer for tests # 1 and # 5 respectively and using setup # 1. Those figures were obtained using the masses and damping coefficients summarized in Table 7.10.

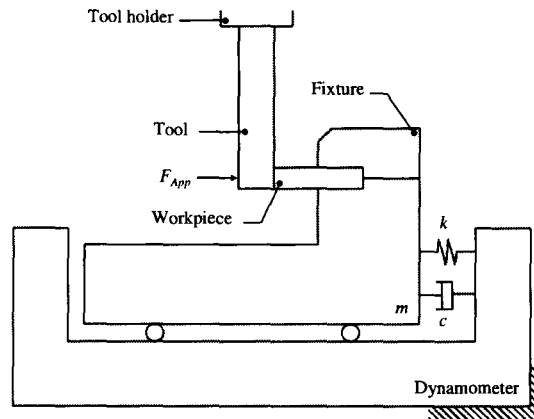


Figure 7.25 – Modeling of dynamometer and fixture to reproduce the measured forces $F_{measured}$ (X and Y directions).

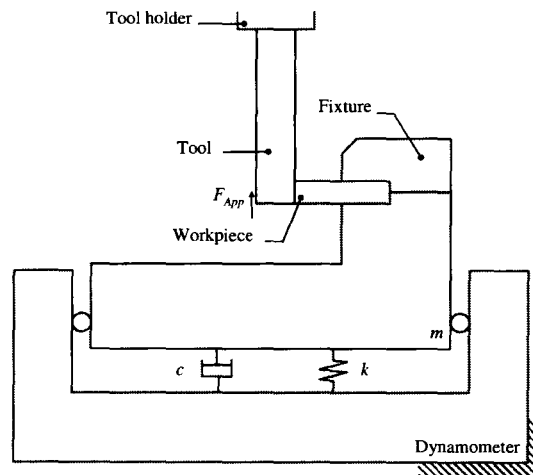
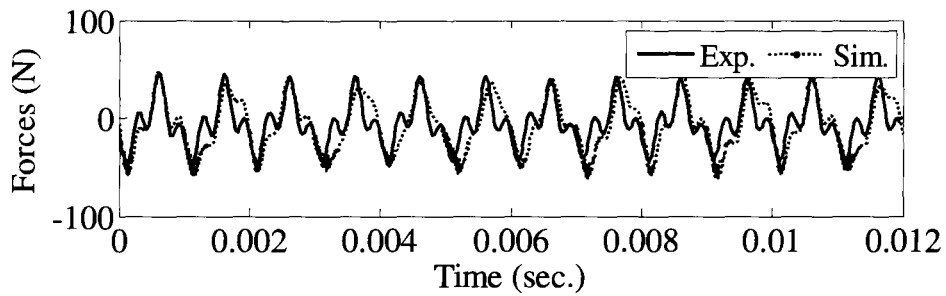
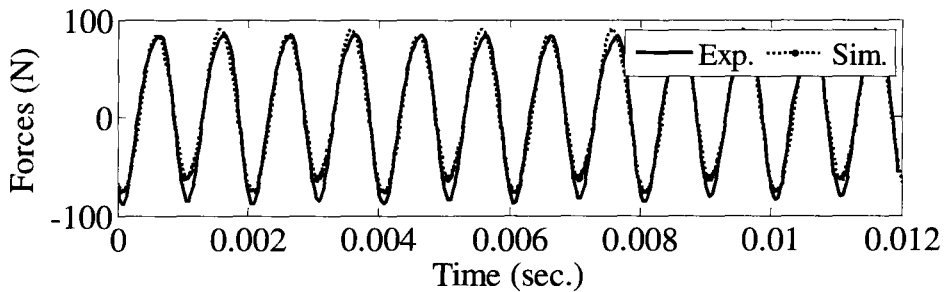


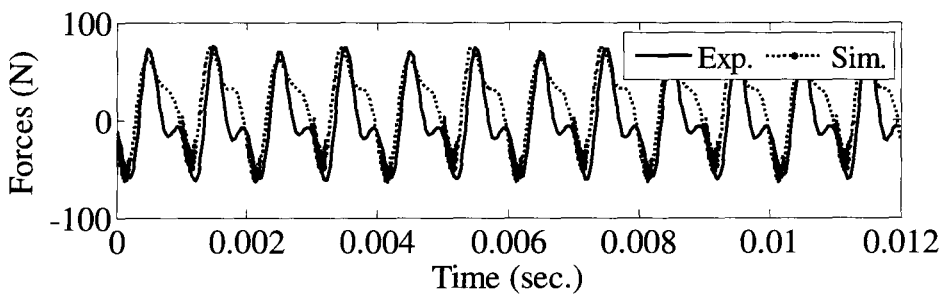
Figure 7.26 – Modeling of dynamometer and fixture to reproduce the measured forces $F_{measured}$ (Z -direction).



a. X-direction.

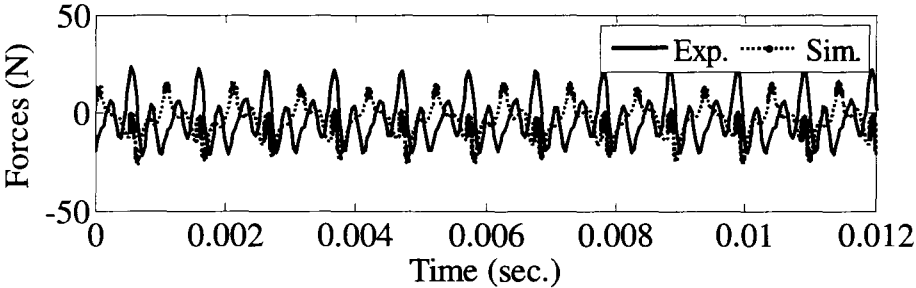


b. Y-direction.

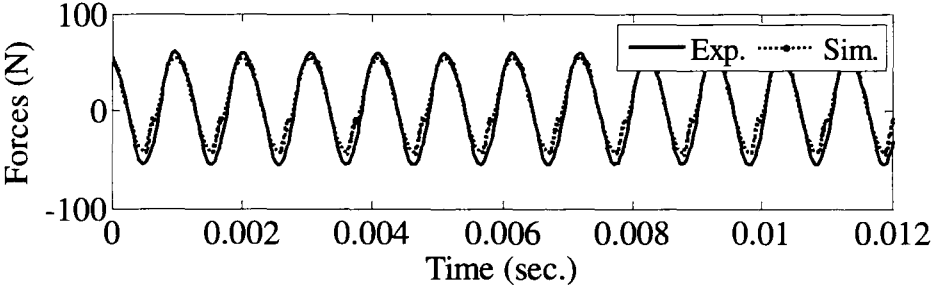


c. Z-direction.

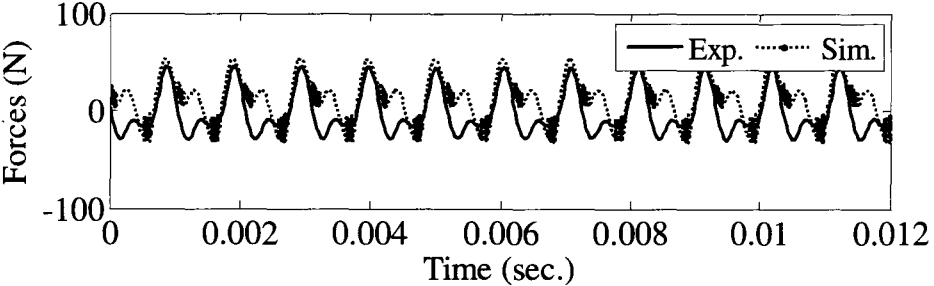
Figure 7.27 – Regenerated measured forces plotted against actual measure forces using the dynamometer for test # 1 and using setup # 1.



a. X-direction.



b. Y-direction.



c. Z-direction.

Figure 7.28 – Regenerated measured forces plotted against actual measure forces using the dynamometer for test # 5 and using setup # 1.

Table 7.10 – Mass and damping coefficient used in Equations 7.10 and 7.11

Direction	Mass (kg)	Damping Coefficient (Nsm ⁻¹)
<i>X</i>	2.10	300
<i>Y</i>	2.10	300
<i>Z</i>	1.05	1300

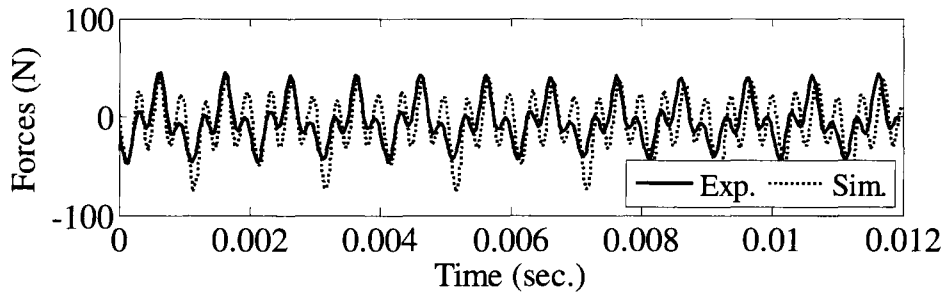
The fixture includes the upper/lower jaws, three M10 × 20 countersunk screws, eight M5 × 12 screws and three accelerometers which tally up ~1.6 kg of weight. The weight of the dynamometer is ~0.75 kg. Assuming that the weight of its upper plate and the internal structure underneath it is ~0.45 kg (~ 50 - 60% of its total weight) explains the existence of a mass of 2.10 kg (see Table 7.10) but doesn't explain the mass of 1.05 unless that mass was the equivalent mass of the approximated system. It was also noticed that using the parameters summarized in Table 7.10 gave almost the same measured forces however some discrepancies were found to exist in the signature. This is believed to be due to the approximation of the dynamometer as a single degree of freedom system. This was especially true in the *X* and *Z* directions.

The measured forces were regenerated another time using the velocity \dot{x} and the acceleration \ddot{x} that were obtained at the piezoelectric cell. Those quantities were obtained by dividing the measured experimental force by the rigidity corresponding to each direction provided by the dynamometer manufacturer. In this way the displacement x was obtained. The velocity \dot{x} and the acceleration \ddot{x} were obtained by differentiating the displacement x once and twice respectively and then filtering. Then they were used in Equations 7.10 and 7.11 to regenerate the measured forces. Figures 7.29 and 7.30 illustrate the regenerated measured forces $F_{Measured,Sim.}$ using the velocity \dot{x} and the acceleration \ddot{x} that were obtained at the piezoelectric cell versus the actual experimental forces measured $F_{Measured,Exp.}$ using the dynamometer for test # 1 and # 5 respectively and using setup # 1. These figures were obtained

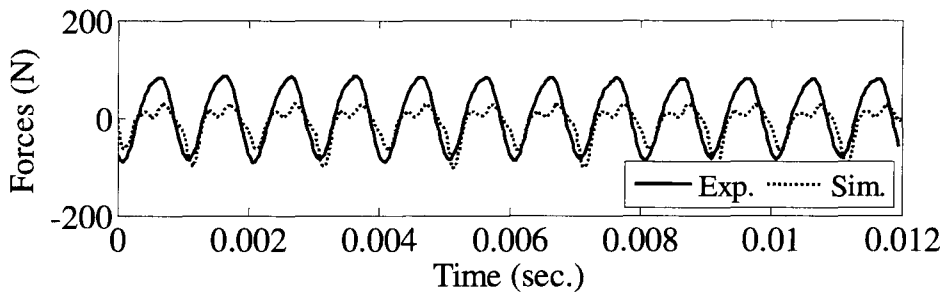
using the masses and damping coefficients summarized in Table 7.12. Even though the signature matches in some cases, for example test # 1 X -direction, the mass used in the model is 1.1 kg which again indicates that this system was only an approximation. In the case of test # 1 Z -direction, a shift appeared in the regenerated force but when a mass of 1.1 kg was used, this shift disappeared, see Figure 7.31. The forces measured using the dynamometer were regenerated for all test cases (9 tests) in the X , Y and Z directions using the first approach (i.e. system response at the fixture) and their magnitude was compared to the experimental ones and are summarized in Table 7.13. From Table 7.13 it is clearly noticed that there was a high match between the experimental forces and the regenerated ones. It should be noted that the system response was obtained after calibrating the specific cutting forces using the proposed technique. It should also be noted that the mass and damping coefficient summarized in Table 7.10 were used for tests 1 - 4 while for tests 5-9 the mass and damping had to change. They are summarized in Table 7.11. The change in mass and the damping coefficient for some cutting directions was expected since the model was an approximated one as mentioned above.

Table 7.11 – Mass and damping coefficient used in Equations 7.10 and 7.11 for tests 5 - 9

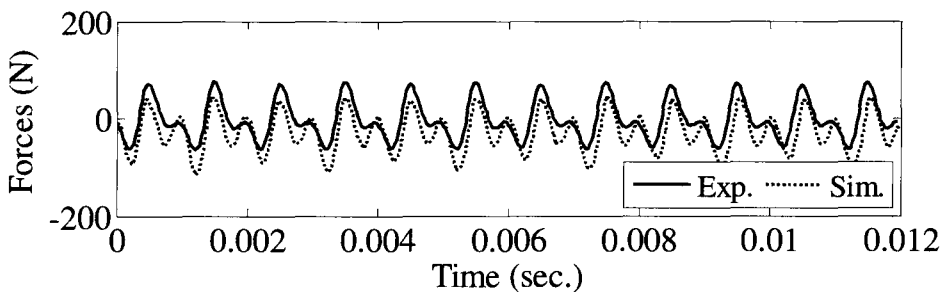
Direction	Mass (kg)	Damping Coefficient (Nsm^{-1})
X	2.05	300
Y	2.05	500
Z	0.90	1300



a. X-direction.

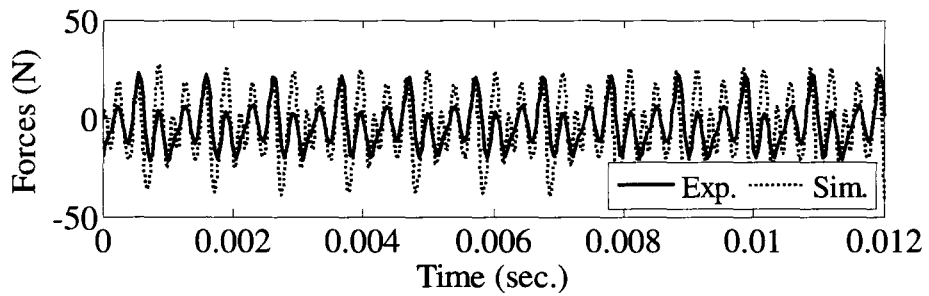


b. Y-direction.

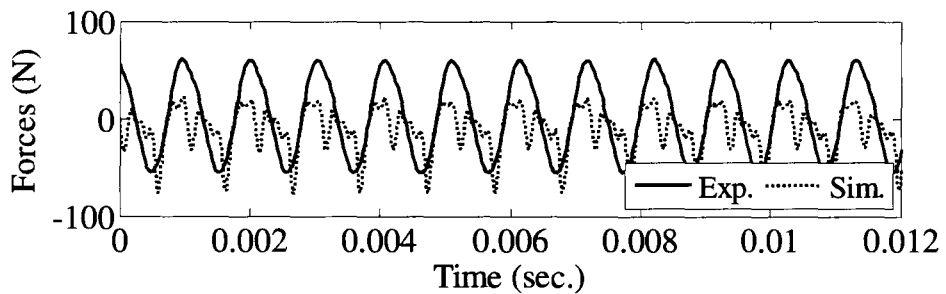


c. Z-direction.

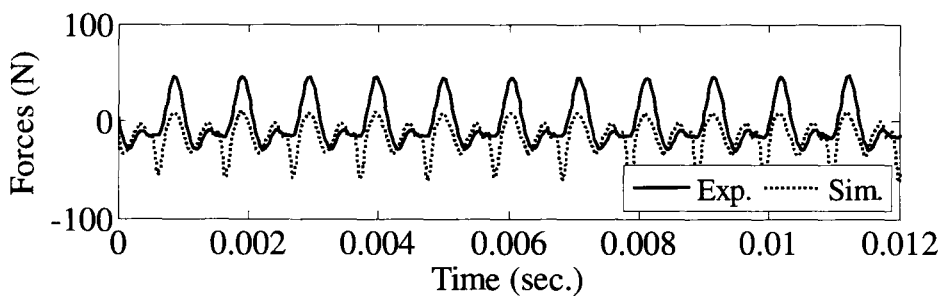
Figure 7.29 – Regenerated measured forces obtained from the displacement of the dynamometer and plotted against actual measure forces for test # 1 and using setup # 1.



a. X-direction.



b. Y-direction.



c. Z-direction.

Figure 7.30 – Regenerated measured forces obtained from the displacement of the dynamometer and plotted against actual measure forces for test # 5 and using setup # 1.

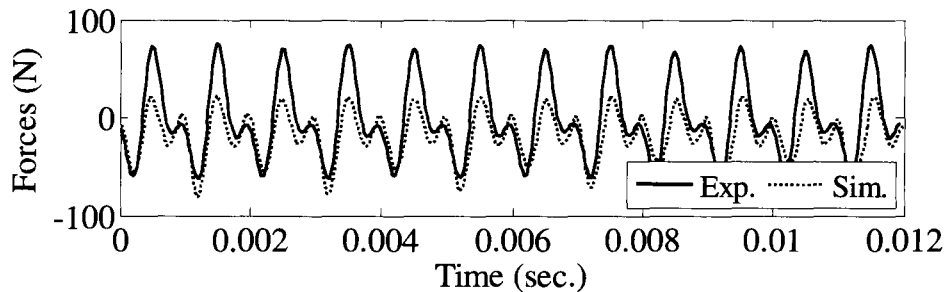


Figure 7.31 – Regenerated measured force in the Z -direction using a mass of 1.1 kg.

Table 7.12 – Mass and damping coefficient used in Equations 7.10 and 7.11

Direction	Mass (kg)	Damping Coefficient (Nsm^{-1})
X	1.10	300
Y	2.10	300
Z	2.10	1300

Table 7.13 – Mass and damping coefficient used in Equations 7.10 and 7.11

Test #	X (N)		Y (N)		Z (N)	
	Exp.	Regen.	Exp.	Regen.	Exp.	Regen.
1	47.0	62.0	88.0	90.0	76.7	74.6
2	78.6	121.0	159.0	168.0	148.0	123.2
3	54.0	98.0	159.0	172.6	141.0	134.6
4	112.0	156.0	278.0	352.0	250.0	204.0
5	24.0	25.7	62.0	55.0	49.9	54.7
6	33.0	45.0	48.0	34.0	55.0	61.0
7	29.0	37.7	69.0	47.0	65.0	74.0
8	48.3	56.9	80.0	55.0	109.0	90.0
9	70.8	68.4	31.3	27.0	34.0	43.0

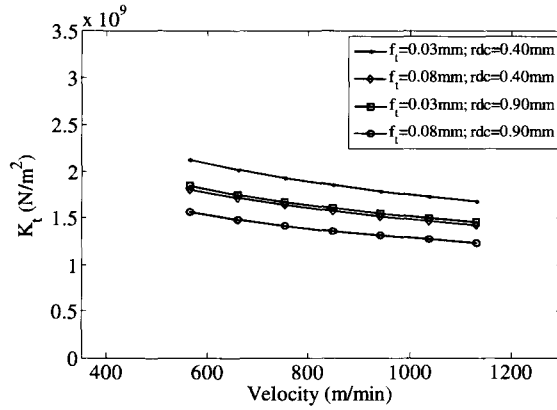
The resultant cutting forces were calculated using Equation 7.1 for the experimental and the simulated cutting forces for each cutting tooth. The experimental resultant cutting forces were then plotted versus the simulated ones for tooth # 1 and tooth # 2 as shown in Figures 7.35 and 7.36 respectively. A linear trend line was

fitted in both figures with a correlation coefficient R^2 of 0.83 and 0.71 respectively which indicated a high level of correlation between the experimental and the simulated cutting forces and also affirmed the previous findings of the effectiveness of the suggested calibration procedure. Note that tests 1 - 9 represented the cutting tests that were used in the calibration process as presented earlier in Table 6.3 and tests 10 - 11 represent cutting tests used in the verification process as presented earlier in Table 6.4.

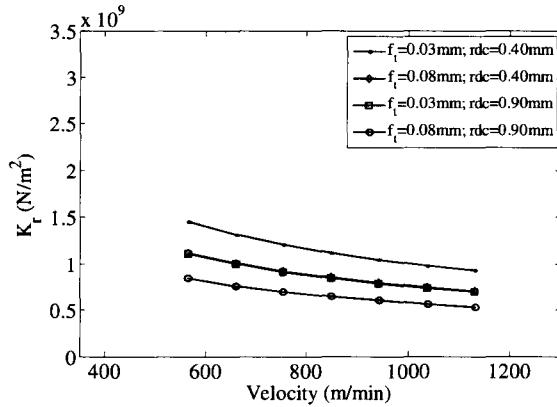
Table 7.14 – Percentage difference between SCF predicted using fixture setup # 1 and fixture setup # 2

Case*	Test #	% K_t	% K_r	% K_a
c	1	8.33	23.53	2.94
c	2	3.41	4.17	4.17
c	3	3.03	6.15	0.00
c	4	3.03	10.00	9.09
c	5	6.06	45.95	13.04
c	6	3.70	0.00	14.29
c	7	0.00	7.50	0.00
c	8	4.17	9.09	18.18
c	9	0.00	4.11	1.37
v	1	3.45	3.70	0.00
v	2	0.00	0.00	45.45
Avg.		3.20	10.38	9.87

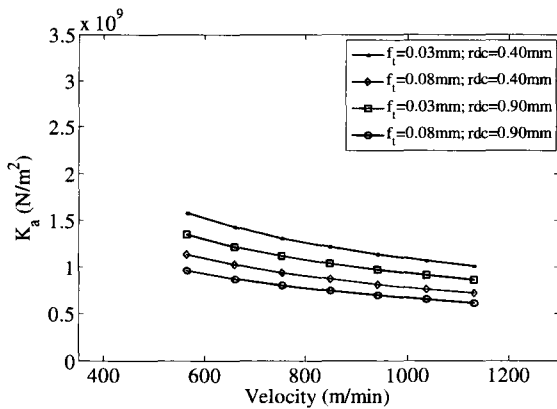
*c = calibration, v = verification.



a. Variation of K_t with the cutting velocity.

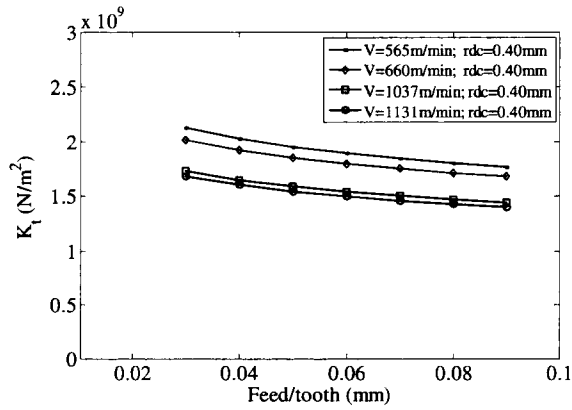


b. Variation of K_r with the cutting velocity.

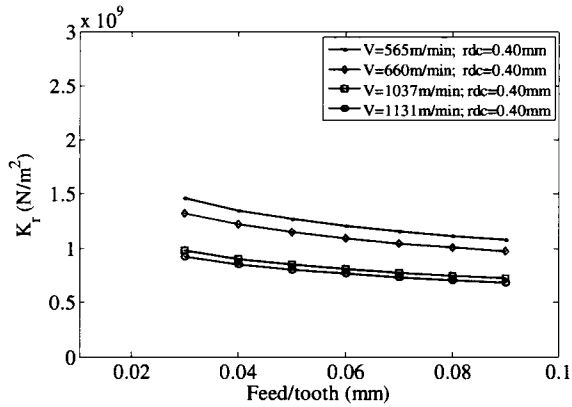


c. Variation of K_a with the cutting velocity.

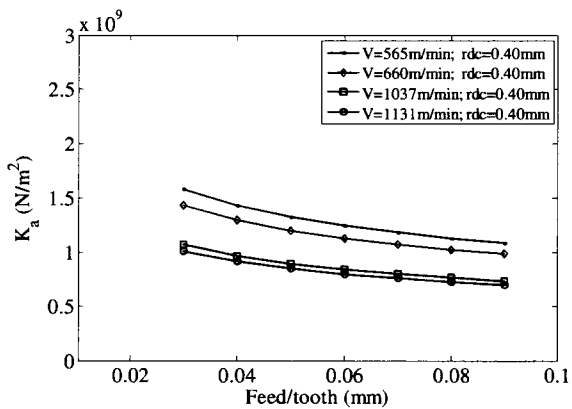
Figure 7.32 – Variation of K_t , K_r , and K_a with the cutting velocity and using setup # 2.



a. Variation of K_t with the feed/tooth.

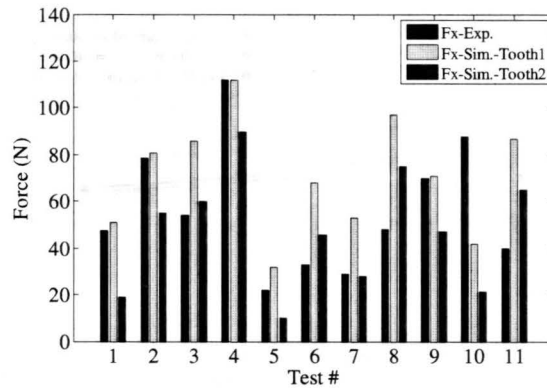


b. Variation of K_r with the feed/tooth.

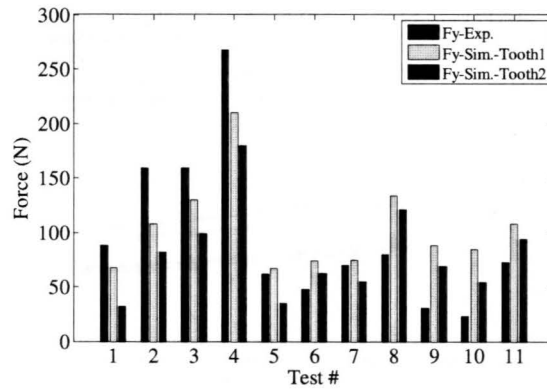


c. Variation of K_a with the feed/tooth.

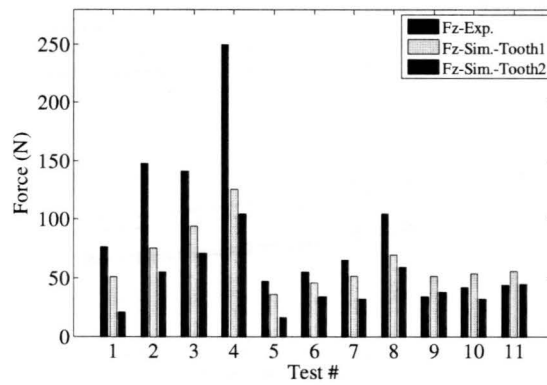
Figure 7.33 – Variation of K_t , K_r , and K_a with the feed/tooth using setup # 2.



a. F_x .



b. F_y .



c. F_z .

Figure 7.34 – Comparison between the cutting forces’ magnitude generated using the mechanistic model and the experimental one using setup # 1.

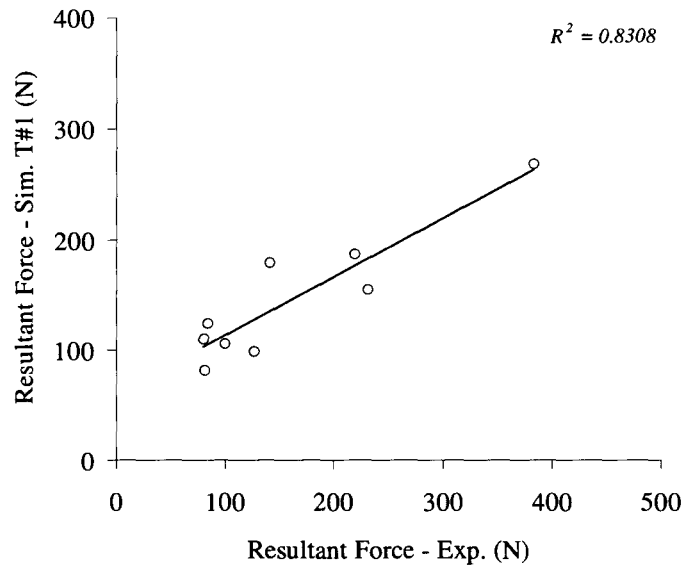


Figure 7.35 – Correlation between the resultant experimental cutting force and the simulated one (tooth # 1).

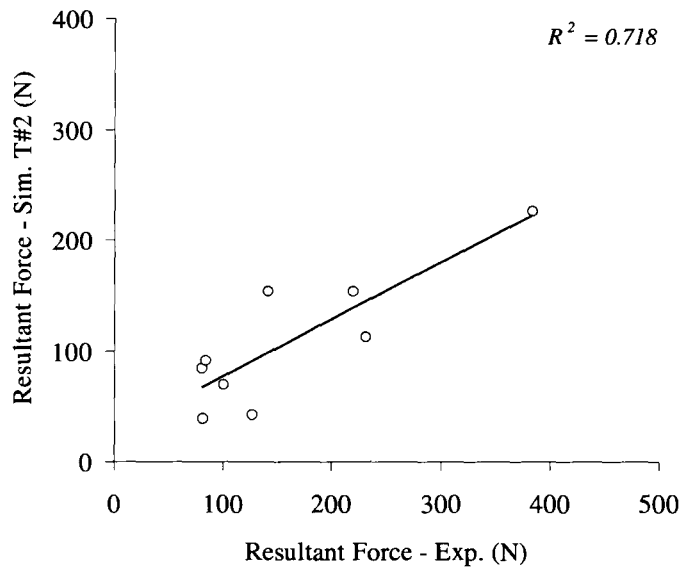


Figure 7.36 – Correlation between the resultant experimental cutting force and the simulated one (tooth # 2).

7.7.2 Analytical model

The analytical force model presented earlier in Section 5.3.2 was used in the simulation model instead of the mechanistic model to evaluate the simulated cutting forces and different system accelerations. In this model, the main inputs to be evaluated were φ_s , μ , and μ_c . The simulation starts by assuming an initial value of each of those variables and then they were varied until a match between the experimental and the simulated acceleration was reached. This was similar to the case when using the mechanistic model. This was repeated for all cutting tests while using setup # 1 and setup # 2.

The process was conducted for the cutting conditions summarized in Tables 6.3. At each cutting condition, some simulation variables were monitored to help examining and analyzing the analytical force model:

- The average temperature in the primary shearing area T_s
- The maximum temperature rise due to cutting T_m
- The specific horsepower due to shear u_s
- The specific horsepower due to friction u_f
- The specific horsepower due to the kinetic energy (momentum) u_m
- The total specific horsepower u
- The simulated cutting forces in all three directions X , Y and Z

Evaluated and monitored variables, except cutting forces, are summarized in Table 7.15. Cutting tests 1 - 4 are for the same cutting speed (565 m/min) of which tests 1 - 2 belong to the same radial depth of cut (0.4 mm), and tests 3 - 4 belong to another radial depth of cut (0.9 mm), the feed/tooth alternates between 0.03 mm and 0.08 mm (1 - 0.03, 2 - 0.08, and so on ...). Similarly, cutting tests 5 - 8 belong to a different cutting speed (1131 m/min) of which tests 5 - 6 belong to the same

radial depth of cut (0.4 mm, similar to tests 1 - 2), and tests 7 - 8 belong to another radial depth of cut (0.9 mm, similar to tests 3 - 4). It was noticed that for the same cutting speed and for the same radial depth of cut but for different feed/tooth the shear angle φ_s and the temperature increase while the friction on the rake face μ and on the helix angle's face μ_c were almost unchanged. This reflected an increased load (bigger feed/tooth, see tests 1 - 2 etc ... for example). Also, for the same cutting speed and for the same feed/tooth but for a different depth of cut the temperature and the shear angle also increased which also reflected in an increased load (bigger feed/tooth, see tests 1 - 2 etc... for example). For the same cutting speed the total specific horsepower u decreased which was believed to be because of the increase in temperature which led to material softening. Notice that the specific horsepower constant decreased due to shear u_s while the specific horsepower due to friction u_f was almost unchanged, also notice that μ and μ_c changed only slightly. The same behavior was noticed when the cutting speed changed from a low to a higher cutting speed (tests 1 - 4 to tests 5 - 8). In this case the specific horsepower due to friction u_f changed to a lower value other than that of the lower cutting speed because μ and μ_c had also decreased. At higher speeds, the build-up edge in front of the rake face disappeared minimizing the friction on the rake angle μ and on the helix face μ_c . This justified the decrease of μ and μ_c when the cutting force increased. Test 9 represented a mid point between the other set of tests, i.e. a mid point in the cutting speed, the radial depth of cut and the axial depth of cut. It was noticed that the evaluated and monitored variables were also mid way among those obtained from tests 1 - 8.

The cutting forces corresponding to each of those test cases are compared to those extracted from the simulation using the mechanistic model. Figures 7.37 and 7.38 compares the simulated cutting forces using the mechanistic model (model 1) and the orthogonal model (model 2) when using setup # 1 and setup # 2 for tooth

1 (T1) and tooth # 2 (T2) respectively. From these figures it was noticed that the cutting forces generated using the mechanistic model were in good agreement with those generated using the orthogonal model. Recall that these forces are all obtained using the same new proposed procedure that uses the fixture acceleration. This implied that regardless of the cutting force model used or the fixture set-up in place it became possible to obtain the same cutting forces. This result supports the effectiveness of the suggested calibration procedure.

Throughout this chapter several issues have been discussed which can affect the process of calibrating the proposed cutting force model with the experimental data while including the effect of the system dynamics during high speed machining. The FRF of the system of interest should be investigated to determine the number of modes that were used in the calibration process. It was recommended that the apparent number of modes be the minimum number of modes to start with the investigation. After reaching the right number of modes the calibration procedure can start taking into account the filtering of the acceleration data. A high order, zero shift, low pass filter was used to ensure minimal distortion in the data used. If cutting was conducted at high speed the cutting tool run-out must be included in the model. If run-out was not included in the model misleading conclusions might result.

The suggested estimation procedure was shown to be accurate and reliable regardless of the force model used as well as for the setup implemented. Similar results were obtained with and without a dynamometer. This makes the process of estimating the cutting force possible during high speed machining. The other advantage of using the suggested estimation procedure is that it is cost effective; the price of three accelerometers together was a fraction of the price of a dynamometer, let alone a dynamometer for high speed machining. The cabling system was much simpler for the case of the accelerometer because they have built in charge amps. In this way

only coaxial cables were needed to provide shielding instead of much more expensive and sensitive low impedance cables that are typically used for dynamometers.

In addition, using the suggested calibration procedure made focusing on the fixture design and the cutting mechanics during high speed machining much easier trying to overcome the dynamic limitations of the instrumentation. Also accelerometers are readily available in the market and have a much higher natural frequency and hence are less affected by the high forcing frequency coming from the machining process.

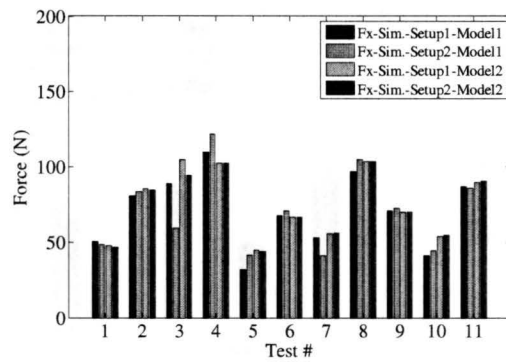
7.8 Conclusion

Chapter 7 deals with the analysis and experimental verification of the suggested SCF estimation procedure. First the methodology to test the new model was introduced. Then the model was investigated to test the effect of choosing the number of fitted modes on the estimated specific cutting forces, the effect of filtering the simulated acceleration and the effect of including the tool/tool holder run-out in the cutting force model while including the system dynamics. A set of cutting tests was used to predict key parameters for different force models using the outlined setup (setup # 1), which includes a dynamometer. The same approach was used to predict the same key parameters using setup # 2, which did not include a dynamometer. For a given force model the suggested estimation procedure succeeded in predicting the same key parameters using the two different setups. Moreover, comparing the magnitude of the cutting forces that resulted from using all four combinations, the estimation procedure succeeded in generating similar forces regardless of the system setup or the force model used. This evidence supports the claimed effectiveness and accuracy of the proposed procedure.

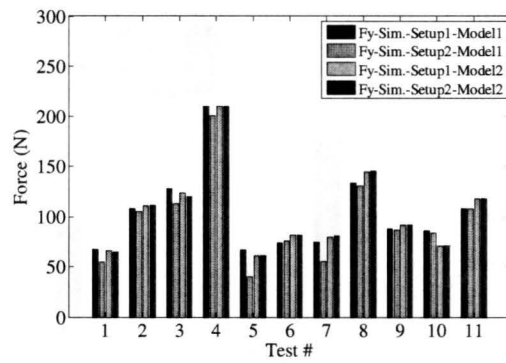
Table 7.15 – Analytical parameters calibrated using setup # 1

Case*	Test #	T_s (°C)	T_{max} (°)	ϕ (°)	μ	μ_c	u_s (hp/in/min)	u_f (hp/in/min)	u_m (hp/in/min)	u (hp/in/min)	u_s (%)	u_f (%)	u_m (%)
c	1	140	275	13.0	1.4	1.4	0.43455	0.15970	8.89E-05	0.594339	73.1	26.9	0.015
c	2	168	350	15.0	1.3	1.4	0.37296	0.15361	8.99E-05	0.526660	70.8	29.2	0.017
c	3	165	305	18.0	1.5	1.5	0.30996	0.16000	9.19E-05	0.470052	65.9	34.0	0.020
c	4	140	380	19.5	1.4	1.4	0.28592	0.15592	9.31E-05	0.441933	64.7	35.3	0.021
c	5	152	320	16.0	1.3	1.3	0.34983	0.15344	3.38E-04	0.503608	69.5	30.5	0.067
c	6	155	380	22.0	1.0	0.9	0.25537	0.13580	3.56E-04	0.391526	65.2	34.7	0.091
c	7	169	287	19.2	0.7	0.8	0.29109	0.11021	3.47E-04	0.401647	72.5	27.4	0.086
c	8	175	370	24.0	0.7	0.8	0.23587	0.11045	3.64E-04	0.346684	68.0	31.9	0.105
c	9	156	390	22.0	0.9	1.0	0.25528	0.12844	2.05E-04	0.383925	66.5	33.5	0.053

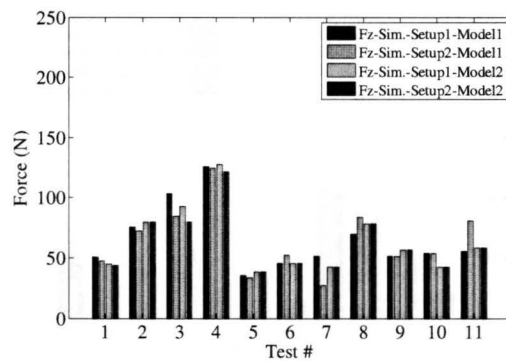
*c = calibration.



a. F_x .

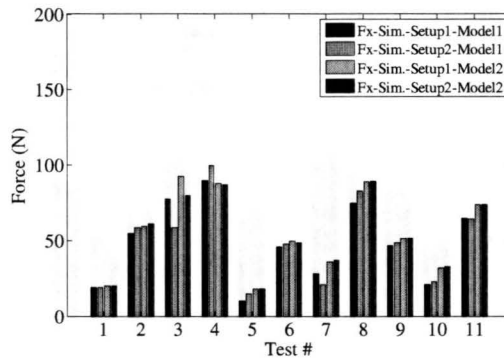


b. F_y .

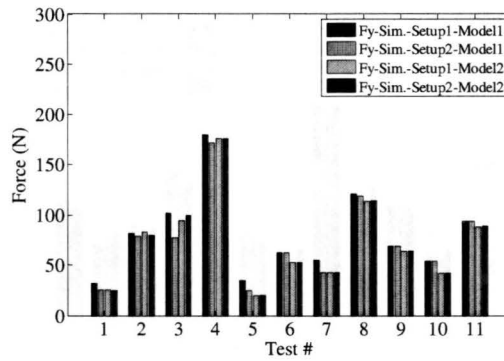


c. F_z .

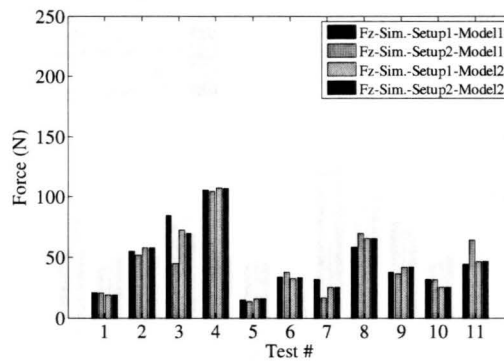
Figure 7.37 – Comparison between the cutting forces’s magnitude generated using different setups and different force models on tooth # 1 in all three directions X , Y , and Z .



a. F_x .



b. F_y .



c. F_z .

Figure 7.38 – Comparison between the forces generated using different setups and different force models on tooth # 2 in all three directions X , Y , and Z .

CHAPTER 8

SUMMARY & FUTURE WORK

8.1 Summary

In HSM, high frequency dynamics was one of the challenges associated with estimating the SCF or measuring the cutting forces. Cutting force measurements obtained from a dynamometer are reliable up to their natural frequency but beyond that value the data has to be modified to account for the dynamics of the dynamometer itself, i.e. account for the system FRF of the dynamometer. This problem also has a direct effect on the SCF estimation.

To overcome this problem, a new technique was introduced in this dissertation to better assess the SCF as well as the cutting forces in HSM. The technique uses the acceleration of the fixture that holds the workpiece being machined.

The suggested technique makes use of the FRF (receptance) of the fixture which is then transformed to the time domain using the Inverse Laplace Transform. The resulting FRF is then integrated with the cutting force model that was originally developed by Tlustý [6], using the convolution theorem, to estimate the displacement of the system. This value was differentiated twice to obtain the acceleration of the system. The simulated acceleration was then compared against the experimental one to assess the effectiveness of this approach.

To implement and investigate the new technique a few challenges were faced that have led to improvements in other areas. The need to establish the FRF of the fixture meant that it needed to be regenerated in numerical form so that it can be used in the suggested estimation technique. Hence an improved technique for modal parameters estimation was developed. This technique was based on the RFP model originally developed by Richardson [5] however it has been improved using a constraint optimization technique. The original RFP model does not necessarily estimate the modal parameters leading to a stable system. Hence, an improved constraint optimization technique was used to ensure that the real part of the poles of the system are always negative. In the improved technique the natural frequency of the pole and its imaginary part, can be pre-defined before the optimization takes place. This is done to match the experimental values, which provides this technique with a much higher degree of flexibility when estimating the modal parameters of the system. In the optimization process an objective function has to be defined. Several objective functions were tested; absolute mean error, maximum error, mean percentage error, maximum percentage error and least square error. The mean error, maximum error and mean percentage error converged giving a solution while the maximum percentage error and the least square error did not converge at all. Thus the mean error was used to test for convergence as it gave better results.

The RFP model was used to define the FRF in the frequency domain. To be able to use it in the time domain it needed to be transformed using the Inverse Laplace Transform. A form that is readily available in the time domain does not exist so one was derived specially for this purpose. Then the RFP model was integrated in the cutting force model using the convolution theorem to obtain the system response. The displacement of the system was then differentiated twice to obtain the acceleration which in turn was compared to the experimental one.

Before verifying the suggested estimation procedure it needed to be tested and investigated. First, the model was investigated to test the effect of choosing the number of fitted modes on the estimated SCF. Depending on the system FRF used, it was found that the value of the estimated SCF varied inversely with the number of fitted modes until it reached an asymptote. The corresponding number of modes becomes the optimum number of modes to be used in the simulation model.

To obtain the acceleration from the simulated system response, this output needed to be differentiated twice. This can result in large values when the displacement signal contains noise. This in turn leads to unnecessary high frequency noise values being superimposed over the acceleration signal. To overcome such problem, the simulated acceleration was filtered using a high-order, low-pass Butterworth filter with zero phase shift, at a reasonable cutoff frequency. This helped to substantially reduce the high frequency noise existing in the simulated acceleration signal and hence the process of estimation of the SCF was easier.

Finally the effect of the tool/tool holder run-out had to be studied since the model was used for HSM where high rotational speeds are present. The centrifugal force was estimated and then was decomposed into the main coordinate axes X , Y and Z . Investigation has led to the conclusion that it is necessary to include the effect of the tool/tool holder run-out, especially at higher RPM, otherwise the estimation

of the SCF was found to be unreliable.

To verify the new model two setups were prepared; the first one, setup # 1, with the workpiece fixture mounted on top of a dynamometer and the second one, setup # 2, with the workpiece fixture mounted on top of an aluminum block. It should be noted that the dynamometer was not present in setup # 2. A set of experiments specially designed for this purpose was conducted using both setups. The SCF were estimated for a calibration set, using setup # 1, which was used when fitting a non-linear equation. Another set was used to verify the fitted equation. The relative difference between the experimental and the fitted data was on average $\sim 10\%$. The same procedure was repeated for setup # 2 and the relative difference between the experimental and the fitted data was found to be on average $\sim 12\%$. In addition, an attempt was made to regenerate the experimental force by assuming that the dynamometer, with the fixture on top of it to be represented by a single-degree of freedom system. This was possible using a mass that was chosen to be close to that of the fixture and the top plate of the dynamometer in one direction but not in the other directions.

A high degree of agreement was found between the experimental cutting forces and those generated using the model. It should be noted that the simulation forces estimated at the fixture were different than those regenerated in terms of magnitude and frequency. A high degree of correlation was found to exist between the resultant simulation forces at the fixture and the resultant experimental cutting forces. No direct connection could be established between the simulation forces obtained using setup # 2 at the fixture and the experimental force obtained using setup # 1 since there was no dynamometer included in setup # 2, however an indirect relation can be made by comparing the magnitude of the simulated cutting forces and the calibrated SCF. In this case good agreement was found between the simulated cutting forces and

the SCF using setup # 1 and setup # 2. This confirms that the SCF were independent of the system dynamics and that the suggested SCF estimation procedure was reliable since it was able to replicate the same simulated cutting forces and the SCF for a different setup using the same technique.

Another type of cutting force model was implemented instead of the mechanistic model that was used in the previous investigation; namely an analytical force model. Instead of obtaining the cutting forces using a mechanistic model and calibrating the SCF an analytical model was used. In the analytical model the conventional cutting forces were estimated using Merchant's analytical model [7]. Since there was a big difference in the cutting velocities considering the effect of material softening due to elevated temperatures was taken into account through the use of the Johnson-Cook equation.

It was then possible to make that model function with three main parameters ϕ , μ and μ_c . For each cutting test, the values of these parameters were obtained by starting with an initial value which was then changed until a match occurred between the simulated and measured acceleration. For both setups, # 1 and # 2, it was possible to obtain similar values of the three parameters in addition to the magnitude of the cutting forces. Furthermore the magnitude of the cutting forces that was obtained using the analytical model was found to be in agreement with the one obtained using the mechanistic model. Based on this result the proposed SCF estimation procedure was deemed effective regardless of the cutting force model used in the analysis.

8.2 Future Work

In the light of the different issues that have been discussed throughout this dissertation, the following are recommended as areas for future research work:

- The acceleration was used to estimate the SCF due to the wide availability and ease of use of accelerometers. Displacement transducers can also be used instead of accelerometers to capture the displacement of the fixture and hence obtain the FRF (receptance) of the system directly in each of the main directions X , Y and Z . Normally the receptance of the system is obtain by integrating the accelerance in the frequency domain (i.e. dividing the accelerance by $-\omega^2$ to obtain the receptance).
- The SCF can be estimated using the acceleration as in the suggested dynamic model at conventional cutting speeds and then compared against the SCF estimated using a conventional dynamometer. At conventional cutting speeds the effect of the system dynamics are minimal and can be ignored.
- The dynamics of the top plate of the dynamometer can also be included in the investigation in order to improve the cutting force model.
- The new SCF estimation procedure can be further developed to produce an instrument to measure the cutting force especially for HSM applications. Such instrument, should the attempt be successful, will be cost effective as a typical dynamometer for HSM application costs $\sim \$10000$ and replacing it with only three generic accelerometers of $\sim \$400$ each forms a saving of almost $\sim 88\%$.

APPENDICES

APPENDIX A

DERIVATIONS

A.1 Temperature Dependent Material's Density

The volumetric thermal expansion is expressed using Equation A.1 obtained from [98].

$$V = V_0(1 + \beta\Delta T) \quad (\text{A.1})$$

β is the coefficient of volumetric thermal expansion which is a well know material property. The material density is given by Equation A.2.

$$\rho = \frac{m}{V} \quad (\text{A.2})$$

Substituting Equation A.1 in Equation A.2 yields

$$\rho = \frac{m}{V_o(1 + \beta\Delta T)} \quad (\text{A.3})$$

$$= \frac{\rho_o}{(1 + \beta\Delta T)} \quad (\text{A.4})$$

At room temperature the reference material density ρ_o is given by Equation A.5.

$$\rho_o = \frac{m}{V_o} \quad (\text{A.5})$$

Rearranging Equation A.3 yields

$$\rho(T) = \frac{\rho_o}{(1 + \beta\Delta T)} \quad (\text{A.6})$$

A.2 Derivation of the RFP Model in Time Domain

The frequency response function (FRF) is expressed as in Equation A.7.

$$h(\omega) = \frac{x(\omega)}{F(\omega)} \quad (\text{A.7})$$

$$= \frac{A}{j\omega - \sigma} + \frac{A^*}{j\omega - \sigma^*} \quad (\text{A.8})$$

Let

$$A = a + bi \quad (\text{A.9})$$

$$A^* = a - bi \quad (\text{A.10})$$

$$\sigma = c + di \quad (\text{A.11})$$

$$\sigma^* = c - di \quad (\text{A.12})$$

Substituting Equations A.9 - A.12 into Equation A.7 gives

$$h(\omega) = \frac{(a + bi)}{s - (c + di)} + \frac{(a - bi)}{s - (c - di)} \quad (\text{A.13})$$

Rearranging Equation A.13 yields

$$h(\omega) = \frac{(a + bi)}{s + (-c - di)} + \frac{(a - bi)}{s + (-c + di)} \quad (\text{A.14})$$

Recall that

$$\mathcal{L}^{-1}\left(\frac{1}{s + \alpha}\right) = e^{-\alpha t} \cdot u(t) \quad (\text{A.15})$$

To obtain the FRF in time domain the inverse Laplace transform operator \mathcal{L}^{-1} is applied to Equation A.14 giving

$$h(t) = \mathcal{L}^{-1}\left(\frac{(a + bi)}{s + (-c - di)} + \frac{(a - bi)}{s + (-c + di)}\right) \quad (\text{A.16})$$

$$h(t) = a \cdot e^{-(c-d \cdot i)t} + b \cdot i \cdot e^{-(c-d \cdot i)t} + c \cdot e^{-(c+d \cdot i)t} - di e^{-(c+d \cdot i)t} \quad (\text{A.17})$$

$$= a \cdot e^{(c+i \cdot d)t} + b \cdot i \cdot e^{(c+i \cdot d)t} + ce^{(c-i \cdot d)t} - d \cdot i \cdot e^{(c-i \cdot d)t} \quad (\text{A.18})$$

$$= a \cdot e^{c \cdot t} e^{i \cdot d \cdot t} + bie^{c \cdot t} e^{i \cdot d \cdot t} + ae^{c \cdot t} e^{-i \cdot d \cdot t} - b \cdot i \cdot e^{c \cdot t} e^{-i \cdot d \cdot t} \quad (\text{A.19})$$

$$= a \cdot e^{c \cdot t} [e^{i \cdot d \cdot t} + e^{-i \cdot d \cdot t}] + b \cdot i \cdot e^{c \cdot t} [e^{i \cdot d \cdot t} - e^{-i \cdot d \cdot t}] \quad (\text{A.20})$$

Rearranging Equation A.20 yields

$$h(t) = 2e^{ct}(a \cos(d \cdot t) - b \sin(d \cdot t)) \quad (\text{A.21})$$

It should be noted that a, b, c, and d are the real and imaginary parts of the FRF's poles and residues respectively. Once these are determined, it becomes relatively easy to determine the response of the system in the time domain using the convolution theorem.

Equation A.21 is for a single mode. For multi-modes it becomes the summation of the displacement of all relevant modes in the system as given by Equation A.22.

$$h(t) = \sum_{r=1}^N \left(2e^{c_r t} (a_r \cos(w_r \cdot t) - b_r \times \sin(w_r \cdot t)) \right) \quad (\text{A.22})$$

APPENDIX B

UNBALANCE MASS ESTIMATION

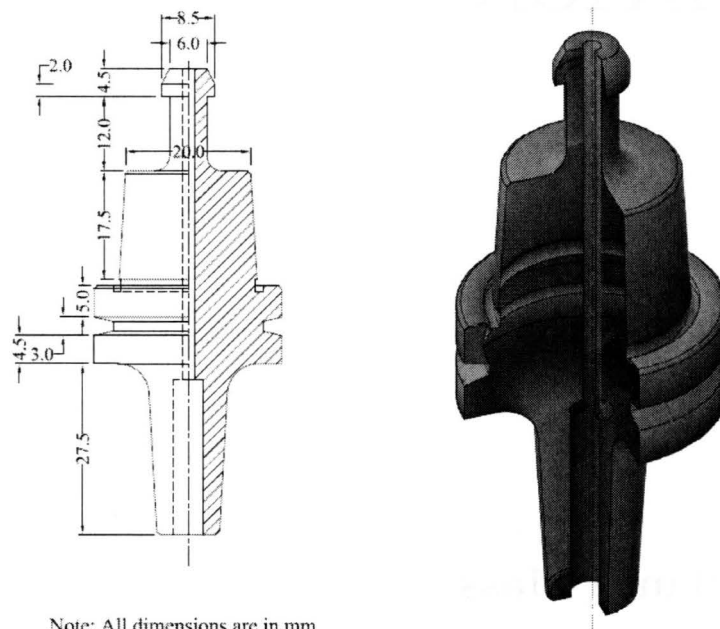
B.1 Unbalance Mass

The process of estimating the unbalanced mass of the cutting tool holder involved several stages:

1. Lift dimensions of the actual cutting tool holder from the part, Figure B.1a.
2. Construct a CAD model for the cutting tool holder, Figure B.1b.
3. Estimate the density of the cutting tool holder by calculating the volume of the cutting tool holder using the command MASSPROP in AutoCad and measuring the mass of the tool holder.
4. Then generating a copy of the CAD model and move it by an amount equivalent

to the run-out distance.

5. Subtract the moved model from the original.
6. Using the command MASSPROP in AutoCad estimate the volume of the remaining material and find its center of gravity. Knowing the density of the material calculate the unbalanced mass. The center of gravity obtained in the radial direction is used as the radius of the unbalanced mass.



Note: All dimensions are in mm

a. Lifted dimensions.

b. CAD model.

Figure B.1 – Regenerating a CAD model of the cutting tool's holder using actual dimensions.

Applying the stages explained above the unbalance mass and its center of gravity expressed from the center of rotation were found to be 0.036 gm and 4.93 mm respectively.

APPENDIX C

PROPERTIES OF TEST MATERIAL

C.1 Tensile Test

A tensile test was conducted to obtain the values of the constants A , B , and n of Equations 5.29 and 5.30. The values were estimated using a curve fitting approach on the portion of the tensile test data after the yield point. The tensile test data and the fitted curve are both illustrated in Figure C.1.

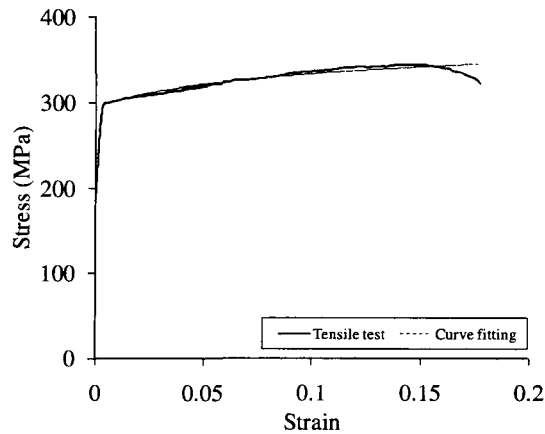


Figure C.1 – Curve fitting tensile test data to obtain the constants A , B , and n of Equations 5.29 and 5.30.

C.2 Specific Heat Capacity C_p

Specific heat capacity for Aluminum 6061-T6 at different temperatures was obtained from [90] and is summarized in Table C.1.

Table C.1 – Specific heat capacity of Aluminum 6061-T6 varying with temperature as obtained from [90]

Temperature (K)	C_p ($J/kg - ^\circ C$)
200	790.5
250	855.4
298	897.0
350	930.6
400	955.5
500	994.8
600	1034

Data illustrated in Figure C.2 was found to be varying logarithmically. Hence a logarithmic equation was fitted to the data with a correlation coefficient R^2 of 0.9913 yielding to

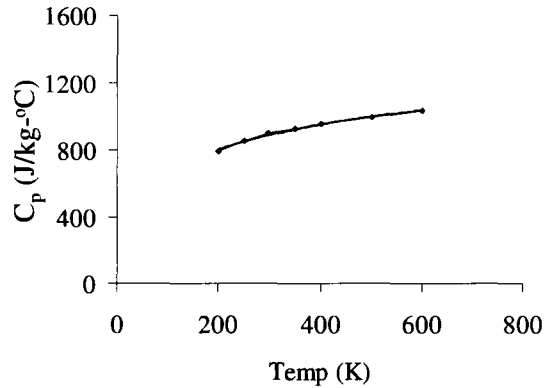


Figure C.2 – Specific heat variation with temperature for Aluminum 6061-T6.

$$C_p(T) = 215.01 \ln(T) - 336.11 \quad (\text{C.1})$$

C.3 Thermal Conductivity K

The thermal conductivity for Aluminum 6061-T6 at different temperatures was obtained from [90] and is summarized in Table C.2.

Table C.2 – Thermal conductivity of Aluminum 6061-T6 varying with temperature as obtained from [90]

Temperature (K)	K
(K)	($W/m - K$)
100	302
150	248
200	237
250	235
300	237
350	240
400	240
500	236

Data illustrated in Figure C.3 can be represented using a polynomial equation. A polynomial equation was fitted to the data with a correlation coefficient R^2 of 0.9934 yielding Equation C.2.

$$K(T) = 3 \times 10^{-8}T^4 - 4 \times 10^{-5}T^3 + 0.0224T^2 - 4.73T + 591.9 \quad (\text{C.2})$$

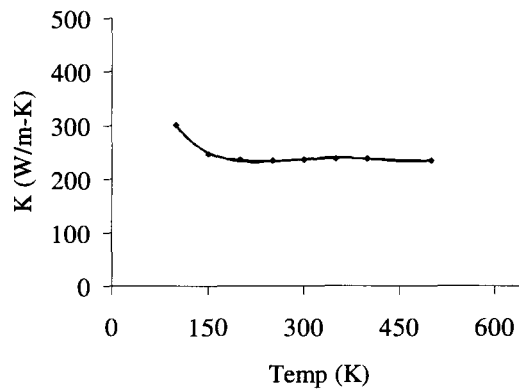


Figure C.3 – Thermal conductivity variation with temperature for Aluminum 6061-T6.

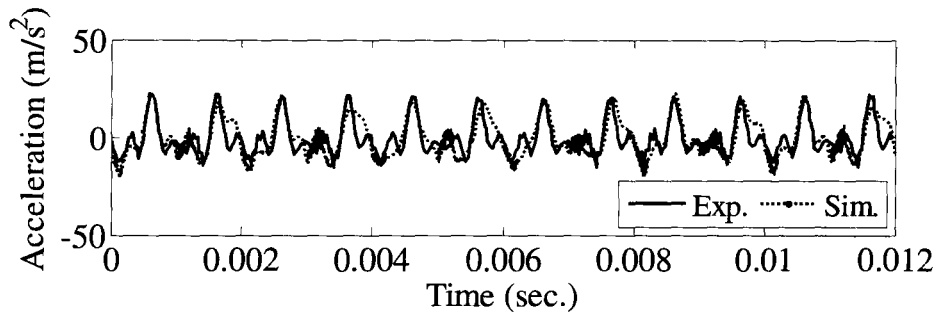
APPENDIX D

CUTTING TEST RESULTS

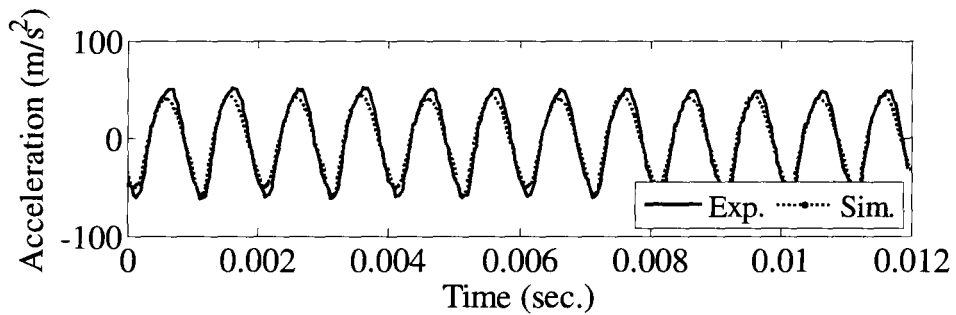
D.1 Introduction

In Sections D.2 and D.3, the simulated acceleration of the fixture is plotted versus the experimental one for both setups, setup # 1 and setup # 2 respectively, in the three directions X , Y , and Z .

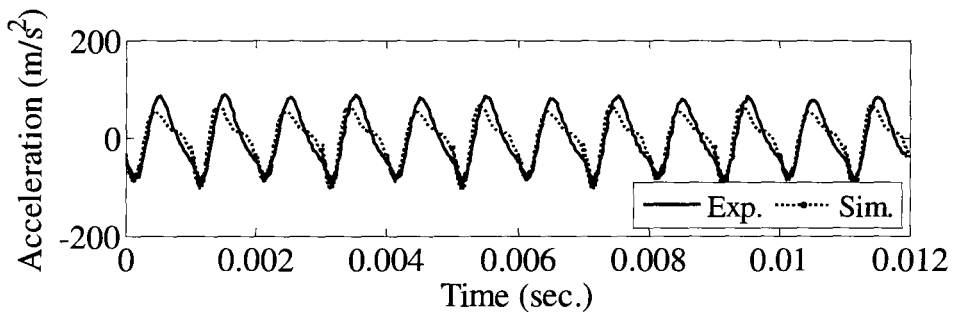
D.2 Fixture's Acceleration using Setup # 1



a. X-direction.

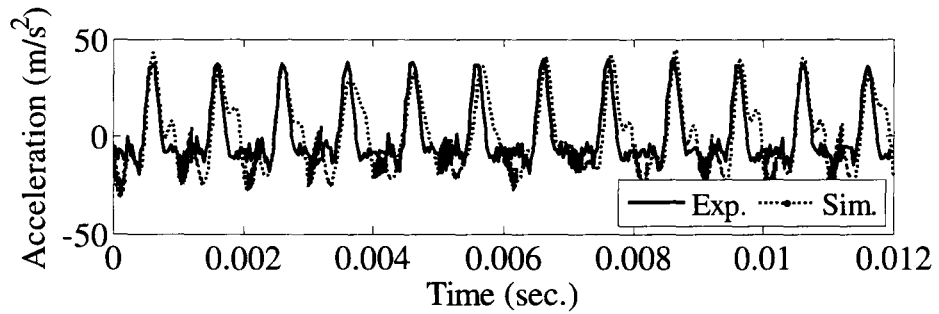


b. Y-direction.

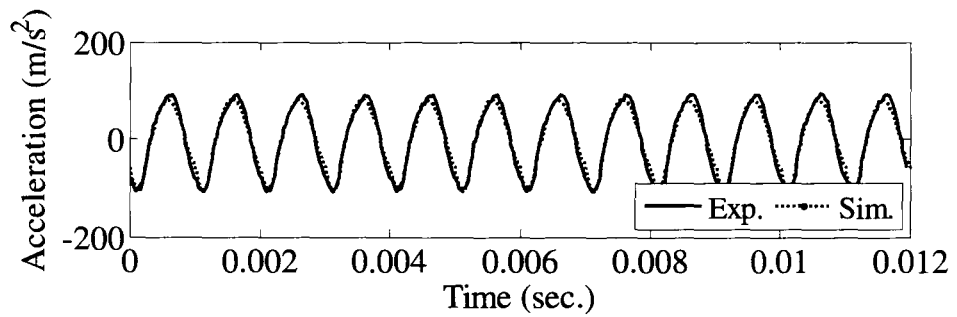


c. Z-direction.

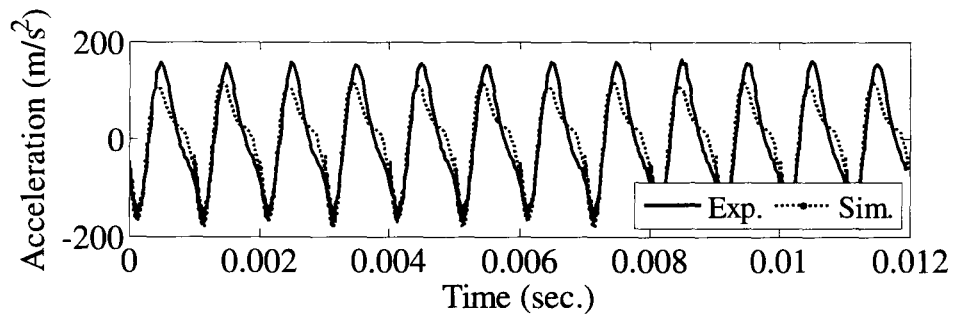
Figure D.1 – Fixture's acceleration using setup # 1 - calibration test # 1.



a. X-direction.

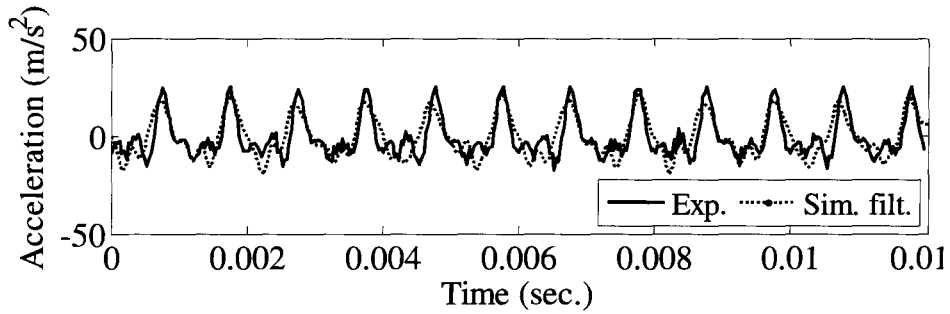


b. Y-direction.

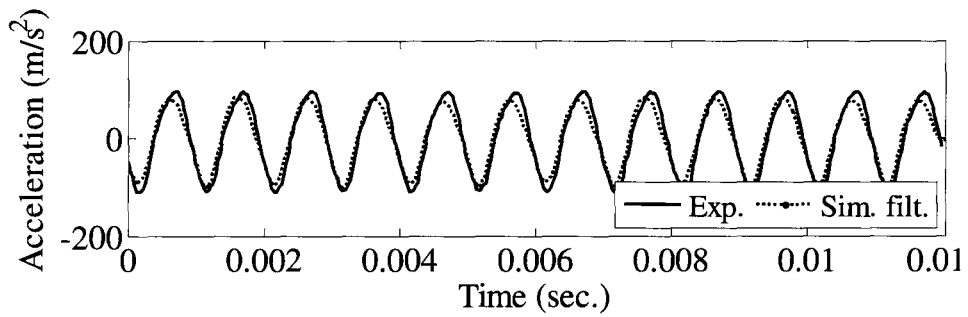


c. Z-direction.

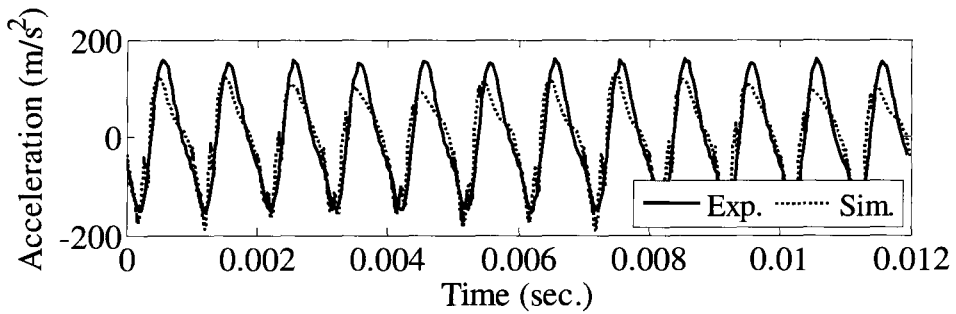
Figure D.2 – Fixture’s acceleration using setup # 1 - calibration test # 2.



a. X-direction.

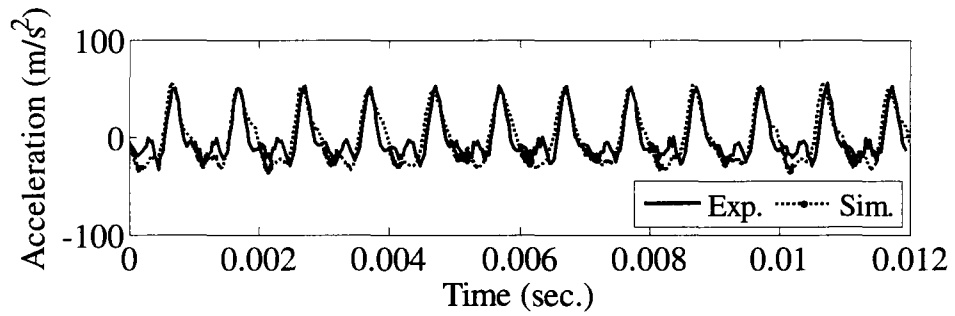


b. Y-direction.

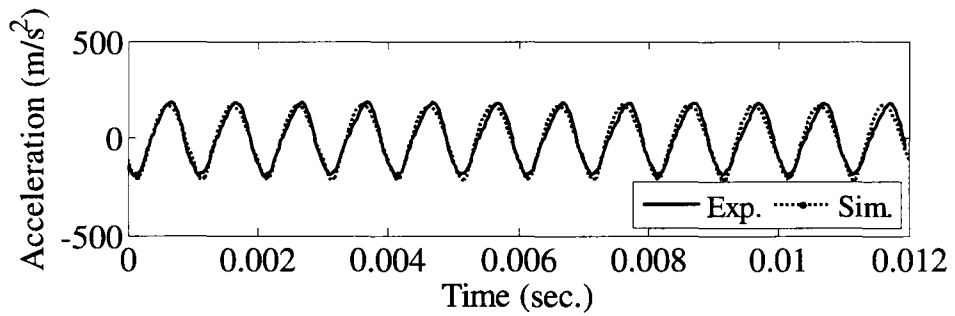


c. Z-direction.

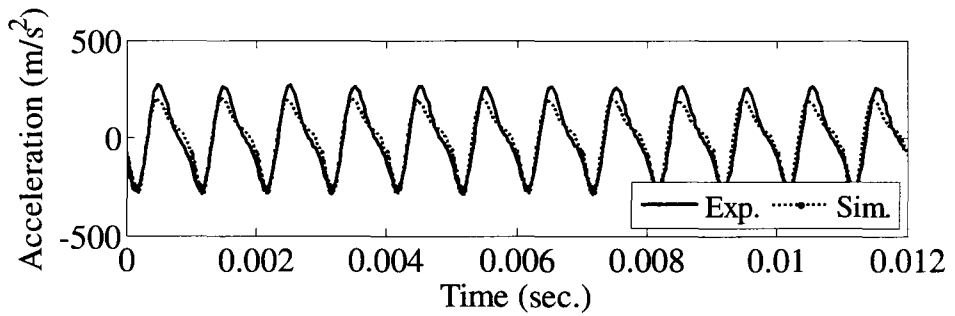
Figure D.3 – Fixture’s acceleration using setup # 1 - calibration test # 3.



a. X-direction.

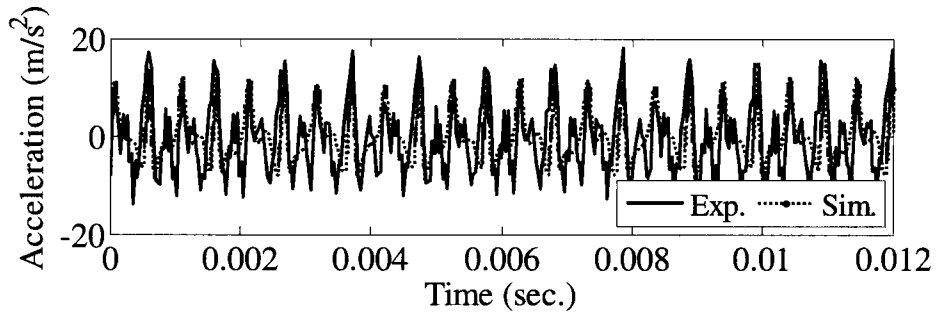


b. Y-direction.

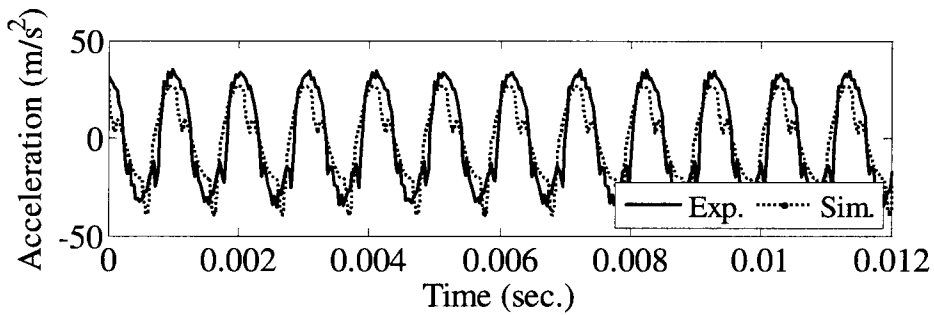


c. Z-direction.

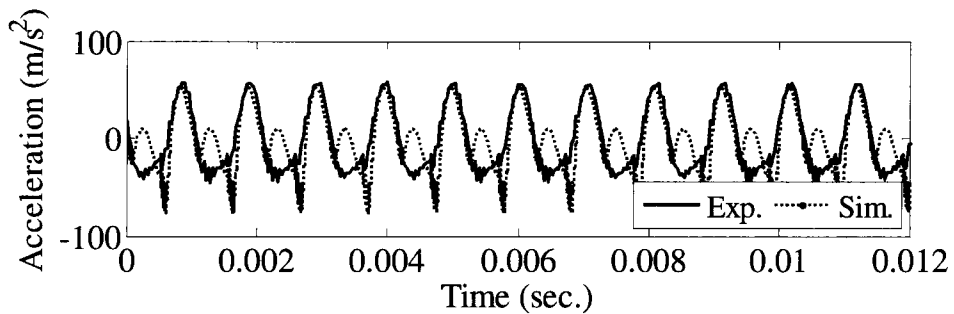
Figure D.4 – Fixture’s acceleration using setup # 1 - calibration test # 4.



a. X-direction.

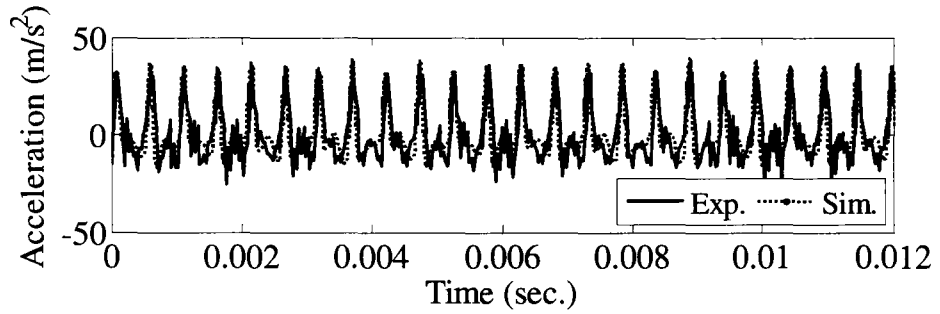


b. Y-direction.

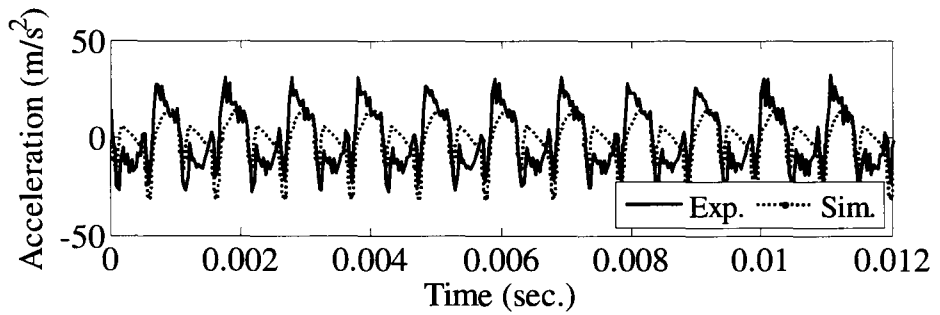


c. Z-direction.

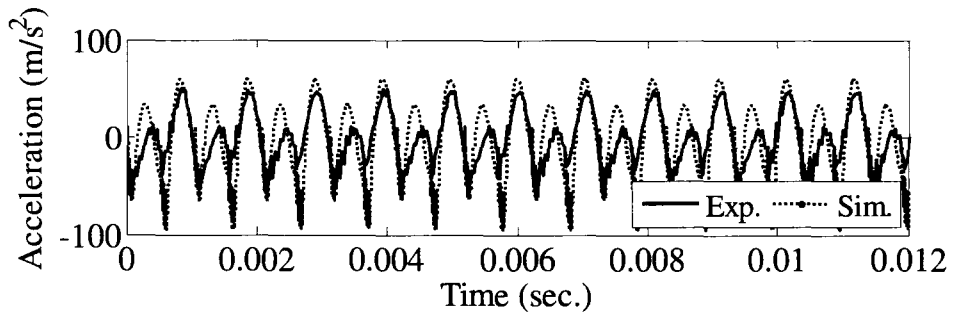
Figure D.5 – Fixture’s acceleration using setup # 1 - calibration test # 5.



a. X-direction.

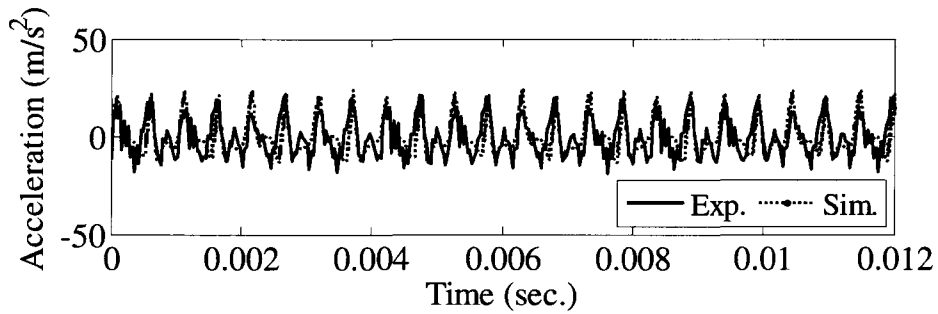


b. Y-direction.

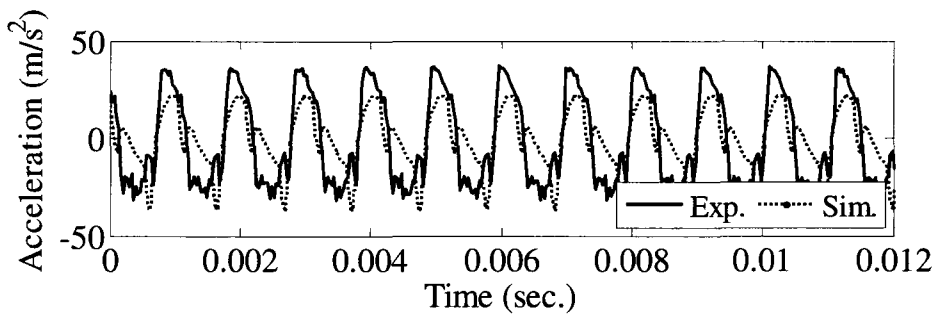


c. Z-direction.

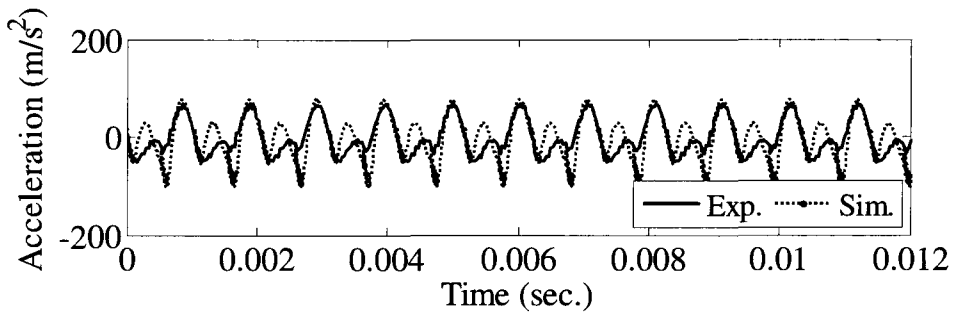
Figure D.6 – Fixture’s acceleration using setup # 1 - calibration test # 6.



a. X-direction.

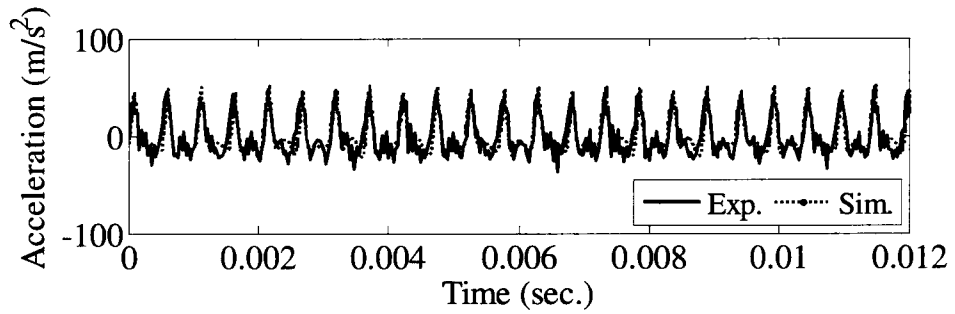


b. Y-direction.

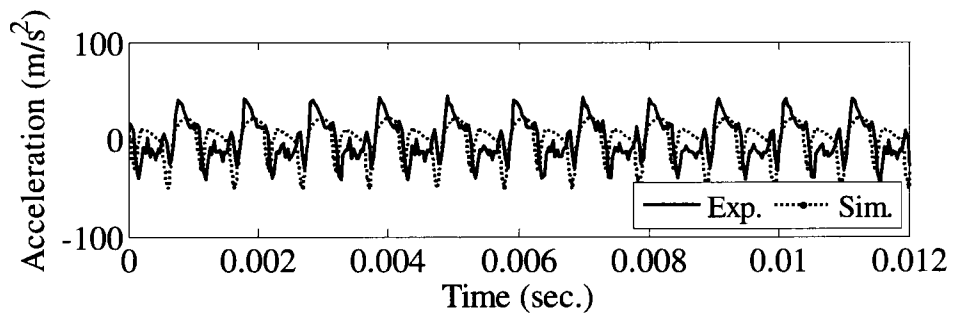


c. Z-direction.

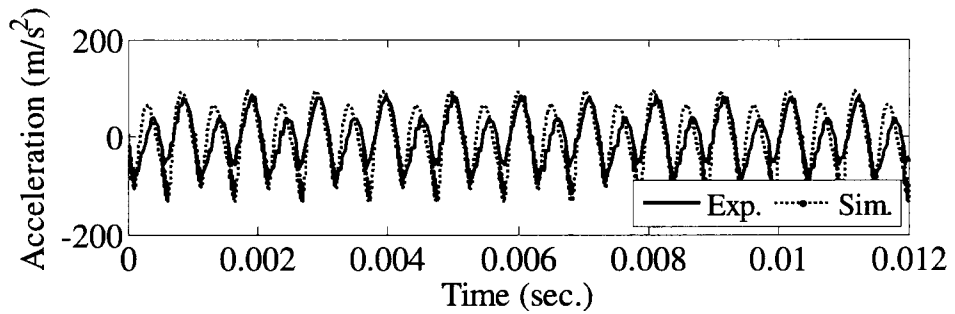
Figure D.7 – Fixture’s acceleration using setup # 1 - calibration test # 7.



a. X-direction.

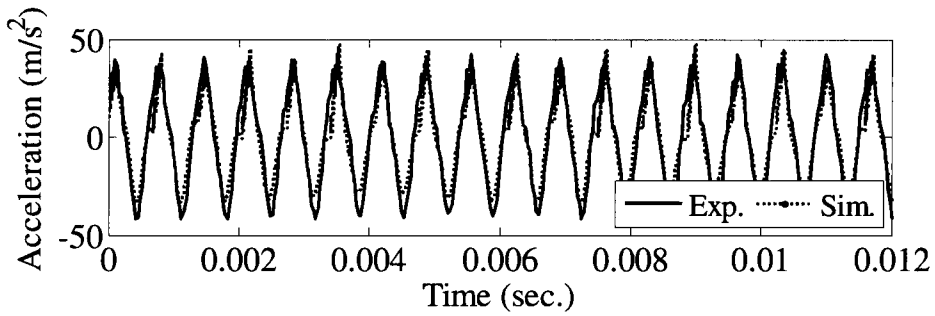


b. Y-direction.

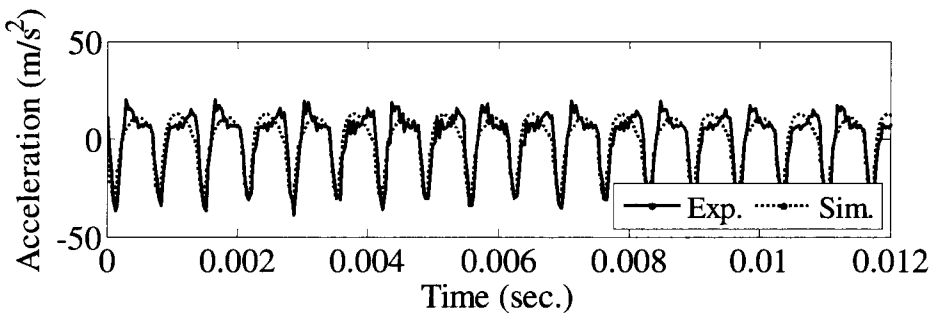


c. Z-direction.

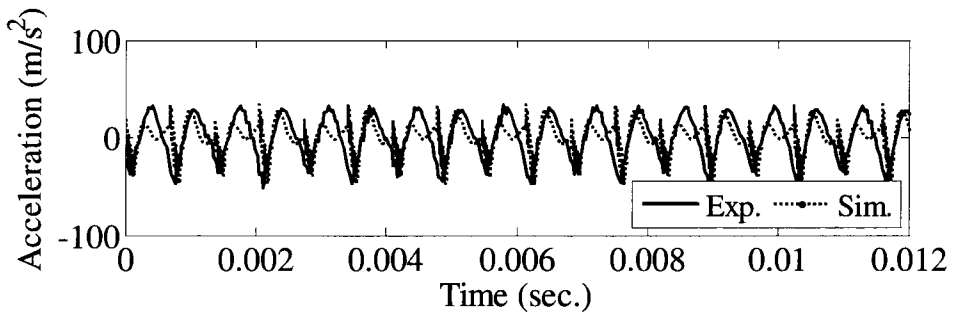
Figure D.8 – Fixture’s acceleration using setup # 1 - calibration test # 8.



a. X-direction.

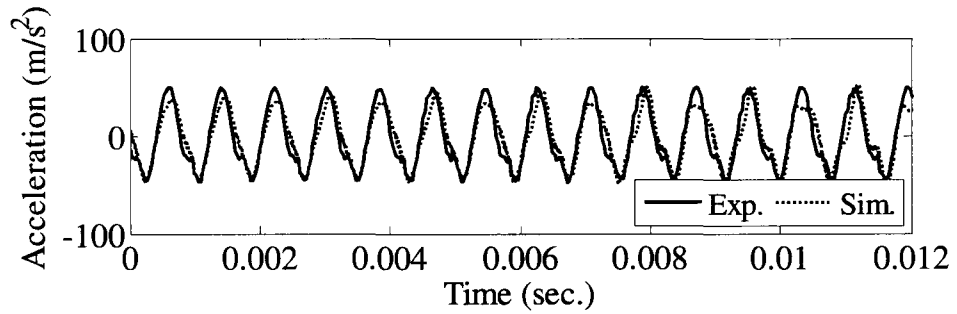


b. Y-direction.

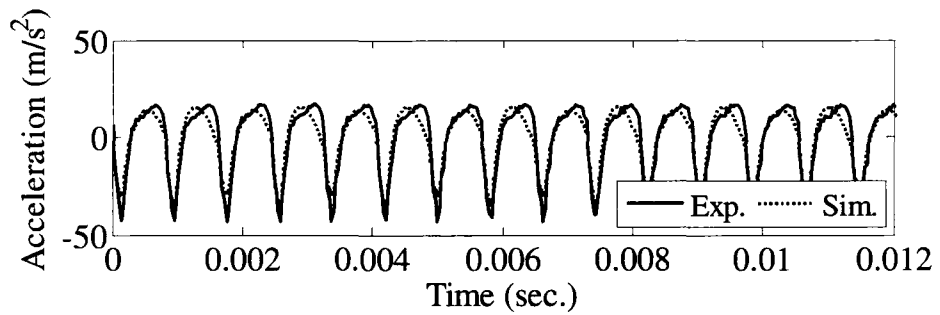


c. Z-direction.

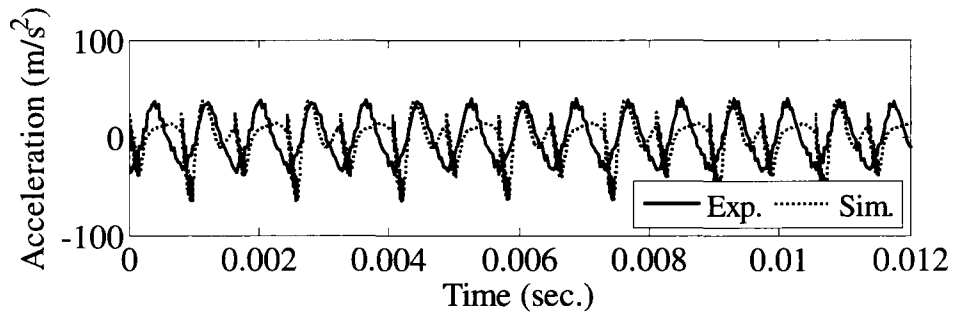
Figure D.9 – Fixture’s acceleration using setup # 1 - calibration test # 9.



a. X-direction.

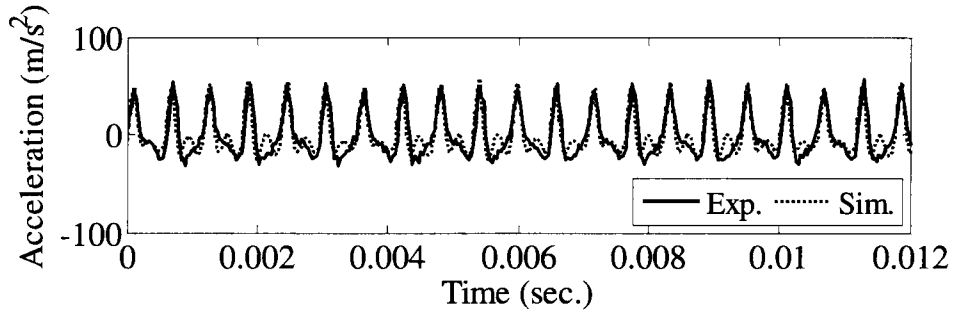


b. Y-direction.

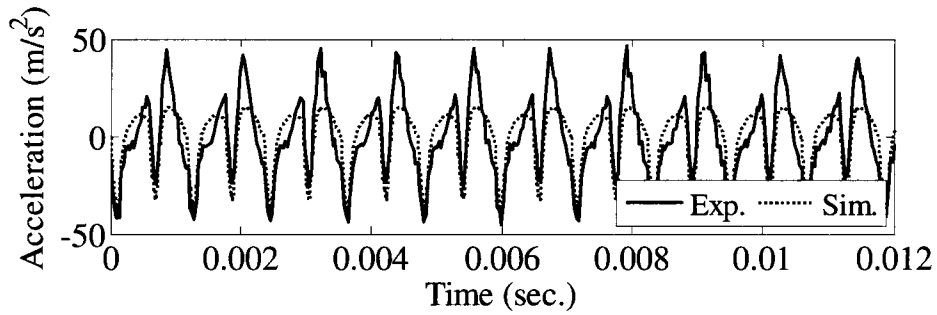


c. Z-direction.

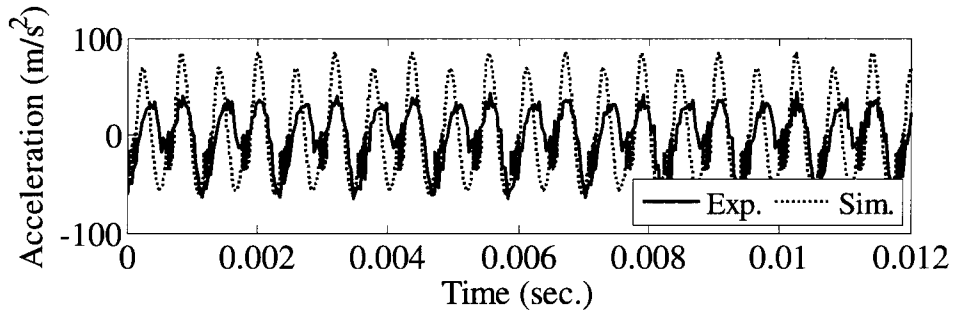
Figure D.10 – Fixture’s acceleration using setup # 1 - verification test # 1.



a. X-direction.

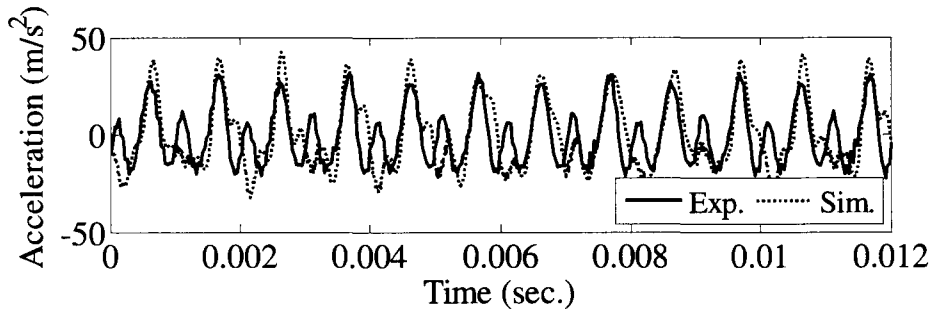


b. Y-direction.

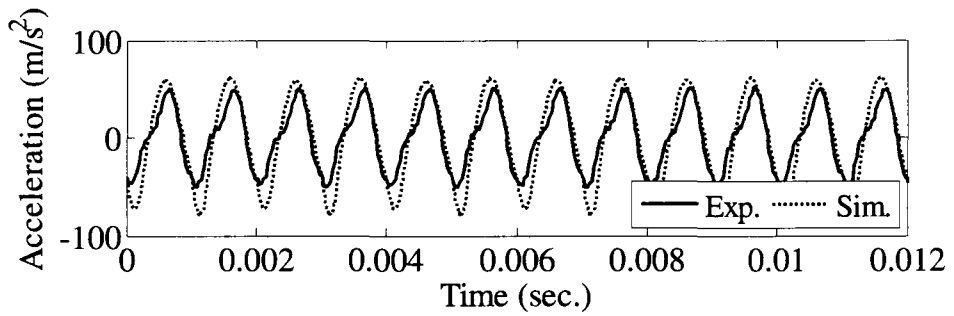


c. Z-direction.

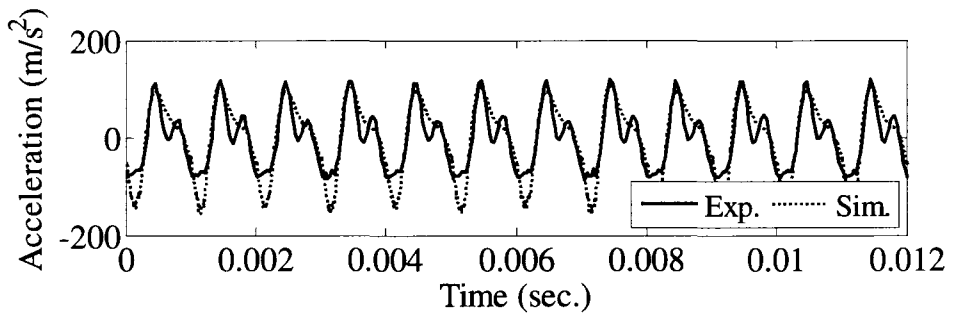
Figure D.11 – Fixture’s acceleration using setup # 1 - verification test # 2.



a. X-direction.

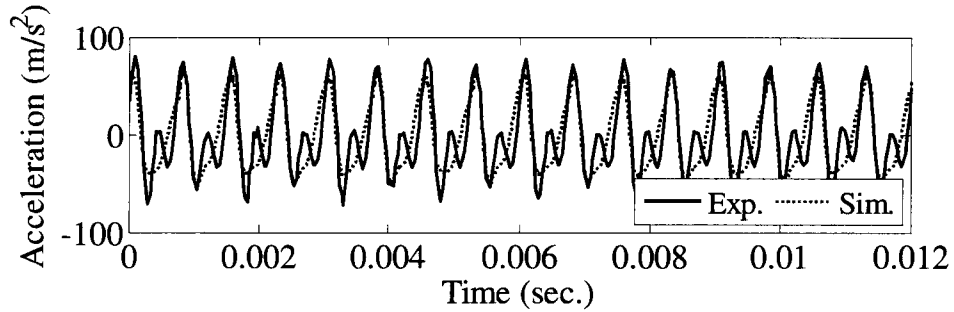


b. Y-direction.

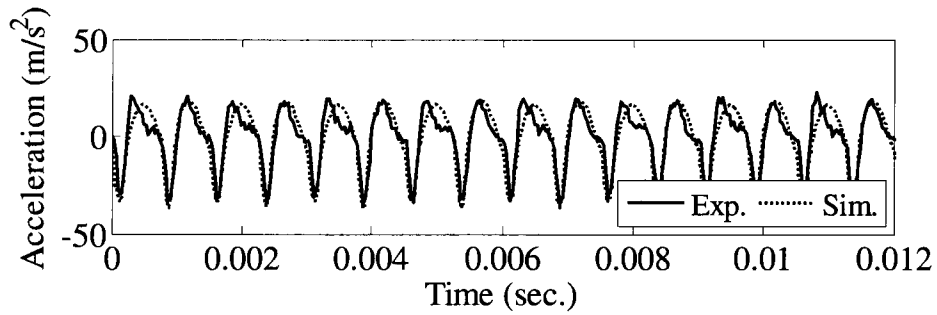


c. Z-direction.

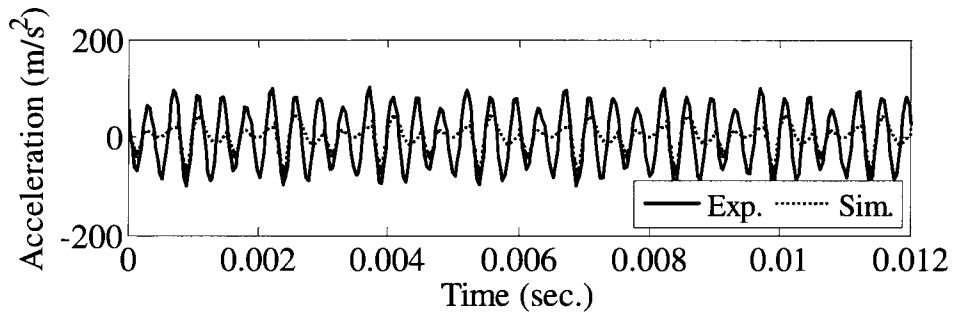
Figure D.12 – Fixture’s acceleration using setup # 1 - verification test # 3.



a. X-direction.

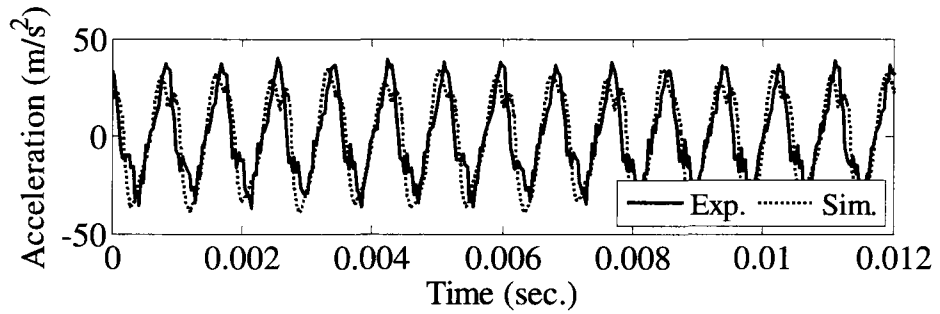


b. Y-direction.

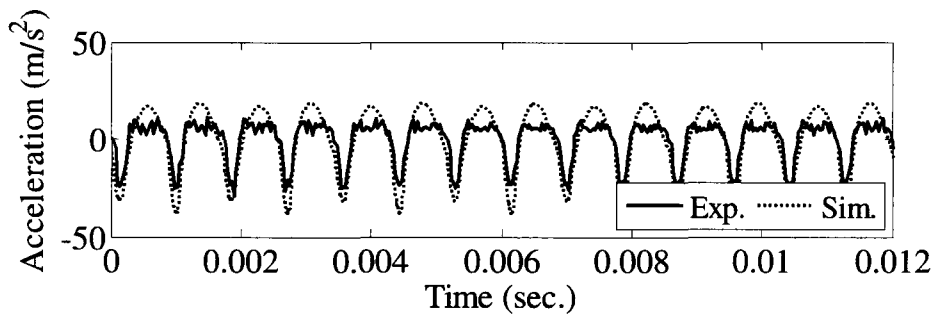


c. Z-direction.

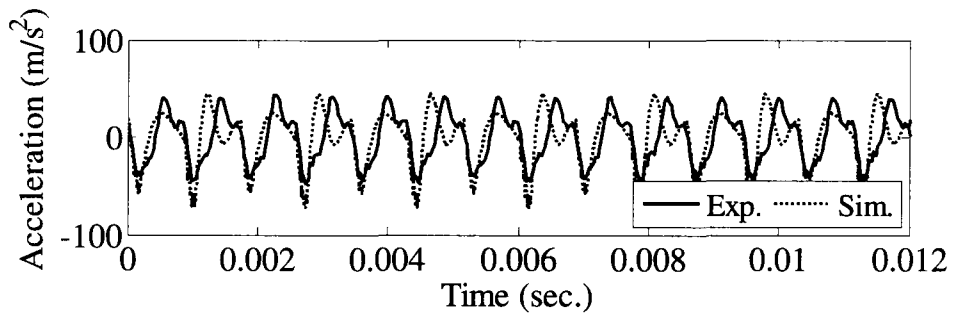
Figure D.13 – Fixture’s acceleration using setup # 1 - verification test # 4.



a. X-direction.

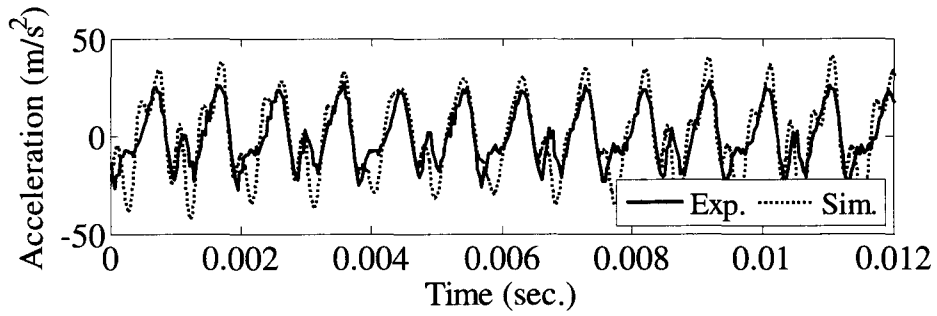


b. Y-direction.

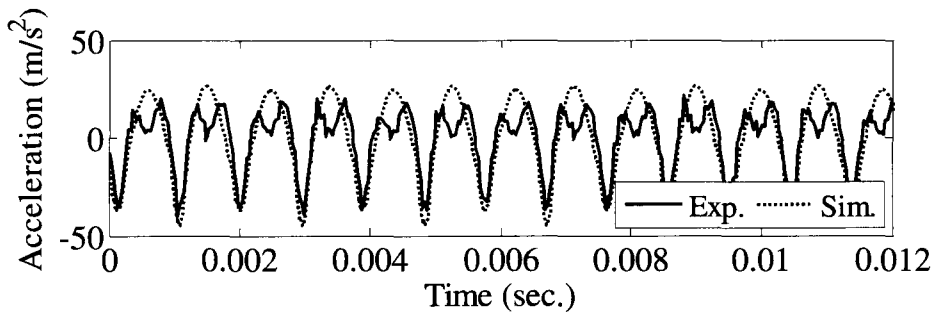


c. Z-direction.

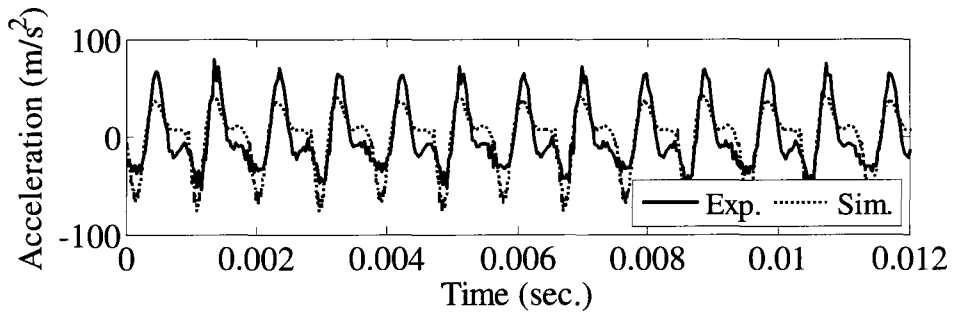
Figure D.14 – Fixture’s acceleration using setup # 1 - verification test # 5.



a. X-direction.

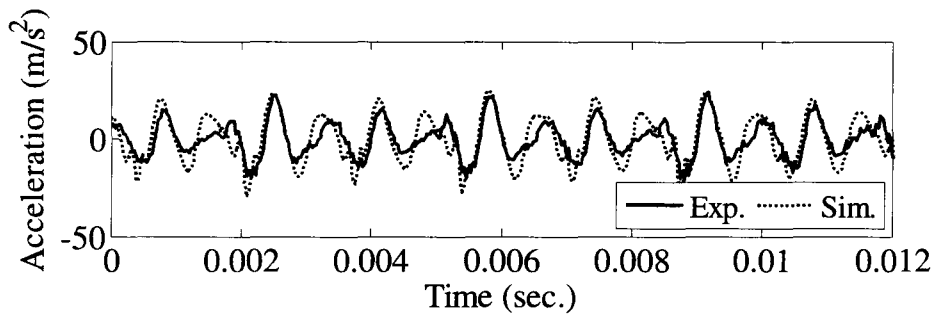


b. Y-direction.

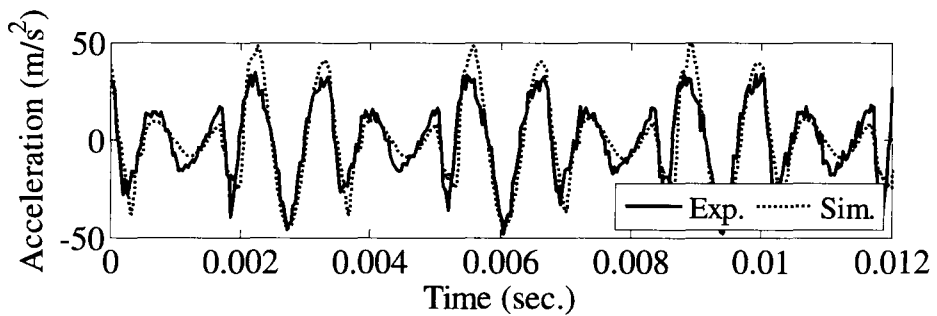


c. Z-direction.

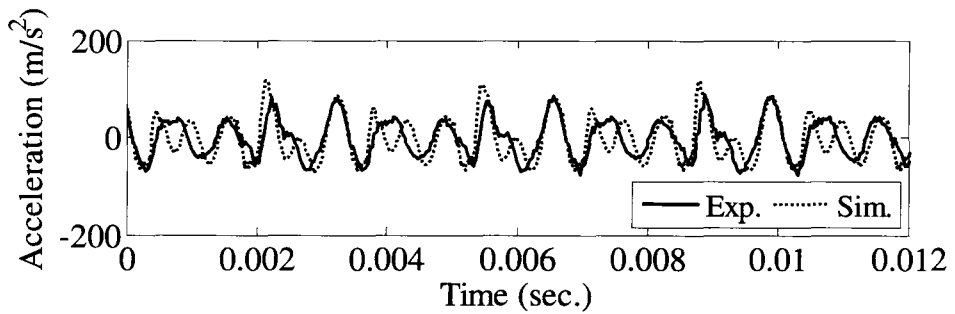
Figure D.15 – Fixture’s acceleration using setup # 1 - verification test # 6.



a. X-direction.

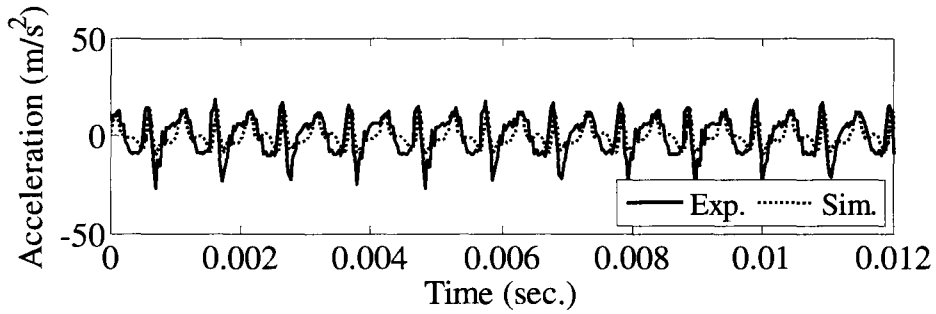


b. Y-direction.

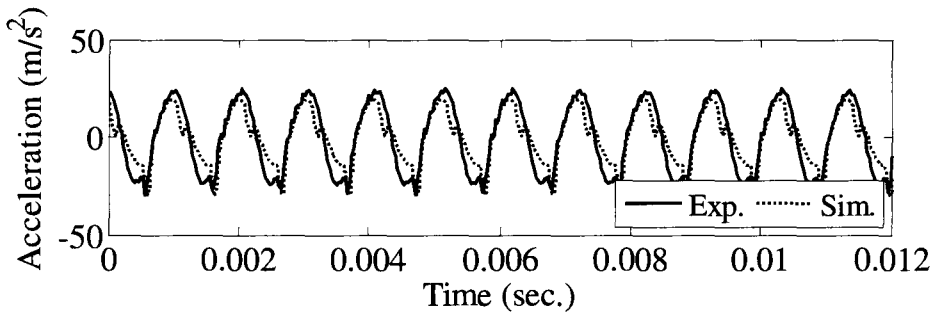


c. Z-direction.

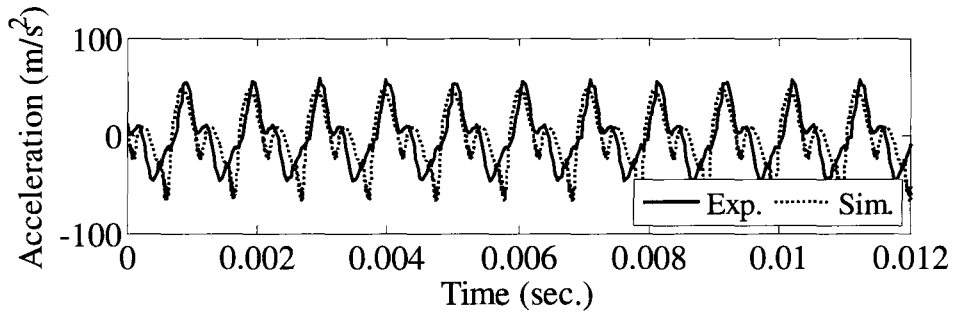
Figure D.16 – Fixture’s acceleration using setup # 1 - verification test # 7.



a. X-direction.

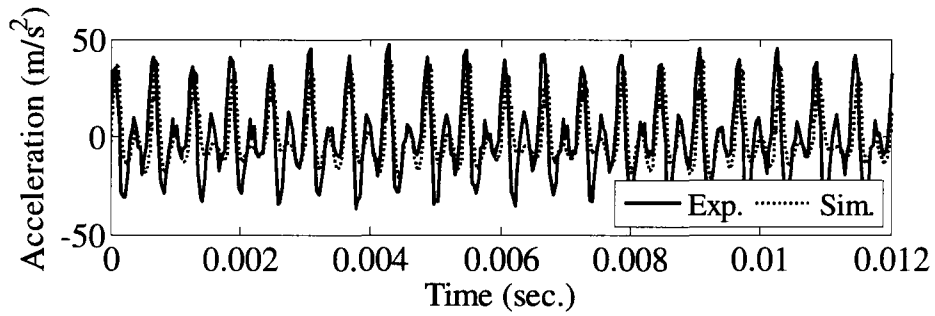


b. Y-direction.

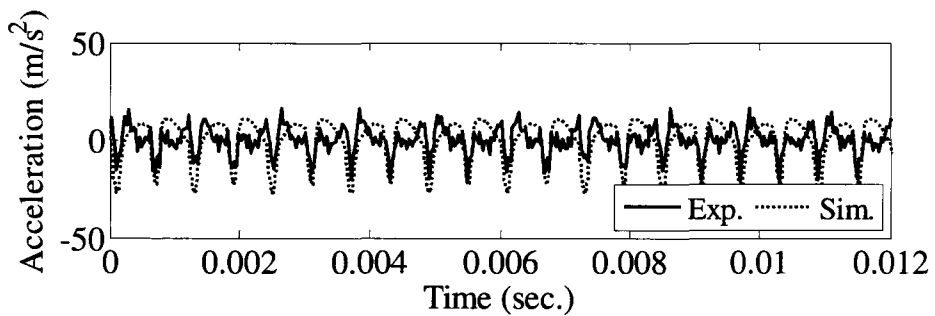


c. Z-direction.

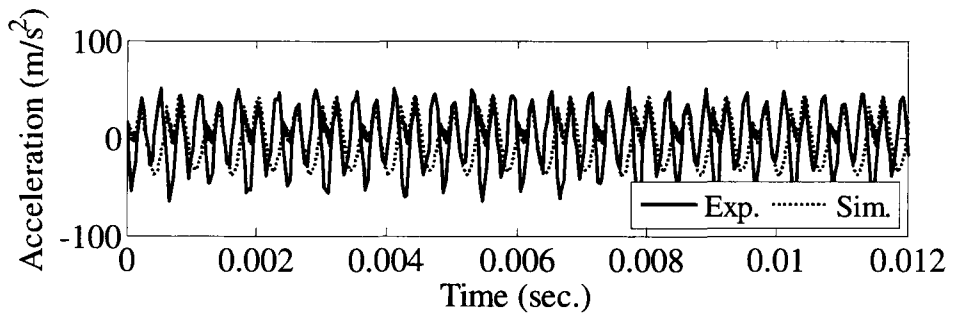
Figure D.17 – Fixture’s acceleration using setup # 1 - verification test # 8.



a. X-direction.

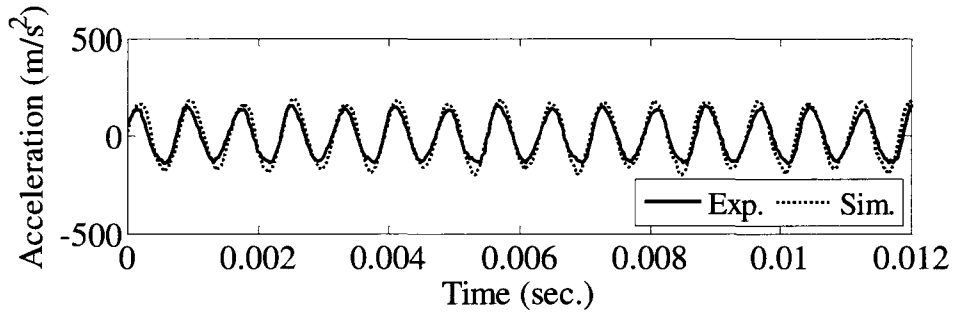


b. Y-direction.

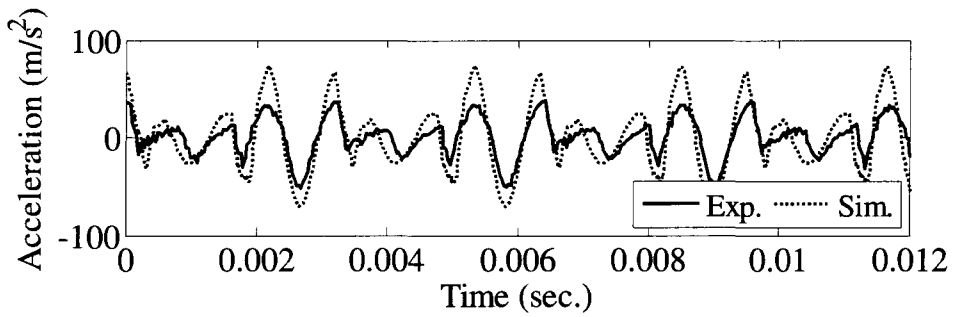


c. Z-direction.

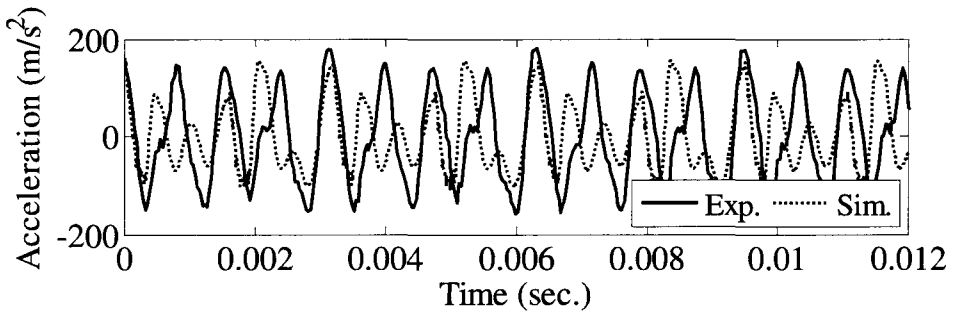
Figure D.18 – Fixture’s acceleration using setup # 1 - verification test # 9.



a. X-direction.

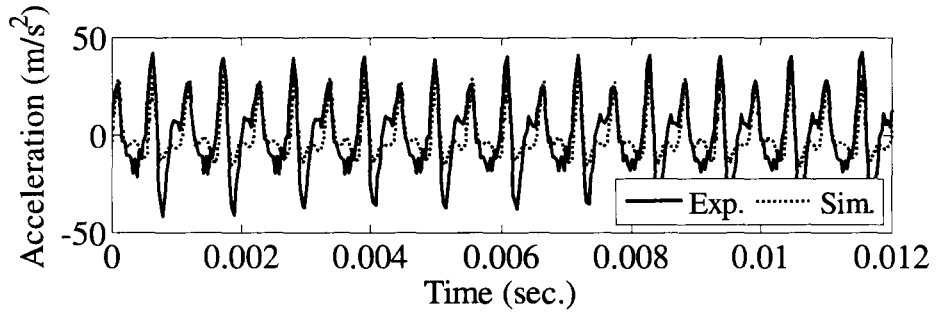


b. Y-direction.

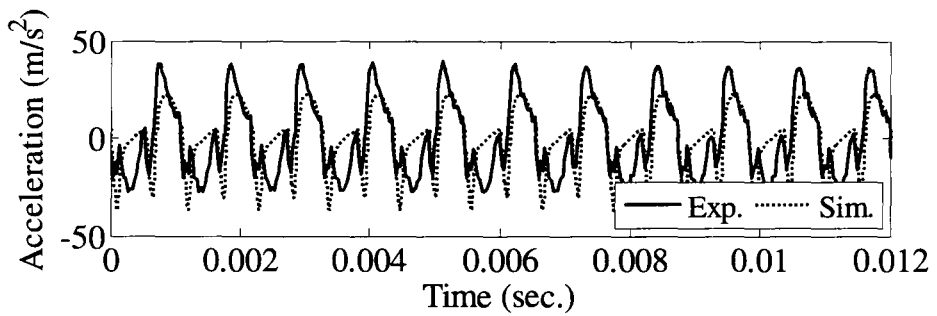


c. Z-direction.

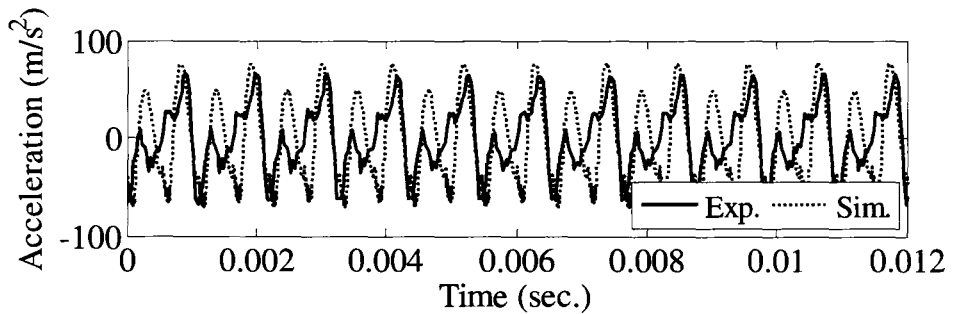
Figure D.19 – Fixture’s acceleration using setup # 1 - verification test # 10.



a. X-direction.

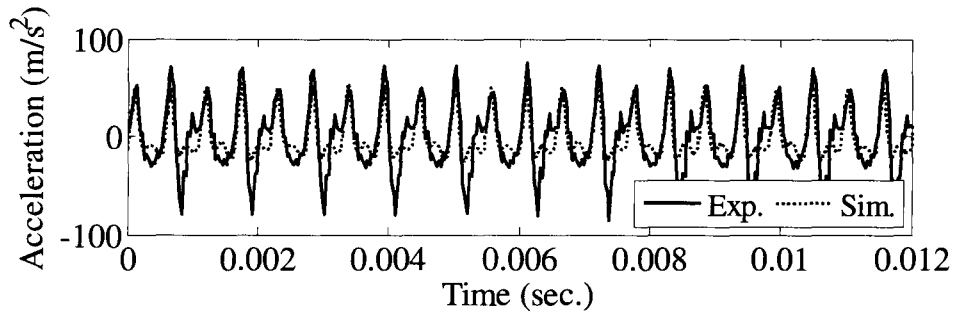


b. Y-direction.

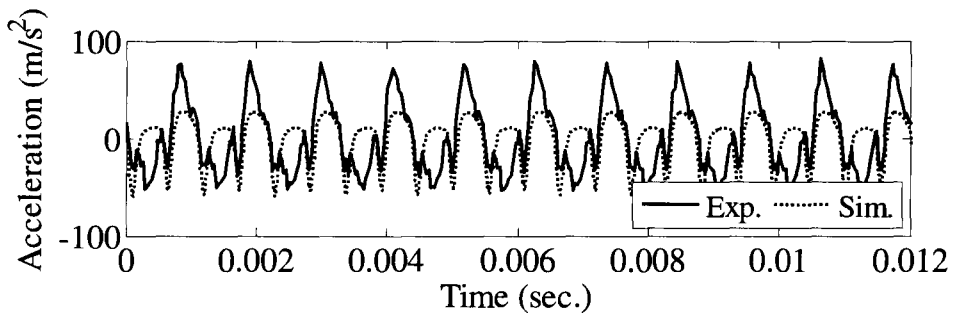


c. Z-direction.

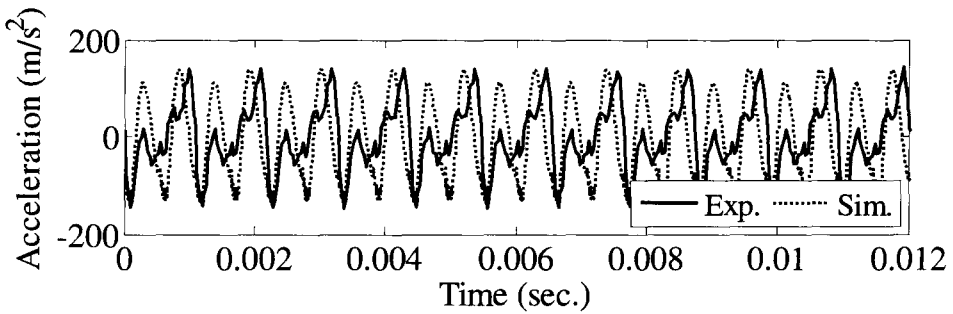
Figure D.20 – Fixture’s acceleration using setup # 1 - verification test # 11.



a. X-direction.

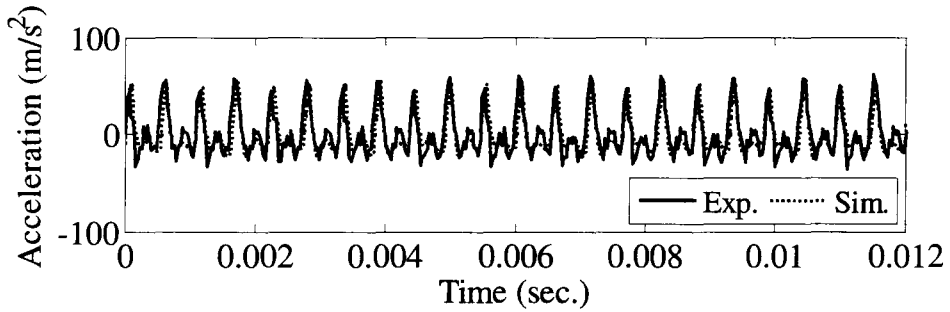


b. Y-direction.

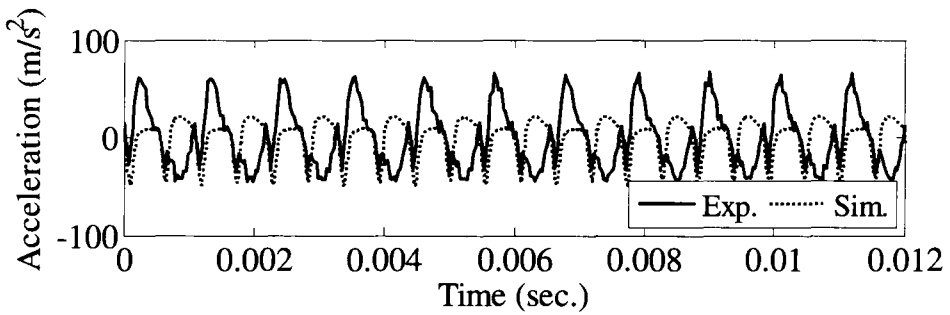


c. Z-direction.

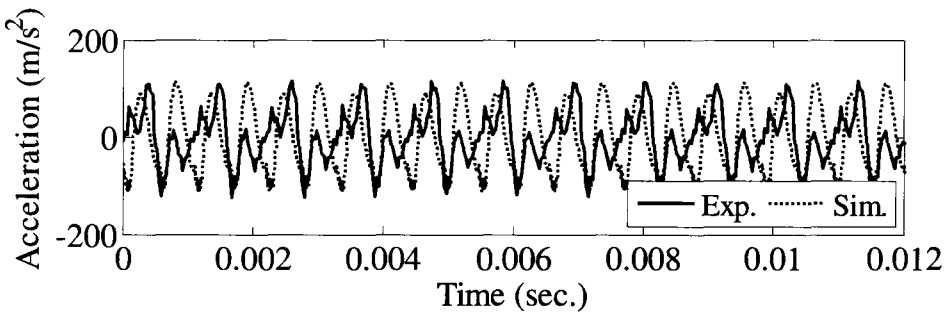
Figure D.21 – Fixture’s acceleration using setup # 1 - verification test # 12.



a. X-direction.



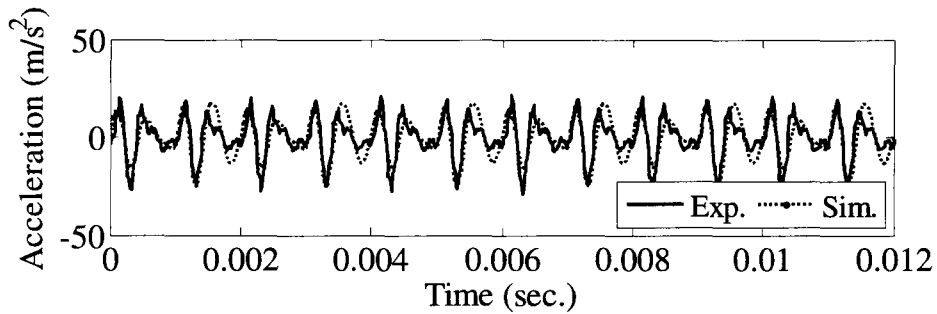
b. Y-direction.



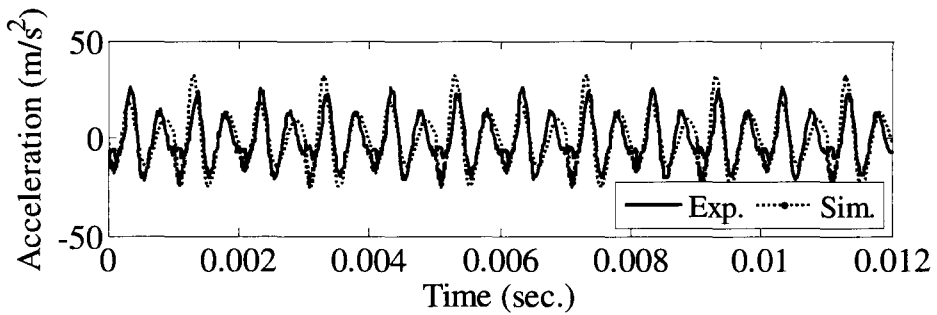
c. Z-direction.

Figure D.22 – Fixture’s acceleration using setup # 1 - verification test # 13.

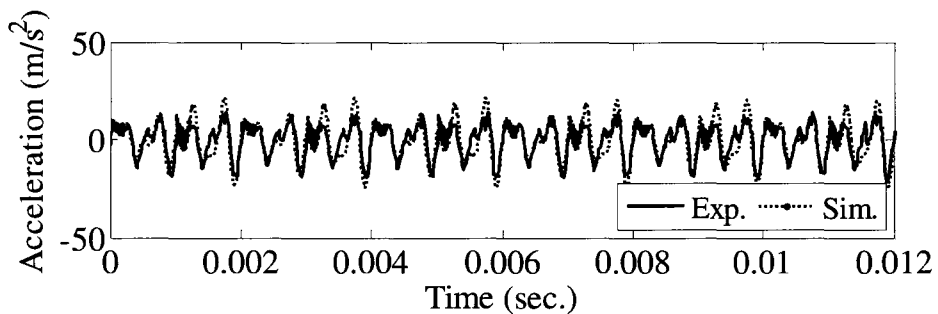
D.3 Fixture's Acceleration using Setup # 2



a. X-direction.

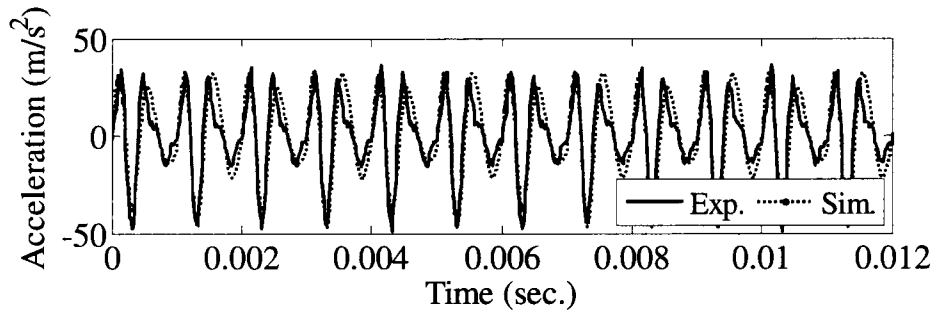


b. Y-direction.

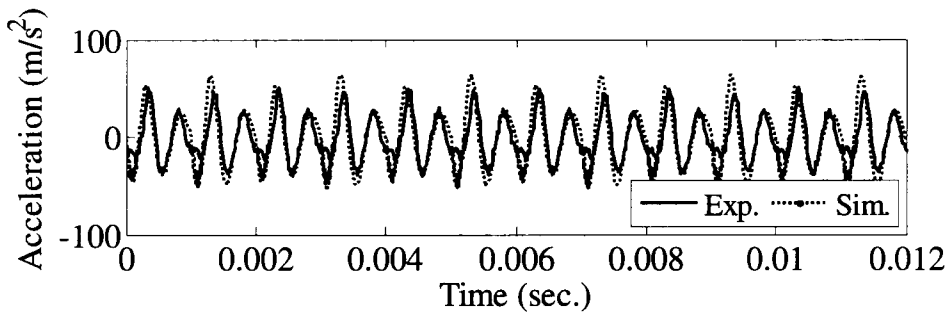


c. Z-direction.

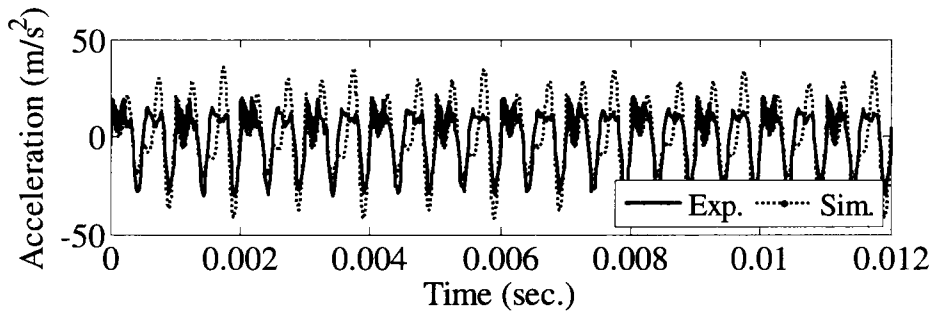
Figure D.23 – Fixture's acceleration using setup # 1 - calibration test # 1.



a. X-direction.

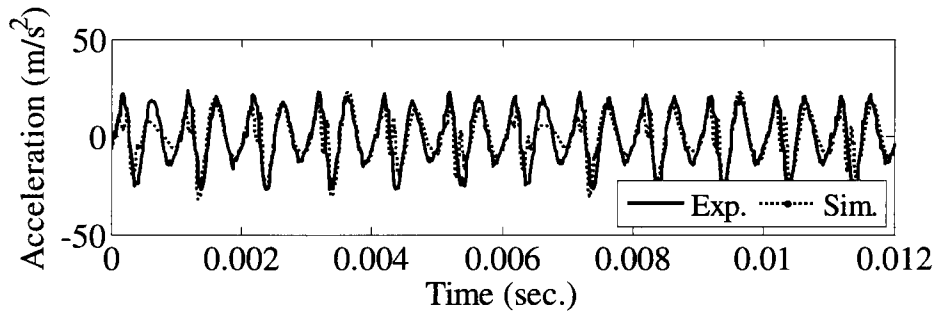


b. Y-direction.

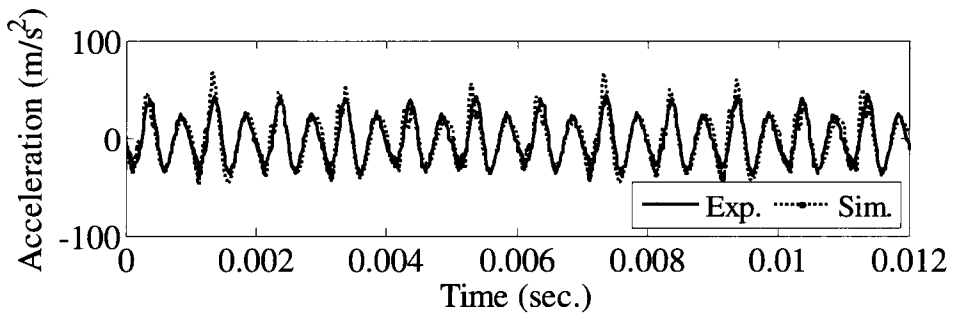


c. Z-direction.

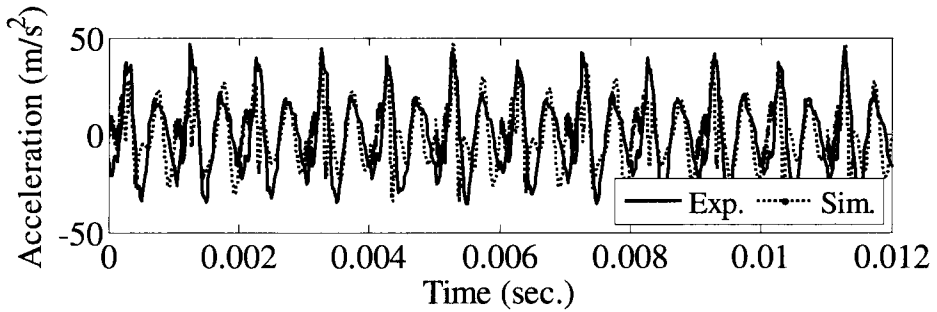
Figure D.24 – Fixture’s acceleration using setup # 2 - calibration test # 2.



a. X-direction.

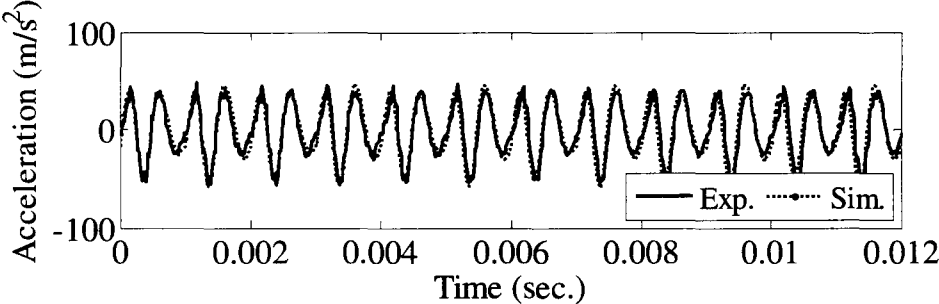


b. Y-direction.

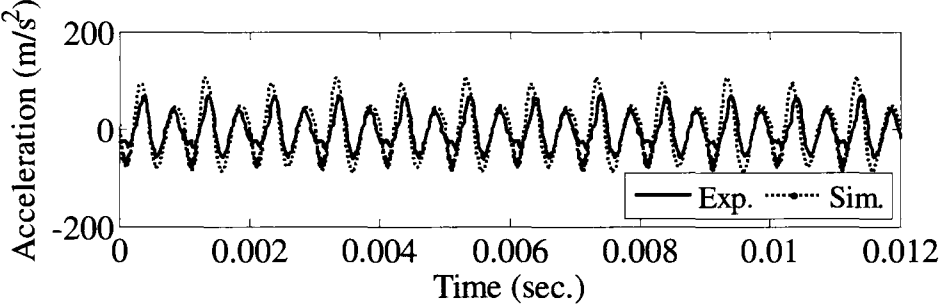


c. Z-direction.

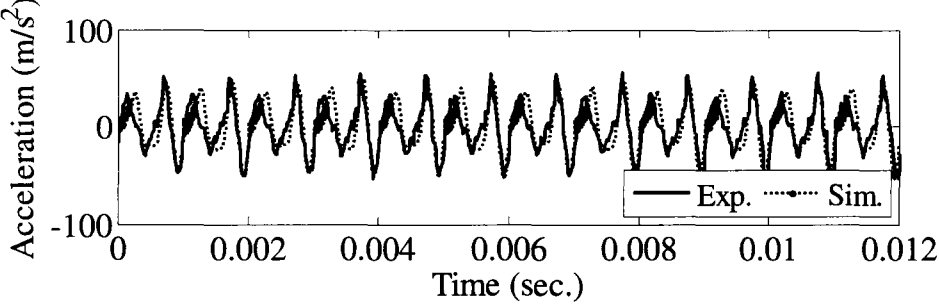
Figure D.25 – Fixture’s acceleration using setup # 2 - calibration test # 3.



a. X-direction.

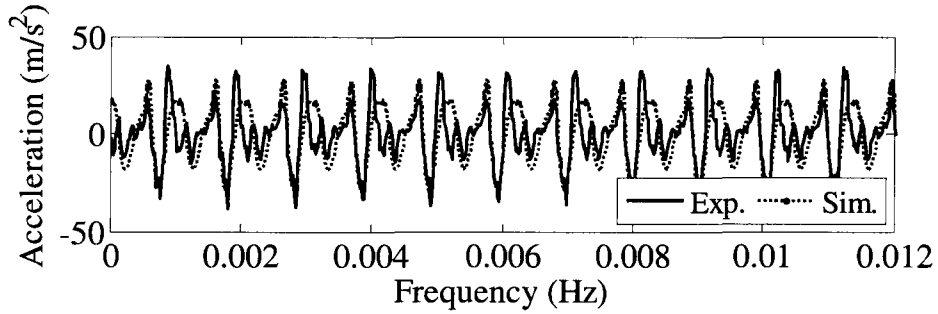


b. Y-direction.

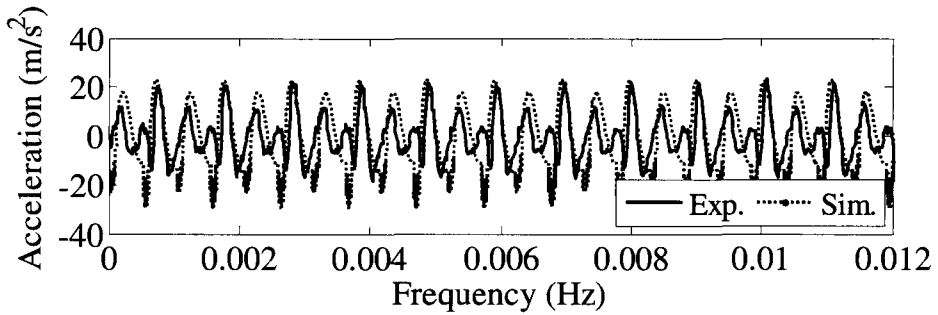


c. Z-direction.

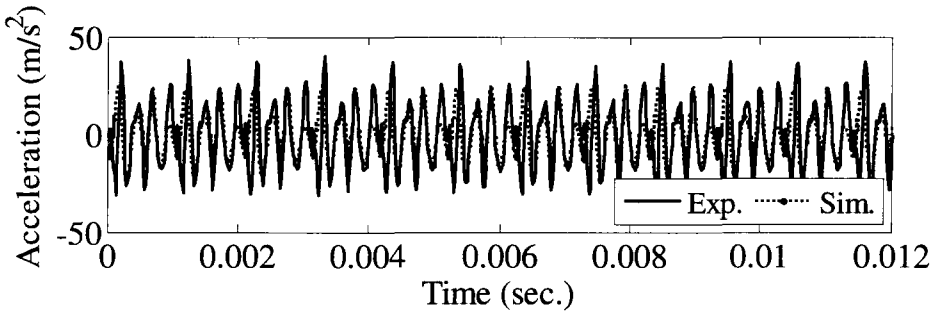
Figure D.26 – Fixture’s acceleration using setup # 2 - calibration test # 4.



a. X-direction.

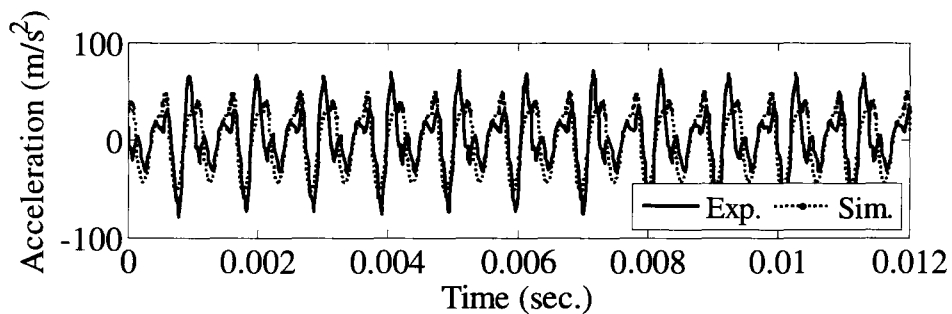


b. Y-direction.

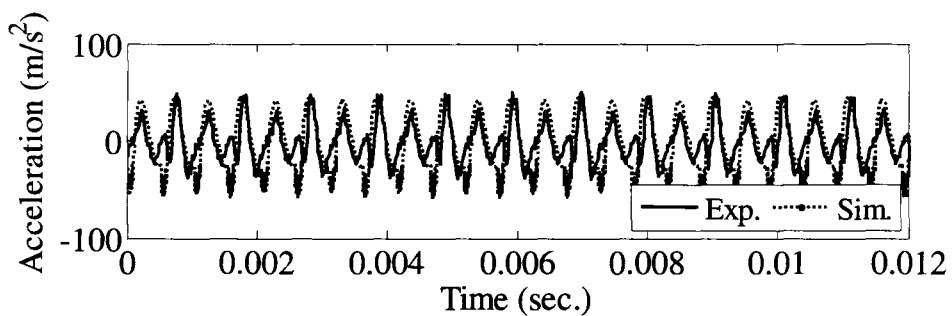


c. Z-direction.

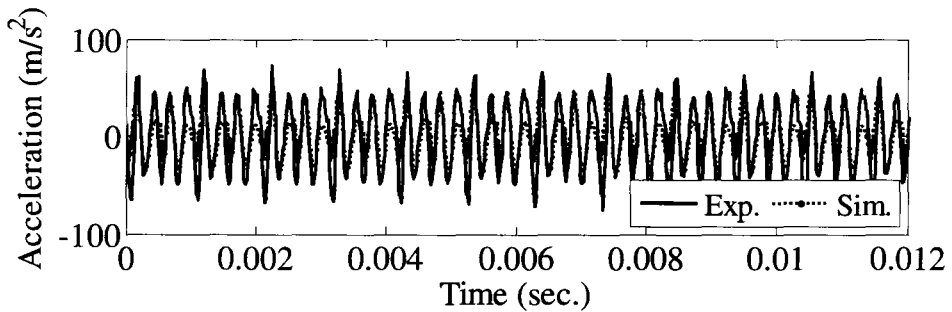
Figure D.27 – Fixture’s acceleration using setup # 2 - calibration test # 5.



a. X-direction.

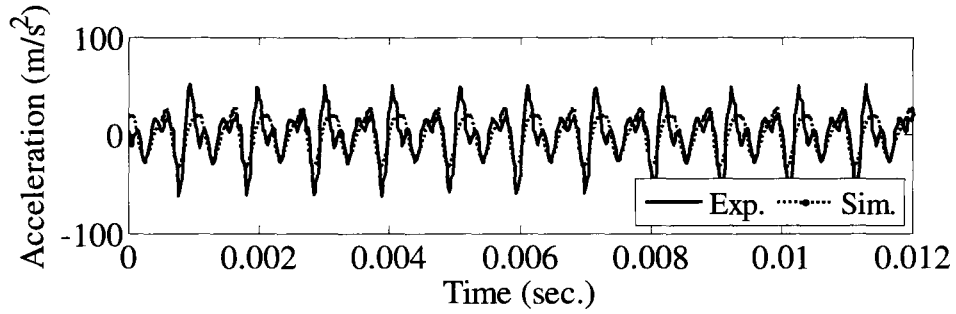


b. Y-direction.

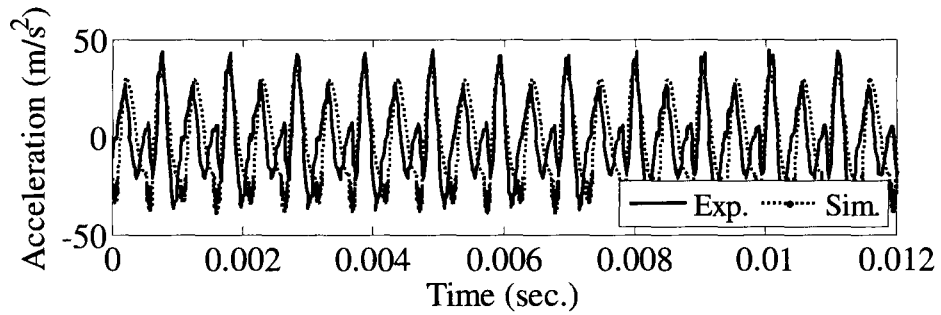


c. Z-direction.

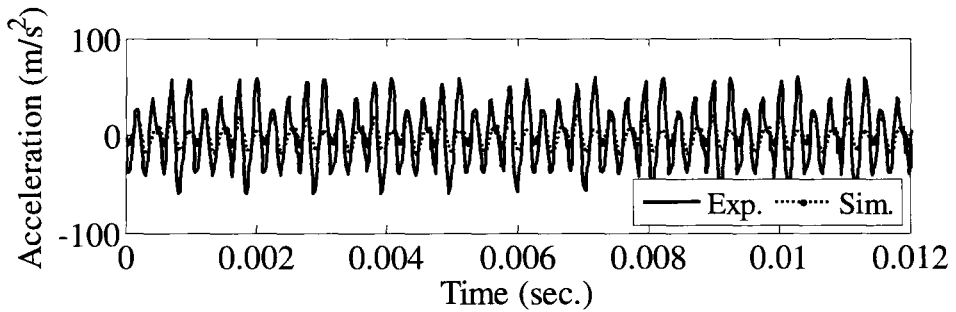
Figure D.28 – Fixture’s acceleration using setup # 2 - calibration test # 6.



a. X-direction.

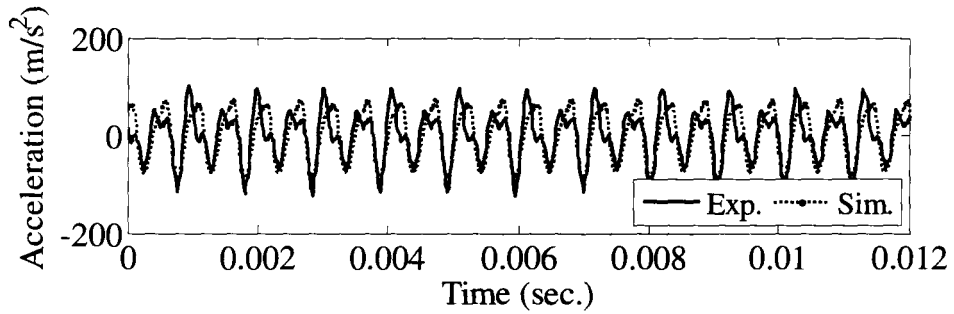


b. Y-direction.

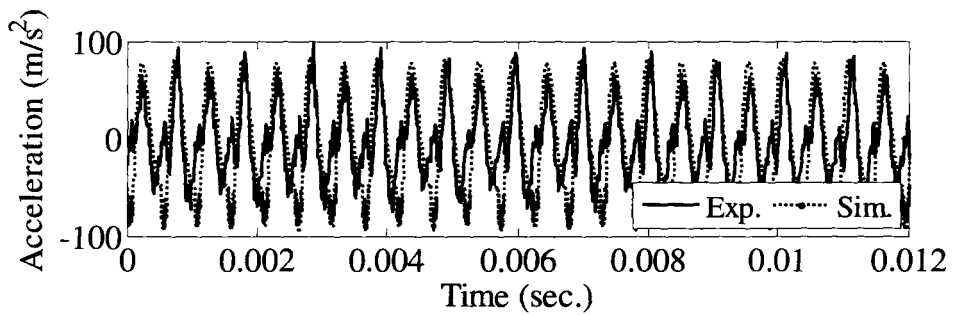


c. Z-direction.

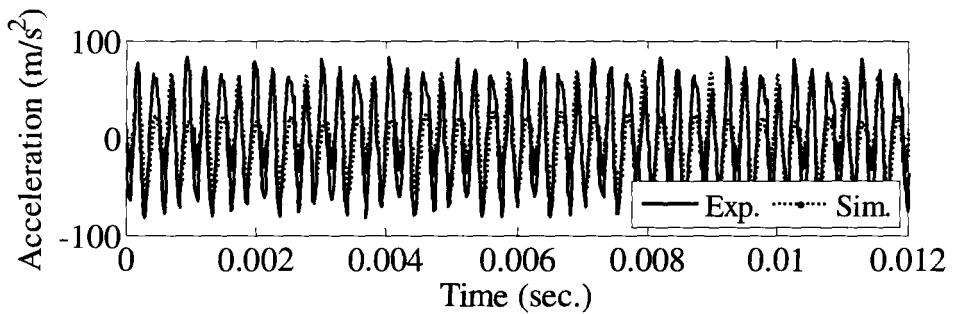
Figure D.29 – Fixture’s acceleration using setup # 2 - calibration test # 7.



a. X-direction.

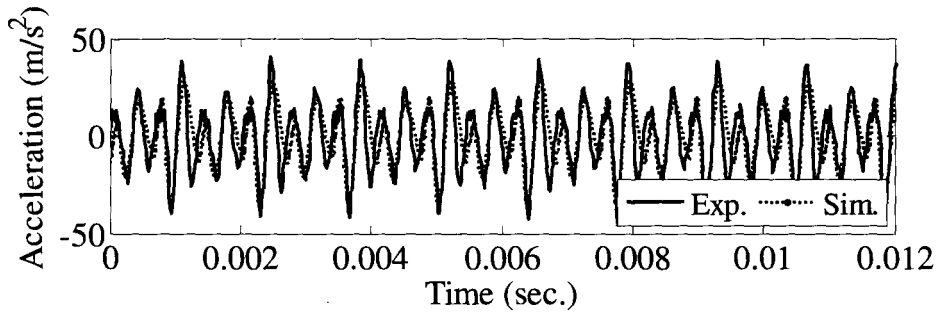


b. Y-direction.

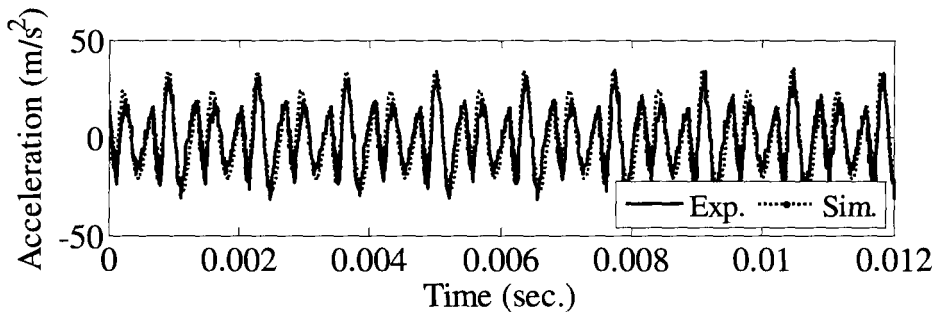


c. Z-direction.

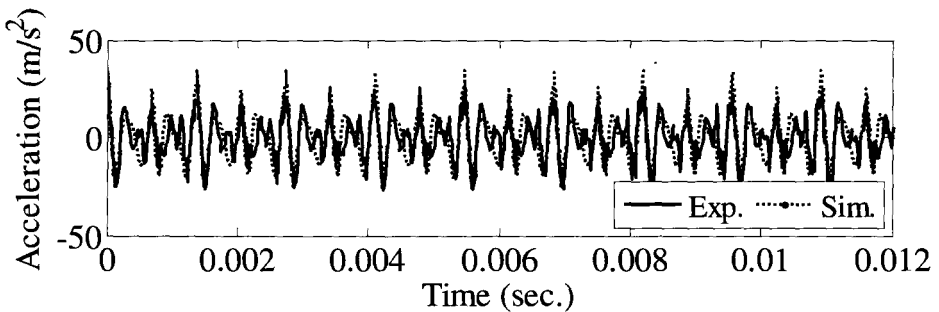
Figure D.30 – Fixture’s acceleration using setup # 2 - calibration test # 8.



a. X-direction.

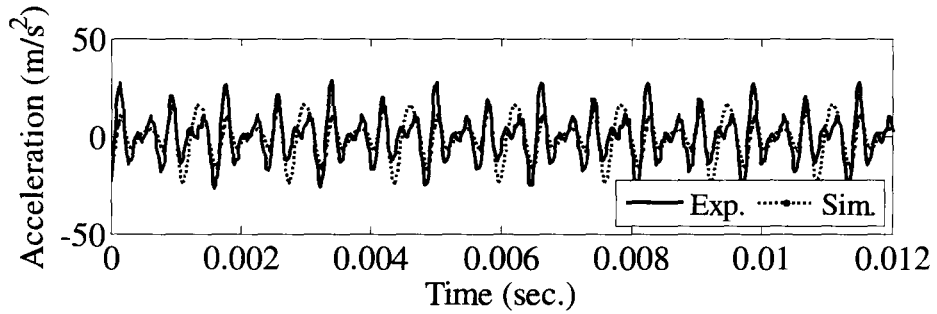


b. Y-direction.

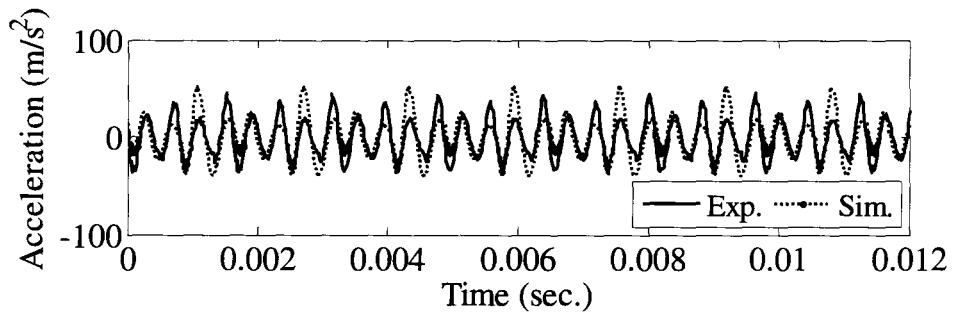


c. Z-direction.

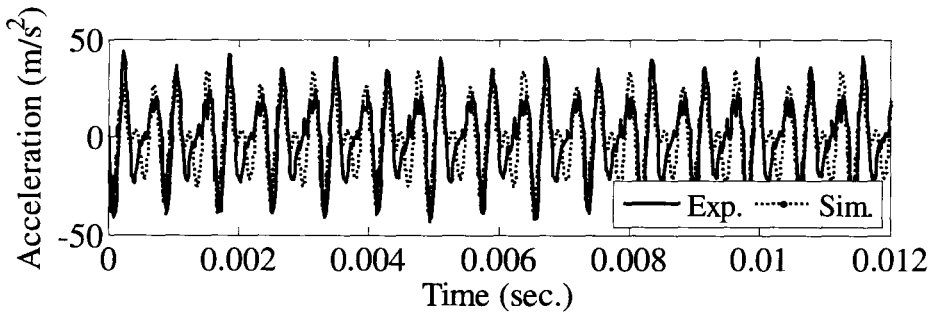
Figure D.31 – Fixture's acceleration using setup # 2 - calibration test # 9.



a. X-direction.

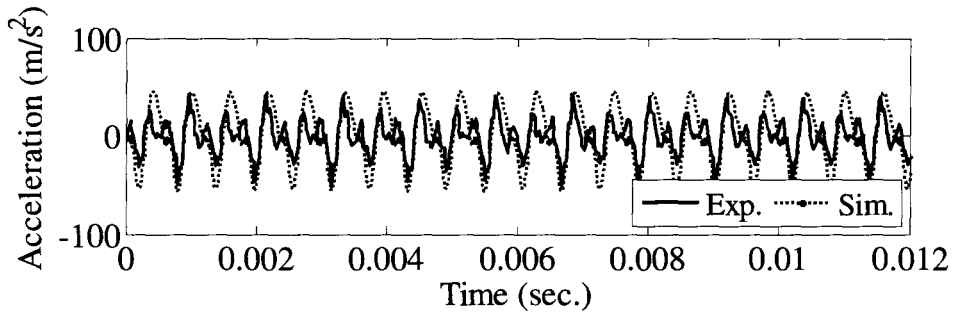


b. Y-direction.

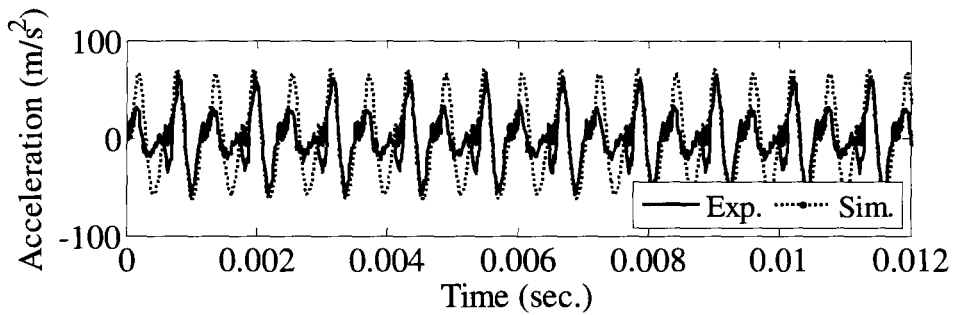


c. Z-direction.

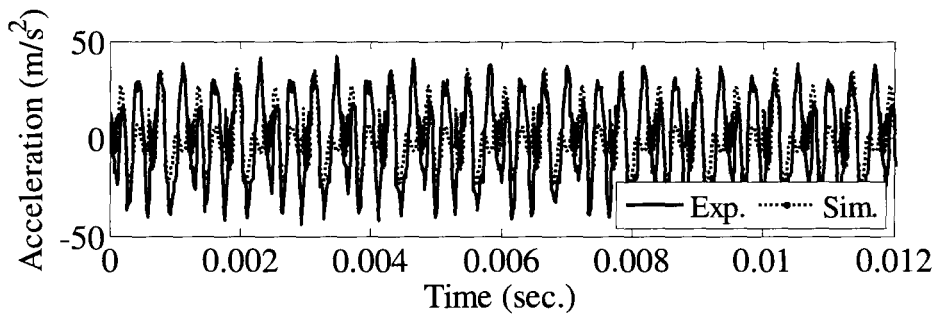
Figure D.32 – Fixture’s acceleration using setup # 2 - verification test # 1.



a. X-direction.



b. Y-direction.



c. Z-direction.

Figure D.33 – Fixture’s acceleration using setup # 2 - verification test # 2.

BIBLIOGRAPHY

- [1] Zhang W. Qiu K. Gao, T. and M. Wan. Numerical simulation of machined surface topography and roughness. *Journal of Manufacturing Science and Engineering*, 128:96–103, 2006.
- [2] Kovacic M. Brezocnik, M. and M. Ficko. Prediction of surface roughness with genetic programming. *Journal of Materials Processing Technology*, 157:28–36, 2004.
- [3] M. A. Elbestawi. High speed machining - definition, requirement, and evaluation. *Revue Internationale d'Ingénierie des Systèmes de Production Mécanique*, pages 1–3, April 2006.
- [4] KISTLER Corporation. Inertia compensated force measurements. "Presentation". <http://www.kistler.com>.
- [5] M. Richardson and D. Formenti. Parameter estimation from frequency response measurements using rational fraction polynomials. In *1st IMAC Conference*, pages 1–15, Orlando, Fl, November 1982.
- [6] J. Tlustý and F. Ismail. Basic non-linearity in machining chatter. *Annals of the CIRP*, 30(1):299–304, 1981.
- [7] M. Shaw. *Metal Cutting Principles*. Oxford, 1997.
- [8] Yucesan G. Bayoumi, A. and L. Kendall. An analytic mechanistic cutting force model for milling operations: A theory and methodology. *Journal of Engineering for Industry*, 116:324–330, 1994.
- [9] D.A. Stephenson and J.S. Agapiou. *Metal Cutting Theory and Practice*. CRC Press, 2006.
- [10] N. Kardes and Y. Altintas. Mechanics and dynamics of the circular milling process. *Journal of Manufacturing Science and Engineering*, 129:21–31, 2007.

-
- [11] E. Budak. Analytical models for high performance milling. Part II: Process dynamics and stability. *International Journal of Machine Tools and Manufacture*, 46:1489–1499, 2006.
- [12] Y. Altintas. Analytical prediction of three dimensional chatter stability in milling. *JSME International Journal, Series C*, 44(3):717–723, 2001.
- [13] I. Lozoglu and S. Liang. Modeling of ball-end milling forces with cutter axis inclination. *Journal of Manufacturing Science and Engineering*, 122:3–11, 2000.
- [14] Sadeghi M. Imani, B. and M. Kazemi. Anticipation of stability limits for two degree-of-freedom interrupted milling. *Journal of Mechanics*, 25(1):41–48, 2009.
- [15] Zhang W. Qin G. Wan, M. and Z. Wang. Consistency study on three cutting force modelling methods for peripheral milling. *Proceedings of the Institution of Mechanical Engineers, Part B: Journal of Engineering Manufacture*, 222(6):665–676, 2008.
- [16] W.-S. Yun and D.-W. Cho. An improved method for the determination of 3D cutting force coefficients and runout parameters in end milling. *International Journal of Advanced Manufacturing Technology*, 16(12):851–885, October 2000.
- [17] Braghini Jr. A. Valente C. Coelho, R. and G. Medalha. Experimental evaluation of cutting force parameters applying mechanistic model in orthogonal milling. *Journal of the Brazilian Society of Mechanical Sciences and Engineering*, 25(3):247–253, 2003.
- [18] H.-Y. Feng and N. Su. A mechanistic cutting force model for 3D ball-end milling. *Journal of Manufacturing Science and Engineering*, 123:23–29, 2001.
- [19] Vizan A. Hernandez J. Perez, H. and Guzman M. Estimation of cutting forces in micromilling through the determination of specific cutting pressures. *International Journal of Computer Integrated Manufacturing*, 190:18–22, 2007.
- [20] Lopez De Lacalle L. Sanchez J. Lamikiz, A. and M. Salgado. Cutting force integration at the cam stage in the high-speed milling of complex surfaces. *International Journal of Computer Integrated Manufacturing*, 18(7):586–600, 2005.
- [21] M. Martellotti. An analysis of the milling process. *Transactions of the ASME*, 63:667–700, 1941.
- [22] B. Ullagadi. Modeling and monitoring of cutting dynamics in end milling. Master's thesis, McMaster University, 1991.
- [23] DeVor R. Kline, W. and J. Lindberg. The prediction of cutting forces in end milling with application to cornering cuts. *International Journal of Machine Tool Design and Research*, 22(1):7, 1982.

- [24] A. Bayoumi T. Teitenberg and G. Yucesan. Tool wear modeling through an analytic mechanistic model of milling processes. *Wear*, 154:287–304, 1992.
- [25] S. Liang and J. Wang. Milling force convolution modeling for identification of cutter axis offset. *Journal of Machine Tools and MANufacture*, 34(8):1177–1190, 1994.
- [26] L. Zheng and S. Liang. Analysis of end milling forces with cutter axis tilt. *Transaction of NAMRI*, 23:137–142, 1995.
- [27] F. Ismail and M. Elbestawi. Generation of milled surfaces including tool dynamics and wear. *Journal of Engineering for Industry*, 115:245–252, 1993.
- [28] Ismail F. Elbestawi, M. and K. Yuen. Surface topography characterization in finish milling. *International Journal of Machine Tools and Manufacture*, 34(2):245–255, 1994.
- [29] L. Zheng and S. Liang. Identification of cutter axis tilt in end milling. *Journal of Manufacturing Science and Engineering*, 119:178–185, 1997.
- [30] Cho D. Yun, W. and K. Ehman. Determination of constant 3D cutting force coefficients and of runout parameters in end milling. *Transaction of NAMRI*, 27:87–92, 1999.
- [31] A. Sabberwal. Chip section and cutting force during the end milling operation. *Annals of the CIRP*, 10(3):197, 1961.
- [32] J. Tlustý and P. MacNeil. Dynamics of cutting forces in end milling. *Annals of the CIRP*, 24(1):21–25, 1975.
- [33] Y. Altintas and A. Spence. End milling force algorithm for CAD systems. *Annals of the CIRP*, 40(1):31–34, 1991.
- [34] E. Budak and Y. Altintas. Modeling and avoidance of static form errors in peripheral milling of plates. *Journal of Machine Tools and Manufacture*, 35, 1995.
- [35] A. Larue and B. Anselmetti. Deviation of a machined surface in flank milling. *International Journal of Machine Tools and Manufacture*, 43:129–138, 2003.
- [36] Y. Altintas and I. Yellowley. In-process detection of tool failure in milling using cutting force models. *Journal of Engineering for Industry*, 111:149–157, 1989.
- [37] Y. Altintas and P. Lee. Manufacturing and dynamics model for helical end mills. *Annals of the CIRP*, 45(1):59–64, 1996.

- [38] K. Shirase and Y. Altintas. Cutting force and dimensional surface error generation in peripheral milling with variable pitch helical end mills. *International Journal of Machine Tools and Manufacture*, 36(5):567–584, 1996.
- [39] Altintas Y. Budak, E. and E. Armarego. Prediction of milling force coefficients from orthogonal cutting data. *Journal of Manufacturing Science and Engineering*, 118(2):216–224, 1996.
- [40] J. MacGee. An assessment of high-speed machining. *SME technical paper*, page 648, 1978.
- [41] Winfough W. Smith, S. and J. Halley. The effect of tool length on stable metal removal rate in high-speed milling. *Annals of the CIRP*, 47:307–310, 1998.
- [42] Carbaloy Systems Department. Milling handbook of high-efficiency metal cutting. Technical report, GE Company, 1980.
- [43] V. Hann. *Kinetik des Schafrtasens*. PhD thesis, Technischen Hochschule, Aachen, 1983.
- [44] Liu X. DeVor R. Jun, M. and S. Kapoor. Investigation of the dynamics of microend milling - Part I: Model development. *Journal of Manufacturing Science and Engineering*, 128:0893 – 0900, 2006.
- [45] F. Koenigsberger and A. Sabberwal. An investigation of into the cutting force pulsations during the milling process. *International Journal of Machine Tools Design and Research*, 1:15, 1961.
- [46] C.M. Zheng and J.-J. Junz Wang. Estimation of in-process cutting constants in ball-end milling. 217:0045 – 0056, 2003.
- [47] M. Wan and W.H. Zhang. Calculations of chip thickness and cutting forces in flexible end milling. *International Journal of Advanced Manufacturing Technology*, 29:0637 – 0647, 2006.
- [48] E. Budak and Y. Altintas. Modeling and avoidance of static form errors in peripheral milling of plates. *International Journal of Machine Tools and Manufacture*, 35(3):0459 – 0476, 1995.
- [49] J.-J. Junz Wang and S. Liang. Chip load kinematics in milling with radial cutter runout. *Journal of Engineering for Industry*, 118:111–116, 1996.
- [50] Hansen H. Bissacco, G. and J. Slunsky. Modeling the cutting edge radius size effect for force prediction in micro milling. *Annals of the CIRP*, 57:113–116, 2008.

- [51] Tan G. Wan M. Zhang, W.-H. and T. Gao. A new algorithm for the numerical simulation of machined surface topography in multiaxis ball-end milling. *Journal of Manufacturing Science and Engineering*, 130:0110031–01100311, 2008.
- [52] Kim H. Lee, K. and S. Park. A run-out measuring method using modeling and simulation in four-fluted end milling. *Journal of Materials Processing Technology*, 187-188:207–211, 2007.
- [53] Zhang W. Tan G. Wan, M. and G. Qin. New algorithm for calibration of instantaneous cutting-force coefficients and radial run-out parameters in flat end milling. *Proceedings of the Institution of Mechanical Engineers, Part B: Journal of Engineering Manufacture*, 221(6):1007–1019, 2007.
- [54] O. Omar. Surface prediction in high speed machining. Master's thesis, McMaster University, June 2003.
- [55] Ismail F. Du R.X. Elbestawi, M.A. and B.C. Ullagaddi. Modeling machining dynamics including damping in the tool-workpiece interface. *ASME, PED, Tribological Aspects*, 54:253–263, 1991.
- [56] Kalveram M. Insperger T. Weinert K. Stepan G. Govekar E. Gradisek, J. and I. Grabec. On stability prediction for milling. *International Journal of Machine Tools and Manufacture*, 45:769–781, 2005.
- [57] Li X.P. Li, H.Z. and X.Q. Chen. A new chatter stability criterion in milling process simulation. *Seventh International Conference on Control, Automation, Robotics and Vision, Singapore*, pages 1371–1376, Dec. 2002.
- [58] Schroeter R. Polli M. Weingaertner, W. and J. Gomesc. Evaluation of high-speed end-milling dynamic stability through audio signal measurements. *Journal of Material Processing Technology*, 179:133 – 138, 2006.
- [59] S.-Y. Liang and L. Zheng. Analysis of end milling surface error considering tool compliance. *Journal of Manufacturing Science and Engineering*, 120:207–210, 1998.
- [60] R. Szalai B.P. Mann P.V. Bayly T. Insperger J. Gradisek G., Stepan and Govekar E. Nonlinear dynamics of high-speed milling - analyses, numerics, and experiments. *Journal of Vibration and Acoustics*, 127:197–203, 2005.
- [61] S. Merdol and Y. Altintas. Multi frequency solution of chatter stability for low immersion milling. *Journal of Manufacturing Science and Engineering*, 126:459–466, 2004.

- [62] Paris H. Peigne, G. and D. Brissaud. A model of milled surface generation for time domain simulation of high speed cutting. *Proceedings of the Institution of Mechanical Engineers, Part B: Journal of Engineering Manufacture*, 217:919–930, 2003.
- [63] Tummond M. Duncan, G.S. and T.L. Schmitz. An investigation of the dynamic absorber effect in high-speed machining. *International Journal of Machine Tools and Manufacture*, 45(4-5), 2005.
- [64] K. Mehdi and J.-F. Rigal. A numerical model for cutting process simulation and prediction of cutting forces in peripheral milling. *2004 IEEE International Conference on Industrial Technology (ICIT)*, pages 734 – 740, 2004.
- [65] A. Iglesias. Investigating various modal analysis extraction techniques to estimate damping ratio. Master’s thesis, Virginia Polytechnic Institute and State University, Blacksburg, Virginia, June 2000.
- [66] N. Maia and J. Silva. *Theoretical and Experimental Modal Analysis*. John Wiley & Sons Inc., 1997.
- [67] W. Ewins. *Modal Testing: Theory and Practice*. John Wiley & Sons Inc., 1984.
- [68] Y. Tamura. Damping in building. Technical report, Tokyo Polytechnic University, Feb. 2006.
- [69] N. M. M. Maia and D. J. Ewins. A new approach for the modal identification of lightly damped structures. *Mechanical Systems and Signal Processing*, 3(2):173–193, 1989.
- [70] Allemang R.J. Zimmerman R. Brown, D.L. and M. Mergeay. Parameter estimation techniques for modal analysis. *SAE technical paper series*, (790221).
- [71] S.R. Ibrahim. Modal identification techniques assessment and comparison. In *Proceedings of the 10th International Seminar on Modal Analysis, Part III*.
- [72] J.M. Longbottom and J.D. Lanham. A review of research related to salomon’s hypothesis on cutting speeds and temperatures. *International Journal of Machine Tools and Manufacture*, 46:1740–1747, 2006.
- [73] H. Schultz and T. Moriwaki. High-speed machining. *Annals of the CIRP*, 41(2):637–645, 1992.
- [74] R. King. *Handbook of High-Speed Machining Technology*. Chapman and Hall, 1985.

- [75] El-Wardany T. Dumitrescu M. Ng, E.-G. and M. Elbestawi. Physics-based simulation of high-speed machining. *Machining Science and Technology*, 6(3):301–329, 1992.
- [76] Subramanian K. Komanduri, R. and B. Von Turkovitch. High-speed machining. *ASME PED*, 12:37–68, 1984.
- [77] Hwang R.-M. Fuh, K.-H. A predicted milling force model for high-speed end milling operation. *Internaitonl Journal of Machine Tools and Manufacture*, 37(7):969–979, 1997.
- [78] G. Abdou and W. Tereshkovich. Optimal operating parameters in high-speed milling operations for aluminum. *International Journal of Production and Research*, 10:2197–2214, 2001.
- [79] Vishay Corporation. Strain gage knowledge base. "Technical Paper". <http://www.vishay.com>.
- [80] Cus F. Milfelner, M. and J. Balic. An overview of data acquisition system for cutting force measuring and optimization in milling. *Journal of Materials Processing Technology*, 164-165:1281–1288, 2005.
- [81] Load Cell Central. Miniature load cell. "Brochure". <http://www.800loadcel.com>.
- [82] L. Kelly. *Handbook of Numerical Methods and Applications*. Addison-Wesley Publishing Company, 1967.
- [83] B. Schwarz and M. Richardson. Experimental modal analysis. Technical report, Vibrant Technology, Inc., 1999.
- [84] M. Richardson. Global frequency and damping estimates from frequency response measurements. In *4th IMAC Conference*, pages 1–7, Los Angeles, CA, February 1986.
- [85] Matlab Corporation. fmincon. "Website". <http://www.mathworks.com>.
- [86] S.J. You and K.F. Ehmann. Synthesis and generation of surfaces milled by ball nose end mills tertiary cutter motion. *Journal of Engineering for Industry*, 113:17–24, 1991.
- [87] B. Ozturk and I. Lazoglu. Machining of free-form surfaces - Part II: Calibration and forces. *International Journal of Machine Tools and Manufacture Design and Application*, 46:736–746, 2006.
- [88] J.-J. Wang and S. Liang. Chip load kinematics in milling with radial cutter runout. *Journal of Engineering for Industry*, 118:111–116, 1996.

- [89] E. Budak and E. Ozlu. Development of a thermomechanical cutting process model for machining process simulations. *Annals of the CIRP*, 57:97–100, 2008.
- [90] Inc. eFunda. Aluminum material properties. "Website". <http://www.efunda.com>.
- [91] KISTLER Corporation. Mini-dyno type 9256 data sheet. "Website". <http://www.kistler.com>.
- [92] KISTLER Corporation. Basic theory of the hammer test method. "Website". <http://www.kistler.com>.
- [93] W.K. Rule. A numerical scheme for extracting strength model coefficients from taylor test data. *International Journal of Impact Engineering*, 19(9-10):797–810, 1997.
- [94] Madhavan M. Adibi-Sedeh, A.H. and B. Bahr. Extension of oxley's analysis of machining to use different materials models. *International Journal of Impact Engineering*, 125:656–666, 2003.
- [95] Y.B. Guo. An integral method to determine the mechanical behavior of materials in metal cutting. *Journal of Materials Processing Technology*, 142:7281, 2003.
- [96] B. Rao and Y.C. Shin. Analysis on high-speed face-milling of 7075-T6 aluminum using carbide and diamond cutters. *International Journal of Machine Tools and Manufacture*, 41:17631781, 2001.
- [97] S. C. Lina and R. J. Yangb. Force-based model for tool wear monitoring in face milling. *International Journal of Machine Tools and Manufacture*, 35(9):1201–1211, 1995.
- [98] Department of Physics and Astronomy. Thermal expansion. "Website". <http://www.ac.wvu.edu/~vawter/PhysicsNet/Topics/Thermal/ThermExpan.html>.